




Chair of Structural and Functional Ceramics

Doctoral Thesis



Strength testing of ceramics:
Reassessment of methods and application
to additive manufacturing

Dipl.-Ing. Maximilian Staudacher, BSc

October 2023



MONTANUNIVERSITÄT LEOBEN

www.unileoben.ac.at

AFFIDAVIT

I declare on oath that I wrote this thesis independently, did not use other than the specified sources and aids, and did not otherwise use any unauthorized aids.

I declare that I have read, understood, and complied with the guidelines of the senate of the Montanuniversität Leoben for "Good Scientific Practice".

Furthermore, I declare that the electronic and printed version of the submitted thesis are identical, both, formally and with regard to content.

Date 17.10.2023

Signiert von: Maximilian Staudacher
Datum: 17.10.2023 15:12:24
 <p>Dieses Dokument ist digital signiert! Dieses mit einer qualifizierten elektronischen Signatur versehenes Dokument hat gemäß Art. 25 Abs. 2 der Verordnung (EU) Nr. 910/2014 vom 23. Juli 2014 (eIDAS/107) die gleiche Rechtswirkung wie ein handschriftlich unterschriebenes Dokument.</p> <p><small>Prüfverfahren: Informationen zur Prüfung der elektronischen Signaturen finden Sie unter: www.a-trust.at/gf/</small></p>

Signature Author
Maximilian Staudacher

Meinen Großeltern

Danksagung

An erster Stelle möchte ich mich bei dem Vorstand des Instituts für Struktur- und Funktionskeramik, Univ. Prof. Dr. Raúl Bermejo, für die Ermöglichung dieser Arbeit bedanken. Trotz einer schwierigen Anfangsphase wurde mir viel Vertrauen und Nachsicht entgegengebracht, die mir schlussendlich den notwendigen Rückhalt für das Projekt einer Dissertation gaben.

Meinem Betreuer, ao. Univ. Prof. Dr. Peter Supancic, danke ich für die durchgehende und exzellente fachliche Unterstützung während der letzten Jahre. Deine Vorlesung zur Modellierung keramischer Werkstoffe begeisterte mich vor 5 Jahren zum ersten Mal für dieses Fach, und jedes Gespräch mit dir bringt neue Begeisterung hervor. Ich konnte unglaublich viel von dir lernen und freue mich, dies auch die kommenden Jahre weiterhin zu dürfen.

Ganz besonderer Dank gilt Ass. Prof. Dr. Tanja Lube. Ich denke nicht, dass ich meine Dankbarkeit an dieser Stelle in sinnvoller Länge in Worte fassen kann. Daher möchte ich hier nur deine Abschluss Worte an em. O. Univ. Prof. Dr. Robert Danzer zu seiner Emeritierung zitieren: "Manchmal braucht man ein bisserl Glück im Leben". Und ich weiß, dass ich unglaubliches Glück hatte, mit dir zusammenzuarbeiten und dich kennenzulernen zu dürfen. Ohne dich hätte ich diese Arbeit wohl nie fortgeführt und abgeschlossen.

Außerdem möchte ich mich bei meinem Mentor, Prof. Dr. Jérôme Chevalier, für die tatkräftige Unterstützung bedanken. Der fachliche Austausch und mein Auslandsaufenthalt in Lyon haben mir große Freude bereitet, und es ehrt mich ungemein, dass du dir die Mühe machst, nach Leoben zu kommen, um an meinem Rigorosum teilzunehmen.

Ebenso möchte ich em. O. Univ. Prof. Dr. Robert Danzer meinen Dank aussprechen. Durch dich habe ich erst von diesem Fach erfahren und es ehrt mich, dass wir uns die letzten Jahre besser kennen lernen durften. Es erfüllt mich mit Stolz, dass auch du an meinem Rigorosum teilnehmen wirst.

Ich danke Dr. Josef Kreith, Dr. Anna Hofer und Sarah Kohlbacher für die unbeschwertere, gemeinsame Zeit am Institut und möchte an dieser Stelle auch allen anderen Mitarbeitern des Lehrstuhls für Struktur- und Funktionskeramik meinen Dank für die reibungslose und erfüllende Zusammenarbeit aussprechen.

Bei meinen Eltern Michaela und Gerhard möchte ich mich ganz besonders für die Unterstützung während der Dissertation, aber auch während der gesamten Studienzeit bedanken. Ohne eure Hilfe hätte ich mich die letzten 9 Jahre nicht so sehr auf mein Studium fokussieren können und wäre nun nicht an diesem Punkt. Danke für das Aushalten meiner Launen, das Aufhelfen nach diversen Rückschlägen, eure grenzenlose Großzügigkeit sowie den gemeinsamen Spaß und familiären Zusammenhalt.

Daran anknüpfend möchte ich mich auch bei meiner Schwester Viktoria von ganzem Herzen bedanken. Ich freue mich ungemein, dass wir uns in den letzten Jahren stets aufeinander verlassen konnten, und ich bin mir sicher, dass das auch wei-

terhin so bleiben wird. Avolechenkia!

Meinen langjährigen Freunden Alex, Christian, Peter und Benoît möchte ich für die vielen gemeinsamen Erlebnisse der letzten Jahre danken. Das gemeinsame Wandern, Schifahren, Kochen und Feiern prägte die letzten Jahre und machte die Zeit zu einer unvergesslichen Periode meines Lebens. Das Wissen, jederzeit auf euren Rückhalt zählen zu können, war mir eine wichtige Stütze. Ebenso möchte ich Harald und Katrin danken, aus unseren zahlreichen gemeinsamen Boulder-Sessions haben sich wunderbare Freundschaften entwickelt, die mir insbesondere während des Verfassens dieser Arbeit enorme Freude bereiteten.

Mit großer Dankbarkeit möchte ich auch Mathis, Alex, Kevin und Stolo erwähnen. Durch euch konnte ich eines meiner liebsten Hobbies, Magic: The Gathering, endlich wieder in vollem Ausmaß ausüben. Wichtiger jedoch, im Zuge der vielen gemeinsamen Partien und spielintensiven Wochenenden am Lachtal haben sich enge Freundschaften entwickelt, die ich unglaublich schätze.

Schlussendlich möchte ich noch meinen Großeltern Gertrud Staudacher sowie Helmut & Waltraut Slanina von ganzem Herzen danken. Ihr wart Vorbilder für mich, gabt mir Kraft und es schmerzt sehr, dass ihr die Fertigstellung dieser Arbeit nicht mehr erleben konntet.

Kurzfassung

Keramische Werkstoffe werden zunehmend in Form von Hochleistungsbauteilen in Gebieten wie der Medizintechnik, Raumfahrt, Elektronik und Sensorik eingesetzt. Die Basis dafür bildet ihre einzigartige Kombination aus mechanischen Materialeigenschaften wie Härte, Dichte, Festigkeit oder ihr Widerstand gegen Verschleiß, und funktionellen Eigenschaften, wie einstellbarer elektrischer und thermischer Leitfähigkeit. Im Zuge der Materialentwicklung für solche Bauteile ist die Festigkeitsprüfung ein essenzielles Mittel, um das mechanische Materialverhalten zu charakterisieren und Eigenschaftsänderungen zu beurteilen. Zusätzlich erlaubt die genaue Kenntnis der Festigkeit und der ihr zugehörigen Streuung, das Versagen spröder Bauteile vorherzusagen und ihre Lebensdauer abzuschätzen. Da sich keramische Werkstoffe durch ihre speziellen Materialeigenschaften stark von anderen Materialklassen unterscheiden, wurden im Zuge der letzten 50 Jahre eine Vielzahl spezieller Prüfmethoden entwickelt.

Ziel der vorliegenden Arbeit war es, bestehende Methoden zur Festigkeitsprüfung in ihrer Anwendbarkeit zu erweitern beziehungsweise weiterzuentwickeln oder neue Methoden zu entwickeln. Dies wurde für eine Auswahl an zweiachsigen Biegeversuchen durchgeführt. Für den Ball-on-Ring-Versuch wurde die mathematische Beschreibung des Verschiebungs- und Spannungsfeldes komplett überarbeitet und mit Finite-Elemente-Simulationen validiert. Für den Ball-on-Three-Balls-Versuch wurde die Auswertung der maximalen Zugspannung vereinfacht und um die Festigkeitsprüfung quadratischer Platten erweitert. Zusätzlich wurden für diese Methode der Einfluss nicht-linearer, lastabhängiger Effekte auf die gemessene Festigkeit analysiert und in die Auswertung mit einbezogen, sodass nun auch Festigkeitsprüfungen bei starker Durchbiegung genau bewertet werden können. Diese Ergebnisse wurden in Einzelfällen auch experimentell mittels Röntgen-Tomographie validiert. Die Vergleichbarkeit des Ball-on-Three-Balls-Versuchs mit anderen Methoden wurde ermöglicht, indem numerisch generierte Daten für die effektiven Größen weitläufig zugänglich gemacht wurden. Die Anwendung dieser Daten wurde durch einen Vergleich mit dem Ring-on-Ring-Versuch demonstriert. Im Zuge dieses Vergleichs wurde der Einfluss reibungsreduzierender Schichten für den Ring-on-Ring-Versuch diskutiert und der Einfluss unebener Oberflächen auf die Festigkeitsprüfung untersucht.

Ein weiterer Fokus dieser Arbeit war die Festigkeitsprüfung additiv gefertigter, keramischer, Bauteile. Im Zuge der additiven Fertigung werden prozess- und orientierungsabhängige, periodische Strukturen auf der Oberfläche jedes Bauteils eingebracht, die Spannungskonzentrationen verursachen und damit das Versagen signifikant beeinflussen. Zusätzlich ist die Größe der Bauplattform in vielen Prozessen begrenzt, sodass die notwendige Menge an Prüfkörpern für eine statistische Festigkeitsauswertung nicht in einem einzelnen Durchgang hergestellt werden kann. Um diese Aspekte berücksichtigen zu können, wurde eine neuartige Versuchsmethode, basierend auf der Prüfung spezieller Kragbalken, entwickelt. Es wurde eine theoretische Betrachtung und Fehlerabschätzung dieser Methode durchgeführt, und dies mit experimentellen Ergebnissen in Bezug gesetzt.

Abstract

Ceramic materials have found their way into a multitude of technical fields such as medical implants, spaceflight, electronics and sensorics in the form of high-performance components. This is due to their unique combination of structural and functional properties, such as hardness, density, strength, or tuneable electrical and thermal conductivity. In the process of material development for such components, strength testing is an essential tool to characterise the structural material behaviour and to assess the development process. Additionally, the knowledge of the material's strength and its underlying scatter allows the prediction of the failure of brittle components and an estimation of the expected lifetime in service. Since ceramic materials differ significantly from other material classes, a variety of testing methods have been specifically developed for ceramics over the past 50 years.

The goal of this work was to develop and extend the application range or further develop existing methods for strength testing. This was done for a selection of biaxial bending tests and, depending on the individual testing method, was accomplished on different levels for each method. For the Ball-on-Ring-test, the mathematical description of the stress- and deflection-field was completely reworked and validated through Finite-Element-Analysis. For the Ball-on-Three-Balls-test, the evaluation of the maximum tensile stress was simplified significantly and extended to allow strength testing of square plates. Furthermore, the influence non-linear, load-dependent effects on the measured strength was analysed and included in the current evaluation, which now enables testing if large deflections occur. These findings were validated not just through simulations, but also through experimental data obtained through X-ray tomography in some cases. Additionally, the comparability of the Ball-on-Three-Balls-test to other testing methods was made possible through providing the numerical data for the effective volume and surface on an open-access scale. The application of this data was demonstrated by a comparison of the Ball-on-Three-Balls-test to the Ring-on-Ring-test. Alongside this comparison, the influence of friction-reducing intermediate layers for the Ring-on-Ring-test was discussed and the influence of uneven surfaces on the measured strength was investigated.

Another focus of this work was set on strength testing of additively manufactured ceramic specimens or components. During fabrication, process- and orientation-specific, periodic structures are created on the surface of each component, which cause stress concentrations and subsequently affect the failure behaviour significantly. Additionally, the maximum component size is restricted for most manufacturing processes, so that the necessary number of specimens for statistical strength analysis cannot be fabricated within a single print-job. In order to consider these aspects appropriately, a novel testing method, based on strength testing of cantilevers, was developed. Within this work, a detailed theoretical analysis of the testing method and possible sources of error was performed, and the results were put into perspective and validated through experimental work.

List of Abbreviations & Symbols

Abbreviation	Description
2D	Two-dimensional
3D	Three-dimensional
4PB	Four-point-bending
3PB	Three-point-bending
APDL	Ansys Parametric Design Language
ATZ	Alumina toughened zirconia
B3B	Ball-on-Three-Balls
BoR	Ball-on-Ring
DIC	Digital Image Correlation
DLP	Digital light processing
FEA	Finite Element Analysis
FFG	Austrian Research Promotion Agency
FPS	First Principal Stress
IKTS	Fraunhofer Institute for Ceramic Technologies and Systems
LCM	Lithography based ceramic manufacturing
LED	Light emitting diode
LVDT	Linear Variable Differential Transformer
PIA	Principle of Independent Action
RoR	Ring-on-Ring
SLA	Stereolithography
USA	United states of America
UTM	Universal testing machine
VPP	Vat photopolymerisation

Symbol	Description	Unit
a	Crack length	m
a_c	Critical crack length	m
b_1, b_2	Cantilever width	m
B	Width of a solid body	m
$c_0 - c_9$	Dimensionless fitting constants	—
D	Specimen diameter	m
D_{eq}	Equivalent specimen diameter	m
D_j	Dimensionless stress magnitude	—
D_{LR}	Load ring diameter	m
D_{rad}	Dimensionless radial stress magnitude	—
D_{tan}	Dimensionless tangential stress magnitude	—
D_{SR}	Support ring diameter	m
E	Young's modulus	GPa
E^*	Effective Young's modulus	GPa
F	Probability of failure	—
f_{B3B}	Dimensionless stress factor	—
$g(x, y, z)$	Shape function	—
G_c	Critical energy release rate	J/m^2
G_I	Mode I energy release rate	J/m^2
h	Specimen thickness (bar or cantilever)	m
H	Height of a solid body	m
i	Ranking number	—
I	Second moment of area	m^3
k	Slope of the cantilever's flanks	—
k_{reg}	Slope determined through regression	—
K_I	Mode I stress intensity factor	$MPa\sqrt{m}$
K_{Ic}	Critical Mode I stress intensity factor	$MPa\sqrt{m}$
l	Support roller span length	m
l_1	Outer roller span length	m
l_2	Inner roller span length	m
L_{mean}	Mean specimen edge length	m
L_1, L_2	Specimen edge lengths	m
m	Weibull modulus	—
m_{reg}	Weibull modulus determined through regression	—
M	Bending stiffness of a plate	$MPa\ m$
N	Total number of measured data	—
$p(r)$	Surface load distribution	MPa
P	Applied load	N
q	Surface load	MPa
q_{con}	Constant surface load	MPa
r	radial distance	m
R	Specimen radius	m
R_B	Support ball radius	m
R_{con}	Radius of the area of constant load	m
R_{con}^*	Corrected radius of the area of constant load	m
$R_{con,Hertz}$	Radius of the area of Hertzian load	m
R_{LR}	Load ring radius	m
R_{LB}	Load ball radius	m
R_S	Support radius	m

Symbol	Description	Unit
R_{SR}	Support ring radius	m
S	Surface area	m^2
S_0	Reference surface	m^2
S_{eff}	Effective surface	m^2
$S_{eff,3PB}$	Effective surface in three-point-bending	m^2
$S_{eff,4PB}$	Effective surface in four-point-bending	m^2
$S_{eff,B3B}$	Effective surface for the B3B-test	m^2
$S_{eff,BoR}$	Effective surface for the BoR-test	m^2
$S_{eff,RoR}$	Effective surface for the RoR-test	m^2
t	Specimen thickness (plate)	m
U	Stored elastic energy	J
V	Specimen volume	m^3
V_0	Reference volume	m^3
V_{eff}	Effective volume	m^3
$V_{eff,3PB}$	Effective volume in three-point-bending	m^3
$V_{eff,4PB}$	Effective volume in four-point-bending	m^3
$V_{eff,B3B}$	Effective volume for the B3B-test	m^3
$V_{eff,BoR}$	Effective volume for the BoR-test	m^3
$V_{eff,RoR}$	Effective volume for the RoR-test	m^3
w	Specimen width (bar)	m
W	Work by external loads	J
Y	Geometry factor	–
z	Distance to the neutral plane	m
α	Dimensionless factor	–
β	Dimensionless factor	–
γ	Surface energy per unit area	J/m^2
δ_{max}	Maximum specimen deflection	m
θ	Angle	$^\circ$
μ	Coefficient of friction	–
ν	Poisson's ratio	–
ρ	Normalized radial position	–
$\sigma(x, y, z)$	Stress	MPa
σ_0	Characteristic strength	MPa
σ_{max}	Maximum tensile stress	MPa
σ_I	First principal stress	MPa
σ_{II}	Second principal stress	MPa
σ_{III}	Third principal stress	MPa
σ_f	Failure stress	MPa
σ_{eq}	Equivalent uniaxial stress	MPa
$\sigma_{eq,FPS}$	Equivalent stress using the FPS-criterion	MPa
$\sigma_{eq,PIA}$	Equivalent stress using the PIA-criterion	MPa
σ_{ref}	Reference stress	MPa
σ_{rad}	Radial stress component	MPa
σ_{tan}	Tangential stress component	MPa
σ_x	Stress in x-direction	MPa
σ_y	Stress in x-direction	MPa
τ_x	Shear stress in xy-direction	MPa

Contents

Affidavit	iii
Danksagung	vii
Kurzfassung	ix
Abstract	xi
List of Abbreviations & Symbols	xiii
Contents	xvii
1 Introduction and motivation	1
2 Strength of brittle materials	3
2.1 Background	3
2.1.1 Brittle failure	3
2.1.2 Defects in conventionally and additively manufactured ceramics	5
2.2 Fracture statistics	8
2.3 Testing methods	13
2.3.1 Uniaxial bending tests	13
2.3.2 The Ring-on-Ring-test	15
2.3.3 The Ball-on-Ring-test	19
2.3.4 The Ball-on-Three-Balls-test	22
2.3.5 Strength testing of additively manufactured ceramics	26
2.4 Practical limitations of strength testing	28
3 Relevant methods	33
3.1 Numerical methods	33
3.2 Experimental methods	34
4 Advancements of established methods and the extension towards additive manufacturing	37
4.1 Deriving an analytical solution for the BoR-test	37
4.2 Extending the range of application of the B3B-test	38
4.3 Comparing the B3B-test to the RoR-test	41
4.4 Applying the obtained knowledge to the development of a novel test method	44
5 Summary & Outlook	47
6 List of Publications	50
6.1 Contributions as first author	50
6.2 Contributions as co-author	51

6.3 Contributions to the publications as first author	51
7 Funding acknowledgements	53
8 References	54

1. Introduction and motivation

Throughout the past and current century technical ceramics and glasses, which are manufactured from synthetic materials, have become a staple in many high-performance fields. Some of the most notable applications of these materials are found in the fields of medical implants, spaceflight, communication systems and microelectronics. For every case, the use of brittle materials can be traced back to one (or often several) of their outstanding structural or functional properties. For the structural aspect, a high compressive strength at comparably low densities, excellent high-temperature stability, an exceptional hardness (and consequently a high wear resistance) are some of the most outstanding properties. Furthermore, a high corrosion resistance and exceptional biocompatibility positions these materials as prime candidates for any applications in the medical field. In terms of functional properties, a unique combination of electrical, optical, and magnetic properties has made these materials attractive contenders for any field related to electronics and sensorics. Especially the highly non-linear dependence of some material's electrical resistance on the acting electric field as well as the piezo-electric effect have made them irreplaceable for electronic components such as varistors, sensors and actuators [1]–[3].

However, one of the biggest drawbacks of ceramics and glasses is their brittle failure behaviour. Due to their chemical bonding, plastic deformation at room temperature is a rare occurrence and single, critical flaws in the material lead to sudden, catastrophic failure of the stressed component. Due to the statistical distribution of such flaws, which occurs in each component or specimen, a certain amount of scatter of the material's strength is generally observed [3]–[6]. In order to ensure a reliable application of ceramic or glass components in service, it is necessary to understand the failure behaviour and the accompanying scatter of all relevant properties [7]–[9]. One of the key methods to gather vital information, predict failure and ultimately improve the reliability of components, is strength testing. It is an essential tool for material development, component design, weakness analysis and often forms the basis for toughness measurements. Since the compressive strength of brittle materials is generally a magnitude (or even more) higher than the tensile strength, only the latter will be of relevance for this work. With the advent of technical ceramics based on synthetic materials in the 50s and 60s of the past century, a better understanding of their characteristics ensued and strength testing was successively adapted to the special requirements of ceramics and glasses. These requirements mostly stem from a high stiffness and the lack of plastic deformation of the investigated materials which cause, if not considered adequately, a number of problems and sources of errors during testing. To the present day, a multitude of strength testing methods have been specifically developed for brittle materials [3], [4], [8], [10].

In general, these methods can be categorised by the dimensionality and shape of their stress field, e.g. into uniaxial and biaxial testing methods. Some other important criteria for method selection or differentiation are the way that the load is applied, the error tolerance as well as the necessary amount of specimen prepa-

ration. Especially the latter is significantly more time- and cost-intensive for ceramics and glasses in comparison to other material classes. Furthermore, it poses the risk of introducing or removing flaws into the surface or sub-surface-region of the specimens, thus altering the material's intrinsic flaw distribution and falsifying the measured strength and its scatter [3], [4], [8], [10]. In this work, the focus was set on biaxial testing methods, such as the Ring-on-Ring-test (RoR), the Ball-on-Ring-test (BoR) and the Ball-on-Three-Balls-test (B3B), as well as a novel uniaxial testing method (CharAM-test) [10]–[14]. It is obvious that each method applies an inherently different stress field on the specimen, and that they each come with their specific advantages and disadvantages. Due to the flaw-based failure of brittle materials, this will result in varying strength values being measured with each method, even if the same material is tested. However, a comparison based on a several assumptions (e.g. weakest-link-hypothesis) and Weibull-theory is still possible and highly relevant [15]–[18]. It should be noted that some emerging fields of ceramic materials, such as additive manufacturing, require special treatment in terms of strength testing due to the characteristics of the manufacturing process itself, specimen warpage and the demands that are placed on the fabricated components themselves [19]. Thus, new strength testing methods are necessary or existing methods have to be adapted appropriately, in order to guarantee accurate strength measurement and to confidently use well-established tools from traditionally manufactured ceramics for strength and reliability prediction.

The overarching goal of this work was to improve the accuracy and range of application of strength testing for ceramics and glasses, to therefore allow for a better understanding of the materials failure behaviour and reliability in service. This goal was achieved by several separate, but related means for various strength testing methods with a biaxial stress field and will be presented in the form of several publications: First, the analytical stress evaluation of two existing testing methods was improved (to be more accurate) and extended (to include load-dependent effects and a wider range of specimen geometries). This was achieved through a combined analytical and numerical approach for both the BoR-test and the B3B-test. For the latter, experimental validation of the otherwise theoretical results was obtained through X-ray tomography. Second, the comparability of strength testing methods to each other was investigated. This aspect was finally made publicly available for the B3B-test, and the underlying principle and possible issues were investigated in detail for both the B3B-test and the RoR-test. Finally, a novel strength testing method was developed, which takes the specific aspects of additive manufacturing and ensuing requirements for strength testing into account. Furthermore, a detailed analysis of the possible sources of error of this new method was performed and supported by both experimental and numerical findings.

While a short introduction is given in each publication, the upcoming chapter (Chapter 2) will provide the necessary background to describe brittle failure, for the statistical treatment of the strength of brittle materials and for each testing method that is relevant within the scope of this work. The utilised numerical methods and experimental techniques will be briefly outlined in Chapter 3, and an extended summary of each publication is given in Chapter 4.

2. Strength of brittle materials

2.1 Background

The typical properties of ceramic materials can often be attributed to their strong atomic bonds within their crystal lattice, which are predominantly ionic and covalent [20]. In general, plastic deformation due to the movement of dislocations is severely limited at room temperature, since any shift of the lattice structure would result in adjacent, but repellingly charged sections of the lattice [21]. Consequently, a low plasticity and fracture toughness with a simultaneously high hardness, Young's modulus and compressive strength ensue for such materials [20]. Furthermore, any form of small-scale stress relief due to plastic deformation is severely impeded. Therefore, individual local stress concentrations, which could be caused by crack-like defects within or at the surface of the material (see section 2.1.2), often initiate catastrophic failure. Generally, the failure of a ceramic component can be attributed to one of the following damage mechanisms [5]:

- Sudden, catastrophic failure (brittle failure)
- Sub-critical crack growth
- Fatigue
- Creep
- Corrosion or oxidation

For the topics presented in this work, only sudden failure will be relevant, hence why the other damage mechanism will not be discussed in any further detail. The upcoming sections (Sections 2.1.1 to 2.2) will deal with the basic principles of brittle failure, the underlying defects that cause failure and the statistical tools that are necessary to describe the failure behaviour of ceramic materials.

2.1.1 Brittle failure

In order to describe the sudden fracture due to brittle failure, crack-growth within the material has to be considered und understood. Due to the low plasticity of ceramics, it is sufficient to rely on linear elastic fracture mechanics. Assume a crack with length a at the edge of a solid body with width B and height H , as displayed in Figure 2.1. For such a case, three possible modes of loading of the crack ensue, as shown in Figure 2.2. Mode I describes a tensile loading perpendicular to the crack plane, Mode II a shear loading in the crack plane perpendicular to the crack front and Mode III a shear loading in the crack plane parallel to the crack front. The most harmful type of loading is Mode I, hence why the remainder of this section will be limited to this case. Note that the following derivations can be performed analogously for Mode II and Mode III as well [3], [4], [22], [23].

Assuming plane stress, for a point with radial distance r at angle Θ from the tip of the crack, the acting stress field due to Mode I loading can be given through [3]

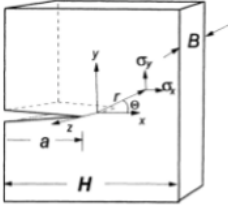


Figure 2.1: Solid body with an edge crack [3].

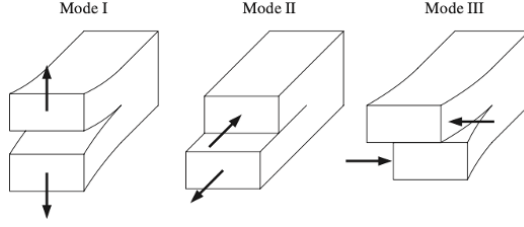


Figure 2.2: Crack opening Modes I to III [4].

$$\sigma_x = \frac{K_I}{\sqrt{2\pi r}} \cos \frac{\Theta}{2} \left(1 - \sin \frac{\Theta}{2} \sin \frac{3\Theta}{2} \right) \quad (2.1)$$

$$\sigma_y = \frac{K_I}{\sqrt{2\pi r}} \cos \frac{\Theta}{2} \left(1 + \sin \frac{\Theta}{2} \sin \frac{3\Theta}{2} \right) \quad (2.2)$$

$$\tau_{xy} = \frac{K_I}{\sqrt{2\pi r}} \sin \frac{\Theta}{2} \cos \frac{\Theta}{2} \cos \frac{3\Theta}{2} \quad (2.3)$$

with K_I as the stress intensity factor given through [3], [4], [22], [23]

$$K_I = Y\sigma\sqrt{\pi a} \quad (2.4)$$

Here, σ refers to the stress in the undamaged body at the position of the crack, and Y is a geometry factor that takes the type of crack, its size, and its position into account. Typical values for Y range from $2/\pi$ to 1.12 [5]. Therefore, K_I describes the magnitude of the stress in front of the crack tip and can be utilised to describe crack growth. If the stress σ within the body increases, K_I increases, until a critical value for unstable crack growth is reached. This critical value is commonly referred to as the fracture toughness K_{Ic} , and it is a material property that can be determined through various testing methods [4], [5], [24]–[27]. Note that Equations 2.1 to 2.3 yield singular stresses at the crack tip ($r = 0$), thus exceeding the theoretical strength of any material, at any load or crack size.

Consequently, a second criterion for crack growth has to be fulfilled. It was derived by Griffith in 1921 by describing the crack growth through consideration of the various energies that determine the state of the observed system [28]. In order for a crack to grow, two new surfaces have to be created within the body, and the necessary energy per unit area G_c is given through [3], [4], [22], [23], [28]

$$G_c = 2\gamma \quad (2.5)$$

with γ as the specific surface energy per unit area. During loading of a cracked structure, energy is provided from two sources: The work W , that is done by external loads, and the elastically stored energy U , which ultimately determine the energy release rate G_I per crack surface S through [3], [4], [22], [23], [28]

$$G_I = \frac{dW}{dS} - \frac{dU}{dS} \quad (2.6)$$

and allow crack growth if the total energy of the system is reduced, namely if

$$G_I \geq G_c \quad (2.7)$$

Irwin has shown that a simple relationship between the stress intensity K_I and the energy release rate G_I can be derived [4], [29]:

$$G_I = \begin{cases} \frac{K_I^2}{E} & \text{Plane stress} \\ \frac{K_I^2}{E} (1 - \nu^2) & \text{Plane strain} \end{cases} \quad (2.8)$$

with E as the Young's modulus and ν as the Poisson's ratio of the material.

If Equation 2.7 and Equation 2.8 are combined for a plane stress state, the so-called Griffith-Irwin failure criterion is obtained [3]–[5], [22], [23]:

$$K_I \geq K_{Ic} \quad (2.9)$$

Inserting Equation 2.9 into Equation 2.4, the maximum tensile stress at failure σ_f is determined through [5]

$$\sigma_f = \frac{K_{Ic}}{Y \sqrt{\pi a_c}} \quad (2.10)$$

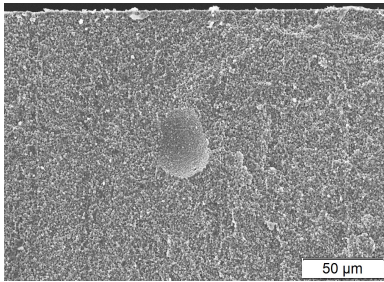
From this equation, it can be deduced that an increased tensile strength is obtained through an increased fracture toughness K_{Ic} or a decreased critical crack length a_c . Through transformation of Equation 2.10, the critical crack length a_c at a given tensile strength σ_f and fracture toughness K_{Ic} is determined through [5]

$$a_c = \frac{1}{\pi} \left(\frac{K_{Ic}}{Y \sigma_f} \right)^2 \quad (2.11)$$

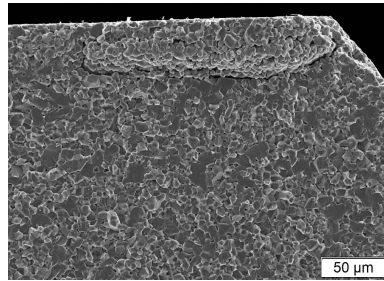
The range of typical defects in brittle materials, which ultimately act as cracks, and their influence on the failure behaviour will be discussed in the upcoming sections.

2.1.2 Defects in conventionally and additively manufactured ceramics

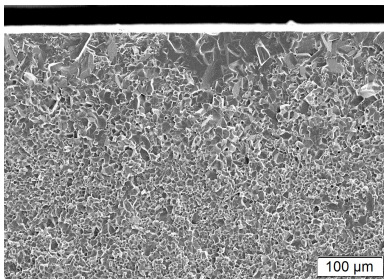
In general, defects refer to small flaws that are randomly distributed within the material or at its surface. Each of these flaws causes stress concentrations, which can be described as cracks, that subsequently lead to failure, as outlined in the previous section. Typically, flaws are caused by the production process, the handling of the finished component or they can be introduced during service. Some examples for processing related flaws are pores, hard agglomerates, glass phases, cavities due to evaporation of an organic component (e.g. hairs), or abnormally large grains, as given in Figures 2.3a to 2.3d. One of the most important sources of defects due to handling or service is found in contact damage. If the component is dropped, damaged during transportation, or installed with inadequate tools, surface defects are formed. In general, surface defects show higher values for Y and



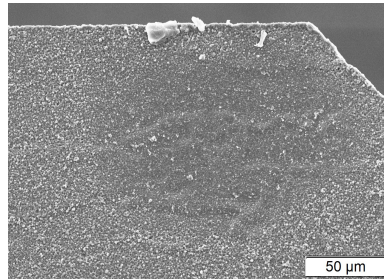
(a)



(b)



(c)



(d)

Figure 2.3: Typical process related flaws in ceramics. (a) gives a pore, (b) shows a hard agglomerate at the surface, (c) depicts a region of abnormally large grains, and (d) shows a region of delamination between two layers. All flaws were observed in alumina manufactured through the LCM-process (Note the subtle layered structure in (a)). (a) and (d) are sourced from [30]

are highly stressed during many load cases, thus further increasing the potential for damage or even failure [5].

For strength testing, an important source of defects is found in the process of specimen machining from the bulk material, which usually causes edge or surface defects. Therefore, it is essential to avoid this damage altogether or implement solutions, such as chamfered edges, which reduce the impact of potential machining defects. Otherwise, the measured strength does not correlate to the intrinsic strength of the investigated material, and the results are misleading. Alternatively, some testing methods allow testing in as-fabricated conditions, and the influence of defects from specimen machining can be avoided altogether. A more detailed discussion on this aspect of the testing methods investigated in this work is given in Section 2.4 [10], [31].

Finally, it is important for the remainder of this work to understand the potential sources of defects that are related to a certain category of processing methods, namely additive manufacturing. While some of the discussed aspects are relevant for a multitude of manufacturing methods, the focus will be set on the lithography-based ceramic manufacturing technology (LCM). This process was developed by LITHOZ GmbH and is a specific version of digital light processing (DLP) methods, which by themselves can be attributed to the stereolithography (SLA) and vat photopolymerisation (VPP) methods [32]–[35]. In general, the LCM-process utilises light with a wavelength of blue, visible light to selectively cure and solidify a liquid suspension of photosensitive polymers mixed with typically ≥ 40 vol% of dispersed ceramic powder particles. A schematic of the process is given in Figure 2.4. The light from the LED-source (Figure 2.4 (1)) is reflected towards the bottom of a transparent vat (Figure 2.4 (3)) through a grid of tiltable mirrors (e.g. with a size in the vicinity of $40\mu\text{m} \times 40\mu\text{m}$) (Figure 2.4 (2)). The size of the individual mirrors, which each act as a single pixel, limits the minimum lateral resolution of this process. Within the transparent vat, the regions illuminated by the mirrors solidify and attach to the building platform (Figure 2.4 (4)), which is submerged in the slurry-filled vat, thus creating one layer of the desired component. The vertical resolution of this process is dependent on the material and printing equipment, but a layer-thickness as low as approximately $25\mu\text{m}$ can be achieved. Subsequently, the building platform is removed from the slurry, a new layer of slurry is spread through rotation of the vat, and the building platform is re-submerged to create a new layer of the desired component. After completion of all layers, the component is debinded through a thermal post-processing step and a ceramic green body is obtained. Through sintering, a dense ceramic component is ultimately produced. For any further information or details of the LCM-process, the reader is referred to [36]–[41].

A typical type of defect within the bulk of the material stems from the layered nature of the process itself, namely the bonding between each individual layer. If the processing parameters are not optimally chosen at any stage of the fabrication, the resulting weak interface between individual layers is highly susceptible to cause material failure. Additionally, an orientation-dependent strength will be observed, as the acting direction of the stresses to the interface plane changes. However, it has been shown that this effect is not significant as long as the processing parameters of fabrication and thermal treatment are understood well [43]. On the other hand, the layered structure also creates defects on the surface of the component

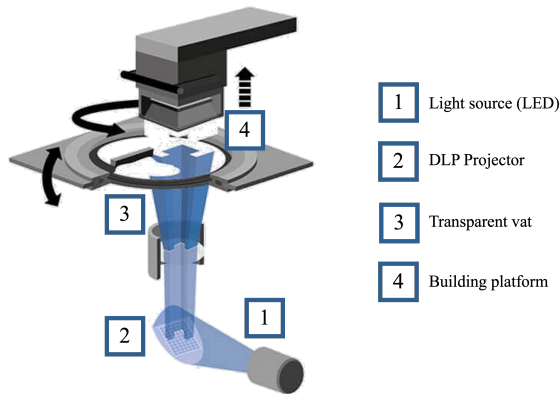


Figure 2.4: Schematic of the LCM-process, with the light source (1), the mirror array (2), the transparent vat (3) and the building platform (4), adapted from [42].

in the form of wavy surface structures on a micrometer-scale. They are caused by two effects and are highly dependent on the printing orientation, i.e. the angle between the surface and the vertical building direction.

On one hand, these surface structures are caused by overpolymerisation of the slurry. This means that the light reflected by each mirror scatters within the slurry, which slightly increases the amount of cured material. Therefore, a deviation from an ideal, square pixel of cured slurry towards a barrel-shaped pixel is observed [44]. On the other hand, the pixel-based nature of the LCM-process causes aliasing effects when inclined surfaces (with respect to the pixel-grid) are manufactured, as shown in Figure 2.5. Note that this effect occurs both within a single layer and in building direction with multiple layers being involved instead of pixels, as highlighted through a historic example in Figure 2.7.

The result of both effects acting together is displayed in Figure 2.6, where two distinct surface structures are observed for the same material but different surface inclinations. If stressed, these structures will act as notches and cause stress concentrations at the surface of the material, which will inevitably affect the failure behaviour of the specimen or component. This effect has been observed for strength testing with both uniaxial and biaxial stress fields, as outlined in [43], [45]. Due to these special types of defects and other process-related effects of additive manufacturing for strength testing, it is clear that these aspects have to be taken into account accordingly, as will be discussed in Section 2.4. This ultimately lead to the development of a novel strength testing method, as shown in **Publication F** ([14]).

2.2 Fracture statistics

Due to the statistical nature of defects in ceramics and their impact on the material's strength, it is necessary to describe the failure of ceramics with some sort of strength distribution. For most materials, it is well established that the two-

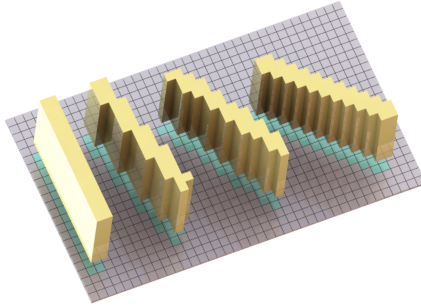


Figure 2.5: In-plane aliasing effect due to the pixel-based LCM-process [14].

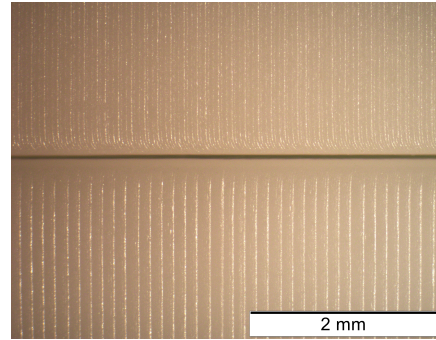


Figure 2.6: Surface structures of specimens printed at different angles [14].



Figure 2.7: Pyramid of Djoser, demonstrating the aliasing effect in building direction due to the discrete layer thickness and limited spatial resolution [46].

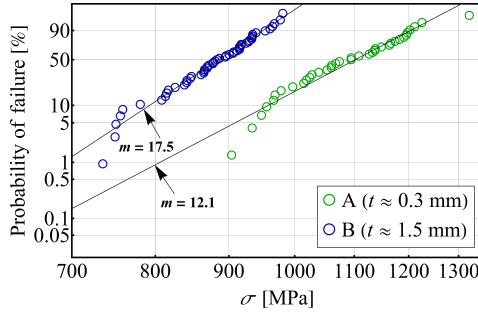


Figure 2.8: Weibull-scaled plot of the empirical cumulative distribution function of two samples from the same material, but with different geometry [51].

parameter Weibull distribution can be utilised, which gives the probability of failure $F(\sigma, V)$ at a given uniaxial, homogeneous stress σ in the form of a cumulative distribution function through [5], [47], [48]

$$F(\sigma, V) = 1 - \exp \left[-\frac{V}{V_0} \left(\frac{\sigma}{\sigma_0} \right)^m \right] \quad (2.12)$$

with σ_0 and m as the distribution's scale and shape parameters, respectively. V refers to the specimen's volume, and V_0 to a chosen reference volume that is invariably linked to σ_0 . Consequently, m , which is known as the Weibull modulus, describes the scatter of strength, with higher values of m indicating less scatter. The characteristic strength σ_0 is given as the strength of a specimen that, with $V = V_0$ and $\sigma = \sigma_0$, exhibits a failure probability $F(\sigma_0, V_0) = 1 - e^{-1} = 63.2\%$. Note that for certain circumstances, it has been shown that the Weibull distribution can be derived analytically [49], [50].

For many cases, it is helpful to rescale Equation 2.12 according to [4]

$$\log \log \left(\frac{1}{1 - F(\sigma, V)} \right) = \log \left(\frac{V}{V_0} \right) + m \log \left(\frac{\sigma}{\sigma_0} \right) \quad (2.13)$$

to better visualise the data in a so-called Weibull-plot, as shown in Figure 2.8. For a given set of (sorted) strength data $\sigma_1 - \sigma_N$ with specimen volume V , an estimation of the respective probability of failure is assigned by [4]

$$F(\sigma_i, V)_i = \frac{i - 0.5}{N} \quad (2.14)$$

with i as the ranking number of the respective strength value and N as the total number of measured data. Through the aforementioned linearisation, and if the tested material behaves according to Weibull-theory, the strength data will (ideally) form a line with slope m . While m and σ_0 could be determined graphically from a Weibull-plot or through a linear regression of the data obtained through Equation 2.12 and Equation 2.14, the recommended procedure utilises the Maximum-Likelihood method [4], [52]. In any case, the obtained results for m and σ_0 are just estimates based on a finite number of random specimens from

the underlying distribution. Therefore, it is standard procedure to include 90%- or 95%- confidence intervals for both parameters, as defined in [52], [53].

An essential aspect of the statistical nature of the strength of brittle materials is the influence of the specimen's or component's size on the measured strength. As outlined in the previous section, the strength of a specimen is generally limited by the most critical defect. Consequently, if a larger specimen is tested, a higher probability to encounter a critical defect at a given size ensues, and the average measured strength decreases notably with an increase of the specimen's size. This aspect is more commonly known as the "size-effect". This resulting shift in strength is displayed in Figure 2.8, where both samples represent the same material, but different specimen geometries (For a more elaborate explanation of the effects causing the shift in Figure 2.8 please refer to [51]). Through the inclusion of the specimen's volume V and a reference volume V_0 in Equation 2.12, the "size effect" is considered for the probability of failure as well [3]–[5].

For samples of the same material, the relationship between the characteristic strength $\sigma_{0,1}$ and reference volume $V_{0,1}$ of a specific specimen geometry and $\sigma_{0,2}$ and $V_{0,2}$ of a different geometry [3]–[5], [16]

$$\frac{\sigma_{0,1}}{\sigma_{0,2}} = \left(\frac{V_{0,2}}{V_{0,1}} \right)^{1/m} \quad (2.15)$$

can be derived from Equation 2.12.

Up until now, only uniaxial, homogeneous stress fields have been considered. For inhomogeneous stress fields, the probability of failure can be determined by considering the spatially varying stress distribution $\sigma(x, y, z)$ through [5], [47], [48]

$$F(\sigma, V) = 1 - \exp \left[-\frac{1}{V_0} \int_V \left(\frac{\sigma(x, y, z)}{\sigma_0} \right)^m dV \right] \quad (2.16)$$

Note that integration is performed for the entire specimen, but only tensile stresses are taken into account, therefore neglecting the damaging effects of compressive stresses. This is due to the much higher compressive strength of brittle materials, and is valid for most cases where the compressive stress is not significantly higher than the tensile stress [5]. If the shape of the stress field is independent of the magnitude of the applied load, $\sigma(x, y, z)$ can be rewritten as $\sigma(x, y, z) = \sigma_{ref} \times g(x, y, z)$ and an effective volume V_{eff} can be defined through [5], [47], [48]

$$V_{eff} = \iiint_{\sigma > 0} [g(x, y, z)]^m dx dy dz \quad (2.17)$$

with σ_{ref} as an arbitrary reference stress. Thus, the effective volume can be interpreted as the volume of a hypothetical, uniaxially and homogeneously (tensile) loaded specimen with the same probability of failure for σ_{ref} as the inhomogeneously loaded specimen. Note that other definitions are commonly used as well, and have to be distinguished with care [54]. Through inserting Equation 2.17, Equation 2.16 can be generalised to [5], [47], [48]

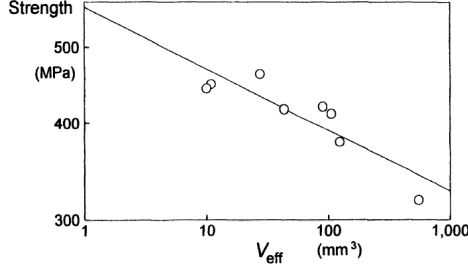


Figure 2.9: Influence of the effective surface on the measured strength if the material behaves according to Weibull-theory [3].

$$F(\sigma_{ref}, V_{eff}) = 1 - \exp \left[-\frac{V_{eff}}{V_0} \left(\frac{\sigma_{ref}}{\sigma_0} \right)^m \right] \quad (2.18)$$

Typically, the maximum first principal stress is chosen as σ_{ref} , thus limiting $g(x, y, z)$ to the numerical range between 0 and +1 for uniaxial stress fields.

For multiaxial stress fields, specific failure criteria are utilised to determine an equivalent uniaxial stress $\sigma_{eq}(x, y, z)$. The criteria used in this work are the First-Principal-Stress-criterion (FPS) and the Principle-of-Independent-Action (PIA) [6], [9], [55], [56]. For the FPS-criterion, it is assumed that solely the first principal stress σ_I contributes to the damaging action, and is therefore simply defined as [55]

$$\sigma_{eq,FPS} = \sigma_I \quad (2.19)$$

The PIA-criterion takes the contribution of all principal stresses to the damaging action into account through [6], [9], [56]

$$\sigma_{eq,PIA} = \sqrt[m]{\sigma_I^m + \sigma_{II}^m + \sigma_{III}^m} \quad (2.20)$$

with σ_{II} and σ_{III} as the second and third principal stress, respectively, and m as defined before. Finally, it should be noted that the concept of effective volume can be applied to failure caused by surface defects as well. Analogously to Equation 2.17, an effective surface S_{eff} can be defined as [5], [47], [48], [57]

$$S_{eff} = \iint_{\sigma > 0} [g(x, y)]^m dx dy \quad (2.21)$$

and the probability of failure due to surface defects is given by [5], [47], [48]

$$F(\sigma_{ref}, S_{eff}) = 1 - \exp \left[-\frac{S_{eff}}{S_0} \left(\frac{\sigma_{ref}}{\sigma_0} \right)^m \right] \quad (2.22)$$

For some well-established testing methods such as 4PB or 3PB, Equations 2.17 and 2.21 can be solved, therefore providing a straightforward way to determine the ef-

fective volume or surface through an analytical expression [15], [58], [59]. However, if this not the case, numerical methods such as FEA have to be utilised to determine the effective quantities for individual specimen geometries. This aspect will be discussed for the testing methods presented in the upcoming section.

On the basis of the size-effect, it is now evident that even specimens with the exact same geometry can exhibit a difference in strength if the shape of the applied stress field is altered. Note that this behaviour requires that all specimens fail due to the same defect population. Thus, if the characteristic strength of each sample is plotted in dependence of the respective effective volume or surface on a logarithmic scale, a linear trend according to Equation 2.15 is observed, as displayed in Figure 2.9. If the investigated material behaves according to Weibull theory, the slope k_{reg} of a linear regression through all samples yields a regression modulus m_{reg} through $m_{reg} = -1/k_{reg}$ that is similar to the Weibull modulus m of each individual sample [3]–[5], [47], [48].

2.3 Testing methods

The upcoming section will deal with the strength testing methods that have either been worked on for this thesis or that are necessary to be known in case they are referenced to. The state-of-the-art for each method will refer to the time at the beginning of this thesis, and chapter 4 will explain the advancements that have been made through this work.

2.3.1 Uniaxial bending tests

The most wide-spread testing methods are variations of uniaxial bending tests (also known as flexural tests), such as three-point-bending (3PB) and four-point-bending (4PB). Due to the experimental complexity of uniaxial tension tests for brittle materials, flexural tests are widely used since the 1950s and 1960s at ceramic manufacturers and research institutes [31]. In general, flexure testing of ceramics is a versatile and simple testing method, and the necessary fixtures can be produced with relatively low cost. In the past decades, several standards have been developed that govern the specimen geometry and related tolerances, the testing setup and stress evaluation, such as [60], [61].

A schematic of the setup for a 3PB-setup for rectangular bars and for a 4PB-setup in a 1/4 point configuration (see [15]) is given in Figures 2.10 and 2.11, respectively. Their respective stress fields can easily be determined through beam theory and are given in Figure 2.12 and Figure 2.13 in dependence of the longitudinal position on the bar. For three-point-bending, the maximum tensile stress σ_{max} in the centre of the specimen is given through [60], [61]

$$\sigma_{max} = \frac{3Pl}{2wh^2} \quad (2.23)$$

with l as the distance between the supporting rollers, w as the width of the specimen, h as its height and P as the applied load. For the region of constant bending

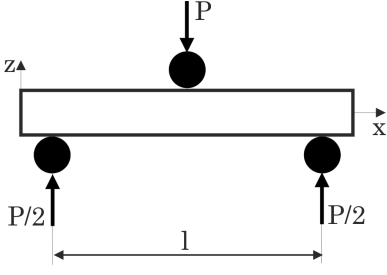


Figure 2.10: Schematic testing setup for three-point-bending.

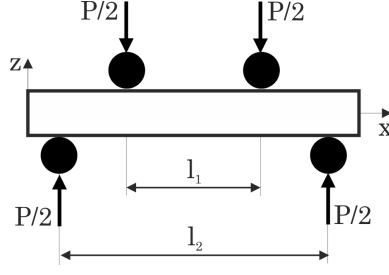


Figure 2.11: Schematic testing setup for four-point-bending.



Figure 2.12: Longitudinal profile of the stress field for three-point-bending.

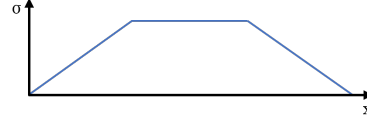


Figure 2.13: Longitudinal profile of the stress field for four-point-bending.

moment (and consequently constant edge fibre stress) in the four-point-bending setup, σ_{max} is given through [60], [61]

$$\sigma_{max} = \frac{3P(l_2 - l_1)}{2wh^2} \quad (2.24)$$

with l_1 as the inner roller span, l_2 as the outer roller span, and the other variables as defined before.

Due to the simplicity of the respective stress field, analytical expressions for the effective volume and surface can be derived according to Equation 2.17. For a 3PB setup, the effective volume $V_{eff,3PB}$ is given through [15]

$$V_{eff,3PB} = \frac{hwl}{2(m+1)} \quad (2.25)$$

with m as the Weibull modulus of the investigated material, and the effective surface $S_{eff,3PB}$ is given through [15]

$$S_{eff,3PB} = l[h + w(m+1)] \frac{1}{(m+1)^2} \quad (2.26)$$

For a 1/4-point 4PB setup, the effective volume $V_{eff,4PB}$ is determined by [15]

$$V_{eff,4PB} = \frac{hwl_2(m+2)}{4(m+1)^2} \quad (2.27)$$

and the effective surface $S_{eff,4PB}$ is calculated through [15]

$$S_{eff,4PB} = l_2[h + w(m+1)] \frac{m+2}{2(m+1)^2} \quad (2.28)$$

The most common specimen geometry is configuration *B* of MIL-STD-1942A (succeeded by ASTM C1161, [61]), i.e. a rectangular bar with a width of 4mm, a height of 3mm and a length of 45mm, which is typically tested on a fixture with an outer span length of 40mm (and an inner span length of 20mm in the case of 4PB). Note that other specimen geometries, apart from bars with a rectangular cross section, are also commonly used, such as bars with a square cross section or cylindrical rods. Finally, a possible testing setup that fulfils all requirements for accurate strength testing according to [62] is shown in Figure 2.14.

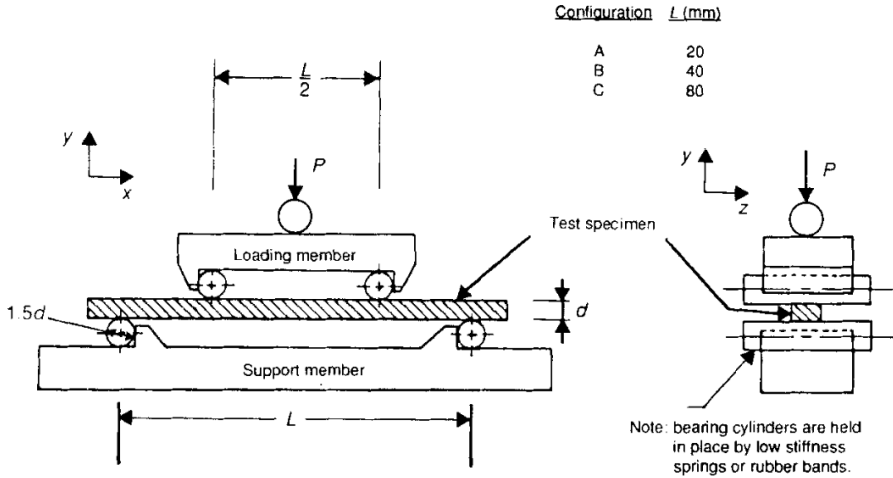


Figure 2.14: A possible design of a testing fixture for 4PB according to [62].

2.3.2 The Ring-on-Ring-test

One of the most prominent biaxial testing methods is the Ring-on-Ring-test. It is widely known and well established due to its standardisation in the ASTM-standard C1499 [11]. As the name implies, the load is applied to the specimen via a centrally positioned steel ring, and the specimen is supported by a concentric steel ring with significantly larger radius. It allows testing of both disc-shaped and square- or slightly rectangular plate specimens. An example for a possible testing setup is given in Figure 2.15.

Due to the rotational symmetry of the testing setup, an analytical description of the stress field can easily be derived through plate theory. In order to simplify the upcoming expressions, several dimensionless factors are defined:

$$\alpha = \frac{R_{LR}}{R_{SR}} \quad (2.29)$$

$$\beta = \frac{R}{R_{SR}} \quad (2.30)$$

$$\rho = \frac{r}{R_{SR}} \quad (2.31)$$

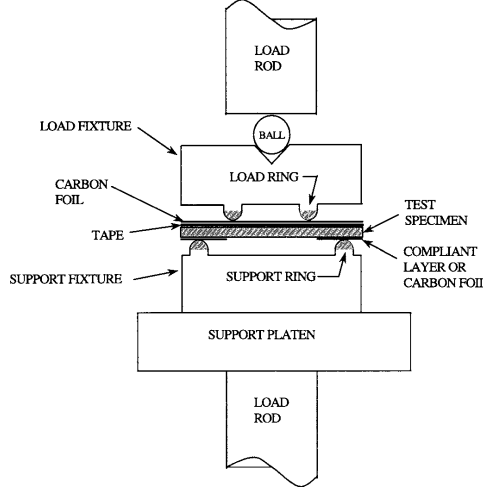


Figure 2.15: A possible design of a testing fixture for the RoR-test according to [11].

with R_{LR} as the load ring radius, R_{SR} as the support ring radius, R as the specimen's radius and r as the radial coordinate from the centre of the specimen. The stress field can be divided into three regions, depending on the distance from the specimen's centre, and two stress components, i.e. a radial stress σ_{rad} and a tangential stress σ_{tan} . For each region, each stress component can generally be expressed through

$$\sigma_j = \frac{3Pz}{2\pi t^3} D_j(\rho, \alpha, \beta, \nu) \quad (2.32)$$

with the subscript j referring to either the radial ($j = rad$) or the tangential ($j = tan$) stress component. P refers to the applied load, z to the distance from the neutral plane, t to the specimen's thickness and ν to the Poisson's ratio of the tested material. D_j determines the value of the stress field and is given for each region through the following expressions:

$$D_{rad} = D_{tan} = (1 - \nu) \frac{1 - \alpha^2}{\beta^2} - (1 + \nu) 2 \log \alpha \quad (2.33)$$

for $0 \leq r \leq R_{LR}$,

$$D_{rad} = (1 - \nu) \left[\frac{1 - \alpha^2}{\beta^2} + \frac{\alpha^2}{\rho^2} - 1 \right] \quad (2.34)$$

$$D_{tan} = (1 - \nu) \left[\frac{1 - \alpha^2}{\beta^2} - \frac{\alpha^2}{\rho^2} + 1 \right] \quad (2.35)$$

for $R_{LR} \leq r \leq R_{SR}$ and

$$D_{rad} = (1 - \nu) (1 - \alpha^2) \left[\frac{1}{\beta^2} - \frac{1}{\rho^2} \right] \quad (2.36)$$

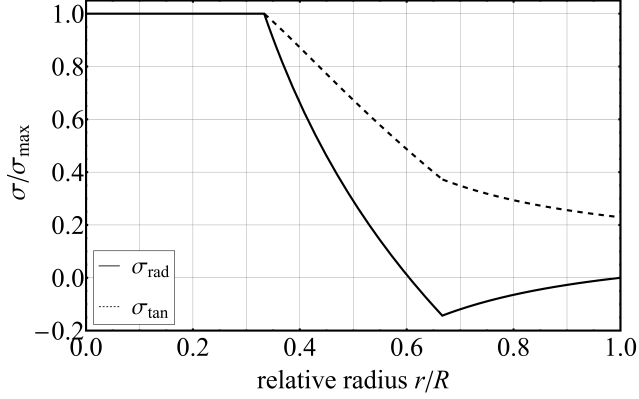


Figure 2.16: Radial profile of the axisymmetric stress field of the RoR-test.

$$D_{tan} = (1 - \nu) (1 - \alpha^2) \left[\frac{1}{\beta^2} + \frac{1}{\rho^2} \right] \quad (2.37)$$

for $R_{SR} \leq r \leq R$.

The resulting stress field for the tensile loaded surface and a typical specimen geometry is shown in Figure 2.16. Note the large region of constant (maximum) stress in the centre of the specimen, which is one of the main points of differentiation to the ball-loaded testing methods that will be presented in the following sections. Since equations 2.33 to 2.37 are derived through plate theory, sufficiently thin specimens have to be tested. Similarly, if the specimens are too thin, large deflections ensue and plate theory is no longer applicable. Therefore, an upper and lower limit for the specimen's thickness is defined by the standard: [11], [63]

$$\frac{D_{SR}}{10} \geq t \geq \sqrt{\frac{2\sigma_f D_{SR}^2}{3E}} \quad (2.38)$$

with D_{SR} as the diameter of the support ring, σ_f as the measured or expected strength of the specimen and E as the Young's modulus of the tested material. Regarding the overhang of the specimen, i.e. the part of the specimen outside the support radius R_{SR} , the following criterion has to be fulfilled:

$$2 \leq \frac{D - D_{SR}}{t} \leq 12 \quad (2.39)$$

with D as the specimen's diameter and the other variables as defined before. This criterion assures that specimen failure seldomly originates from its edge, as the stress at the edge of the specimen decreases with an increase in overhang. For both of these criteria, square or slightly rectangular plates are taken into account through the conversion

$$D = 0.54 (L_1 + L_2) \quad (2.40)$$

with L_1 and L_2 as the edge lengths of the plate. Note that $0.98 \leq L_1/L_2 \leq 1.02$ has to be given.

If these criteria are met, the strength of a failed specimen is determined through the maximum tensile stress σ_{max} according to

$$\sigma_{max} = \frac{3qD_{LR}^2(1+\nu)}{4t^2} \left[2\log\left(\frac{D_{SR}}{D_{LR}}\right) + \frac{1-\nu}{1+\nu} \left(1 - \frac{D_{LR}^2}{D_{SR}^2}\right) \frac{D_{SR}^2}{D^2} \right] \quad (2.41)$$

with

$$q = \frac{4P}{\pi D_{LR}^2} \quad (2.42)$$

and all other symbols as defined before. The deflection in the centre of the specimen, δ_{max} , can be estimated through

$$\delta_{max} = \frac{3P(1-\nu^2)D_{LR}^2}{8\pi Et^3} \left\{ \frac{D_{SR}^2}{D_{LR}^2} \left[1 + \frac{(1-\nu)(D_{SR}^2 - D_{LR}^2)}{2(1+\nu)D^2} \right] - \left(1 + \log\frac{D_{SR}}{D_{LR}} \right) \right\} \quad (2.43)$$

with E as the Young's modulus of the tested material. If square or rectangular specimens are tested, Eq. 2.41 can still be utilised by determining an equivalent specimen diameter D_{eq} according to

$$D_{eq} = \frac{1}{\left(0.90961 + 0.12652 \frac{t}{D_{SR}} + 0.00168 \log \frac{L_{mean} - D_{SR}}{t} \right)} \quad (2.44)$$

where $L_{mean} = 0.5(L_1 + L_2)$. Due to the simplicity and symmetry of the stress field, it is possible to derive a single equation that fits the analytical results (after the PIA-criterion) for the effective surface $S_{eff,RoR}$ and effective volume $V_{eff,RoR}$. For $m > 5$, the effective surface is given through

$$S_{eff,RoR} = \frac{\pi}{2} D_{LR}^2 \left\{ 1 + \frac{44(1+\nu)}{3(1+m)} \frac{(5+m)}{2+m} \left(\frac{D_{SR} - D_{LR}}{D_{SR}D} \right)^2 \times \left[\frac{2D^2(1+\nu) + (D_{SR} - D_{LR})^2(1-\nu)}{(3+\nu)(1+3\nu)} \right] \right\} \quad (2.45)$$

and the effective volume can be determined from

$$V_{eff,RoR} = S_{eff,RoR} \left[\frac{t}{2(m+1)} \right] \quad (2.46)$$

with a maximum error to the exact, analytical results of less than 5%.

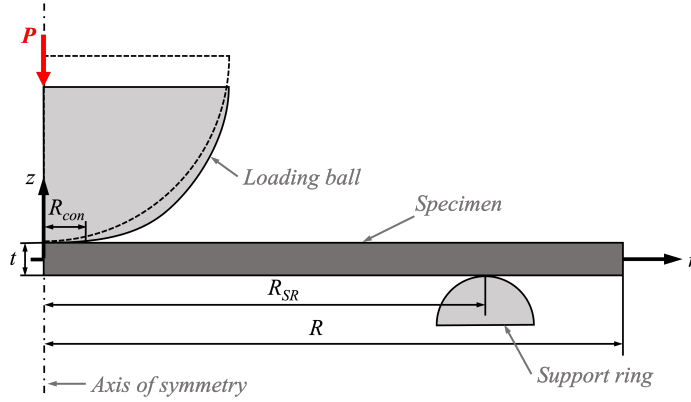


Figure 2.17: Schematic of the BoR testing setup.

2.3.3 The Ball-on-Ring-test

Another ring-supported, biaxial testing method is the Ball-on-Ring-test. Similar to the RoR-test, a steel ring is utilised as the support for the specimen, but the load is applied in the centre of the support ring through a (steel) ball, as illustrated in Figure 2.17. Due to this difference, the influence of friction due to load application is significantly less pronounced [12]. Due to the symmetry and simplicity of the testing method, it is possible to describe the stress field and deflection field of disc-shaped specimens analytically. However, this aspect has been a point of discussion for many years and several solutions have since been developed, which will be briefly outlined in the following paragraphs. One of the main problems is that the unknown load distribution beneath the contacting sphere is simplified to ease the derivation of an analytical solution. Unless stated otherwise, all of the presented solutions will assume that a concentric, uniform load distribution is applied to the specimen.

The first solution for the stress field and deflection field was published by *Roark & Young* [64], [65]. In this solution, the stiffening effect of the overhang, i.e. the region outside the loading ring radius, was not taken into account. Furthermore, it was found that the equation for the maximum tensile stress is erroneous, as outlined in [66]. The correct solution for the maximum tensile stress σ_{max} , determined through plate theory, is given through

$$\begin{aligned} \sigma_{max} &= \sigma_{rad,r=0} = \sigma_{tan,r=0} \\ &= \frac{3q_{con}R_{con}^2(1+\nu)}{4t^2} \left[1 + 2\log\left(\frac{R_{SR}}{R_{con}}\right) + \frac{1-\nu}{1+\nu} \left(1 - \frac{R_{con}^2}{R_{SR}^2}\right) \right] \end{aligned} \quad (2.47)$$

with

$$q_{con} = \frac{P}{\pi R_{con}^2} \quad (2.48)$$

and R_{con} as the radius of the area of constant load. An improvement was provided

by *Vitman et al.* in 1962 through a solution for the RoR-test, which takes the effect of the overhang into account [67]. By replacing R_{LR} with R_{con} in Equation 2.41, a solution for the maximum tensile stress σ_{max}

$$\sigma_{max} = \frac{3q_{con}R_{con}^2(1+\nu)}{4t^2} \left[2 \log \left(\frac{R_{SR}}{R_{con}} \right) + \frac{1-\nu}{1+\nu} \left(1 - \frac{R_{con}^2}{R_{SR}^2} \right) \frac{R_{SR}^2}{R^2} \right] \quad (2.49)$$

and the central deflection of the plate δ_{max}

$$\begin{aligned} \delta_{max} &= \delta_{r=0} \\ &= \frac{qb^4}{8M} \left(1 - \log \left(\frac{R_{SR}}{R_{con}} \right) - \left[1 + \frac{1-\nu}{1+\nu} \left(1 - \frac{R_{con}^2}{R_{SR}^2} \right) \frac{R_{SR}^2}{R^2} \right] \frac{R_{SR}^2}{R_{con}^2} \right) \end{aligned} \quad (2.50)$$

with the bending stiffness of the plate M as

$$M = \frac{I \times E}{1 - \nu^2} \quad (2.51)$$

and the second moment of area I given by

$$I = \frac{t^3}{12} \quad (2.52)$$

is obtained. It has been shown that this solution underestimates σ_{max} and overestimates δ_{max} for the BoR-test [68].

Kirstein & Woolley derived a solution for the stress and deflection in centrally loaded discs on a finite amount of support points in 1967, which also takes the contribution of the overhang into account [69]. Through the application of *Bassali's* theory, equations for the stress distribution for the entire disc were derived [70]. Furthermore, they have shown analytically that σ_{max} is independent of the number of support points, hence why their solution can be applied to the BoR-test (infinite number of support points) through

$$\sigma_{max} = \frac{3q_{con}R_{con}^2(1+\nu)}{4t^2} \left[1 + 2 \log \left(\frac{R_{SR}}{R_{con}} \right) + \frac{1-\nu}{1+\nu} \left(1 - \frac{R_{con}^2}{R_{SR}^2} \right) \frac{R_{SR}^2}{R^2} \right] \quad (2.53)$$

with the symbols as defined before. Due to its length, the solution for the deflection will not be shown in this work. Note the similarity of Equations 2.47, 2.49 and 2.53.

Finally, *Frandsen* published his results for the application of plate theory to the BoR-problem in 2012. His work contains the radial-, tangential- and shear-stress distributions, as well as solutions for the deflection-, slope-, curvature-field for the entire disc. While his solution for σ_{max} is identical to that of *Kirstein & Woolley* (Equation 2.53), the central deflection of the disc is given through

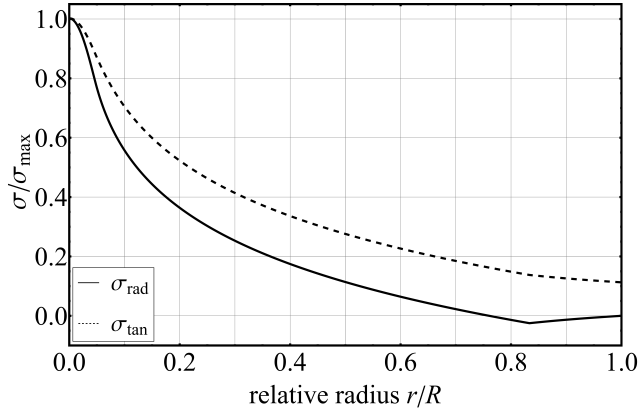


Figure 2.18: Radial profile of the axisymmetric stress field of the BoR-test.

$$\delta_{max} = \frac{qb^4}{16M} \left(\frac{7}{4} + \left[\log \left(\frac{R_{SR}}{R_{con}} \right) - \frac{1}{2} \right] \frac{2R_{SR}^2 + R_{con}^2}{R_{con}^2} - \left[1 + 2 \log \left(\frac{R_{SR}}{R_{con}} \right) + \frac{1-\nu}{1+\nu} \left(1 - \frac{R_{con}^2}{2R_{SR}^2} \right) \frac{R_{SR}^2}{R^2} \right] \frac{R_{SR}^2}{R_{con}^2} \right) \quad (2.54)$$

The radial and tangential stress component in dependence of the radial position for a typical geometry is shown in Figure 2.18.

As mentioned before, all of the solutions presented so far assume a constant load distribution with a known radius R_{con} . It is obvious that the actual load distribution beneath the loading ball is not constant, and that the extent of the simplified load distribution R_{con} has to be determined according to some criterion. Based on the results of FEA, *Shetty et al.* proposed that $R_{con} \approx t/3$, while *McKinney & Herbert* proposed $R_{con} \approx t$ based on experimental strain gauge measurements [71], [72].

Additionally, all solutions based on plate theory include terms that approach infinite stress values for $R_{con} \rightarrow 0$. A method to solve both of these problems is found based on work by *Westergaard* from 1926 in combination with *Hertz's* theory of elastic contact [73], [74]. Based on an analytical approach by *Nádai* [75], *Westergaard* proposed a correction to avoid infinite stress values through replacing small contact radii R_{con} with a corrected contact radius R_{con}^* :

$$R_{con}^* = \begin{cases} R_{con} & \text{for } R_{con} \geq 1.724t \\ \sqrt{1.6R_{con}^2 + t^2} - 0.675t & \text{for } R_{con} < 1.724t \end{cases} \quad (2.55)$$

In later work, R_{con} is often determined according to the Hertzian solution for elastic contact of a sphere and a planar half-space [12], [72]:

$$R_{con,Hertz} = \sqrt[3]{\frac{3PR_{LB}}{4E^*}} \text{ with } \frac{1}{E^*} = \frac{1-\nu_1^2}{E_1} + \frac{1-\nu_2^2}{E_2} \quad (2.56)$$

with R_{LB} as the load ball radius, E^* as the effective Young's modulus, E_1 and ν_1 as the elastic constants of one contact partner, and E_2 and ν_2 as the elastic constants of the other one. While Equation 2.56 would generally yield contact radii that are too small for a meaningful result for σ_{max} from the analytical solution given in Equation 2.53, the combination with the correction given in Equation 2.55 has provided satisfactory results, as shown in [12] and [66]. Hertzian theory further provides a solution for the stress distribution $p(r)$ beneath a sphere pressed against a half space through

$$p(r) = q \frac{3}{2} \sqrt{1 - \frac{r^2}{R_{con,Hertz}^2}} \quad \text{for } 0 \leq r \leq R_{con,Hertz} \quad (2.57)$$

with the symbols as defined before.

In the early 1980s, *Hu* utilised superposition to derive a solution for the maximum tensile stress for a disc with such a load applied in its centre, even including the effect of the overhang [76]

$$\sigma_{max} = \frac{3q_{con}R_{con}^2(1+\nu)}{4t^2} \left[\frac{8}{3} + 2 \log \left(\frac{R_{SR}}{2R_{con}} \right) + \frac{1-\nu}{1+\nu} \left(1 - \frac{2R_{con}^2}{5R_{SR}^2} \right) \frac{R_{SR}^2}{R^2} \right] \quad (2.58)$$

but did not derive any further solutions for other parts of the disc or its deflection. Equation 2.53 and Equation 2.58 have been validated through FEA for various geometries by Chae et al. [77]. In 2014, *Frandsen* derived an analytical expression for the effective surface $S_{eff,BoR}$ using the PIA-criterion by solving Equation 2.17 for the solution of the stress field he published two years earlier [68], [78]. However, the solution is too long to be included in this work and is only applicable to integer values of the Weibull modulus m , which is rarely the case in actual testing scenarios. Following the procedure demonstrated for the effective volume for the RoR-test, the effective volume of the BoR-test, $V_{eff,BoR}$ is derived from the effective surface $S_{eff,BoR}$ through the relationship given in Equation 2.46.

2.3.4 The Ball-on-Three-Balls-test

The Ball-on-Three-Balls test was already mentioned in the 1980s, but substantial development of this testing method was made starting from the early 2000s by *Börger et al.* [13], [79]–[81]. At that time, it was initially conceptualised as a method to determine the strength of functional ceramics or components, but it has since been applied to many other classes of ceramics and brittle materials in general. Similar to the RoR-test, both disc-shaped and square specimens can be utilised, with special fixtures allowing the testing of rectangular plates as well [82]–[93]. Recently, the testing of hexagonal plates has also been investigated, as outlined in [94].

As with the BoR-test, a single ball is employed to apply a load on a specimen, and it is typically positioned in the centre of the specimen. The support is realised

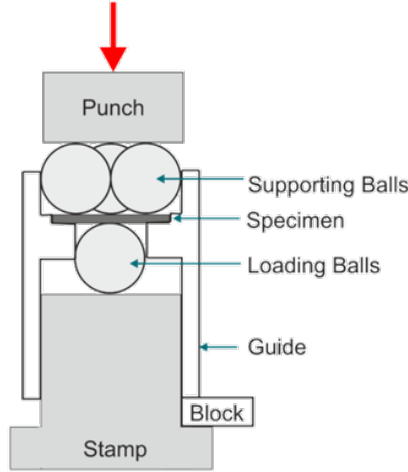


Figure 2.19: Schematic of a B3B testing setup. The block has to be removed prior to testing and helps with specimen alignment until a pre-load is applied.

through three balls which are in contact with each other and not constrained in any other way. A schematic of a possible testing setup is given in Figure 2.19. Therefore, the support radius R_S is determined by the radius of the supporting balls R_B and is given through

$$R_S = \frac{2R_B}{\sqrt{3}} \quad (2.59)$$

If not stated otherwise, it is assumed that the load ball is of equal size to the supporting balls. On one hand, this increases the simplicity of the testing setup, and, on the other hand, reduces the risk of contact damage in the specimen at high loads. For most brittle materials, it is sufficient to utilise bearing balls made from steel, which are widely available in different sizes and manufactured to strict tolerances. For high-strength materials, plastic deformation of the load ball might become an issue, and ceramic- or cemented carbide balls are used instead. In contrast to the RoR- and BoR-test, no accurate analytical solution for the stress field of the B3B-test is available. Therefore, FEA has to be utilised to determine the maximum tensile stress σ_{max} for strength evaluation [13], [80].

The stress distribution with the characteristic three-fold symmetry for a disc with a typical geometry is given in Figure 2.20. Furthermore, Figure 2.21a and Figure 2.21b depict the radial and tangential stress distribution along the 0° and 60° direction, as marked in Figure 2.20, in dependence of the relative radial position. For small deflections and elastic specimen behaviour, a linear relationship between the applied load P and the maximum tensile stress σ_{max} is given through [13], [95]

$$\sigma_{max} = f_{B3B} \left(\frac{t}{R}, \frac{R_S}{R}, \nu \right) \frac{P}{t^2} \quad (2.60)$$

with the variables as defined before and f_{B3B} as a dimensionless factor that takes the specimen geometry, testing setup and material into account. The factor f_{B3B}

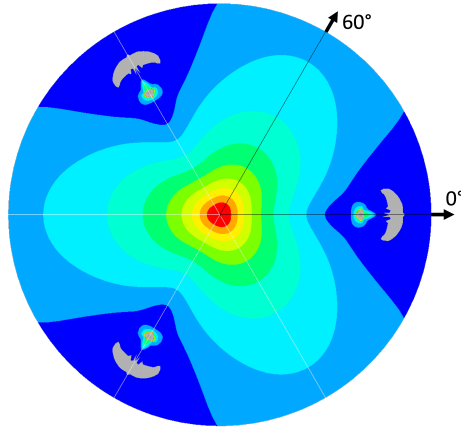


Figure 2.20: Stress field (1st principal stress) of the tensile loaded surface for a typical specimen geometry of the B3B-test. The coloured contours give the magnitude of stress from 0 (blue) to the maximum tensile stress (red) in intervals of 10%. Grey areas represent compressive stresses.

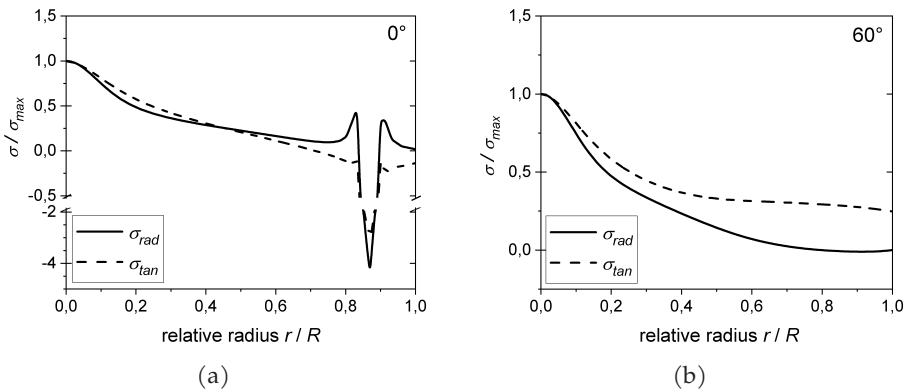


Figure 2.21: Radial (σ_{rad}) and tangential (σ_{tan}) stress components in dependence of the radial position for two angles (0° in (a), 60° in (b)) as defined in Figure 2.20, adapted from [13].

Table 2.1: Fitting constants $c_0 - c_6$ for various values of ν from [95]

ν	0.10	0.15	0.20	0.25	0.30	0.35	0.40
c_0	-39.96	-42.09	-42.54	-46.07	-47.82	-46.84	-49.70
c_1	42.24	44.50	45.07	48.72	50.60	49.74	52.72
c_2	499.46	532.09	538.14	592.59	618.42	602.64	645.51
c_3	-11.69	-12.53	-13.07	-14.14	-14.86	-15.22	-16.12
c_4	4.69	5.18	5.49	6.14	6.57	6.76	7.31
c_5	12.34	12.47	12.47	12.68	12.75	12.67	12.79
c_6	0.0242	0.0232	0.0232	0.0216	0.0210	0.0216	0.0206

has been determined through FEA by [13] and later by [95] for a wide range of specimen geometries and materials. Note that an idealised model was utilised, which assumes punctiform load introduction and supports.

In order to make these results available, a non-linear fit for f_{B3B} was developed [95]:

$$f_{B3B} \left(\frac{t}{R}, \frac{R_S}{R}, \nu \right) = c_0 + \frac{\left(c_1 + c_2 \frac{t}{R} + c_3 \left(\frac{t}{R} \right)^2 + c_4 \left(\frac{t}{R} \right)^3 \right)}{1 + c_5 \frac{t}{R}} \left(1 + c_6 \frac{R_S}{R} \right) \quad (2.61)$$

with the constants $c_0 - c_6$ as given in Table 2.1 for different Poisson's ratios ν of the tested material. This fit is valid within the range $0.1 \leq t/R \leq 0.5$, $0.7 \leq R_S/R \leq 0.9$ and $0.1 \leq \nu \leq 0.4$. For many cases, the Poisson's ratio ν of the tested material is in between the tabulated values. Then, the value for f_{B3B} can be determined through interpolation according to [95]

$$f_{B3B} \left(\frac{t}{R}, \frac{R_S}{R}, \nu \right) = f_{B3B} \left(\frac{t}{R}, \frac{R_S}{R}, \nu_1 \right) + \frac{\nu - \nu_1}{\nu_2 - \nu_1} \left[f_{B3B} \left(\frac{t}{R}, \frac{R_S}{R}, \nu_2 \right) - f_{B3B} \left(\frac{t}{R}, \frac{R_S}{R}, \nu_1 \right) \right] \quad (2.62)$$

with ν_1 and ν_2 as the next higher and lower values to ν in Table 2.1. Within the given range of parameters, the maximum stress for the B3B-test is given with a maximum error of less than 2%. This error stems from the general error of the FEA-model ($\approx \pm 1\%$) and the accuracy of the fit given through equations 2.61 and 2.62 ($\approx \pm 1\%$).

For a slightly extended range of parameters ($0.05 \leq t/R \leq 0.5$, $0.6 \leq R_S/R \leq 0.95$ and $0.1 \leq \nu \leq 0.4$) and without a decrease in accuracy, a simpler function for the fit of f_{B3B}

Table 2.2: Fitting constants $c_0 - c_9$ from [96]

c_0	c_1	c_2	c_3	c_4
1.12613	-2.00184	0.993698	11.91891	0.89157
c_5	c_6	c_7	c_8	c_9
-5.20337	0.253034	5.58097	1.12707	-18.4977

$$f_{B3B} \left(\frac{t}{R}, \frac{R_S}{R}, \nu \right) = c_0 + c_1 \left(\frac{t}{R} \right) + c_2 \left(\frac{R_S}{R} \right) + c_3 \nu + c_4 \left(\frac{t}{R} \right)^2 + c_5 \left(\frac{t}{R} \right) \nu + c_6 \left(\frac{R_S}{R} \right) \nu + c_7 \left(\frac{t}{R} \right)^2 \nu + c_8 \exp \left(c_9 \left(\frac{t}{R} \right) \right) \quad (2.63)$$

was published in 2016, with the constants as given in Table 2.2 [96]. However, due to the lack of an accurate analytical solution, the effective surface $S_{eff,B3B}$ and effective volume $V_{eff,B3B}$ have to be determined through FEA as well. Up until the publication of **Publication C** ([51]), the effective quantities were available online through a Flash-based webtool (for which support was seized by most browsers in 2020) or as fits for limited parameter ranges [97].

2.3.5 Strength testing of additively manufactured ceramics

While all of the testing methods presented so far are widely used for a wide range of ceramic materials and glasses, some problems arise for the testing of additively manufactured specimens in as-fabricated condition, as will be discussed in more detail in Section 2.4. Furthermore, due to the effects outlined in Section 2.1.2, a distinct anisotropy (i.e. a dependency of the measured strength on the relation between the tensile load during testing and the orientation of the deposited layers) might be expected. As a reference, Figure 2.22 gives typical possibilities for the flexure specimen's orientation in relation to a coordinate system. During manufacturing, a single layer is always applied in the xy-plane, and the specimen is therefore built along the z-axis (=printing direction). The orientation of a specimen that is manufactured with its tensile loaded face (see section 2.3) in the xy-plane (XY) will be referred to as "horizontal", if it is in x-z-plane (XZ) then it will be referred to as "sideways", and if it is manufactured upright (YZ), it will be referred to as "vertical".

In this section, an overview of strength testing of additively manufactured ceramics in regard to this anisotropy in recent literature will be given. While this effect is relevant for a plethora of manufacturing methods, this section will focus on VPP-based methods. For a recent and general overview of strength testing of alumina and zirconia, manufactured through many different fabrication methods, the reader is referred to [99]. While many publications for the anisotropy for the SLA process are found, such as [100], [101], this section will solely deal with DLP-based methods like the LCM-process, since no other techniques have been investigated

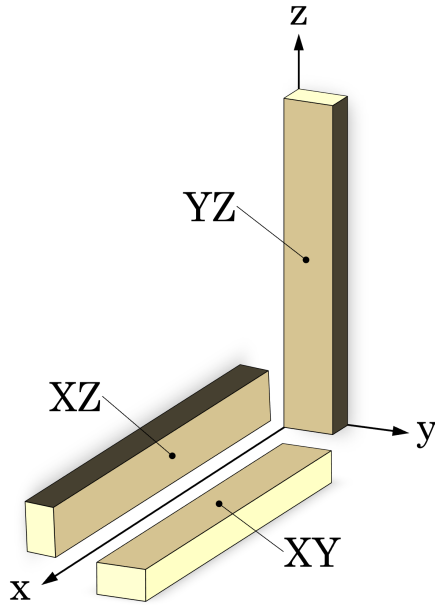


Figure 2.22: Coordinate system utilised to define the specimen orientation, adapted from [98].

within the scope of this work.

For the LCM-process, initial studies did acknowledge the existence and importance of the printing orientations' influence on the measured strength but did not perform any further investigations on the quantitative aspects. *Schwentenwein & Homa* performed four-point bending measurements on alumina, with the bending bars printed in an upright (vertical) orientation [102]. Similarly, *Schwarzer et al.* considered the orientation of square plates made from alumina toughened zirconia (ATZ) tested with the B3B-test, while *Borlaf et al.* adequately compared their results of four-point bending of zirconia to studies on the influence of the printing orientation performed by *Harrer et al.* [103]–[105]. Speaking of, *Harrer et al.* published two studies on this effect in 2017 [105], [106]. The former publication ([106]), which deals with binder development for zirconia that is subsequently tested with the B3B-test, only acknowledged this effect. The latter ([105]) presents the results of two orientations (horizontal and vertical) of zirconia bars tested in four-point bending. Furthermore, the vertical orientation is also tested with the B3B-test. In the same year, *Osman et al.* published an investigation on zirconia-discs manufactured in horizontal and vertical orientation as well as specimens tilted by 45°, which were tested using the Piston-on-Three-Balls-test [107]. All publications have noted a distinct difference of the measured strength between specimens manufactured in vertical and horizontal orientation, with the latter one exhibiting a higher strength compared to the vertical orientation. This effect can be attributed to both weak interfaces between layers if the processing parameters are not yet optimised, or to the influence of the specimen's surface, as outlined in 2.1.2

A thorough investigation of the influence of the printing orientation on the measured strength is provided by *Schlacher et al.* for alumina. Three different orientations are considered for four-point-bending, while two different orientations are considered for B3B-testing. Furthermore, the influence of as-printed surfaces versus machined surfaces (and of the sintering parameters) was also investigated [43]. They have shown that for machined specimens, no difference for the measured strength between different printing orientations is observed. *Saâdaoui et al.* investigated the defect distribution in zirconia in relation to the measured strength (three-point-bending) through X-ray tomography for both the horizontal and vertical orientation [108]. Recently, *Kammler et al.* presented results of conventionally manufactured alumina in comparison to additively manufactured alumina in 3 different printing orientations, i.e. horizontal, sideways and vertical [109].

For the DLP-process in general, *Lu et al.* performed both three-point-bending as well as RoR-tests on yttria-stabilised, tetragonal zirconia and purposely chose the more favourable (horizontal) printing orientation, but did not perform any further investigations on its influence on the measured strength [110]. Meanwhile, *Marsico et al.* presented results for partially stabilised zirconia for five different orientations (vertical, horizontal and tilted by 45°, with the latter two in a sideways-variation as well) using three-point-bending [111]. *Shen et al.* took a different, systematic approach for zirconia specimens tested in three-point-bending: Seven orientations were investigated, with all specimens being printed horizontally and the difference of each orientation being a tilt of 15° along their longitudinal axis [112]. A distinct difference in strength, with a minimum for the specimens rotated by 45°, has been found. Finally, *Zhao et al.* determined the strength of zirconia for dental implants using three point bending of "test strips" in both horizontal and vertical orientation [113]. Again, the same tendencies as outlined in the previous paragraph have been found within these publications.

Overall, while a number of investigations on the influence of the printing orientation on the measured strength have been performed, all of these investigations rely on the same testing methods that are used for conventionally manufactured ceramics. These procedures have some issues, as will be outlined in Section 2.4, and the capabilities of additive manufacturing with respect to specimen design have not yet been fully utilised for strength testing.

2.4 Practical limitations of strength testing

This section will present and discuss the advantages, disadvantages, practical limitations, and most prominent sources of error for each testing method introduced in the previous section. These errors are one of the main motivations for this work, as a significant (unsystematic) error greatly inhibits the maximum Weibull-modulus that can be measured due to the added scatter of strength results [114]. Therefore, in order to only measure the material's inherent strength and scatter thereof, it is essential to minimise any potential source of error in the testing method itself.

Uniaxial bending

For uniaxial bending tests, which seldomly allow direct testing of components, specimen preparation is an issue that has to be addressed properly. It is essential that machining is performed with care so that no critical defects are introduced at or beneath the surface. If that is not the case, the measured strength and scatter of the material will be influenced by specimen preparation and the resulting data will not be relevant for design purposes anymore. Furthermore, the surface condition of the test specimen should resemble that of the component in service. In order to reduce the risk of specimen failure due to machining-induced edge defects, the tensile loaded edges are chamfered. However, this is a possible source of error for stress evaluation, as the cross-section is reduced, which decreases the moment of inertia and increases the maximum tensile stress. Depending on the geometry of the chamfered edges, this effect can be as much as 1% to 5% [62]. Note that these issues are nearly irrelevant for biaxial testing methods, as the edge stresses are typically less than 25% of the maximum tensile stress and are therefore seldomly the cause of specimen failure [11].

Other potential issues arise from the influence of friction at the load-points, which can be as high as 13% [115]. By using moving rollers instead of fixed structures, this issue can be neglected. On the flip side, this causes the possibility of a tangency shift of the contact points due to the specimen's movement on the roller. The influence of this effect is dependent on the roller size, specimen thickness, and the flexibility as well as bending strength of the investigated material. It has been shown that this effect causes a potential error of up to 4% [115]. If smaller rollers are utilised, this error is significantly reduced, but the problem of contact stresses and wedging beneath the rollers increases [116]. Note that these two effects can only be reduced through contrasting measures and some middle-ground for the roller size has to be chosen. In general, a misalignment of the roller positions of 1% will be amplified to an error of 2 % to 4% in maximum tensile stress for 3PB and 4PB setups, respectively [115].

Finally, another significant source of error is a twisted specimen or testing setup, which can have severe influences on the whole stress field [117]. Through articulating rollers, this error can be significantly reduced. *Lube & Manner* have shown that a miniaturisation of the 4PB-setup for an outer span length of 15 mm is possible with an error of less than 10% [118]. However, further miniaturisation is limited by the positioning accuracy of the rollers and specimen manufacturing.

To conclude, it should be noted that many components are not stressed in pure uniaxial tension or bending during service, and are often subjected to a more complex, multi-axial stress state, which inhibits the meaningfulness of strength results obtained through uniaxial bending for design purposes.

The RoR-test

One of the essential aspects during testing is the reduction of friction between the load- or support ring and the specimen. As shown by *Fessler & Fricker*, friction causes stress concentrations at the regions of contact of the specimen with the rings, while simultaneously reducing the level of the constant, tensile maximum stress within the load ring radius [119]. The impact of these effects on the stress

field increases with an increase in friction.

In order to reduce friction, some sort of intermediate layers or lubricants have to be used. While lubricants have the least impact on load application, their use often impedes fractographic analysis [11]. Typically, thin intermediate layers such as carbon-, teflon- or polymer foils are applied in the regions of contact, as shown in Figure 2.15. While their drawback is an influence on the load application itself through deformation, an additional benefit of these layers is that they improve the contact between the rings and the specimen by compensating small misalignments and machining inaccuracies. This effect and its consequences on the measured strength has been discussed in more detail in **Publication D** ([120]). Due to the necessity of planar contact between the specimen surface and the load- and support rings, smooth and parallel surfaces of the specimen have to be ensured. Furthermore, the surfaces of the load- and support rings have to be machined to a high degree of flatness as well. This aspect drastically impedes the potential for miniaturisation of this testing method, as steel rings with a diameter of less than 10mm are increasingly difficult to manufacture to the required tolerances [10].

Other important aspects during testing are the alignment of the rings. More specifically, their concentricity has a severe influence on the accuracy of the analytical solution. If the centre of the load ring is shifted by 1% of the support radius, an error of 2% in the maximum stress ensues [121].

Overall, if specimens shall be tested according to the standard for RoR-test, their geometry is quite limited, but the conditions for testing are well defined. In many cases, this method is therefore not suited to test components directly or to test specimens in as-sintered conditions. However, the RoR-test allows testing of a large effective volume or surface, especially in comparison to the other biaxial testing methods described in this work [11], [51], [78], [120].

The BoR-test

While friction due to load application plays a significantly less important role in the BoR-test compared to the RoR-test [12], the problem with friction at the support ring still remains. Additionally, the ring support requires a planar surface and even contact of the specimen with the testing fixture. If this is not the case, the axisymmetric stress field is disturbed and stress concentrations at the support are formed. Furthermore, the usage of rings inhibits the miniaturisation capabilities of this testing method as well, as outlined in the previous paragraph [10].

A big advantage of the BoR-test is the simple testing setup and the availability of a complete, analytical description of its stress- and deflection-field (within the aforementioned limitations, see Chapter 2.3.3. Consequently, the effective volume and surface can either be directly determined through analytical expressions (see Chapter 2.3.3) or through numerical integration of the analytical solutions for the stress field according to Equation 2.17 [68], [78].

Still, the effective surface or volume is significantly smaller compared to that of the RoR-test, but slightly larger than that of the B3B-test, which positions this testing method as an intermediate option between these two [11], [51], [78], [120].

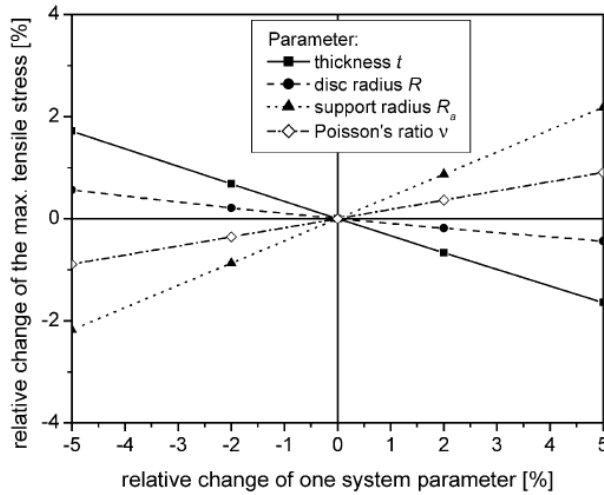


Figure 2.23: Influence of a potential change of several system parameters on the measuring accuracy for the B3B-test [80].

The B3B-test

In contrast to the other biaxial testing methods discussed so far, friction does not play a significant role for the B3B-test, as the balls are free to roll instead of the specimen sliding on their surface. This aspect and many others have been discussed in detail by *Börger et al.* [80]. In summary, some of the most prominent sources of error stem from the limited measuring accuracy of the specimen geometry and insufficient knowledge of material parameters. The influence of a potential error of some parameters on the measured strength is displayed in Figure 2.23. While the specimen's thickness t has the biggest influence, it is often the Poisson's ratio ν that causes the biggest error, as its value is usually not known as well as the geometric parameters [80], [95].

An important aspect of the B3B-test is the potential for miniaturisation. Since bearing balls are manufactured to a high degree of accuracy and are widely available in small sizes ($R_B \leq 1\text{mm}$), specimens as small as $2\text{mm} \times 2\text{mm}$ have successfully been tested [122], [123]. Due to the well-defined support by three points of contact, this method allows testing of warped or tapered specimens, which is not possible with any ring-supported testing method.

Another important aspect of the B3B-test is the small region of maximum stress. On one hand, this allows localised testing of specimens or components [124], [125], but, on the other hand, results in the comparatively smallest effective surface or volume of the biaxial testing methods discussed in this work.

Finally, one of the biggest drawbacks of this method is the absence of a sufficiently accurate analytical solution. As shown in Section 2.3.4, numerical methods have to be utilised for strength evaluation instead. However, the existing fits are lengthy and cumbersome to use, and the number of necessary constants makes them prone to errors. Similarly, the effective surface and volume are also based on a numerical evaluation and are only available for a limited range of parameters, which drasti-

cally impedes a comparison of the B3B-test to other testing methods on the basis of Weibull-theory.

"CharAM-test"

An error analysis of this testing method which is based on strength testing of cantilevers, is performed in **Publication D** ([14]). Therefore, it will not be discussed at this point and the reader is referred to Chapter 4.4 of this work. Instead, the necessity for a novel testing method for strength testing in the context of additive manufacturing will be discussed. Some of the presented arguments can also be found in [19].

As outlined in Chapter 2.1.2, additive manufacturing methods introduce specific, process-related defects to the material, on top of the range of defects that is already present in conventionally manufactured ceramics. Therefore, it is essential to employ testing methods that allow the assessment of these specific defects. For this work, an important example of typical defects are the surface structures created by the LCM-process, which depend on the printing orientation and are severe enough to cause a significant variation in strength. As a consequence, it is necessary to investigate the strength of the material in multiple orientations (relative to the printing direction).

Furthermore, the specimens should be tested in as-fabricated condition, as any machining would counter one of the biggest advantages of additive manufacturing, which is the near-net-shape aspect of the manufacturing process. However, the requirements of many established testing methods are difficult to meet under these circumstances. First and foremost, for a well-founded statistical analysis of the material's strength, a minimum of 30 specimens have to be tested, otherwise the uncertainty increases disproportionately high [52], [53]. Due to the restricted amount of printing area or volume for many processes, multiple print-jobs are required to produce the necessary number of specimens. Not only does this introduce an additional aspect of variation within a single set of specimens, it is also time- and material-intensive. Note that in some cases, this aspect can be desired, as outlined in [126]. While miniaturisation of the test specimens would help to reduce the number of print-jobs, it is seldom possible due to limits in the process tolerances or due to limits in the testing methods, as outlined above.

Another aspect to consider is the final geometry of the specimen. During sintering, specimen warpage is rarely avoided, which prevents testing with any ring-loaded or even ring-supported methods, as proper contact between the specimen and the fixture will not be achieved. For other methods, such as 4PB or the B3B-test, warped specimens can be tested, but the warpage's influence on the measured strength has to be considered adequately, sometimes even for each specimen individually. Additionally, structured surfaces further impair the contact between the specimen and the testing fixture, which has to be taken into account.

While the B3B-test could take all of these considerations into account, it's small region of maximum stress and consequently small effective volume results in inefficient testing, as the majority of the volume or surface of each specimen remains relatively unstressed [13].

3. Relevant methods

This chapter will briefly introduce the numerical and experimental tools or methods that were used in this work. However, it is out of scope of this work to explain the utilised methods in detail, and the reader will be referred to the cited literature for a better, in-depth description of the respective methods.

3.1 Numerical methods

One of the key methods that was utilised in this work is Finite-Element-Analysis (see [127]–[131] for more information on the method itself) through a total of 14 individual models. All simulations conducted were performed with ANSYS Mechanical by ANSYS Inc. (Southpointe 2600 Ansys Drive, PA 15317, Canonsburg, USA), with versions R19.1 for **Publication A** ([120]) to R22.1 for **Publication D** ([51]). Each model was implemented through the internal coding language APDL (Ansys Parametric Design Language) for better traceability and documentation. Most importantly, it enables script-based parametric studies to assess the influence of a variety of input parameters on an automated basis. Both two-dimensional models as well as three-dimensional models were utilised, with runtimes that varied from several seconds for the simplest models to multiple hours for the most demanding ones.

For all models, linear elastic and isotropic material behaviour was assumed. For 2D-models, 8-node quad elements (PLANE183) were used for the specimen and loading structures. For simulations that involved the contact between two solid bodies, CONTA172 and TARGE169 elements were employed. Similarly, for 3D-models, 20-node brick elements (SOLID186) were utilised for the specimen's and the fixture's mesh and contact was also implemented through CONTA172 and TARGE169 elements. The coefficient of friction μ was either varied, or, if not stated otherwise, $\mu = 0.5$ was assumed. An example of a meshed 3D-model for the B3B-test for square plates is given in Figure 3.1. For each model, a mesh convergence analysis was performed in order to assure a sufficiently fine mesh. This was especially important for the calculation of the effective quantities in **Publication D** ([51]), since they are highly sensitive to the shape of the stress field in the vicinity of the position of maximum tensile stress. The post-processing procedure to obtain the effective quantities is outlined in [132] and the appendix of **Publication D** [51].

Due to the high number of simulations that were conducted for this work, efficient data processing was essential. This step was performed within the scientific programming package Mathematica from Wolfram Research, Inc. (100 Trade Center Drive, Champaign IL 61820–7237, USA). Throughout this work, versions 12.0 to 13.1 were employed. Furthermore, the majority of analytical derivations were assisted or at least implemented within Mathematica scripts to ensure reproducibility and to minimise errors. This was especially relevant for solving the differential equation and the resulting system of equations in **Publication A** for

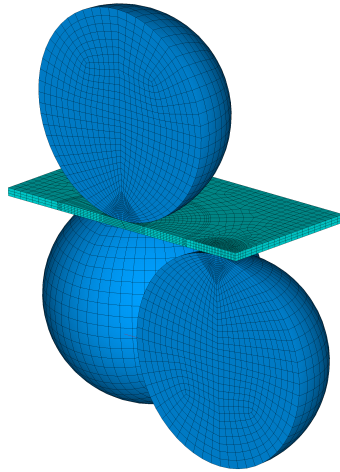


Figure 3.1: 3D-model of the B3B-test for square plates, which considers the interaction of the load/support balls and the specimen, from **Publication C**.

the analytical solution of the Ball-on-Ring-test [133].

Another numerical technique that was utilised in **Publication F** ([14]) was Monte-Carlo analysis (see [53], [114]). Through a high number of repetitions (≥ 1000) of a process that is dependent on a statistical distribution, a trend towards certain values for the results of the process can be observed. An overview of the process of such an analysis from **Publication F** is given in Figure 3.2.

3.2 Experimental methods

All strength results presented in **Publication D**, **Publication E** and **Publication F** ([14], [51], [120]) were obtained with a universal testing machine (Model Z1010) by ZwickRoell GmbH & Co. KG (August-Nagel-Strasse 11, 89079 Ulm, Germany). The load frame is equipped with either a KAP-S load cell (maximum load = 200N) by AST GmbH (Marschnerstrasse 26, 01307 Dresden, Germany) or a Xforce HP by ZwickRoell (maximum load = 10kN). It is operated through a control system by Doli Elektronik GmbH (Rudolf-Diesel- Strasse 3, 72525 Münsingen, Germany). For the strength results presented in **Publication C**, a prototype developed at INSA Lyon was utilised. The B3B-fixture was placed inside a transparent PMMA tube which is mounted to a loading stage with a 5kN load cell.

Fractography was performed on the specimens of **Publications C-F** ([14], [51], [120]) with a SZH10 stereomicroscope by Olympus K.K. (2-3-1 Nishi-Shinjuku, 163-0914 Tokyo, Japan) which was operated through the "Olympus Stream Motion" software, version 2.2. Fracture surfaces were investigated in more detail using a scanning electron microscope (Model NeoScope JCM-6000Plus) by JEOL K.K. (3-1-2 Musashino Akishima-Shi, 196- 8558 Tokyo, Japan). Prior to imaging, each

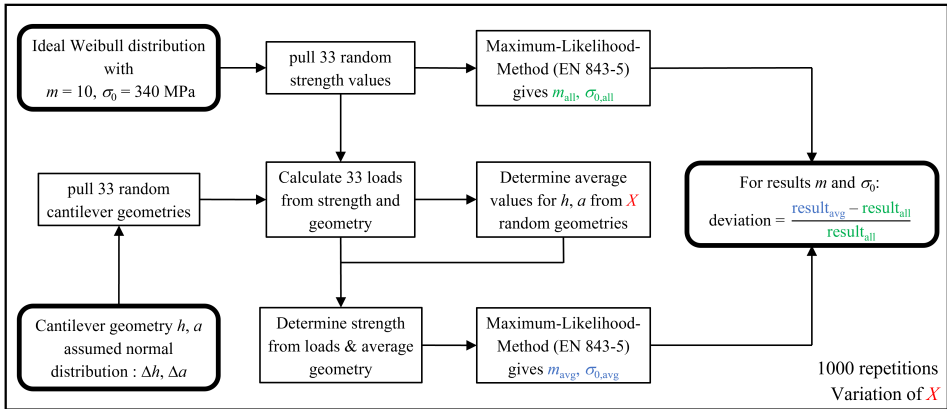


Figure 3.2: Outline of the Monte-Carlo analysis as performed in **Publication F** [14].

specimen was coated with gold sputtering and conducted to a metal base through copper wires and silver paste. For a comprehensive overview of fractography for ceramics and glasses, the reader is referred to [134].

For the radiography and tomography experiments presented in **Publication C**, a Vtomex tomograph by phoenix|x-ray systems (Niels-Bohr-Strasse 7, Wunstorf 31515, Germany) was utilised. The software “datos|x”, version 2.0, was used for post-processing and volume reconstruction of the raw data from the detector. A detailed account of the necessary filtering is given in **Publication C**. Any further analysis or processing of the scans was conducted through the open-source program ImageJ, version 1.53t, with the use of built-in extensions and the MATEIS plug-in. For an introduction to in-situ experiments through X-ray tomography, the reader is referred to [135], [136].

For the analysis of the surface topology in **Publication E**, **Publication F** and **Publication H** [14], [45], [120], a laser confocal microscope (Model VK-X1000) by Keyence Corporation (1-3-14 Higashi-Nakajima, 533-8555 Osaka, Japan) was utilised. Data evaluation was performed within the accompanying software “MultiFileAnalyzer”, version 2.2.0.93, by Keyence Corporation. The underlying principles are explained in [137]–[139].

For the specimens fabricated through additive manufacturing in **Publication F** and **Publication H** ([14], [45]), a 3D-printer utilising the LCM-process (as outlined in section 2.1.2) was employed. More specifically, a CeraFab 7500 by Lithoz GmbH (Mollardgasse 85A, 1060 Vienna, Austria) was used. Most test specimens were manufactured in-house from the alumina-based slurry LithaLox350, with some specimens from **Publication H** ([45]) being manufactured from the alumina-based slurry LithaLox HP500. In either case, any excess slurry was removed from the manufactured green bodies with an airbrush and the use of the solvent LithaSol20, produced by Lithoz GmbH. For thermal post-processing, debind-

ing was performed in a vented furnace (Model KU15/06/A) by ThermConcept (Friedrich-List-Strasse 17, 28309 Bremen, Germany) and sintering was conducted in a HTL10/17 furnace by ThermConcept. While the details of each thermal post-processing step were varied, the maximum temperature and holding times were identical. During debinding, a maximum temperature of 430 °C was reached, and during sintering a maximum of 1650 °C was reached for 2h.

4. Advancements of established methods and the extension towards additive manufacturing

This chapter will present the most notable findings of each publication within this work. In the case of the Ball-on-Three-Balls-test, several publications are combined to a single section to give a more general conclusion on the advancements of this method. Since all publications presented have been published independently of each other, some variables will be defined repeatedly and will not always correspond to the nomenclature used so far. Therefore, if necessary, each variable will be re-defined accordingly in the corresponding section.

4.1 Deriving an analytical solution for the BoR-test

This section will summarise the contents of **Publication A** ([133]), which focuses on the Ball-on-Ring-test and its analytical solution. As outlined in Section 2.3.3, the analytical description of the stress- and deflection-field was investigated for many years. In most cases, the solutions provided so far were based on a simplified approach by assuming a constant load distribution beneath the loading ball. In this work, a Hertzian load distribution was assumed instead. Kirchhoff-Love-plate theory was utilised to derive a solution for the radial-, tangential- and shear-stress field for the full disc, with the effect of the overhang considered as well. Furthermore, analytical expressions for the deflection, slope and curvature of the disc are given. For the maximum tensile stress σ_{max} in the centre of the disc, the same solution as provided by *Hu* (see Equation 2.58) was obtained.

Since this quantity is essential for strength testing, further investigations on σ_{max} were conducted, such as a comparison to σ_{max} obtained through the assumption of a constant load by *Frandsen*. The result is shown in Figure 4.1. Depending on the relative overhang α of the disc and the relative loading radius β , an increase in σ_{max} between 3.5% to 7.5% was observed. However, plate theory does not take the thickness of the specimen into account. A comparison of σ_{max} obtained through either the analytical solution or FEA was performed for various specimen geometries and loading conditions and is shown in 4.2. It is evident that plate theory fails to describe specimens with a small relative loading radius β , and that this effect increases with an increasing relative thickness γ of the plate. For $\beta \rightarrow 0$, a singular (infinite) stress is approached.

This shortcoming has been dealt with through a correction by *Westergaard*, but was obtained under the assumption of a constant, central load distribution. Therefore, a new correction based on the ansatz by *Westergaard* and the results of FEA was derived. The difference for σ_{max} between the analytical solution in combination with the respective correction to results obtained by FEA is shown in Figure 4.3a and

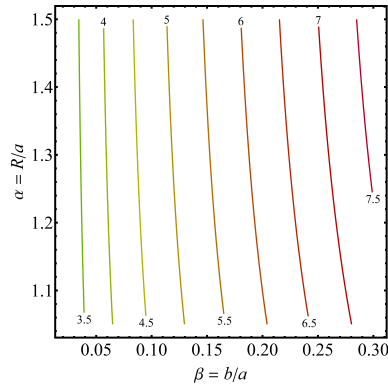


Figure 4.1: Relative difference of the maximum tensile stress (in %) between considering a Hertzian load distribution and considering a constant stress distribution for various specimen and loading geometries. R refers to the specimen’s radius, a to the support radius, and b to the radius of the Hertzian load distribution [133].

Figure 4.3b. With the new analytical solution and correction, a maximum error of less than $\pm 1\%$ is achieved for a wide range of specimen geometries. Consequently, a highly accurate description of the maximum tensile stress is provided, which eliminates the need for FEA to determine σ_{max} . Additionally, this solution for σ_{max} can be applied to any ball-loaded biaxial bending test, as the maximum tensile stress in the centre of the disc is independent of the number of support points, as shown by *Kirstein & Woolley* (see Section 2.3.3). A comparison of σ_{max} to FEA-results of the B3B-test has given an error of less than $\pm 3.3\%$, thus showing excellent agreement with these theoretical findings.

4.2 Extending the range of application of the B3B-test

This section deals with the improvements that were made for the B3B-test, and includes the work of three publications, namely **Publication B**, **Publication C** and **Publication D** ([51], [140]). Within **Publication B** ([140]), the stress evaluation of the Ball-on-Three-Balls-test was extended to include square plates, on top of providing a significantly simpler fit (compared to Equations 2.61 and 2.63) for both discs and squares.

Additionally, non-linear, load-dependent effects were incorporated into the evaluation through a pseudo-analytical approach as multiplicative correction factors. These effects stem from two major sources: On one hand, an increased area of contact between the loading ball and the specimen leads to a deviation from an idealised, punctiform load introduction towards a Hertzian surface load. On the other hand, the deflection of the specimen causes an inwardly shift of the point of contact between the support ball and the specimen. Both effects decrease the applied bending moment and cause an overestimation of the measured strength, if not considered properly. While the impact of these effects on the measured strength is smaller than 2% for many specimens, they should not be neglected if high-strength ceramics or glasses are tested.

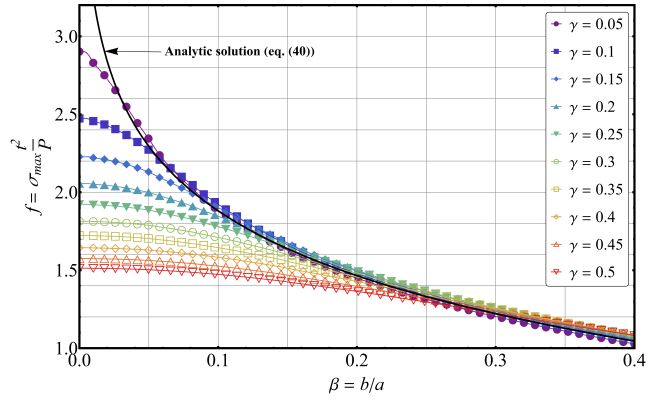


Figure 4.2: Comparison of the results for the normalised maximum tensile stress from the analytical solution to FEA. Note that the annotation refers to Equation 40 in [133]. t refers to the specimen's thickness, and γ refers to the specimen's thickness in relation to the support radius a , i.e. $\gamma = t/a$ [133].

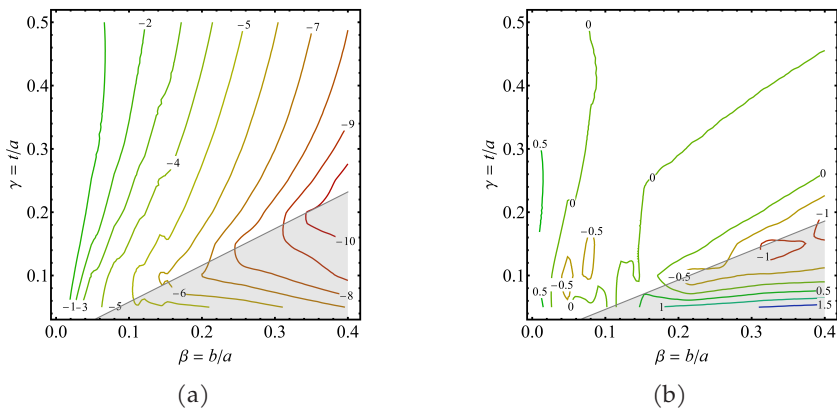


Figure 4.3: Relative difference (in %) for σ_{max} between FEA and the analytical solution in combination with the correction by Westergaard (a) or by the author (b) [133].

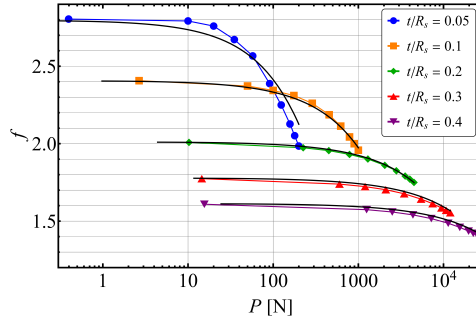


Figure 4.4: Comparison of the normalised maximum stress $f = \sigma_{max}t^2/P$ in dependence of the applied load obtained through the pseudo-analytical solution (black lines) or through non-linear FEA (coloured lines and markers) [140].

Overall, excellent agreement between the pseudo-analytical approach and non-linear FEA was achieved, as displayed in Figure 4.4. Thus, the stress evaluation for the B3B-test was notably simplified, while also providing a significant increase in accuracy for high-strength specimens, hence omitting the need for individual FEA in many cases.

A follow-up to **Publication B** is given through **Publication C**. Since all of the results presented in **Publication B** rely on theoretical considerations and are only validated by FEA, some sort of experimental validation is still necessary. Therefore, an attempt to measure the specimen's deflection during B3B-testing and subsequent comparison to FEA-results was made. Due to the special construction of the B3B-testing fixture, well established methods to measure deflection during strength tests such as the use of a Linear Variable Differential Transformer (LVDT) (which requires specimen contact) or Digital Image Correlation (DIC) (which requires a direct view of the specimen) cannot be utilised. Instead, X-ray tomography was employed to open the opportunity for a "direct" view of the specimen and the loading/supporting balls, as given in Figure 4.5.

From a three-dimensional reconstruction (tomograph) of the testing assembly, the specimen's deflection can be determined, as well as the movement of the loading and supporting balls during loading. Alternatively, two-dimensional radiographs were also evaluated to allow a continuous recording of the deflection during testing in contrast to the discontinuous method that tomography is providing. Through this procedure, a vast increase in the number of datapoints was achieved and better load-wise resolution is obtained. Furthermore, a higher displacement compared to tomography measurements was observed, since the impact of sub-critical crack growth is significantly lower.

In general, a good agreement between the tomography measurements and FEA was obtained. As shown in Figure 4.6, the behaviour significantly deviates from the linear model, which highlights the importance of considering these effects under such circumstances. The radiography measurements show good agreement with the general tendencies as well, but they do not yield the same absolute values as FEA. Instead, both measurements deviate by a systematic offset of about $200\mu\text{m}$. Overall, these two approaches are promising, but several aspects still need to be improved until they are a suitable alternative to other, well-established methods.

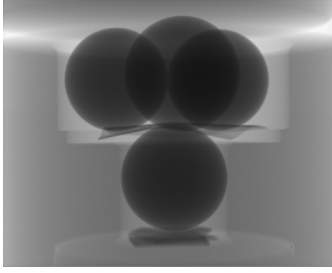


Figure 4.5: Deformed glass specimen at maximum load (26N) before failure, see **Publication C**.

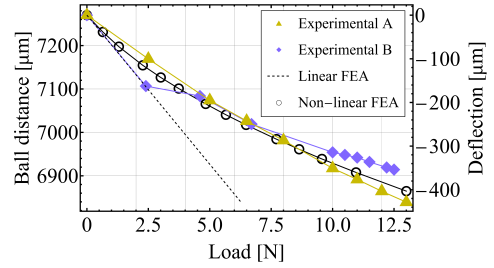


Figure 4.6: Experimental tomography results compared to linear and non-linear FEA, see **Publication C**.

However, the validity of FEA was shown with both tomography and radiography measurements, thus also validating the pseudo-analytical equations obtained in **Publication B**, which generally describe a range of less extreme testing circumstances.

Further developments of the B3B-test include the determination of the effective volume and surface for a wide range of specimen geometries and materials, as given in **Publication D** ([51]). The data for the effective quantities was generated through FEA and is published for both discs and square plates. For each geometry, results for both the maximum principal stress criterion (FPS) and the principle of independent action (PIA) were made available.

Also, a fit for the dependency of the effective quantities on the Weibull modulus for any one specific geometry was provided. The necessity of this fit is shown through a pooled evaluation of strength data obtained with specimens of varying geometry, which opens up the possibility to use the available information more efficiently. The results are given in Figure 4.7 through a Weibull-plot with both specimen geometries extrapolated to the same reference surface S_0 . This plot highlights the importance of testing at different effective quantities for a for a more reliable extrapolation of the probability of failure.

But, most importantly, this work now enables all users of the B3B-test to compare their results to other testing methods through the concept of the effective volume, as outlined and performed in the upcoming section within **Publication E** ([120]). Finally, it should be noted that the use of a hexagonal specimen geometry (due to better printability for additive manufacturing) for the B3B-test was investigated in **Publication G** ([94]).

4.3 Comparing the B3B-test to the RoR-test

This work, as given in **Publication E** ([120]), demonstrates the process of comparing two biaxial testing methods on the basis of Weibull theory. More specifically, the B3B-test was compared to the RoR-test, and the numerical results for the effective quantities, as outlined in the previous section, were utilised. Good agreement according to Weibull theory was found for most of the investigated samples, but some outliers demanded further attention, as shown in Figure 4.8. These outliers

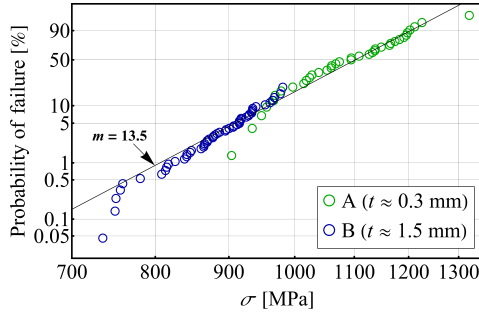


Figure 4.7: Results of a pooled Weibull analysis with the probability of failure of Sample B extrapolated to the same reference surface S_0 as Sample A [51].

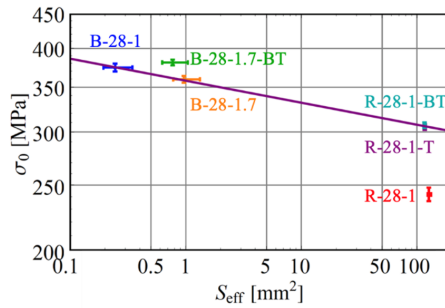


Figure 4.8: Characteristic strength of samples from different methods and geometries in dependence of their respective effective surface. Note the difference of the effective surface of approximately two magnitudes [120].

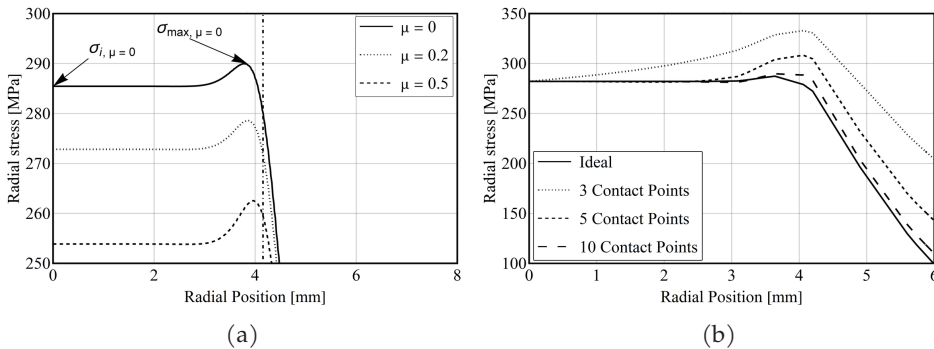


Figure 4.9: Influence of friction (a) or uneven contact for a different number of contact points (b) on the radial stress component in dependence of the radial position for the RoR-test [120].

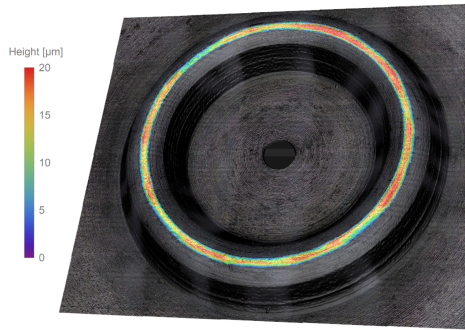


Figure 4.10: Topographic scan of a load ring for the RoR-test, obtained with a laser confocal microscope [120]

were a B3B-sample that was tested with an intermediate layer under the load ball, and a RoR-sample that was tested without any layers at all.

Consequently, another important aspect of this investigation was to assess the influence of surface layers and friction on the stress field in both testing methods. For the B3B-test, it was found that the usage of soft intermediate layers underneath the loading ball overestimates the measured strength. This can be explained through the deformation of the surface layer, which increases the area of contact, which is an effect that was already discussed in other work (see **Publication B** [140]) and decreases the bending moment. If this effect is not accounted for, the strength is overestimated, as higher loads are necessary for fracture and therefore higher apparent strengths are measured.

For the RoR-test, omitting the surface layers introduces friction to the contact between the rings and the specimen. The influence of friction on the radial stress component is given in Figure 4.9a, which shows a decrease of the constant stress level with an increase in friction, but also leads to the formation of stress concentrations at the load ring radius. Additionally, through the lack of soft layers, small misalignments or the uneven contact between the load ring and the specimen's surface are not compensated for. Again, this effect leads to stress concentrations at the load ring, and especially at the position of uneven contact, as shown in Figure 4.9b. Therefore, at a given load, a higher stress than expected is applied in those regions, which results in a general underestimation of the measured strength.

This finding is backed up by fractography of the specimens tested with and without intermediate layers. For those tested without layers, a significantly higher number of fracture origins were located at or close to the radius of the load ring as compared to the specimens tested with intermediate layers. An investigation of the load ring's surface through laser confocal microscopy revealed significant undulations with an amplitude in the range of $20\mu\text{m}$, as shown in Figure 4.10. Subsequent Finite-Element-Analysis has shown that these undulations are not compensated through elastic deformation and contact to the specimen is limited to several points.

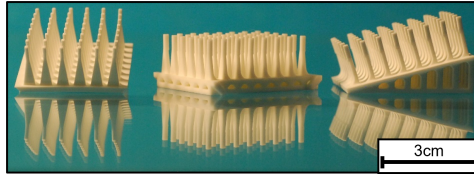


Figure 4.11: Overview of the three different configurations of the CharAM specimen, adapted from [14].

4.4 Applying the obtained knowledge to the development of a novel test method

This section deals with the results of **Publication F** ([14]), which presents an introduction to and development of a novel strength testing method based on cantilever bending for ceramics manufactured through the LCM-process. As outlined in previous sections (see Section 2.1.2 and Section 2.4), additive manufacturing causes process-specific defects and issues, which impede the use of well-established testing methods. Therefore, a novel testing method was conceptualised at the IKTS Dresden within the scope of a master's thesis [141]. Through the bi-national project "CharAM" (FFG 877684) of the COIN/IraSME program, the method was further developed, refined, and validated. Some aspects of this process are discussed in **Publication F**, hence why only a brief introduction to the testing method will be given here.

The novelty of the method is based on the test specimen, which is displayed in different configurations in Figure 4.11. The characteristic features of the test specimen are a baseplate, which consists of two solid plates connected through an arched structure, and 48 cantilevers, which are attached to the upper part of the baseplate. As discussed in Section 2.1.2, the surface structure of a printed specimen has a distinct influence on its failure behaviour and strength, and is strongly dependent on the printing orientation of the specimen's surface. In order to assess this influence of surface structures, multiple configurations of the test specimen were developed. By tilting the upper solid plate, the inclination of each cantilever is changed accordingly. For now, three configurations are available: A specimen with no inclination to the printing direction, one with an inclination of 15° , and one with an inclination of 15° combined with rotation of 180° of the cantilevers along their respective longitudinal axis. The baseplate of each configuration is approximately $26\text{mm} \times 35\text{mm}$, and the height varies from 15mm to 20mm.

While the structure of the baseplate changes, the geometry of the cantilevers is the same for each configuration. Figures 4.12a and 4.12b show the geometry of the cantilever from the top and side, respectively. A small bulge is printed on each cantilever to ensure a consistent position of load introduction. Due to the special design of the cantilever, namely its linear increase in width, a region of constant bending stress is obtained, and marked as "Testing region" within Figures 4.12a and 4.12b. The maximum tensile stress σ_{max} in this region is determined through Euler-Bernoulli beam theory and is given by [142]

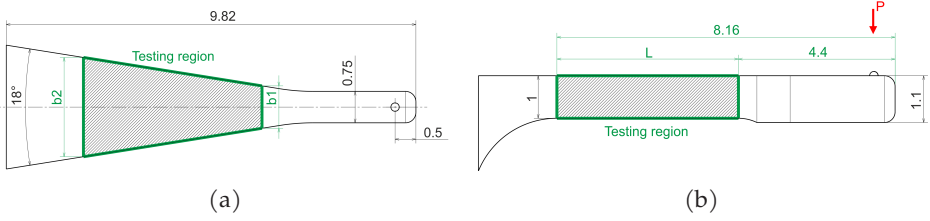


Figure 4.12: Dimensions of the cantilever (in mm) in top-view (a) and side-view (b) [14].

$$\sigma_{max} = \frac{6P}{kh^2} \quad (4.1)$$

with h as the thickness of the cantilever, and k as the slope of the inclined flanks, which is determined through

$$k = \frac{b_2 - b_1}{L} \quad (4.2)$$

The parameters L , b_1 and b_2 refer to dimensions of the cantilever, as marked in Figures 4.12a and 4.12b. Due to the simplicity of the stress field in the testing region, analytical expressions for the effective volume and effective surface can be determined according to Equations 2.17 and 2.21, respectively.

While the method itself was developed at the IKTS in Dresden, the details of strength evaluation and possible sources of error were investigated within the scope of this work. Initially, a comparison between the ideal maximum tensile stress as given through Euler-Bernoulli beam theory and the stress field according to FEA was conducted. The results are shown in Figure 4.13a. Overall, a maximum difference of less than $\pm 2.5\%$ is observed. If the analytical solution is utilised, the maximum tensile stress will be overestimated at the borders of the testing region and edges of the cantilever, while it will be underestimated in the centre of the testing region. From the analytical stress field, a closed form expression for the effective volume and surface were derived. Again, a comparison to FEA has shown only a slight deviation, as displayed in Figure 4.13b. Especially for a Weibull modulus $m \geq 5$, excellent agreement between the analytical and numerical solution was achieved.

A major focus of this publication was the influence of geometrical inconsistencies on the measured strength and on the subsequent statistical evaluation. First, a significant variation in the height and opening angle of each cantilever was observed, which necessitates additional measurements of these values. While averaging the geometries of several random cantilevers on each specimen could reduce the measurement effort, it is shown that the impact on statistical strength analysis is too severe and that individual geometrical measurements are necessary. Second, the impact of a non-rectangular cross section of the cantilevers was analysed and discussed. Due to overpolymerisation, a barrel-shaped cross section is obtained, and, if not considered adequately, the strength of the material is underestimated. On average, this effect can be as large as 10%. Third, the effect of a shift in the position of load introduction was discussed and quantified. However, this effect is less severe

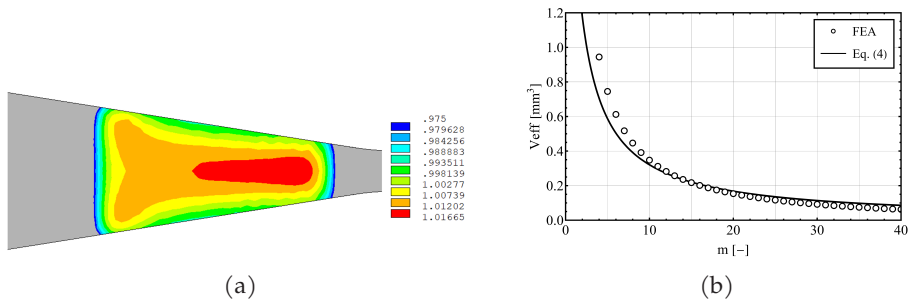


Figure 4.13: Deviation of the cantilever’s stress field obtained through FEA to beam theory (a) and comparison of its effective volume obtained through FEA and Equation 2.17 (b) [14].

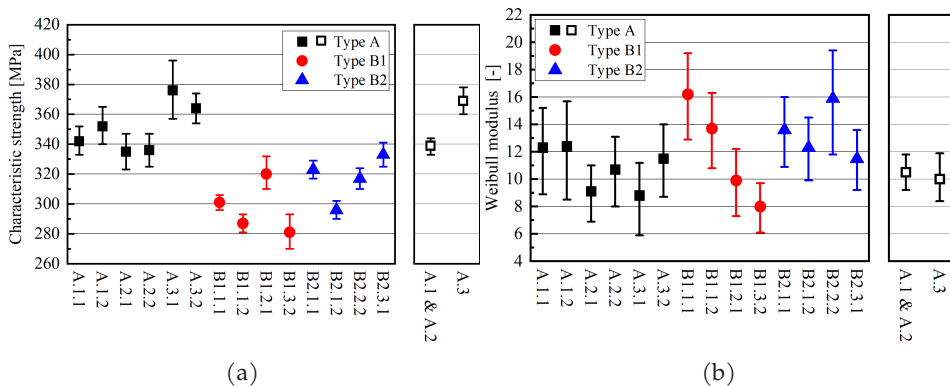


Figure 4.14: Characteristic strength (a) and Weibull modulus (b) for various configurations and multiple specimens [14].

than the ones mentioned beforehand and taking it into account for each cantilever would require too much experimental effort. Thus, this effect adds about 1.5% to 3% to the general measurement uncertainty of $\pm 2\%$ of this testing method.

Finally, several specimens of each testing configuration were manufactured and tested in a universal testing machine (UTM). The results of statistical strength analysis is shown in Figure 4.14a and Figure 4.14b. As expected, a significant decrease of the characteristic strength σ_0 for 15°-specimens was observed, while the Weibull modulus m remained unchanged. This is in good agreement with the results obtained through other testing methods and theoretical considerations based on Weibull theory, as given in **Publication H** ([45]).

5. Summary & Outlook

In this work, an in-depth analysis of several strength testing methods for brittle materials was performed. The findings of this work were obtained through a combination of theoretical considerations (e.g. plate- or beam-theory), numerical methods such as Finite-Element-Analysis, and experimental validation through means such as fractography and X-ray tomography. More specifically, the advancements made can be summed up as follows:

- For the Ball-on-Ring-test, the analytical expressions for the stress- and displacement field for the whole specimen were reworked to consider a Hertzian surface load beneath the loading ball instead of a simplified, constant load distribution. It was shown that, depending on the specimen geometry, a significant difference in the value for the maximum stress is obtained. The analytical expressions were validated through FEA and the applicability of the provided equations for other ball-load strength testing methods was demonstrated.
- For the Ball-on-Three-Balls-test, a new fit of numerical results for the evaluation of the maximum tensile stress for both discs and square plates was provided. In comparison to previous fits, a simpler equation for the same range of geometry and materials was obtained, without any loss in accuracy. Additionally, the influence of non-linear, load-dependent effects was discussed and corrections for the stress evaluation are presented. These expressions were validated through Finite-Element-Analysis and experimental findings. The experimental results were obtained through X-ray-tomography and radiography and a good agreement to theoretical considerations and Finite-Element-Analysis was observed. Furthermore, the effective volume and surface for this testing method were determined and were made publicly available. This allows a comparison of the strength results of the Ball-on-Three-Balls-test to the results of any other testing method. An example of the application of these results was given through a pooled Weibull-analysis.
- A comparison of the Ball-on-Three-Balls-test to the Ring-on-Ring-test, based on Weibull-theory, was performed. While most investigated samples have shown excellent agreement to theory, a few outliers were identified and discussed. These outliers have formed the basis for an investigation of the influence of soft, intermediate layers on the measured strength for both the Ball-on-Three-Balls-test and the Ring-on-Ring-test. Additionally, the influence of friction and uneven contact between the fixture and the specimen was investigated for the Ring-on-Ring-test and the findings were validated through fractography.
- Finally, a novel strength testing method for ceramics manufactured through the LCM-process was introduced and investigated in detail. Due to the pixel-based nature of the LCM-process and the layered manufacturing, well-

established testing methods cannot be utilised or have been proven to be inefficient. Therefore, a novel strength testing method was developed to take the special aspects of additive manufacturing into account. However, several issues due to process-related inconsistencies had to be analysed qualitatively and quantitatively. These findings were incorporated into the strength evaluation and the capability of this testing method was demonstrated experimentally.

For future work, the experimental validation of the theoretical findings for the Ball-on-Three-Balls-test through X-ray tomography or radiography shall be further developed through the use of better equipment, such as the use of a beam line and load-cells with a higher accuracy and resolution. This will allow an investigation of other, stiffer materials with less deformation, which are encountered more frequently. Through modifications of the testing fixture, well established methods for deflection measurement could be implemented and allow further assessment of the applicability of this method. Another aspect that is worth considering is the influence of non-linear material behaviour on the measured strength, as would be encountered if specimens with a transformation plasticity are tested. Finally, the possibility of contact damage through load application could be assessed experimentally for a number of different material- and testing configurations, as this consideration is one of the biggest hindrances for the wide-spread use of this testing method.

Additionally, a thorough investigation of the variability of the Ball-on-Three-Balls-test should be performed, whereas a round-robin trial could lay the groundwork for future standardisation. Practical aspects of the testing method, such as the usability of the provided equations or the user-friendliness of the tools provided for the evaluation of the effective quantities should be investigated. Furthermore, a comparison of results obtained through multiple laboratories could give further insight to the reproducibility of the method. Overall, important aspects such as comparability, effort, applicability, accuracy, and reproducibility of the B3B-test shall be compared to existing, standardised strength testing methods.

For the CharAM-test, the automated optical scanning of the specimen after testing is currently under development. This will allow a fast and reliable acquisition of the necessary geometrical data for accurate strength evaluation. Furthermore, possible sources of error, such as the varying cross-section of the cantilevers, will be negated through individual scanning and evaluation of the exact cross-section. Additionally, automated acquisition of the relevant geometrical parameters will allow a better assessment of the influence of fabrication parameters on the final component geometry. Due to the small absolute size of the cantilevers, small changes in the relevant parameters will have a higher relative impact on the final geometry compared to existing specimens for strength testing. This aspect, in combination with the aforementioned benefits of the testing method, might ultimately even serve as a benchmark for the quality of the fabrication equipment or processing method. Furthermore, round-robin trials could highlight the variability of the measured strength due to the manufacturing equipment and conditions, such as the 3D-printer itself, the furnace, and the positioning of specimens within the furnace. Beyond that, the number of possible configurations for the specimens of this testing method could be extended to include other inclinations as well. Finally,

the application of the CharAM-test could be extended towards other DLP-based methods ,or the specimen could even be up- or downscaled for entirely different additive manufacturing methods.

6. List of Publications

6.1 Contributions as first author

Publication A:

The Ball-on-Ring-test: Enhancing an analytical solution by numerical analysis for elastic deformation and small displacements

Maximilian Staudacher, Peter Supancic, Tanja Lube

in Journal of the European Ceramic Society 43, Issue 15 (2023) 7167-7177.

doi: <https://doi.org/10.1016/j.jeurceramsoc.2023.06.016>

Publication B:

The Ball-on-Three-Balls strength test for discs and plates: Extending and simplifying stress evaluation

Maximilian Staudacher, Tanja Lube, Peter Supancic

in Journal of the European Ceramic Society 43, Issue 2 (2023) 648-660.

doi: <https://doi.org/10.1016/j.jeurceramsoc.2022.09.047>

Publication C:

The Ball-on-Three-Balls strength test: In-situ testing through X-ray radiography and tomography

Maximilian Staudacher, Gustavo Pinzon, Jérôme Adrien, Joël Lachambre, Eric Maire, Jérôme Chevalier, Tanja Lube

(Submitted for publication in Open Ceramics, under review)

Publication D:

The Ball-on-Three-Balls strength test: Effective volumes and surfaces for Weibull strength scaling

Maximilian Staudacher, Anna Eggel, Peter Supancic, Tanja Lube

in Journal of the European Ceramic Society 44, Issue 1 (2024) 173-183.

doi: <https://doi.org/10.1016/j.jeurceramsoc.2023.09.018>

Publication E:

Comparison of biaxial strength measured with the Ball-on-Three-Balls- and the Ring-on-Ring-test

Maximilian Staudacher, Tanja Lube, Josef Schlacher, Peter Supancic

in Open Ceramics 6, (2021) 100101.

doi: <https://doi.org/10.1016/j.oceram.2021.100101>

Publication F:

A novel test specimen for strength testing of ceramics for additive manufacturing

Maximilian Staudacher, Tanja Lube, Jürgen Glettler, Uwe Scheithauer, Martin Schwentenwein

in *Open Ceramics* 15, (2023) 100410.

doi: <https://doi.org/10.1016/j.oceram.2023.100410>

6.2 Contributions as co-author

Publication G:

Stereolithography-based additive manufacturing of polymer-derived SiO₂/SiC ceramic composites

Johannes Essmeister, Altan Alpay Altun, Maximilian Staudacher, Tanja Lube, Martin Schwentenwein, Thomas Konegger

in *Journal of the European Ceramic Society* 42, Issue 13 (2022) 5343-5354.

doi: <https://doi.org/10.1016/j.jeurceramsoc.2022.06.021>

Publication H:

Stereolithographic 3D Printing of Ceramics: Challenges and Opportunities for Structural Integrity

Tanja Lube, Maximilian Staudacher, Anna-Katharina Hofer, Josef Schlacher, Raul Bermejo

in *Advanced Engineering Materials* 25, (2022) 2200520.

doi: <https://doi.org/10.1002/adem.202200520>

6.3 Contributions to the publications as first author

Publication A:

Manuscript preparation, Analytical derivation, FEA-model and simulations, Data analysis

Publication B:

Manuscript preparation, Analytical derivation, Numerical fitting, FEA-model and simulations, Data analysis, Validation

Publication C:

Majority of manuscript preparation, X-Ray experiments, Image analysis, FEA-model and simulations, Data analysis

Publication D:

Manuscript preparation, Numerical fitting, FEA-model and simulations, Data analysis

Publication E:

Manuscript preparation, Strength tests, Fractography, FEA-model and simulations, Data analysis

Publication F:

Manuscript preparation, Analytical derivation, Monte-Carlo-Analysis, Specimen manufacturing, FEA-model and simulations, Data analysis, Fractography

An quantitative overview of the author's contributions to each publication is given in Table 6.1

Table 6.1: Contributions of the author to the appended publications in percent

Publication	Conception	Experiments	Interpretation	Manuscript preparation
A	80	100	80	95
B	80	100	70	75
C	80	100	80	85
D	90	80	85	85
E	80	80	90	90
F	70	70	90	95

7. Funding acknowledgements

The funding for this research, provided by the Austrian BMVIT and BMWWF in the project "CharAM" (FFG 877684) of the COIN/IraSME program, is gratefully acknowledged. The author is also grateful to the JECS Trust for funding his visit to INSA Lyon (Contract No. 2022305).

8. References

- [1] R. Nathan Katz, "Overview of ceramic materials, design, and application", in *Mechanical Engineers' Handbook*. John Wiley Sons, Ltd, 2015, ch. 12, pp. 1–21, ISBN: 9781118985960. DOI: <https://doi.org/10.1002/9781118985960.meh112>.
- [2] W. Ching, "Theoretical studies of the electronic properties of ceramic materials", *Journal of the American Ceramic Society*, vol. 73, no. 11, pp. 3135–3160, 1990.
- [3] D. Munz and T. Fett, *Ceramics: Mechanical Properties, Failure Behaviour, Materials Selection* (Springer Series in Materials Science). Berlin and Heidelberg: Springer, 1999, vol. 36, ISBN: 9783642635809. DOI: [10.1007/978-3-642-58407-7](https://doi.org/10.1007/978-3-642-58407-7).
- [4] J. B. Wachtman, M. J. Matthewson, and W. R. Cannon, *Mechanical properties of ceramics*, Second edition. Hoboken, New Jersey: Wiley, 2009, ISBN: 9780471735816. DOI: [10.1002/9780470451519](https://doi.org/10.1002/9780470451519).
- [5] R. Danzer, T. Lube, P. Supancic, and R. Damani, "Fracture of ceramics", *Advanced Engineering Materials*, vol. 10, no. 4, pp. 275–298, 2008, ISSN: 14381656. DOI: [10.1002/adem.200700347](https://doi.org/10.1002/adem.200700347).
- [6] A. M. Freudenthal, "Statistical approach to brittle fracture", *Fracture*, vol. 2, pp. 591–619, 1968.
- [7] C. R. Brinkman and S. F. Duffy, *Life Prediction Methodologies and Data for Ceramic Materials*. 100 Barr Harbor Drive, PO Box C700, West Conshohocken, PA 19428-2959: ASTM International, 1994, ISBN: 978-0-8031-1864-5. DOI: [10.1520/STP1201-EB](https://doi.org/10.1520/STP1201-EB).
- [8] D. C. Cranmer and D. W. Richerson, Eds., *Mechanical testing methodology for ceramic design and reliability*. Boca Raton, London, and New York: CRC Press, Taylor & Francis Group, 2018, ISBN: 0824795679.
- [9] P. Stanley, H. Fessler, and A. D. Sivill, "An engineer's approach to the prediction of failure probability of brittle components", *Proc. Brit. Ceram. Soc.*, vol. 22, pp. 453–487, 1973.
- [10] R. Morrell, *Biaxial flexural strength testing of ceramic materials: A National Measurement Good Practice Guide No. 12*. National Physical Laboratory, 2007.
- [11] *Astm c 1499-05: Test method for monotonic equibiaxial flexural strength of advanced ceramics at ambient temperature*, West Conshohocken, PA, 2005. DOI: [10.1520/C1499-05](https://doi.org/10.1520/C1499-05).
- [12] G. With and H. H. M. Wagemans, "Ball-on-ring test revisited", *Journal of the American Ceramic Society*, vol. 72, no. 8, pp. 1538–1541, 1989, ISSN: 0002-7820. DOI: [10.1111/j.1151-2916.1989.tb07702.x](https://doi.org/10.1111/j.1151-2916.1989.tb07702.x).
- [13] A. Börger, P. Supancic, and R. Danzer, "The ball on three balls test for strength testing of brittle discs: Stress distribution in the disc", *Journal of the European Ceramic Society*, vol. 22, no. 9-10, pp. 1425–1436, 2002, ISSN: 09552219. DOI: [10.1016/S0955-2219\(01\)00458-7](https://doi.org/10.1016/S0955-2219(01)00458-7).

- [14] M. Staudacher, T. Lube, J. Glettler, U. Scheithauer, and M. Schwentenwein, "A novel test specimen for strength testing of ceramics for additive manufacturing", *Open Ceramics*, vol. 15, p. 100410, 2023, ISSN: 2666-5395. DOI: <https://doi.org/10.1016/j.oceram.2023.100410>.
- [15] G. D. Quinn, "Weibull strength scaling for standardized rectangular flexure specimens", *Journal of the American Ceramic Society*, vol. 86, no. 3, pp. 508–510, 2003, ISSN: 0002-7820. DOI: [10.1111/j.1151-2916.2003.tb03329.x](https://doi.org/10.1111/j.1151-2916.2003.tb03329.x).
- [16] *Astm c 1683 - 10: Practice for size scaling of tensile strengths using weibull statistics for advanced ceramics*, West Conshohocken, PA, 2019. DOI: [10.1520/C1683-10R19](https://doi.org/10.1520/C1683-10R19).
- [17] C. A. Johnson and W. T. Tucker, "Advanced statistical concepts of fracture in brittle materials, ceramics and glasses", *Engineered Materials Handbook*, vol. 4, pp. 709–715, 1991.
- [18] C. A. Johnson and W. T. Tucker, "Weibull estimators for pooled fracture data", vol. Life Prediction Methodologies and Data for Ceramic Materials, ASTM STP 1201, 1994.
- [19] A. J. Allen, I. Levin, and S. E. Witt, "Materials research & measurement needs for ceramics additive manufacturing", *Journal of the American Ceramic Society*, vol. 103, no. 11, pp. 6055–6069, 2020. DOI: <https://doi.org/10.1111/jace.17369>.
- [20] M. W. Barsoum, *Fundamentals of ceramics* (Series in materials science and engineering), Second edition. Boca Raton, FL: CRC Press, Taylor & Francis Group, 2019, ISBN: 1498708137.
- [21] J. Rabier, "Plastic deformation and dislocations in ceramic materials", *Radiation Effects and Defects in Solids*, vol. 137, no. 1-4, pp. 205–212, 2006, ISSN: 1042-0150. DOI: [10.1080/10420159508222721](https://doi.org/10.1080/10420159508222721).
- [22] B. Lawn, *Fracture of Brittle Solids*. Cambridge University Press, 2010, ISBN: 9780521409728. DOI: [10.1017/CB09780511623127](https://doi.org/10.1017/CB09780511623127).
- [23] D. Gross and T. Seelig, *Fracture Mechanics: With an Introduction to Micromechanics* (Mechanical Engineering Series). Berlin, Heidelberg: Springer Berlin Heidelberg, 2011, ISBN: 9783642192395. DOI: [10.1007/978-3-642-19240-1](https://doi.org/10.1007/978-3-642-19240-1).
- [24] *Din en iso 23146:2016: Fine ceramics (advanced ceramics, advanced technical ceramics) - test methods for fracture toughness of monolithic ceramics - single-edge v-notch beam (sevn) method (iso 23146:2012); german version en iso 23146:2016*, Geneva, Switzerland, Nov. 2016. DOI: <https://dx.doi.org/10.31030/2482452>.
- [25] *Iso 24370:2005: Fine ceramics (advanced ceramics, advanced technical ceramics) - test method for fracture toughness of monolithic ceramics at room temperature by chevron-notched beam (cnb) method*, Geneva, Switzerland, Jun. 2005.
- [26] *Iso 18756:2005: Fine ceramics (advanced ceramics, advanced technical ceramics) — determination of fracture toughness of monolithic ceramics at room temperature by the surface crack in flexure (scf) method*, Geneva, Switzerland, Sep. 2005. DOI: <https://dx.doi.org/10.31030/9643610>.

- [27] *Din en iso 15732:2005: Fine ceramics (advanced ceramics, advanced technical ceramics) - test method for fracture toughness of monolithic ceramics at room temperature by single edge precracked beam (sepb) method*, Geneva, Switzerland, Sep. 2005. DOI: <https://dx.doi.org/10.31030/9643611>.
- [28] A. A. Griffith, "The phenomena of rupture and flow in solids", *Philosophical Transactions of the Royal Society of London. Series A, Containing Papers of a Mathematical or Physical Character*, vol. 221, pp. 163–198, 1921, ISSN: 02643952.
- [29] G. Irwin, "Analysis of stresses and strains near the end of a crack traversing a plate", *Journal of Applied Mechanics-Transactions of ASME*, vol. 24, pp. 351–369, 1957.
- [30] T. Lube, J. Schlacher, W. Harrer, R. Danzer, G. Mitteramskogler, and M. Schwentenwein, "Mechanische eigenschaften von gedruckten keramiken", Deutsch, in *Praktische Metallographie Sonderband*, 15. Int. Metallographie-Tagung ; Conference date: 19-09-2018 Through 21-09-2018, vol. 52, INVENTUM GmbH, 2018, pp. 229–234.
- [31] G. D. Quinn and R. Morrell, "Design data for engineering ceramics: A review of the flexure test", *Journal of the American Ceramic Society*, vol. 74, no. 9, pp. 2037–2066, 1991. DOI: <https://doi.org/10.1111/j.1151-2916.1991.tb08259.x>.
- [32] A. Zocca, P. Colombo, C. Wirth (Cynthia M. Gomes), and J. Günster, "Additive manufacturing of ceramics: Issues, potentialities, and opportunities", *Journal of the American Ceramic Society*, vol. 98, Jul. 2015. DOI: [10.1111/jace.13700](https://doi.org/10.1111/jace.13700).
- [33] N. Travitzky, A. Bonet, B. Dermeik, *et al.*, "Additive manufacturing of ceramic-based materials", *Science of Advanced Materials*, vol. 16, pp. 729–754, Apr. 2014.
- [34] Z. Chen, Z. Li, J. Li, *et al.*, "3d printing of ceramics: A review", *Journal of the European Ceramic Society*, vol. 39, no. 4, pp. 661–687, 2019, ISSN: 0955-2219. DOI: <https://doi.org/10.1016/j.jeurceramsoc.2018.11.013>.
- [35] J.-C. Wang, H. Dommati, and S.-J. Hsieh, "Review of additive manufacturing methods for high-performance ceramic materials", *The International Journal of Advanced Manufacturing Technology*, vol. 103, Aug. 2019. DOI: [10.1007/s00170-019-03669-3](https://doi.org/10.1007/s00170-019-03669-3).
- [36] J. Homa and M. Schwentenwein, "A novel additive manufacturing technology for high-performance ceramics", *Ceramic Engineering and Science Proceedings*, vol. 35, pp. 33–40, Jan. 2014. DOI: [10.1002/9781119040354.ch4](https://doi.org/10.1002/9781119040354.ch4).
- [37] M. Schwentenwein, P. Schneider, and J. Homa, "Lithography-based ceramic manufacturing: A novel technique for additive manufacturing of high-performance ceramics", *Advances in Science and Technology*, vol. 88, pp. 60–64, Oct. 2014. DOI: [10.4028/www.scientific.net/AST.88.60](https://doi.org/10.4028/www.scientific.net/AST.88.60).
- [38] G. Mitteramskogler, R. Gmeiner, R. Felzmann, *et al.*, "Light curing strategies for lithography-based additive manufacturing of customized ceramics", *Additive Manufacturing*, vol. 1-4, pp. 110–118, 2014, Inaugural Issue, ISSN: 2214-8604. DOI: <https://doi.org/10.1016/j.addma.2014.08.003>.

- [39] A. Diaz Lantada, A. De Blas Romero, M. Schwentenwein, C. Jellinek, and J. Homa, "Lithography-based ceramic manufacture (lcm) of auxetic structures: Present capabilities and challenges", *Smart Materials and Structures*, vol. 25, Apr. 2016.
- [40] J. Halloran, "Ceramic stereolithography: Additive manufacturing for ceramics by photopolymerization", *Annual Review of Materials Research*, vol. 46, Aug. 2016. DOI: [10.1146/annurev-matsci-070115-031841](https://doi.org/10.1146/annurev-matsci-070115-031841).
- [41] R. Phillips, "Photopolymerization", *Journal of Photochemistry*, vol. 25, no. 1, pp. 79–82, 1984, ISSN: 0047-2670. DOI: [https://doi.org/10.1016/0047-2670\(84\)85016-9](https://doi.org/10.1016/0047-2670(84)85016-9).
- [42] 2023. [Online]. Available: <https://lithoz.com/de/technologie/lcm-technologie/>.
- [43] J. Schlacher, T. Lube, W. Harrer, *et al.*, "Strength of additive manufactured alumina", *Journal of the European Ceramic Society*, vol. 40, no. 14, pp. 4737–4745, 2020, ISSN: 09552219. DOI: [10.1016/j.jeurceramsoc.2020.03.073](https://doi.org/10.1016/j.jeurceramsoc.2020.03.073).
- [44] A. de Blas Romero, M. Pfaffinger, G. Mitteramskogler, *et al.*, "Lithography-based additive manufacture of ceramic biodevices with design-controlled surface topographies", *The International Journal of Advanced Manufacturing Technology*, vol. 88, no. 5, pp. 1547–1555, 2017. DOI: [10.1007/s00170-016-8856-1](https://doi.org/10.1007/s00170-016-8856-1).
- [45] T. Lube, M. Staudacher, A.-K. Hofer, J. Schlacher, and R. Bermejo, "Stereolithographic 3d printing of ceramics: Challenges and opportunities for structural integrity", *Advanced Engineering Materials*, vol. 25, p. 2200 520, 2023. DOI: <https://doi.org/10.1002/adem.202200520>.
- [46] 2009 4. [Online]. Available: https://de.wikipedia.org/wiki/Djoser-Pyramide#/media/Datei:Sakkara_01.jpg.
- [47] W. Weibull, *A Statistical Theory of the Strength of Materials*. Stockholm: Generalstabens Litografiska Anstalts Förlag, 1939.
- [48] W. Weibull, "A statistical distribution function of wide applicability", *Journal of Applied Mechanics*, vol. 18, pp. 293–297, 1951.
- [49] R. Danzer, "A general strength distribution function for brittle materials", *Journal of the European Ceramic Society*, vol. 10, no. 6, pp. 461–472, 1992, ISSN: 09552219. DOI: [10.1016/0955-2219\(92\)90021-5](https://doi.org/10.1016/0955-2219(92)90021-5).
- [50] A. D. S. Jayatilaka and K. Trustrum, "Statistical approach to brittle fracture", *Journal of Materials Science*, vol. 12, no. 7, pp. 1426–1430, 1977. DOI: [10.1007/BF00540858](https://doi.org/10.1007/BF00540858).
- [51] M. Staudacher, A. Eggel, P. Supancic, and T. Lube, "The ball-on-three-balls strength test: Effective volumes and surfaces for weibull strength scaling", *Journal of the European Ceramic Society*, vol. 44, no. 1, pp. 173–183, 2024, ISSN: 0955-2219. DOI: <https://doi.org/10.1016/j.jeurceramsoc.2023.09.018>.
- [52] *Din en 843-5: 2007: Advanced technical ceramics - mechanical properties of monolithic ceramics at room temperature - part 5: Statistical analysis*, 2007.

- [53] R. Danzer, T. Lube, and P. Supancic, "Monte carlo simulations of strength distributions of brittle materials – type of distribution, specimen and sample size", *International Journal of Materials Research*, vol. 92, no. 7, pp. 773–783, 2001, issn: 1862-5282. doi: [10.1515/ijmr-2001-0143](https://doi.org/10.1515/ijmr-2001-0143).
- [54] A. Heger, A. Brueckner-Foit, and D. Munz, "Stau - a computer code to calculate the failure probability of multiaxially loaded ceramic components", in *In: Euro-Ceramics II. Ed.: G. Ziegler. Vol. 2. Koeln: Dt. Keram. Ges. 1993. S. 1143-1147.* 1993.
- [55] D. Gross and T. Seelig, *Bruchmechanik: Mit einer Einführung in die Mikro-mechanik (Lehrbuch)*, 6., erweiterte Auflage. Berlin: Heidelberg : Springer Vieweg, 2016, ISBN: 9783662467374.
- [56] R. L. Barnett, P. C. Hermann, J. R. Wingfield, and C. L. Connors, *Fracture of brittle materials under transient mechanical and thermal loading*, 1967.
- [57] R. Danzer, P. Supancic, W. Harrer, T. Lube, and A. Börger, "Biaxial strength testing on mini specimens", in *Gdoutos E.E. (eds) Fracture of Nano and Engineering Materials and Structures. Springer, Dordrecht*, pp. 589–590.
- [58] G. D. Quinn, "Weibull effective volumes and surfaces for cylindrical rods loaded in flexure", *Journal of the American Ceramic Society*, vol. 86, no. 3, pp. 475–479, 2003, issn: 0002-7820. doi: [10.1111/j.1151-2916.2003.tb03324.x](https://doi.org/10.1111/j.1151-2916.2003.tb03324.x).
- [59] R. Jain, J. Lock, and S. F. Duffy, "Effective area and effective volume calculations for ceramic test specimens", in *ASME Turbo Expo Orlando (Ed.) – ASME Turbo Expo 2009*, pp. 231–239. doi: [10.1115/GT2009-59028](https://doi.org/10.1115/GT2009-59028).
- [60] Göller Verlag, 2008, ISBN: 3-87426-022-4.
- [61] *Astm c1161 - 18: Test method for flexural strength of advanced ceramics at ambient temperature*, West Conshohocken, PA, 2018. doi: [10.1520/C1161-18](https://doi.org/10.1520/C1161-18).
- [62] G. Quinn, "Advanced structural ceramics: A round robin", *Journal of the American Ceramic Society*, vol. 73, no. 8, pp. 2374–2384, 1990. doi: <https://doi.org/10.1111/j.1151-2916.1990.tb07601.x>.
- [63] J. A. Salem and L. Powers, "Guidelines for the testing of plates", in *27th International Cocoa Beach Conference on Advanced Ceramics and Composites*, ser. Ceramic engineering & science proceedings, H.-T. Lin and W. M. Kriven, Eds., vol. 24, Westerville, Ohio: American Ceramic Society, 2003, pp. 357–364, ISBN: 9780470294826. doi: [10.1002/9780470294826.ch52](https://doi.org/10.1002/9780470294826.ch52).
- [64] R. J. Roark, W. C. Young, and H. Saunders, *Formulas for Stress and Strain – 5th Edition*. 1975. doi: [10.1115/1.3454034](https://doi.org/10.1115/1.3454034).
- [65] R. Budynas and A. Sadegh, *Roark's Formulas for Stress and Strain - 9th Edition*, 9th edition. New York: McGraw-Hill, 2020, ISBN: 9781260453768.
- [66] M. Staudacher, T. Lube, and P. Supancic, "The ball-on-three-balls strength test for discs and plates: Extending and simplifying stress evaluation", *Journal of the European Ceramic Society*, vol. 43, no. 2, pp. 648–660, 2023, issn: 09552219. doi: [10.1016/j.jeurceramsoc.2022.09.047](https://doi.org/10.1016/j.jeurceramsoc.2022.09.047).
- [67] F. F. Vitman, G. M. Bartenev, V. P. Pukh, and L. P. Tsepkov, "A method for measuring the strength of sheet glass", *Glass and Ceramics*, vol. 19, no. 8, pp. 412–414, 1962, issn: 0361-7610. doi: [10.1007/BF00681213](https://doi.org/10.1007/BF00681213).

- [68] H. L. Frandsen, "The small displacement elastic solution to the ball-on-ring testing method", *Mechanics of Materials*, vol. 55, pp. 33–40, 2012, ISSN: 01676636. DOI: [10.1016/j.mechmat.2012.07.007](https://doi.org/10.1016/j.mechmat.2012.07.007).
- [69] A. F. Kirstein and R. M. Woolley, "Symmetrical bending of thin circular elastic plates on equally spaced point supports", *Journal of Research of the National Bureau of Standards, Section C: Engineering and Instrumentation*, vol. 71C, no. 1, p. 1, 1967. DOI: [10.6028/jres.071C.002](https://doi.org/10.6028/jres.071C.002).
- [70] W. A. Bassali and H. G. Eggleston, "The transverse flexure of thin elastic plates supported at several points", *Mathematical Proceedings of the Cambridge Philosophical Society*, vol. 53, pp. 728–743, 1957.
- [71] K. R. McKinney and C. Herbert, "Effect of surface finish on structural ceramic failure", *Journal of the American Ceramic Society*, vol. 53, no. 9, pp. 513–516, 1970. DOI: <https://doi.org/10.1111/j.1151-2916.1970.tb16003.x>.
- [72] D. Shetty, A. R. Rosenfield, P. McGuire, G. K. Bansal, and W. H. and Duckworth, "Biaxial flexure tests for ceramics", *American Ceramic Society Bulletin*, vol. 1180, no. Vol 59, No.12, 1980.
- [73] H. M. Westergaard, "Stresses in concrete pavements computed by theoretical analysis", in *Public Roads*, 1926.
- [74] H. Hertz, "Ueber die berührung fester elastischer körper", *Journal für die reine und angewandte Mathematik*, no. 92, pp. 156–171, 1881. DOI: [10.1515/crll.1882.92.156](https://doi.org/10.1515/crll.1882.92.156).
- [75] A. Nádai, "Die biegungsbeanspruchung von platten durch einzelkräfte", *Schweizerische Bauzeitung*, vol. 23, no. 75/76, pp. 257–260, 1920. DOI: [10.5169/seals-36559](https://doi.org/10.5169/seals-36559).
- [76] S. M. Hu, "Critical stress in silicon brittle fracture, and effect of ion implantation and other surface treatments", *Journal of Applied Physics*, vol. 53, no. 5, pp. 3576–3580, 1982, ISSN: 0021-8979. DOI: [10.1063/1.331137](https://doi.org/10.1063/1.331137).
- [77] S.-H. Chae, J.-H. Zhao, D. R. Edwards, and P. S. Ho, "Verification of ball-on-ring test using finite element analysis", in *2010 12th IEEE intersociety conference on thermal and thermomechanical phenomena in electronic systems*, Piscataway, N.J.: IEEE, 2010, pp. 1–6, ISBN: 978-1-4244-5342-9. DOI: [10.1109/ITHERM.2010.5501307](https://doi.org/10.1109/ITHERM.2010.5501307).
- [78] H. L. Frandsen, "Weibull statistics effective area and volume in the ball-on-ring testing method", *Mechanics of Materials*, vol. 73, pp. 28–37, 2014, ISSN: 01676636. DOI: [10.1016/j.mechmat.2013.10.010](https://doi.org/10.1016/j.mechmat.2013.10.010).
- [79] D. J. Godfrey and S. John, "Disc flexure tests for the evaluation of ceramic strength", *Proceedings 2nd International Conference of Ceramic materials and Components for Engines*, pp. 657–665, 1986.
- [80] A. Börger, P. Supancic, and R. Danzer, "The ball on three balls test for strength testing of brittle discs: Part ii: Analysis of possible errors in the strength determination", *Journal of the European Ceramic Society*, vol. 24, pp. 2917–2928, 2004, ISSN: 09552219. DOI: [10.1016/j.jeurceramsoc.2003.10.035](https://doi.org/10.1016/j.jeurceramsoc.2003.10.035).

- [81] R. Danzer, A. Börger, P. Supancic, and M. A. Ruiz Villanueva, "Ein einfacher festigkeitsversuch für scheiben aus spröden werkstoffen", *Materialwissenschaft und Werkstofftechnik*, vol. 34, no. 5, pp. 490–498, 2003, issn: 09335137. doi: [10.1002/mawe.200390098](https://doi.org/10.1002/mawe.200390098).
- [82] A. Börger, R. Danzer, and P. Supancic, "Biaxial strength test of discs of different size using the ball on three balls test", *Ceramic Engineering and Science Proceedings*, vol. 25, no. 4, pp. 283–289, 2004, issn: 0196-6219. doi: [10.1002/9780470291191.ch43](https://doi.org/10.1002/9780470291191.ch43).
- [83] W. Harrer, R. Danzer, and P. Supancic, "Influence of surface quality on the biaxial strength of silicon nitride", *Praktische Metallographie Sonderband*, vol. 42, pp. 141–146, 2010.
- [84] M. A. Lodes, F. S. Kachold, and S. M. Rosiwal, "Mechanical properties of micro- and nanocrystalline diamond foils", *Philosophical transactions. Series A, Mathematical, physical, and engineering sciences*, vol. 373, no. 2038, 2015. doi: [10.1098/rsta.2014.0136](https://doi.org/10.1098/rsta.2014.0136).
- [85] F. Fleischhauer, R. Bermejo, R. Danzer, A. Mai, T. Graule, and J. Kuebler, "Strength of an electrolyte supported solid oxide fuel cell", *Journal of Power Sources*, vol. 297, pp. 158–167, 2015. doi: [10.1016/j.jpowsour.2015.07.075](https://doi.org/10.1016/j.jpowsour.2015.07.075).
- [86] M. Gruber, A. Leitner, I. Kraveva, D. Kiener, P. Supancic, and R. Bermejo, "Understanding the effect of surface flaws on the strength distribution of brittle single crystals", *Journal of the American Ceramic Society*, no. 101, pp. 5705–5716, 2018. doi: [10.1111/jace.15800](https://doi.org/10.1111/jace.15800).
- [87] E. Chicardi, R. Bermejo, F. J. Gotor, L. Llanes, and Y. Torres, "Influence of temperature on the biaxial strength of cemented carbides with different microstructures", *International Journal of Refractory Metals & Hard Materials*, vol. 71, pp. 82–91, 2018. doi: [10.1016/j.ijrmhm.2017.11.003](https://doi.org/10.1016/j.ijrmhm.2017.11.003).
- [88] S. Lowum, R. Floyd, R. Bermejo, and J.-P. Maria, "Mechanical strength of cold-sintered zinc oxide under biaxial bending", *Journal of Materials Science*, vol. 54, no. 6, pp. 4518–4522, 2019. doi: [10.1007/s10853-018-3173-8](https://doi.org/10.1007/s10853-018-3173-8).
- [89] E. Dashjav, M. Gellert, G. Yan, *et al.*, "Microstructure, ionic conductivity and mechanical properties of tape-cast $\text{Li}_1.5\text{Al}_0.5\text{Ti}_1.5\text{P}_3\text{O}_{12}$ electrolyte sheets", *Journal of the European Ceramic Society*, vol. 40, pp. 1975–1982, 2020, issn: 09552219. doi: [10.1016/j.jeurceramsoc.2020.01.017](https://doi.org/10.1016/j.jeurceramsoc.2020.01.017).
- [90] L. M. González, E. Chicardi, F. J. Gotor, R. Bermejo, L. Llanes, and Y. Torres, "Influence of the test configuration and temperature on the mechanical behaviour of wc-co", *Metals*, vol. 10, no. 3, p. 322, 2020. doi: [10.3390/met10030322](https://doi.org/10.3390/met10030322).
- [91] N. Sheth, C. Greenly, R. Bermejo, J. C. Mauro, C. G. Pantano, and S. H. Kim, "Effects of acid leaching treatment of soda lime silicate glass on crack initiation and fracture", *Journal of the American Ceramic Society*, vol. 104, pp. 4550–4558, 2021. doi: [10.1111/jace.17840](https://doi.org/10.1111/jace.17840).
- [92] J. P. Gross, J. Malzbender, and R. Schwaiger, "Strength assessment of Al_2O_3 and MgAl_2O_4 using micro- and macro-scale biaxial tests", *Journal of Materials Science*, vol. 57, no. 15, pp. 7481–7490, 2022, issn: 1573-4803. doi: [10.1007/s10853-022-07143-6](https://doi.org/10.1007/s10853-022-07143-6).

- [93] H. P. R. Corado, P. H. P. M. Da Silveira, V. L. Ortega, G. G. Ramos, and C. N. Elias, "Flexural strength of vitreous ceramics based on lithium disilicate and lithium silicate reinforced with zirconia for cad/cam", *International Journal of Biomaterials*, vol. 2022, p. 5896511, 2022, ISSN: 1687-8787. DOI: [10.1155/2022/5896511](https://doi.org/10.1155/2022/5896511).
- [94] J. Essmeister, A. A. Altun, M. Staudacher, T. Lube, M. Schwentenwein, and T. Konegger, "Stereolithography-based additive manufacturing of polymer-derived sioc/sic ceramic composites", *Journal of the European Ceramic Society*, vol. 42, no. 13, pp. 5343–5354, 2022, ISSN: 0955-2219. DOI: <https://doi.org/10.1016/j.jeurceramsoc.2022.06.021>.
- [95] R. Danzer, P. Supancic, and W. Harrer, "Der 4-kugelversuch zur ermittlung der biaxialen biegefestigkeit spröder werkstoffe", *Kriegsmann, J. (Hrsg): Technische keramische Werkstoffe*, no. 113, pp. 1–48, 2009.
- [96] T. Lube, S. Rasche, and T. G. T. Nindhia, "A fracture toughness test using the ball-on-three-balls test", *Journal of the American Ceramic Society*, vol. 99, no. 1, pp. 249–256, 2016. DOI: <https://doi.org/10.1111/jace.13842>.
- [97] S. Nohut, "A general formulation for strength prediction of advanced ceramics by ball-on-three-balls (b3b)-test with different multiaxial failure criteria", *Ceramics International*, vol. 38, no. 3, pp. 2411–2420, 2012, ISSN: 02728842. DOI: [10.1016/j.ceramint.2011.11.007](https://doi.org/10.1016/j.ceramint.2011.11.007).
- [98] E. Padovano, M. Galfione, P. Concialdi, G. Lucco, and C. Badini, "Mechanical and thermal behavior of ultem® 9085 fabricated by fused-deposition modeling", *Applied Sciences*, vol. 10, p. 3170, May 2020. DOI: [10.3390/app10093170](https://doi.org/10.3390/app10093170).
- [99] S. M. Olhero, P. Torres, J. Mesquita-Guimarães, J. Baltazar, J. Pinho-da-Cruz, and S. Gouveia, "Conventional versus additive manufacturing in the structural performance of dense alumina-zirconia ceramics: 20 years of research, challenges and future perspectives", *Journal of Manufacturing Processes*, vol. 77, pp. 838–879, 2022, ISSN: 1526-6125. DOI: [10.1016/j.jmapro.2022.02.041](https://doi.org/10.1016/j.jmapro.2022.02.041).
- [100] M. Dehurtevent, L. Robberecht, A. Thuault, *et al.*, "Effect of build orientation on the manufacturing process and the properties of stereolithographic dental ceramics for crown frameworks", *The Journal of prosthetic dentistry*, vol. 125, no. 3, pp. 453–461, 2021, ISSN: 0022-3913. DOI: [10.1016/j.prosdent.2020.01.024](https://doi.org/10.1016/j.prosdent.2020.01.024).
- [101] S. Miura, A. Shinya, Y. Ishida, and M. Fujisawa, "Mechanical and surface properties of additive manufactured zirconia under the different building directions", *Journal of prosthodontic research*, vol. 67, no. 3, pp. 410–417, 2023, ISSN: 2212-4632. DOI: [10.2186/jpr.JPR_D_22_00166](https://doi.org/10.2186/jpr.JPR_D_22_00166).
- [102] M. Schwentenwein and J. Homa, "Additive manufacturing of dense alumina ceramics", *International Journal of Applied Ceramic Technology*, vol. 12, no. 1, pp. 1–7, 2015, ISSN: 1546-542X. DOI: [10.1111/ijac.12319](https://doi.org/10.1111/ijac.12319).
- [103] E. Schwarzer, S. Holtzhausen, U. Scheithauer, *et al.*, "Process development for additive manufacturing of functionally graded alumina toughened zirconia components intended for medical implant application", *Journal of the European Ceramic Society*, vol. 39, no. 2-3, pp. 522–530, 2019, ISSN: 09552219. DOI: [10.1016/j.jeurceramsoc.2018.09.003](https://doi.org/10.1016/j.jeurceramsoc.2018.09.003).

- [104] M. Borlaf, A. Serra-Capdevila, C. Colominas, and T. Graule, "Development of uv-curable zro2 slurries for additive manufacturing (lcm-dlp) technology", *Journal of the European Ceramic Society*, vol. 39, no. 13, pp. 3797–3803, 2019, ISSN: 09552219. DOI: [10.1016/j.jeurceramsoc.2019.05.023](https://doi.org/10.1016/j.jeurceramsoc.2019.05.023).
- [105] W. Harrer, M. Schwentenwein, T. Lube, and R. Danzer, "Fractography of zirconia-specimens made using additive manufacturing (lcm) technology", *Journal of the European Ceramic Society*, vol. 37, no. 14, pp. 4331–4338, 2017, ISSN: 09552219. DOI: [10.1016/j.jeurceramsoc.2017.03.018](https://doi.org/10.1016/j.jeurceramsoc.2017.03.018).
- [106] W. Harrer, M. Schwentenwein, and R. Danzer, "Strength optimisation of a zirconia-ceramic made using additive manufacturing (lcm)-technology", *Ceramic forum international (CFI)*, vol. 94, no. 10, E49–E54, 2017, ISSN: 0173-9913.
- [107] R. B. Osman, A. J. van der Veen, D. Huiberts, D. Wismeijer, and N. Alharbi, "3d-printing zirconia implants; a dream or a reality? an in-vitro study evaluating the dimensional accuracy, surface topography and mechanical properties of printed zirconia implant and discs", *Journal of the mechanical behavior of biomedical materials*, vol. 75, pp. 521–528, 2017, ISSN: 1878-0180. DOI: [10.1016/j.jmbbm.2017.08.018](https://doi.org/10.1016/j.jmbbm.2017.08.018). [Online]. Available: <https://pubmed.ncbi.nlm.nih.gov/28846981/>.
- [108] M. Saâdaoui, F. Khaldoun, J. Adrien, H. Reveron, and J. Chevalier, "X-ray tomography of additive-manufactured zirconia: Processing defects – strength relations", *Journal of the European Ceramic Society*, vol. 40, no. 8, pp. 3200–3207, 2020, ISSN: 09552219. DOI: [10.1016/j.jeurceramsoc.2019.04.010](https://doi.org/10.1016/j.jeurceramsoc.2019.04.010).
- [109] D. R. Kammler, D. E. Cillessen, K. R. Ford, *et al.*, "Flexural strength of a conventionally processed and additively manufactured debased 94% alumina", *International Journal of Applied Ceramic Technology*, vol. 19, no. 3, pp. 1640–1649, 2022, ISSN: 1546-542X. DOI: [10.1111/ijac.13968](https://doi.org/10.1111/ijac.13968).
- [110] Y. Lu, Z. Mei, J. Zhang, *et al.*, "Flexural strength and weibull analysis of yt-zp fabricated by stereolithographic additive manufacturing and subtractive manufacturing", *Journal of the European Ceramic Society*, vol. 40, no. 3, pp. 826–834, 2020, ISSN: 09552219. DOI: [10.1016/j.jeurceramsoc.2019.10.058](https://doi.org/10.1016/j.jeurceramsoc.2019.10.058).
- [111] C. Marsico, M. Øilo, J. Kutsch, M. Kauf, and D. Arola, "Vat polymerization-printed partially stabilized zirconia: Mechanical properties, reliability and structural defects", *Additive Manufacturing*, vol. 36, p. 101450, 2020, ISSN: 2214-8604. DOI: [10.1016/j.addma.2020.101450](https://doi.org/10.1016/j.addma.2020.101450).
- [112] M. Shen, W. Zhao, B. Xing, *et al.*, "Effects of exposure time and printing angle on the curing characteristics and flexural strength of ceramic samples fabricated via digital light processing", *Ceramics International*, vol. 46, no. 15, pp. 24379–24384, 2020, ISSN: 02728842. DOI: [10.1016/j.ceramint.2020.06.220](https://doi.org/10.1016/j.ceramint.2020.06.220).
- [113] Y. Zhao, P. Li, P. Dong, Y. Zeng, and J. Chen, "Investigation on 3d printing zro2 implant abutment and its fatigue performance simulation", *Ceramics International*, vol. 47, no. 1, pp. 1053–1062, 2021, ISSN: 02728842. DOI: [10.1016/j.ceramint.2020.08.221](https://doi.org/10.1016/j.ceramint.2020.08.221).

- [114] R. Bermejo, P. Supancic, and R. Danzer, "Influence of measurement uncertainties on the determination of the weibull distribution", *Journal of the European Ceramic Society*, vol. 32, no. 2, pp. 251–255, 2012, ISSN: 0955-2219. DOI: <https://doi.org/10.1016/j.jeurceramsoc.2011.09.008>.
- [115] F. Baratta, G. Quinn, and W. Matthews, "Errors associated with flexure testing of brittle materials", p. 58, Jul. 1987.
- [116] R. G. Hoagland, C. W. Marschall, and W. H. Duckworth, "Reduction of errors in ceramic bend tests", *Journal of the American Ceramic Society*, vol. 59, no. 5-6, pp. 189–192, 1976. DOI: <https://doi.org/10.1111/j.1151-2916.1976.tb10929.x>.
- [117] G. Quinn, "Twisting and friction errors in flexure testing", *Ceram. Eng. Sci. Proc.*, vol. 13, pp. 319–330, Jul. 1992. DOI: [10.1002/9780470313954.ch32](https://doi.org/10.1002/9780470313954.ch32).
- [118] T. Lube and M. Manner, "Development of a bending-test device for small samples", English, in *Key engineering materials* (Key engineering materials), Key engineering materials. Trans Tech Publications, Dec. 1997, vol. 132-136, pp. 488–491.
- [119] H. Fessler and D. C. Fricker, "A theoretical analysis of the ring-on-ring loading disk test", *Journal of the American Ceramic Society*, vol. 67, no. 9, pp. 582–588, 1984, ISSN: 0002-7820. DOI: [10.1111/j.1151-2916.1984.tb19598.x](https://doi.org/10.1111/j.1151-2916.1984.tb19598.x).
- [120] M. Staudacher, T. Lube, J. Schlacher, and P. Supancic, "Comparison of biaxial strength measured with the ball-on-three-balls- and the ring-on-ring-test", *Open Ceramics*, vol. 6, p. 100 101, 2021, ISSN: 2666-5395. DOI: [10.1016/j.oceram.2021.100101](https://doi.org/10.1016/j.oceram.2021.100101).
- [121] L. M. Powers, J. A. Salem, and A. S. Weaver, "Stresses in ceramic plates subjected to loading between concentric rings", in *Fracture resistance testing of monolithic and composite brittle materials*, ser. ASTM STP, J. A. Salem, Ed., West Conshohocken, Pa.: ASTM International, 2002, pp. 30–45, ISBN: 978-0-8031-2880-4. DOI: [10.1520/STP104708](https://doi.org/10.1520/STP104708).
- [122] M. Gruber, I. Kraveva, P. Supancic, J. Bielen, D. Kiener, and R. Bermejo, "Strength distribution and fracture analyses of linbo 3 and litao 3 single crystals under biaxial loading", *Journal of the European Ceramic Society*, vol. 37, no. 14, pp. 4397–4406, 2017, ISSN: 09552219. DOI: [10.1016/j.jeurceramsoc.2017.02.002](https://doi.org/10.1016/j.jeurceramsoc.2017.02.002).
- [123] M. Gruber, A. Leitner, D. Kiener, P. Supancic, and R. Bermejo, "Effect of crystal orientation on the hardness and strength of piezoelectric linbo3 substrates for microelectronic applications", *Materials Design*, vol. 213, p. 110 306, 2022, ISSN: 0264-1275. DOI: <https://doi.org/10.1016/j.matdes.2021.110306>.
- [124] R. Bermejo, I. Kraveva, F. Aldrian, P. Supancic, and R. Morrell, "Mechanical behaviour of low temperature co-fired ceramics under biaxial loading: Influence of internal architecture on the fracture response", M. M. Bućko, K. Haberko, Z. Pędzich, and Ł. Zych, Eds., Polish Ceramic Society, 2010, pp. 277–280, ISBN: 978-83-60958-54-4.

- [125] R. Bermejo, P. Supancic, I. Kraveva, F. Aldrian, and R. Morrell, "Influence of multilayer architecture on the fracture response of low temperature co-fired ceramics under biaxial loading", G. Ravichandran, Ed., 2010, Paper WB1-2.
- [126] S. Boardman and C. E. Packard, "Strength of additively manufactured alumina with different debinding and sintering heat treatments", *Journal of the American Ceramic Society*, vol. 106, no. 7, pp. 4076-4088, 2023. DOI: <https://doi.org/10.1111/jace.19094>.
- [127] B. Szabó and I. Babuška, *Introduction to finite element analysis: formulation, verification and validation*. John Wiley & Sons, 2011, vol. 35.
- [128] B. Szabó and I. Babuška, "Finite element analysis: Method, verification and validation", 2021.
- [129] R. De Borst, M. A. Crisfield, J. J. Remmers, and C. V. Verhoosel, *Nonlinear finite element analysis of solids and structures*. John Wiley & Sons, 2012.
- [130] E. Madenci and I. Guven, *The Finite Element Method and Applications in Engineering Using ANSYS®*, 2nd ed. 2015. Boston, MA and s.l.: Springer US, 2015, ISBN: 9781489975492. DOI: [10.1007/978-1-4899-7550-8](https://doi.org/10.1007/978-1-4899-7550-8).
- [131] N. S. Gokhale, *Practical finite element analysis*. Finite to infinite, 2008.
- [132] D. Mevec, *Auslegung einer festigkeitsprüfung von dentalkeramik mittels des b3b-tests*, Chair of Structural and Functional Ceramics, Montanuniversität Leoben, 2016.
- [133] M. Staudacher, P. Supancic, and T. Lube, "The ball-on-ring-test: Enhancing an analytical solution by numerical analysis for elastic deformation and small displacements", *Journal of the European Ceramic Society*, vol. 43, no. 15, pp. 7167-7177, 2023, ISSN: 0955-2219. DOI: <https://doi.org/10.1016/j.jeurceramsoc.2023.06.016>.
- [134] G. Quinn, *Nist recommended practice guide: Fractography of ceramics and glasses, 3rd edition*, en, 2020-09-14 04:09:00 2020. DOI: <https://doi.org/10.6028/NIST.SP.960-16e3>.
- [135] E. Maire and P. J. Withers, "Quantitative x-ray tomography", *International Materials Reviews*, vol. 59, no. 1, pp. 1-43, 2014. DOI: [10.1179/1743280413Y.0000000023](https://doi.org/10.1179/1743280413Y.0000000023).
- [136] J. Y. Buffiere, E. Maire, J. Adrien, J. P. Masse, and E. Boller, "In situ experiments with x ray tomography: An attractive tool for experimental mechanics", *Experimental Mechanics*, vol. 50, no. 3, pp. 289-305, 2010. DOI: [10.1007/s11340-010-9333-7](https://doi.org/10.1007/s11340-010-9333-7).
- [137] B. Tata and B. Raj, "Confocal laser scanning microscopy: Applications in material science and technology", *Bulletin of Materials Science*, vol. 21, pp. 263-278, 1998.
- [138] S. W. Paddock, "Confocal laser scanning microscopy", *Biotechniques*, vol. 27, no. 5, pp. 992-1004, 1999.
- [139] X. Teng, F. Li, and C. Lu, "Visualization of materials using the confocal laser scanning microscopy technique", *Chemical Society Reviews*, vol. 49, no. 8, pp. 2408-2425, 2020.

- [140] M. Staudacher, T. Lube, and P. Supancic, "The ball-on-three-balls strength test for discs and plates: Extending and simplifying stress evaluation", *Journal of the European Ceramic Society*, vol. 43, no. 2, pp. 648–660, 2023, ISSN: 0955-2219. DOI: <https://doi.org/10.1016/j.jeurceramsoc.2022.09.047>.
- [141] A. L. Gebhardt, "Prüfkörperauslegung und ergebnisinterpretation für die festigkeitsbewertung gedruckter filigraner keramikstrukturen", Master's Thesis, TU Dresden & Fraunhofer-Institut für Keramische Technologien und Systeme IKTS, Dresden, 16.07.2020.
- [142] S. Timoshenko, *History of strength of materials: With a brief account of the history of theory of elasticity and theory of structures*. New York: Dover Publications, 1983, ISBN: 0486611876.

Publication A

The Ball-on-Ring-test: Enhancing an analytical solution by numerical analysis for elastic deformation and small displacements

Maximilian Staudacher, Peter Supancic, Tanja Lube

Department of Materials Science, Montanuniversität Leoben, Franz Josef-Strasse 18, A-8700 Leoben, Austria

Journal of the European Ceramic Society 43, Issue 15 (2023) 7167-7177
doi: <https://doi.org/10.1016/j.jeurceramsoc.2023.06.016>

Reuse under the terms of license CC-BY 4.0



Contents lists available at ScienceDirect

Journal of the European Ceramic Society

journal homepage: www.elsevier.com/locate/jeurceramsoc

The Ball-on-Ring-test: Enhancing an analytical solution by numerical analysis for elastic deformation and small displacements

Maximilian Staudacher, Peter Supancic, Tanja Lube*

Department of Materials Science, Montanuniversität Leoben, Franz Josef-Strasse 18, A-8700 Leoben, Austria

ARTICLE INFO

Keywords:

Ball-on-Ring (BoR)
Finite Element Analysis
Biaxial testing
Ceramics
Analytic solution

ABSTRACT

The Ball-on-Ring-test is a biaxial strength testing method utilized to test brittle materials such as ceramics, glass, or semiconductor wafers. In this work, an analytical solution for the BoR-test is derived using plate theory. In contrast to previous work, a Hertzian load distribution beneath the loading ball is considered. The solution provided in this work is extensively analyzed and validated by two Finite-Element-Analysis (FEA) models. For thin specimens, excellent agreement between FEA and the analytical solution was found. For many specimen geometries and loading configurations, it is shown that plate theory generally fails to accurately describe the maximum stress. Therefore, a simple correction for these cases is proposed. With this correction, an error $< 2\%$ to the FEA-results is achieved. By combining these methods, accurate functional expressions for the displacement field, its derivatives, and the shear force-, the bending moment- and stress distributions are provided for the entire disc.

1. Introduction

Strength testing of brittle materials is well known as one of the key methods to assess component reliability. Due to a large number of components being either disc or plate-shaped, biaxial strength testing methods have found their way into many fields and are used for a wide range of materials [1–6]. Apart from well-known ceramic materials, thin plates made from glass, silicon wafers or ceramic membranes for solid oxide fuel cells are frequently tested [7–11]. Furthermore, biaxial testing methods provide a better representation of real-world loading situations (which are rarely uniaxial) and require less effort for specimen preparation due to the maximum tensile stress acting at the specimen's center far from the specimen's edges. Some of the most prominent biaxial testing methods are the Ring-on-Ring-test (RoR), the Piston-on-Ring-test (PoR), the Ball-on-Three-Balls-test (B3B) and the Ball-on-Ring-test (BoR) [1,12–16]. Each testing method applies a different stress field to the specimen, depending on the geometry of the indenter and the support conditions. Whilst the support conditions generally change the overall shape or symmetry of the stress field, the indenter geometry significantly influences the maximum stress by defining the shape of the applied load distribution. Common indenter geometries are spheres or cylindrical pistons. A major upside of cylindrical over spherical indenters is the arbitrary and load-independent

contact radius with the specimen. This is not the case for spherical indenters, whose contact radius is dependent on both the load and the curvature of the specimen, as will be discussed later. When comparing the resulting elastic load distributions, a nearly opposing trend towards the edge of contact ($\rho \rightarrow 1$) is observed, as displayed in Fig. 1 [17].

However, the load distribution underneath the piston-shaped indenter is very likely to deviate from the displayed ideal case. On one hand, the sharp edge of the indenter causes a stress singularity at its edge, which induces plastic deformation of the indenter and favors wear. This is especially pronounced if high-hardness materials such as ceramics are tested, and if the same piston is used repeatedly [17]. On the other hand, small deformation of the specimen results in a shift from planar contact to a ring-like contact along the edges of the piston-shaped indenter. Both effects can be neglected with the use of a spherical indenter, leading to a well-defined load distribution. This aspect contributes to the attractiveness of ball-loaded biaxial tests such as the Ball-on-Ring-test. Whilst the load distribution for this test is well-defined, some problems arise from its small extent, as will be explained later on.

In general, the BoR-test is performed by loading a ring-supported specimen (usually discs) with a ball located in the center of the disc. A schematic of the testing setup is shown in Fig. 2.

The maximum tensile stress in both radial and tangential direction is

* Corresponding author.

E-mail address: tanja.lube@unileoben.ac.at (T. Lube).

<https://doi.org/10.1016/j.jeurceramsoc.2023.06.016>

Received 27 January 2023; Received in revised form 5 June 2023; Accepted 6 June 2023

Available online 8 June 2023

0955-2219/© 2023 The Author(s). Published by Elsevier Ltd. This is an open access article under the CC BY license (<http://creativecommons.org/licenses/by/4.0/>).

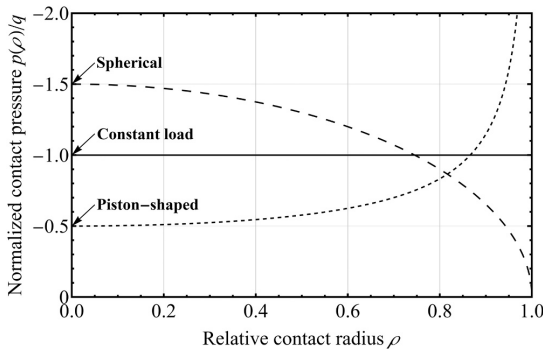


Fig. 1. Normalized axis-symmetric pressure distribution $p(\rho)$ for an ideal constant load and the elastic contact between two indenter types and an elastic half space. The relative contact radius ρ is given through the radial distance from the center r divided by the contact radius b . Each distribution is displayed for the same total load P and is normalized to its mean stress $q = P/\pi b^2$ [17].

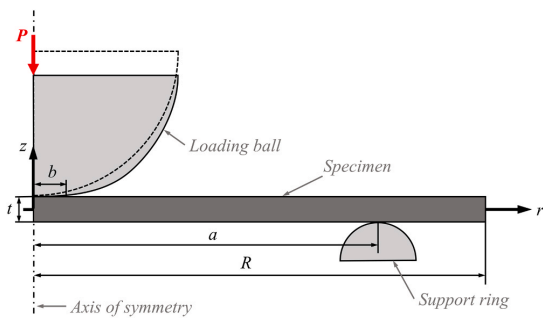


Fig. 2. Cross sectional schematic of the Ball-on-Ring testing setup. R denotes the specimen's radius, t its thickness, a the support ring radius, b the loading (or contact) radius and P the total applied load. Note that the deflection of the specimen due to the applied load is not displayed in this Figure.

found at the bottom surface in the center of the disc, opposing the loading ball. In order to assess the strength of the tested specimen and relate it to results from other testing methods, the maximum stress as well as the effective tested volume and surface [5], respectively, have to be known. The full stress distribution of the disc is necessary to allow determination of these parameters. Such can be provided through an analytical approach based on linear Kirchhoff-Love plate theory [18] for elastic isotropic specimens. If they are disc-shaped, the problem can be reduced to one dimension through cylindrical symmetry. According to plate theory, the radial and tangential stress component σ_{rad} and σ_{tan} in distance z from the neutral plane can be derived from the radial and tangential bending moment per unit length M_{rad} and M_{tan} according to

$$\sigma_{rad} = \frac{M_{rad}}{I} z, \sigma_{tan} = \frac{M_{tan}}{I} z \quad (1)$$

with I being the second moment of area, i.e. $I = t^3/12$. The shear stress τ is determined by

$$\tau = \frac{Q_{rad} S}{I} \quad (2)$$

with the radial shear force per unit length Q_{rad} and S as the first moment of area external to the horizontal section at z which is given by $S = 1/2((t/2)^2 - z^2)$. A thorough analysis of the history of the BoR-test and its general analytical solutions was also given by With & Wagemans in

1989 and Frandsen in 2012 [16,19]. In this work, an overview of the advancements in the analytic description of the maximum tensile stress will be given. If not stated otherwise, all solutions presented assume a constant central load (as shown in Fig. 1), but were still utilized to calculate the maximum stress for the Ball-on-Ring problem. Roark & Young [20] published a solution for a ring supported plate loaded with a central constant load distribution q . The maximum tensile stress σ_{max} is given by

$$\sigma_{max} = \sigma_{rad,r=0} = \sigma_{tan,r=0} = \frac{3qb_{con}^2}{4t^2} \left[(1+\nu)2 \ln\left(\frac{a}{b_{con}}\right) + 2 \right] \quad (3)$$

with b_{con} as the radius of the area of constant load, t as the specimen's thickness, a as the support radius and ν as the Poisson's ratio of the tested material. Note that this solution only considers a disk without overhang, i.e. $R=a$. Furthermore, this solution (Eq. (3)), is erroneous for the problem described in [20] and in the most recent edition [21], since the correct solution according to plate theory, determined by the authors, is:

$$\sigma_{max} = \frac{3qb_{con}^2(1+\nu)}{4t^2} \left[1 + 2 \ln\left(\frac{a}{b_{con}}\right) + \frac{(1-\nu)}{(1+\nu)} \left(1 - \frac{b_{con}^2}{2a^2}\right) \right] \quad (4)$$

A significant improvement for the same loading conditions was provided by Kirstein & Woolley in 1967 [22]. Here, the increased stiffness caused by the added constraint of the overhang is taken into account by including the specimen's radius R in the term a^2/R^2 :

$$\sigma_{max} = \frac{3qb_{con}^2(1+\nu)}{4t^2} \left[1 + 2 \ln\left(\frac{a}{b_{con}}\right) + \frac{(1-\nu)}{(1+\nu)} \left(1 - \frac{b_{con}^2}{2a^2}\right) \frac{a^2}{R^2} \right] \quad (5)$$

The same expression was also derived by Frandsen in 2012 along with a description of the displacement field and its derivatives for the full disc. From these expressions, he further derived the solutions for the distribution of the radial and tangential bending moment as well as the shear force distribution [19]. A very similar solution is found when investigating the Ring-on-Ring-problem, with only the constant term missing. Vitman and Pukh [23] provided this solution in 1962

$$\sigma_{max} = \frac{3qb_{ring}^2(1+\nu)}{4t^2} \left[2 \ln\left(\frac{a}{b_{ring}}\right) + \frac{1-\nu}{1+\nu} \left(1 - \frac{b_{ring}^2}{a^2}\right) \frac{a^2}{R^2} \right] \quad (6)$$

with b_{ring} as the radius of the loading ring. A problem throughout all solutions presented is the determination of the maximum stress for small loading radii b_{con} or b_{ring} . Since an infinite stress is approached for $b_{con} \rightarrow 0$, the analytical solution will only give accurate values above a minimum loading radius, which is mainly dependent on the specimen's thickness. For a different bending problem (plates loaded by a narrow constant surface pressure on complete elastic support), Westergaard derived a correction for small loading radii by utilizing Nádai's theory in 1926 [24,25]. It is based on replacing a small loading radius b with an equivalent loading radius b_{con}^* , which is dependent on the specimen's thickness t and is determined by

$$b_{con}^* = \begin{cases} b & \text{for } b \geq 1.724t \\ \sqrt{1.6b^2 + t^2} - 0.675t & \text{for } b < 1.724t \end{cases} \quad (7)$$

(Note that the first line of the correction by Westergaard has sometimes been miscited as $b_{con}^*=t$ for $b \geq 1.724t$ instead of $b_{con}^*=b$, as in [16]). Later work [15,16] utilized Eq. (7) to describe the Ball-on-Ring problem with $b_{con} = b_{con}^*$, and b as the Hertzian contact radius between a sphere and the planar surface of a half space calculated through [26].

$$b = \sqrt[3]{\frac{3PR_B}{4E^*}} \quad \text{with} \quad \frac{1}{E^*} = \frac{1-\nu_1^2}{E_1} + \frac{1-\nu_2^2}{E_2} \quad (8)$$

Here, P denotes the load applied on the sphere, R_B denotes the loading ball's radius and E^* an effective Young's modulus which is determined from the Young's modulus E_1 and E_2 and the Poisson's ratio ν_1 and ν_2 of the contacting bodies. The correction by Westergaard was

experimentally validated by With & Wagemans using strain gauge measurements [16]. On the other hand, Shetty et al. proposed that $b_{con}^* = t/3$, since the influence of the loading ball radius on b is expected to be small [15]. According to Hertz's theory of contact between elastic solids [26], the pressure distribution $p(r)$ between a sphere and an elastic half-space is defined as

$$p(r) = q \frac{3}{2} \sqrt{1 - \frac{r^2}{b^2}} \text{ with } q = \frac{P}{\pi b^2} \quad \text{for } 0 \leq r \leq b \quad (9)$$

with P as the applied load, q as the average pressure and b as the contact radius as given above in Eq. (8). Hu [7] derived an expression for the maximum tensile stress at the center of a disc loaded by a Hertzian stress distribution, which is given by

$$\sigma_{max} = \frac{3qb^2(1+\nu)}{4r^2} \left[\frac{8}{3} + 2 \ln\left(\frac{a}{2b}\right) + \frac{1-\nu}{1+\nu} \left(1 - \frac{2b^2}{5a^2}\right) \frac{a^2}{R^2} \right] \quad (10)$$

but did not derive any further information about the stress distribution or deformation of the disc. The validity of this solution and the one by Klein & Woolley (Eq. (5)) was discussed and compared to Finite Element Analysis results for a single disc geometry and multiple loading ball radii by Chae et al. [27]. It will be shown later (Section 4) that this load distribution is also obtained in case of pressing a ball on the center of a circular plate. The main difference to contact with a half space is the deflection of the plate and the resultant curvature of the surface.

In the upcoming chapters, plate theory will be utilized to derive an analytical solution for the Ball-on-Ring problem for small displacements and assuming isotropic elasticity. A central Hertzian load distribution will be assumed. A schematic of the load distribution $p(r)$ and the sign convention used in this work are given in Fig. 3. The expressions for the displacement field and its derivatives for the entire disc will be presented. Consequently, expressions for the shear force, radial and tangential bending moments will be provided. These results will be

2. Deriving an analytical solution for the BoR-problem

2.1. Formulating the general equations

This chapter will describe the derivation of an analytical solution to the BoR-problem. Due to the cylindrical symmetry of the problem, a one-dimensional expression $w(r)$ describing the displacement w of the neutral plane can be derived by Kirchhoff-Love plate theory. The calculations have been performed both by hand and with the aid of Mathematica 13.1 (Wolfram Research, IL 61820, Champaign, USA). The Mathematica-script, which provides the full solution to this problem, can be found in the [Supplementary material](#). This script can easily be adjusted to provide an analytical solution for any type of central load distribution. As shown in Fig. 3, the problem was divided into three different regions: The central loaded region I, the load-free region II up to the supporting ring and the load-free region III outside the supporting ring. Roman numeral superscripts will be used to assign variables to their region of validity. By splitting the problem, a functional expression $w(r)$ describing the displacement w of each section individually can be formulated. Their general form for bending of a circular, transverse loaded plate is given as a linear 4th order differential equation by Kirchhoff-Love plate theory [18,28,29] through

$$\frac{d^4 w}{dr^4} + \frac{2}{r} \frac{d^3 w}{dr^3} - \frac{1}{r^2} \frac{d^2 w}{dr^2} + \frac{1}{r^3} \frac{dw}{dr} = -\frac{p(r)}{D} \quad (11)$$

where the load is defined by $p(r)$. While the pressure itself is defined as a positive quantity (see Eq. (9)), the direction of load application demands a negative sign, see Fig. 3. Note that Eq. (11) reduces to a homogeneous differential equation outside the centrally loaded region. In contrast to earlier work on the Ball-on-Ring Problem [19,20], a Hertzian load-distribution $p(r)$ (see Eq. (9)) will be applied instead of a constant load-distribution. Solving Eq. (11) analytically then yields the displacement and its derivatives

$$\begin{aligned} w &= \Theta + \frac{1}{2}c_I r^2 \left(\ln r - \frac{1}{2} \right) + c_{II} \ln r + \frac{1}{2}c_{III} r^2 + c_{IV} \\ \frac{dw}{dr} &= \frac{d\Theta}{dr} + c_I r \ln r + c_{II} \frac{1}{r} + c_{III} r \\ \frac{d^2 w}{dr^2} &= \frac{d^2 \Theta}{dr^2} + c_I (\ln r + 1) - c_{II} \frac{1}{r^2} + c_{III} \\ \frac{d^3 w}{dr^3} &= \frac{d^3 \Theta}{dr^3} + c_I \frac{1}{r} + c_{II} \frac{1}{r^3} \end{aligned} \quad (12)$$

with

$$\Theta(r) = \frac{qr^4}{600D} \left[\sqrt{1 - \frac{r^2}{b^2}} \left(61 \frac{b^4}{r^4} + 48 \frac{b^2}{r^2} - 4 \right) + 15 \left(2 \frac{b^4}{r^4} + 3 \frac{b^2}{r^2} \right) \left(\ln r - \ln \left(1 + \sqrt{1 - \frac{r^2}{b^2}} \right) \right) \right]$$

compared to previous work by Frandsen, Kirstein & Woolley and Hu [7, 19,22]. To validate the presented results, especially regarding the maximum tensile stress, two FEA models will be employed and compared to each other. One model represents the ideal case with a Hertzian surface load applied, while the other one includes a model of the loading ball and utilizes contact calculations to better represent the actual loading situation. Furthermore, the applicability of the presented solution will be discussed for a wide range of loading conditions and disc geometries. For cases where the maximum stress is not represented accurately by the analytical solution, a correction will be provided. It is formally based on the proposition by Westergaard [24] and yields an equivalent loading radius for stress evaluation. Its validity will be shown through a comparison to FEA-results.

for the loaded region I. The bending stiffness of the plate, D , is given by $D = IE/(1 - \nu^2)$. For regions II and III, no external load q is applied, therefore $\Theta(r) = 0$. The integration constants $c_I - c_{IV}$ will be determined individually by the boundary and continuity conditions for each region. The radial and tangential bending moments, M_{rad} and M_{tan} , respectively, are given through [18,28,29].

$$M_{rad} = -D \left(\frac{d^2 w}{dr^2} + \frac{\nu}{r} \frac{dw}{dr} \right) \quad (13)$$

$$M_{tan} = -D \left(\frac{1}{r} \frac{dw}{dr} + \nu \frac{d^2 w}{dr^2} \right) \quad (14)$$

with the shear moment $M_{rad tan}$

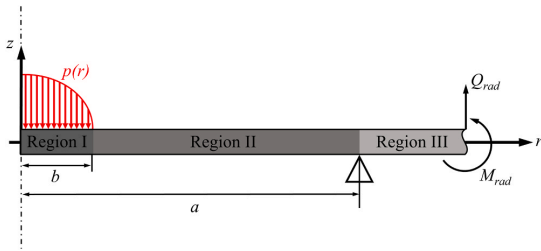


Fig. 3. Sign conventions utilized in this work and segmentation of the specimen into three regions displayed in a 2D-cross section of the axisymmetric problem. $p(r)$ denotes the applied surface load, w the specimen's deflection, Q_{rad} the shear force and M_{rad} the cross-sectional bending moment.

$$M_{rad,III} = 0 \tag{15}$$

and the shear force normal to the radial plane Q_{rad} given by

$$Q_{rad} = -D \left(\frac{d^3 w}{dr^3} + \frac{1}{r} \frac{d^2 w}{dr^2} - \frac{1}{r^2} \frac{dw}{dr} \right) \tag{16}$$

2.2. Field equations for the BoR-problem

This section provides the equations that describe the plate's displacement and its derivatives for each region.

2.2.1. Region I, $0 \leq r \leq b$

As for region I, where the location $r = 0$ is included, all instances of $\ln(r)$ have to be removed in order to maintain a non-singular solution for the deflection of the plate. The same is true for all instances of $r^2 \ln(r)$ to maintain a non-singular solution for the curvature of the plate. This is achieved if $c_{II}^j = -\frac{15qb^2}{600D}$ and $c_{II}^k = -\frac{30qb^4}{600D}$. This reduces $\theta(r)$ from Eq. (12) to the expression $\psi(r)$ and leaves

$$w^I = \Psi + \frac{1}{2}r^2 \left(c_{III}^j - \frac{1}{2}c_{II}^j \right) + c_{IV}$$

with

$$\Psi(r) = \frac{qr^4}{600D} \left[\sqrt{1 - \frac{r^2}{b^2}} \left(61 \frac{b^4}{r^4} + 48 \frac{b^2}{r^2} - 4 \right) - 15 \left(2 \frac{b^4}{r^4} + 5 \frac{b^2}{r^2} \right) \ln \left(1 + \sqrt{1 - \frac{r^2}{b^2}} \right) \right] \tag{17}$$

to describe the displacement field for region I. (Note that $\psi(r)$ at $r = 0$ yields a numerically undefined expression, that is analytically determined to be $(61 - 30 \ln 2)qb^4/600D$). Due to the relatively large number of terms of $\psi(r)$ and especially its derivatives, the authors refrained from stating their full form for the remainder of this work. By forming a new constant c_1 from the constant expression $(c_{III}^j - \frac{1}{2}c_{II}^j)$, Eq. (17) is significantly simplified. To ease traceability, the integration constants $c_I - c_{IV}$ for each region will be denoted by continuous subscripts $c_1 - c_{10}$ from this point on. This gives

$$w^I = \Psi + \frac{1}{2}c_1 r^2 + c_2$$

$$\frac{dw^I}{dr} = \frac{d\Psi}{dr} + c_1 r \tag{18}$$

$$\frac{d^2 w^I}{dr^2} = \frac{d^2 \Psi}{dr^2} + c_1$$

$$\frac{d^3 w^I}{dr^3} = \frac{d^3 \Psi}{dr^3}$$

to describe the displacement field for region I.

2.2.2. Region II, $b \leq r \leq a$

Due to the absence of external loads, $\theta(r) = 0$ for this region, which leaves a simpler form of Eq. (12). However, all other terms and integration constants are included with

$$w^{II} = \frac{1}{2}c_3 r^2 \left(\ln r - \frac{1}{2} \right) + c_4 \ln r + \frac{1}{2}c_5 r^2 + c_6$$

$$\frac{dw^{II}}{dr} = c_3 r \ln r + c_4 \frac{1}{r} + c_5 r \tag{19}$$

$$\frac{d^2 w^{II}}{dr^2} = c_3 (\ln r + 1) - c_4 \frac{1}{r^2} + c_5$$

$$\frac{d^3 w^{II}}{dr^3} = c_3 \frac{1}{r} + c_4 \frac{1}{r^3}$$

describing the displacement field for region II.

2.2.3. Region III, $a \leq r \leq R$

For region III, the same conditions as for region II apply, i.e. all terms and integration constants of Eq. (12) with $\theta(r) = 0$ are utilized. The displacement field for region III is therefore given by

$$w^{III} = \frac{1}{2}c_7 r^2 \left(\ln r - \frac{1}{2} \right) + c_8 \ln r + \frac{1}{2}c_9 r^2 + c_{10}$$

$$\frac{dw^{III}}{dr} = c_7 r \ln r + c_8 \frac{1}{r} + c_9 r \tag{20}$$

$$\frac{d^2 w^{III}}{dr^2} = c_7 (\ln r + 1) - c_8 \frac{1}{r^2} + c_9$$

$$\frac{d^3 w^{III}}{dr^3} = c_7 \frac{1}{r} + c_8 \frac{1}{r^3}$$

In conclusion, two integration constants for region I and four integration constants each for regions II and III have to be determined, totaling 10 unknown variables. By formulating the boundary and continuity equations, a set of 10 independent linear equations can be derived. Solving this system yields the solution for the displacement field and its derivatives.

2.3. Boundary and continuity conditions

This section forms the basis for the system of equations that are used to determine $c_1 - c_{10}$. Starting with deflection, the first equation is given through the continuity from region I to region II by

$$w'(b) = w''(b) \tag{21}$$

Furthermore, the deflection of the plate at the position of the support ring ($r = a$) is zero, which gives

$$w''(a) = 0 \tag{22}$$

and

$$w'''(a) = 0 \tag{23}$$

for region I and region II, respectively. Due to the absence of external moments, the slope and curvature of the plate has to be continuous from region I to region II and from region II to region III. However, evaluating Eq. (18) at position $r = b$ gives the indeterminate form $0/0$ for both the

$$w = \frac{qb^4}{16D} \begin{cases} \psi \frac{16D}{qb^4} + \frac{r^2 - a^2}{b^2} \left[2 + \frac{1 - \nu}{1 + \nu} \left(1 - \frac{2b^2}{5a^2} \right) \frac{a^2}{R^2} \right] + 2 \ln\left(\frac{a}{b}\right) \left(\frac{2}{5} + \frac{r^2}{b^2} \right) & \text{for } 0 \leq r \leq b \\ 2 \ln\left(\frac{a}{r}\right) \left(\frac{2}{5} + \frac{r^2}{b^2} \right) + \left[2 + \frac{1 - \nu}{1 + \nu} \left(1 - \frac{2b^2}{5a^2} \right) \frac{a^2}{R^2} \right] \frac{r^2 - a^2}{b^2} & \text{for } b \leq r \leq a \\ 2 \ln\left(\frac{r}{a}\right) \left(1 - \frac{2b^2}{5a^2} \right) \frac{a^2}{b^2} + \frac{1 - \nu}{1 + \nu} \left(1 - \frac{2b^2}{5a^2} \right) \frac{a^2}{R^2} \frac{r^2 - a^2}{b^2} & \text{for } a \leq r \leq R \end{cases} \tag{33}$$

slope and the curvature. Therefore, L'Hôpital's rule has to be applied in order to obtain a regular expression that can be evaluated. This then yields the continuity conditions for the slope at positions $r = b$ and $r = a$ through

$$\lim_{r \rightarrow b} \frac{dw'}{dr}(r) = c_1 b - \frac{7qb^3}{40D} = \frac{dw''}{dr}(b) \tag{24}$$

$$\frac{dw''}{dr}(a) = \frac{dw'''}{dr}(a) \tag{25}$$

and the continuity condition for the curvature at the same positions with

$$\lim_{r \rightarrow b} \frac{d^2w'}{dr^2}(r) = c_1 - \frac{13qb^2}{40D} = \frac{d^2w''}{dr^2}(b) \tag{26}$$

$$\frac{d^2w''}{dr^2}(a) = \frac{d^2w'''}{dr^2}(a) \tag{27}$$

Two further equations can be derived from the stress-state at the edge of the plate. Here, both the radial stress and the shear stress have to be zero, which gives

$$M_{rad}(R) = 0 \tag{28}$$

$$Q_{rad}'''(R) = 0 \tag{29}$$

Finally, the reaction force per unit length R_a from the support ring at position $r = a$ causes a discontinuity in the shear field, which can be expressed by

$$Q_{rad}''(a^-) + R_a = Q_{rad}''(a^+) \tag{30}$$

with positions close to $r = a$ towards the center or towards the edge denoted as a^- and a^+ , respectively. By using a vertical force equilibrium, R_a is given through the total load applied, F_a , divided by the total line length of the support at $r = a$:

$$R_a = \frac{F_a}{2a\pi} \tag{31}$$

The total load F_a is given by an integral over the load distribution $p(r)$, which gives

$$F_a = \int_0^{2\pi} \int_0^b p(r)rdrd\varphi = \int_0^{2\pi} \int_0^b q \frac{3}{2} \sqrt{1 - \frac{r^2}{b^2}} rdrd\varphi = qb^3\pi \tag{32}$$

3. Solution for the Ball-on-Ring problem

This chapter provides the solution for the Ball-on-Ring problem assuming a Hertzian pressure distribution. The system of equations from the previous chapter was solved by Mathematica 13.1 and the constants $c_1 - c_{10}$ were obtained, which are listed in the Appendix of this work. Inserting these constants in Eqs. (18)–(20) gives the solution for the displacement field and its derivatives. Special care was taken to simplify the constants and equations in similar way to the work by Frandsen [19] in order to identify similarities between the two solutions.

$$\frac{dw}{dr} = \frac{qb^3}{8D} \begin{cases} \frac{d\psi}{dr} \frac{8D}{qb^3} + \left[2 + 2 \ln\left(\frac{a}{b}\right) + \frac{1 - \nu}{1 + \nu} \left(1 - \frac{2b^2}{5a^2} \right) \frac{a^2}{R^2} \right] \frac{r}{b} & \text{for } 0 \leq r \leq b \\ -\frac{2b}{5r} + \left[1 + 2 \ln\left(\frac{a}{r}\right) + \frac{1 - \nu}{1 + \nu} \left(1 - \frac{2b^2}{5a^2} \right) \frac{a^2}{R^2} \right] \frac{r}{b} & \text{for } b \leq r \leq a \\ \left(1 - \frac{2b^2}{5a^2} \right) \frac{a^2}{b^2} \frac{r}{1 + \nu} + \frac{1 - \nu}{1 + \nu} \left(1 - \frac{2b^2}{5a^2} \right) \frac{a^2}{R^2} \frac{r}{b} & \text{for } a \leq r \leq R \end{cases} \tag{34}$$

$$\frac{d^2w}{dr^2} = \frac{qb^2}{8D} \begin{cases} \frac{d^2\psi}{dr^2} \frac{8D}{qb^2} + \left[2 + 2 \ln\left(\frac{a}{b}\right) + \frac{1 - \nu}{1 + \nu} \left(1 - \frac{2b^2}{5a^2} \right) \frac{a^2}{R^2} \right] & \text{for } 0 \leq r \leq b \\ \frac{2b^2}{5r^2} - 1 + 2 \ln\left(\frac{a}{r}\right) + \frac{1 - \nu}{1 + \nu} \left(1 - \frac{2b^2}{5a^2} \right) \frac{a^2}{R^2} & \text{for } b \leq r \leq a \\ \left(1 - \frac{2b^2}{5a^2} \right) \left(\frac{1 - \nu}{1 + \nu} \frac{a^2}{R^2} - \frac{a^2}{r^2} \right) & \text{for } a \leq r \leq R \end{cases} \tag{35}$$

$$\frac{d^3w}{dr^3} = \frac{qb}{4D} \begin{cases} \frac{d^3\psi}{dr^3} \frac{4D}{qb} & \text{for } 0 \leq r \leq b \\ -\frac{b}{r} - \frac{2b^3}{5r^3} & \text{for } b \leq r \leq a \\ \frac{a^2b}{r^3} - \frac{2b^3}{5r^3} & \text{for } a \leq r \leq R \end{cases} \tag{36}$$

With the slope and curvature known for each region, the radial Moment M_{rad} is derived by inserting Eqs. (34) and (35) in Eq. (13).

$$M_{rad} = -\frac{(1+\nu)qb^2}{8} \begin{cases} D\left(\frac{d^2\psi}{dr^2} + \frac{\nu}{r}\frac{d\psi}{dr}\right) \frac{8}{(1+\nu)qb^2} + \left[2 + 2\ln\left(\frac{a}{b}\right) + \frac{1-\nu}{1+\nu}\left(1 - \frac{2b^2}{5a^2}\right) \frac{a^2}{R^2}\right] & \text{for } 0 \leq r \leq b \\ 2\ln\left(\frac{a}{r}\right) + \frac{1-\nu}{1+\nu}\left(\frac{a^2}{R^2} - \frac{2b^2}{5R^2} + \frac{2b^2}{5r^2} - 1\right) & \text{for } b \leq r \leq a \\ \frac{1-\nu}{1+\nu}\left(1 - \frac{R^2}{r^2}\right)\left(1 - \frac{2b^2}{5a^2}\right) \frac{a^2}{R^2} & \text{for } a \leq r \leq R \end{cases} \quad (37)$$

and the tangential moment M_{tan} through inserting Eqs. (34) and (35) in Eq. (14).

$$M_{tan} = -\frac{(1+\nu)qb^2}{8} \begin{cases} D\left(\frac{d\psi}{dr} + \nu\frac{d^2\psi}{dr^2}\right) \frac{8}{(1+\nu)qb^2} + \left[2 + 2\ln\left(\frac{a}{b}\right) + \frac{1-\nu}{1+\nu}\left(1 - \frac{2b^2}{5a^2}\right) \frac{a^2}{R^2}\right] & \text{for } 0 \leq r \leq b \\ 2\ln\left(\frac{a}{r}\right) + \frac{1-\nu}{1+\nu}\left(\frac{a^2}{R^2} - \frac{2b^2}{5R^2} - \frac{2b^2}{5r^2} + 1\right) & \text{for } b \leq r \leq a \\ \frac{1-\nu}{1+\nu}\left(1 + \frac{R^2}{r^2}\right)\left(1 - \frac{2b^2}{5a^2}\right) \frac{a^2}{R^2} & \text{for } a \leq r \leq R \end{cases} \quad (38)$$

The radial and tangential stress components can be determined by inserting Eqs. (37) and (38) in the respective expressions in Eq. (1). Finally, the shear force is given by inserting Eqs. (34)–(36) in Eq. (16).

$$Q_{rad} = \begin{cases} -D\left(\frac{d^3\psi}{dr^3} + \frac{1}{r}\frac{d^2\psi}{dr^2} - \frac{1}{r^2}\frac{d\psi}{dr}\right) & \text{for } 0 \leq r \leq b \\ \frac{qb}{2}\frac{b}{r} & \text{for } b \leq r \leq a \\ 0 & \text{for } a \leq r \leq R \end{cases} \quad (39)$$

Utilizing either Eq. (37) or (38) to determine the maximum tensile stress σ_{max} at the center of the plate ($r = 0$) yields

$$\sigma_{max} = \frac{3qb^2(1+\nu)}{4r^2} \left[\frac{8-2\ln(8)}{3} + 2\ln\left(\frac{a}{b}\right) + \frac{1-\nu}{1+\nu}\left(1 - \frac{2b^2}{5a^2}\right) \frac{a^2}{R^2} \right] = \frac{3qb^2(1+\nu)}{4r^2} \left[\frac{8}{3} + 2\ln\left(\frac{a}{2b}\right) + \frac{1-\nu}{1+\nu}\left(1 - \frac{2b^2}{5a^2}\right) \frac{a^2}{R^2} \right] \quad (40)$$

Note that this expression is identical to the solution derived by Hu (see Eq. (10)) [7]. As expected, it is also very similar to the solution by Kirstein and Woolley [22] (see Eq. (5)) in terms of the basic mathematical structure, but with different coefficients. The term $(8-2\ln(8))/3$ amounts to about 1.28 (in contrast to 1 in Eq. (5)) and the factor $2/5$ is found in the later part of the equation (in contrast to $1/2$ in Eq. (5)). Such similarities are found throughout all expressions

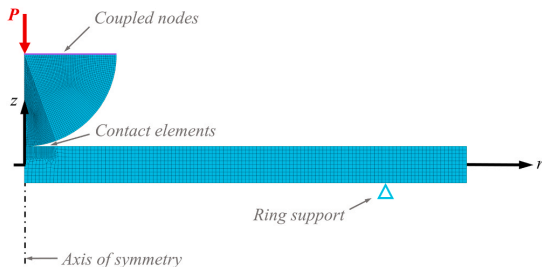


Fig. 4. Meshed FEA model (Model 2) and applied boundary conditions. The mesh has been coarsened for better visualization. Contact elements are utilized at the surface of the finer regions next to the axis of symmetry.

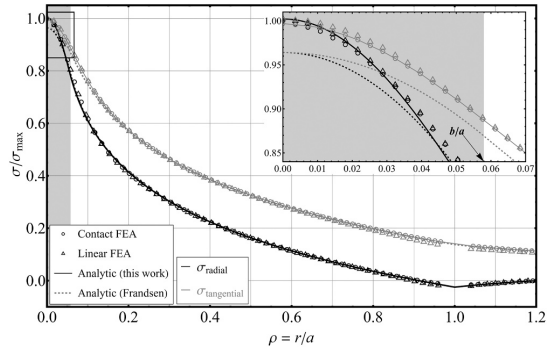


Fig. 5. Radial and tangential stress components in dependence of the relative radial position derived by analytical and numerical methods. The results shown are valid for a specimen with radius $R = 12$ mm, thickness $t = 1$ mm, support radius $a = 10$ mm and a loading radius $b = 0.5796$ mm (gray region). The specimen's Young's modulus E is 420 GPa, and the Poisson's ratio $\nu = 0.25$. The specimen was loaded by a steel ball with Young's modulus $E_b = 210$ GPa, a Poisson's ratio $\nu_b = 0.33$, a ball radius $R_b = 50$ mm and a load $P = 600$ N.

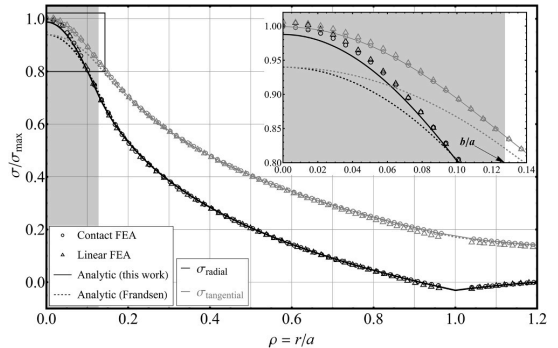


Fig. 6. Radial and tangential stress components in dependence of the relative radial position derived by analytical and numerical methods. The results shown are valid for a specimen with radius $R = 12$ mm, thickness $t = 1$ mm, support radius $a = 10$ mm and a loading radius $b = 1.276$ mm (gray region). The specimen's Young's modulus E is 420 GPa, and the Poisson's ratio $\nu = 0.25$. The specimen was loaded by a steel ball with Young's modulus $E_b = 210$ GPa, a Poisson's ratio $\nu_b = 0.33$, a ball radius $R_b = 200$ mm and a load $P = 1000$ N.

presented in this chapter when compared to the work by Frandsen [19]. The expressions describing region I additionally include the term $\psi(r)$ or its derivatives. Note that this solution also becomes singular for small (more precisely: vanishing) contact radii b .

4. Comparison and validation with FEA

In order to validate the derived expressions, they will be compared to FEA results. All simulations were conducted utilizing ANSYS Mechanical R.22.1 (ANSYS Inc., PA 15317, Canonsburg, USA) with the model implemented in APDL (Ansys Parametric Design Language). This allowed for easy reproducibility with automated scripts. Two FEA models were utilized in this work. One model, which will be referred to as *linear FEA* or *Model 1* throughout the following chapters, applied an ideal Hertzian surface load at the center of the disc, as shown in Fig. 3. The support ring was implemented as a nodal displacement constraint (vertical displacement $u_z = 0$) at $r = a$. If not stated otherwise, this model was used to generate the FEA results that the expressions from the previous chapter are compared to. As this model only considers the ideal

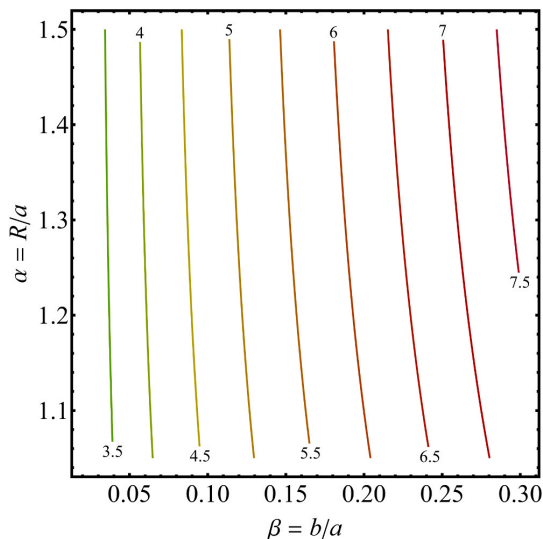


Fig. 7. Relative difference of the maximum tensile stress between the analytic solutions of this work and the one by Frandsen (and Kirstein & Woolley) in dependence of the specimen's relative overhang $\alpha = R/a$ and relative loading radius $\beta = b/a$.

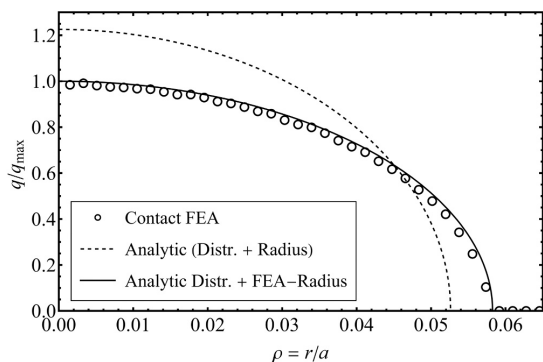


Fig. 8. Load distribution beneath the loading ball for the same set of parameters as used for Fig. 5. The round markers represent the results obtained with *Model 2*, the dashed line shows the distribution given by Eqs. (8) & (9). The through line shows the distribution given by Eq. (9) for the contact radius obtained from the FEA results.

case of a perfect elliptic load, which is independent of the specimen's curvature, another model was utilized. This model, which will be referred to as *contact FEA* or *Model 2*, implemented the interactions of the loading ball and the specimen through contact analysis. This model therefore represents a more realistic representation of real-world testing situations. Since the problem is axisymmetric, a 2D-representation of the full testing assembly sufficed, as shown in Fig. 4. The load was applied on a single node at the loading ball, with the vertical displacement of other nodes on the same surface being coupled to it. This ensures even load distribution by forcing their respective translation to be identical. Both models utilize linear geometric deformation, but *Model 2* includes the nonlinear change in contact radius between the loading ball and the specimen. Another major difference between both models is the way that the contact radius b is defined. While it can be specified by the user in *Model 1*, it is dependent on the applied load and the curvature of the

plate in *Model 2*.

The results in the following chapters will be shown as a function of normalized variables, with them being

$$\rho = \frac{r}{a}, \beta = \frac{b}{a}, \alpha = \frac{R}{a}, \gamma = \frac{t}{a} \tag{41}$$

Additionally, the stress will be normalized with respect to the maximum tensile stress obtained with *Model 2* at the center of the plate. In Fig. 5 and Fig. 6, the tangential and radial stress distributions on the tensile side of the disc ($z = -t/2$) are shown for two loading conditions, i. e. different loading radii b . The contact radii were chosen to be $b = 0.5796$ mm and $b = 1.276$ mm, respectively. In order to achieve sufficiently large loading radii for the analytical solution to be valid, as will be discussed in Section 5, large ball diameters R_B and high loads P had to be utilized in the contact FEA. These are $R_B = 50$ mm and $P = 600$ N for the results shown in Figure 5 and $R_B = 200$ mm and $P = 606.67$ N for the results shown in Fig. 6. Such large loading ball diameters could be realized by utilizing a slightly domed punch.

It is evident from Fig. 5 that excellent agreement between Eqs. (37) and (38) and the results from FEA is achieved. Furthermore, the different FEA models show the same results throughout the whole specimen and both stress components, indicating that running a full contact analysis can be substituted by a simulation with an idealized surface load. Note that the lack of datapoints at $\rho = 1$ stems from the use of pointwise boundary conditions, which result in singularities at and close to that point, hence why the datapoints were removed on purpose. Fig. 6 shows good agreement as well, with a small difference of about 1 % between Eqs. (37) and (38) and the results of FEA. For the situations shown here, the solution for the maximum stress by Frandsen (which is identical to the one derived by Kirstein & Woolley) deviates by about 4 % for $b = 0.5796$ mm and about 6 % for $b = 1.276$ mm to the results of Eqs. (37) and (38) and FEA. To get a better understanding of the difference between the solution for a constant central load, $\sigma_{max, const.}$ and the one presented in this work, σ_{max} , the relative difference of the maximum stress

$$\text{Relative difference} \left[\% \right] = 100 \frac{\sigma_{max} - \sigma_{max, const.}}{\sigma_{max, const.}} \tag{42}$$

was investigated for a range of different plate geometries and loading radii with a Poisson's ratio of 0.25. The result is shown in Fig. 7. The relative difference is strongly affected by the relative loading radius β , while the relative overhang α only has a minor influence. The best agreement is found for small relative loading radii where the difference reaches a minimum of 3.5 %. The maximum of 7.5 % is found for large relative loading radii.

Fig. 8 shows a comparison of the load distribution beneath the

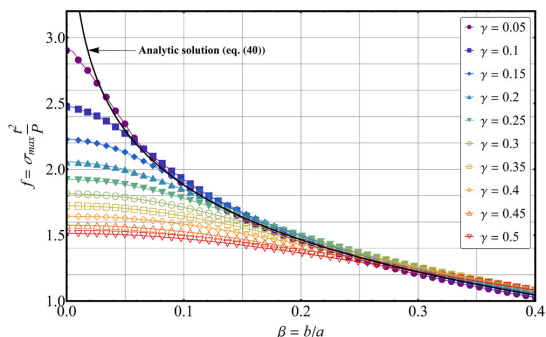


Fig. 9. Comparison of f derived with either FEA from *Model 1* (colored markers) or Eq. (40) (black line) for discs with $R/a = 1.2$, $E = 100$ GPa and $\nu = 0.25$.

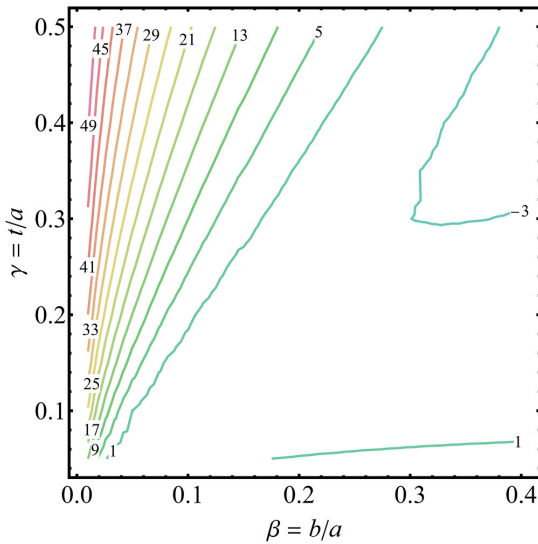


Fig. 10. Relative error between $f_{analytic}$ and f_{FEA} in dependence of the relative loading radius $\beta = b/a$ and the specimen's relative thickness $\gamma = t/a$.

loading ball for the same conditions as in Fig. 5. Shown are the load distribution obtained by FEA with *Model 2*, the analytic load distribution (see 9(9)) for the contact radius derived with Eq. (8), and the analytic load distribution with the contact radius as obtained from FEA. It is evident that if the contact radius from FEA is utilized, the analytic load distribution is in excellent agreement with the numeric result. Therefore, even though Eq. 9 is derived for the contact of a sphere with an elastic half-space, it can also be utilized to describe the load distribution of a sphere with a plate as thin as $\gamma = 0.05$. If the contact radius is determined with Eq. (8), it will be underestimated by about 12 %, causing the deviation shown in Fig. 8. This is due to the deformation of the plate not being considered in combination with the exceptionally large diameter of the loading ball used to obtain Fig. 5. This results in a significant change in contact radius through a small increase of the plate's curvature. For loading ball radii used in practice, this deviation will be significantly smaller.

5. Extending the limits of plate theory

To determine the applicability of the solution presented in this work for stress evaluation, more specimen geometries and loading situations were compared to FEA, with a focus on the influence of the specimen's thickness t on the maximum tensile stress. The maximum stress will be normalized and expressed through

$$f = \sigma_{max} \frac{t^2}{P} \tag{43}$$

to allow a better visualization of the results. The constant f therefore represents a dimensionless value which is linked to the respective maximum stress and is dependent on the specimen's thickness and radius, the loading radius, and the Poisson's ratio of the specimen. Fig. 9 shows f derived from 43(43) in dependence of the relative loading radius $\beta = b/a$, which is independent of the specimen's thickness. The colored markers represent results obtained with *Model 1* for specimens with varying relative thickness $\gamma = t/a$ and relative loading radius, totaling 500 individual simulations, which will be referred to as *Dataset 1*. Both analytical and numerical results were generated for specimens with a relative overhang $\alpha = R/a$ of 1.2, a Young's modulus of 100 GPa and a

Poisson's ratio of 0.25.

It is obvious that the analytic solution derived by plate theory does not agree with FEA-results for all combinations of loading radius and specimen thickness. This is especially pronounced for thick plates ($\gamma > 0.15$). Additionally, the analytic solution significantly overestimates the maximum tensile stress for small loading radii ($\beta < 0.025$) and approaches an infinite stress if $\beta \rightarrow 0^1$. To better quantify these results, the relative error between the analytic solution $f_{analytic}$ (derived by inserting Eq. (40) in Eq. (43)) and FEA results f_{FEA}

$$Relative\ error \left[\% \right] = 100 \frac{f_{analytic} - f_{FEA}}{f_{FEA}} \tag{44}$$

is presented as contours in Fig. 10.

Universally good agreement, i.e. independent of the specimen's thickness, is only achieved for relative loading radii $b/a \geq 0.3$. However, loading radii this large will only rarely occur in real-life testing and material configurations. Mostly, small relative loading radii of about 0.05–0.1 are to be expected [15]. In this region, previous analytic solutions and the one derived in this work will significantly overestimate the maximum stress for most practical specimens. Better results are achieved if the correction by Westergaard (eq. (7)) is utilized in combination with the analytic solution by Kirstein & Woolley (Eq. (5)) [22, 24]. The relative error, according to Eq. (46), between this corrected analytic solution and the FEA results is shown in Fig. 11a. Since both the correction and Eq. (5) were derived for a constant load distribution, good agreement is only achieved for exceptionally small loading radii. Therefore, a new correction based on the ansatz provided by Westergaard is proposed:

$$b^* = \begin{cases} b & \text{for } b \geq 2.15t \\ \sqrt{1.459b^2 + t^2} - 0.633t & \text{for } b < 2.15t \end{cases} \tag{45}$$

Again, this correction provides an equivalent loading radius b^* , which is based on the Hertzian contact radius b and the specimen's thickness t . This correction will come into play if the ideal Hertzian loading radius b is small in comparison to the specimen's thickness. The values for the numerical constants in Eq. (45) were derived by fitting the FEA results generated with *Model 1*. To determine the accuracy of this fit, the relative error between the corrected analytic solution (that is Eq. (40) evaluated with the equivalent loading radius under the conditions from Eq. (45)) and the fitted FEA results was calculated with

$$Relative\ error \left[\% \right] = 100 \frac{f_{analytic,corr} - f_{FEA}}{f_{FEA}} \tag{46}$$

The results are shown as contours in Fig. 11b.

It is evident that the correction yields significantly better results compared to the uncorrected stress evaluation, as shown in Fig. 10, with a reduction in the maximum relative error in f to less than 2 %. Since the expressions for the correction have been derived from this set of FEA-results (*Dataset 1*), it is obvious that good agreement will be achieved. So far, only one relative overhang and Poisson's ratio, i.e. $R/a = 1.2$ and $\nu = 0.25$, have been investigated. Therefore, two additional sets of FEA-results have been generated with *Model 1*, this time with $R/a = 1.5$ and ν being either 0.25 (*Dataset 2*) or 0.35 (*Dataset 3*), respectively. As before, the same range of parameters has been simulated, yielding a total of 1000 additional results. The relative error of the corrected analytical solution provided above (Eqs. (40) & (45)) to the new sets of FEA results is shown in Fig. 12a and b. Again, excellent agreement is observed. The change in maximum tensile stress due to the change in relative overhang or Poisson's ratio is accurately described by Eq. (40) alone. Therefore, these influences do not need to be additionally included in the correction

¹ While the stress approaches a singularity for $b \rightarrow 0$ when the applied load is represented by a δ -function) at the center of the plate, the displacement remains regular, i.e. $w(r = 0, b = 0) = Pa^2 / (16\pi D)(2 + a^2/R^2(1 - \nu)/(1 + \nu))$

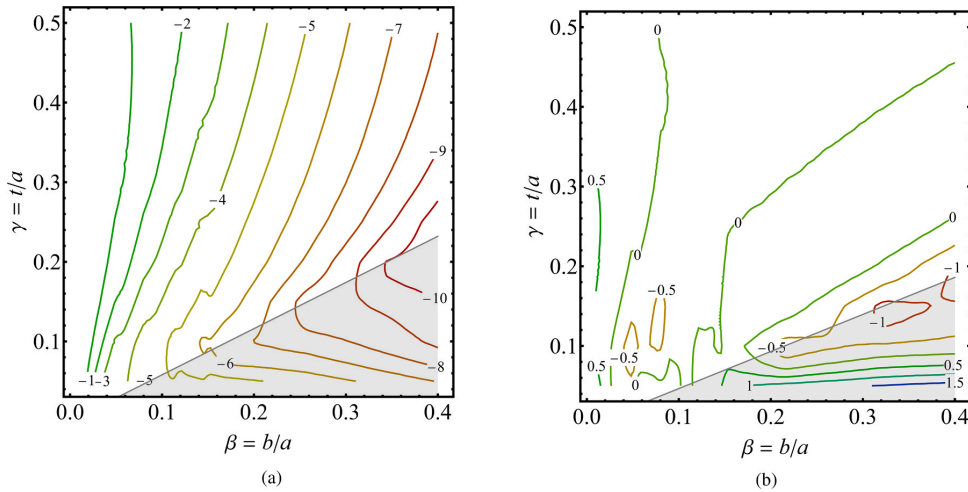


Fig. 11. Relative error between the maximum tensile stress of the corrected analytic solution (Eqs. (5) & (7) in a, Eqs. (40) & (45) in b) and FEA results from *Model 1* for discs with $R/a = 1.2$ and $\nu = 0.25$. Shown is the error for the analytic solution provided in this work (Eq. (40)) with the correction from Eq. (45) applied. The grey region marks the geometry and load configurations where the use of the equivalent loading radius is not necessary ($b \geq 1.724t$ for a, $b \geq 2.15t$ for b).

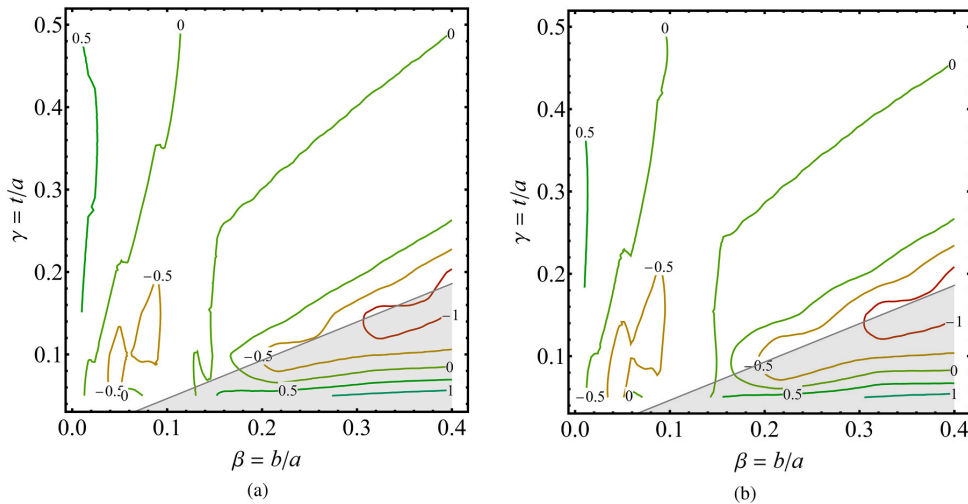


Fig. 12. Relative error between the maximum tensile stress of the corrected analytic solution and FEA results from *Model 1* for discs with $R/a = 1.5$ and $\nu = 0.25$ (i.e. *Dataset 2*, shown in a) or $\nu = 0.35$ (i.e. *Dataset 3*, shown in b). The grey region marks the geometry and load configurations where the use of the equivalent loading radius is not necessary ($b \geq 2.15t$).

(Eq. (45)) itself.

Furthermore, Kirstein & Woolley investigated the general case of a plate supported on several equally spaced point supports in their work. They have found that the maximum tensile stress at the center of the plate is independent of the number of supports [22]. For an infinite number of supports, a ring support is realized. Utilizing these findings for the corrected evaluation presented in this work, it can therefore be used for all ball-loaded biaxial testing methods. This includes the Ball-on-Three-Balls test, for which no analytically derived description of the maximum stress has been used so far. If compared to FEA results in recent work of the authors (see chapter 4.1 of [30]), a maximum relative error of about 3.3% for the maximum tensile stress of the B3B-test is achieved.

6. Summary

In this work, the Ball-on-Ring problem for elastic deformation and small displacements of discs has been investigated. In contrast to previous work, which utilized a constant central load distribution, a Hertzian load distribution was analyzed. The problem was segmented into 3 separate regions, and the differential equation for the displacement field based on Kirchhoff-Love plate theory was solved for each region. In combination with the boundary and continuity conditions of this problem, 10 equations containing 10 unknown integration variables have been stated.

Solving this system of equations leads to novel expressions for the displacement field, its derivatives, and the shear force-, the bending moment- and stress distributions for the entire disc. From these, an

expression for the maximum tensile stress at the center of the disc is derived, which is identical to the solution by Hu [7] and in good agreement to the solution by Frandsen [19] or Kirstein & Woolley [22]. Upon further investigation, a difference of 3.5–7.5 % to the latter, depending on the specimen's geometry and loading condition, was found.

The solution for the stress field provided in this work was analyzed and validated by two different Finite-Element-Analysis (FEA) models. One model represents the idealized case with an ideal Hertzian load distribution being applied, while the other included a model of the loading ball and utilized contact calculations to represent the non-linear testing situation more realistically. This model was used to validate the assumption of a Hertzian contact stress distribution $p(r) \propto \sqrt{1 - r^2/b^2}$ for the analytical solution. For thin specimens (i.e. thickness over support radius ≤ 0.1), and large enough contact radii (i.e. contact radius over support radius > 0.05), excellent agreement between both FEA models and the solution based on plate theory was found. For thicker specimens and exceptionally small loading radii, a comparison to FEA results has shown that plate theory generally fails to accurately describe the maximum stress.

Therefore, a correction based on the approach by Westergaard [24] and derived through FEA-results has been proposed. For small loading radii (relative to the specimen's thickness), an equivalent loading radius

is determined from the ideal Hertzian loading radius and the specimen's thickness. With this substitution model, an error of less than 2 % to the FEA-results is achieved. This has been shown for a wide range of specimen geometries and loading configurations. Through a combined analytical and numerical approach, an accurate description of the Ball-on-Ring problem is presented. Additionally, its applicability to other testing methods is discussed.

Declaration of Competing Interest

The authors declare that they have no known competing financial interests or personal relationships that could have appeared to influence the work reported in this paper.

Data Availability

Data can be made available on request.

Acknowledgements

M. Staudacher gratefully acknowledges financial support by the Austrian BMVIT and BMWFW in the project "CharAM" (FFG 877684) of the COIN/IraSME Program.

Appendix A. Integration Constants c_1 – c_{10}

$$c_1 = \frac{qb^2}{4D} \left[1 + \ln\left(\frac{a}{b}\right) + \frac{1-\nu}{1+\nu} \frac{a^2}{R^2} \left(\frac{1}{2} - \frac{b^2}{5a^2} \right) \right] \quad (47)$$

$$c_2 = \frac{qb^4}{80D} \left[4 \ln\left(\frac{a}{b}\right) - 10 \frac{a^2}{b^2} - \frac{1-\nu}{1+\nu} \frac{a^2}{R^2} \left(\frac{5a^2}{b^2} - 2 \right) \right] \quad (48)$$

$$c_3 = -\frac{qb^2}{4D} \quad (49)$$

$$c_4 = -\frac{qb^4}{20D} \quad (50)$$

$$c_5 = \frac{qb^2}{40D} \left[5(1 + 2 \ln(a)) + \frac{1-\nu}{1+\nu} \frac{a^2}{R^2} \left(5 - 2 \frac{b^2}{a^2} \right) \right] \quad (51)$$

$$c_6 = \frac{qb^2}{80D} \left[4 \ln(a)b^2 - 10a^2 - \frac{1-\nu}{1+\nu} \frac{a^4}{R^2} \left(5 - 2 \frac{b^2}{a^2} \right) \right] \quad (52)$$

$$c_7 = 0 \quad (53)$$

$$c_8 = \frac{qb^2}{40D} (5a^2 - 2b^2) \quad (54)$$

$$c_9 = \frac{qb^2}{40D} \frac{1-\nu}{1+\nu} (5a^2 - 2b^2) \frac{1}{R^2} \quad (55)$$

$$c_{10} = \frac{qb^2}{80D} (5a^2 - 2b^2) \left(-2 \ln(a) - \frac{1-\nu}{1+\nu} \frac{a^2}{R^2} \right) \quad (56)$$

Appendix B. Supporting information

Supplementary data associated with this article can be found in the online version at [doi:10.1016/j.jeurceramsoc.2023.06.016](https://doi.org/10.1016/j.jeurceramsoc.2023.06.016).

References

- [1] R. Morrell, Biaxial flexural strength testing of ceramic materials: a National Measurement Good Practice Guide No. 12, Natl. Phys. Lab. (2007).
- [2] J.R. Wachtmann Jr, W. Capps, J. Mandel, Biaxial flexure tests of ceramic substrates, *J. Mater.* (1972) 188–194.
- [3] D.J. Godfrey, S. John, Disc flexure tests for the evaluation of ceramic strength, in: *Proceedings 2nd International Conference of Ceramic materials and Components for Engines*, 14–17, 1986, pp. 657–665.
- [4] A. Wereszczak, T.P. Kirkland, K. Breder, H. Lin, M. Andrews, Biaxial strength, strength-size-scaling, and fatigue resistance of alumina and aluminum nitride substrates, *Int. J. Microcircuits Electron. Packag.* 22 (1999) 446–458.
- [5] D. Munz, T. Fett, *Ceramics: Mechanical Properties, Failure Behaviour, Materials Selection*, Springer, Berlin, Heidelberg, 1999.
- [6] J.B. Wachtman, M.J. Matthewson, W.R. Cannon, *Mechanical Properties of Ceramics*, Wiley, Hoboken, New Jersey, 2009.
- [7] S.M. Hu, Critical stress in silicon brittle fracture, and effect of ion implantation and other surface treatments, *J. Appl. Phys.* 53 (1982) 3576–3580.
- [8] A. Faes, H.L. Frandsen, A. Kaiser, M. Pihlatie, Strength of anode-supported solid oxide fuel cells, *Fuel Cells* 11 (2011) 682–689.
- [9] J. Malzbender, R.W. Steinbrech, Fracture test of thin sheet electrolytes for solid oxide fuel cells, *J. Eur. Ceram. Soc.* 27 (2007) 2597–2603.
- [10] J.-H. Zhao, J. Tellkamp, V. Gupta, D.R. Edwards, Experimental evaluations of the strength of silicon die by 3-point-bend versus ball-on-ring tests, *IEEE Trans. Electron. Packag. Manufact.* 32 (2009) 248–255.
- [11] B. Cotterell, Z. Chen, J.-B. Han, N.-X. Tan, The strength of the silicon die in flip-chip assemblies, *J. Electron. Packag.* 125 (2003) 114–119.
- [12] ASTM C 1499–05: Test Method for Monotonic Equibiaxial Flexural Strength of Advanced Ceramics at Ambient Temperature, ASTM International, West Conshohocken, PA, 2005.
- [13] EN ISO 6872:2015: Zahnheilkunde - Keramische Werkstoffe, Europäisches Komitee für Normung, 2015.
- [14] A. Börger, P. Supancic, R. Danzer, The ball on three balls test for strength testing of brittle discs: Stress distribution in the disc, *J. Eur. Ceram. Soc.* 22 (2002) 1425–1436.
- [15] D. Shetty, A.R. Rosenfield, P. McGuire, G.K. Bansal, W.H. Duckworth, Biaxial Flexure Test for Ceramics, *Am. Ceram. Soc. Bull.* (1980) 1193–1197.
- [16] G. With, H.H.M. Wagemans, Ball-on-Ring Test Revisited, in: J. 72, American Ceramic Society, 1989, pp. 1538–1541.
- [17] A.C. Fischer-Cripps. *Introduction to Contact Mechanics*, 2nd ed., Springer, New York, 2007.
- [18] A.E.H. Love, On the small free vibrations and deformation of a thin elastic shell, *Philos. Trans. R. Soc. Lond. A* 179 (1888) 491–546.
- [19] H.L. Frandsen, The small displacement elastic solution to the ball-on-ring testing method, *Mech. Mater.* 55 (2012) 33–40.
- [20] R.J. Roark, W.C. Young, H. Saunders, *Formulas for Stress and Strain – 5th Edition*, 1975.
- [21] R. Budynas, A. Sadegh, *Roark's Formulas for Stress and Strain - 9th Edition*, 9th ed., McGraw-Hill, New York, 2020.
- [22] A.F. Kirstein, R.M. Woolley, Symmetrical bending of thin circular elastic plates on equally spaced point supports, *Journal of Research of the National Bureau of Standards, J. Res. Natl. Bureau Sect. C: Eng. Instrum.* 71C (1967) 1.
- [23] F.F. Vitman, G.M. Bartenev, V.P. Pukh, L.P. Tsepkov, A method for measuring the strength of sheet glass, *Glass Ceram.* 19 (1962) 412–414.
- [24] H.M. Westergaard, *Stresses in concrete pavements computed by theoretical analysis*, in: *Public Roads*, 1926.
- [25] A. Nádai, Die Biegungsbeanspruchung von Platten durch Einzelkräfte, *Schweiz. Bauztg.* 23 (1920) 257–260.
- [26] H. Hertz, Ueber die Berührung fester elastischer Körper, *J. für die reine und Angew. Math.* (1881) 156–171.
- [27] S.-H. Chae, J.-H. Zhao, D.R. Edwards, P.S. Ho, Verification of ball-on-ring test using finite element analysis, in: *Proceedings of the 2010 12th IEEE intersociety conference on thermal and thermomechanical phenomena in electronic systems: (Therm 2010)*, Las Vegas, Nevada, USA, 2–5 June 2010, IEEE, Piscataway, N.J., 2010, pp. 1–6.
- [28] S. Timoshenko, S. Woinowsky-Krieger. *Theory of Plates and Shells*, 2nd ed., McGraw-Hill, Auckland, 1959.
- [29] I. Szabó. *Höhere Technische Mechanik: Nach Vorlesungen*, 6th ed., Springer Berlin Heidelberg, Berlin, Heidelberg, 2001.
- [30] M. Staudacher, T. Lube, P. Supancic, The Ball-on-Three-Balls strength test for discs and plates: extending and simplifying stress evaluation, *J. Eur. Ceram. Soc.* 43 (2023) 648–660.

Publication B

The Ball-on-Three-Balls strength test for discs and plates: Extending and simplifying stress evaluation

Maximilian Staudacher, Tanja Lube, Peter Supancic

Department of Materials Science, Montanuniversität Leoben, Franz Josef-Strasse 18, A-8700
Leoben, Austria

Journal of the European Ceramic Society 43, Issue 2 (2023) 648-660
doi: <https://doi.org/10.1016/j.jeurceramsoc.2022.09.047>

Reuse under the terms of license CC-BY 4.0



Contents lists available at ScienceDirect

Journal of the European Ceramic Society

journal homepage: www.elsevier.com/locate/jeurceramsoc

The Ball-on-Three-Balls strength test for discs and plates: Extending and simplifying stress evaluation

Maximilian Staudacher^{*}, Tanja Lube, Peter Supancic

Department of Materials Science, Montanuniversität Leoben, Franz Josef-Strasse 18, A-8700 Leoben, Austria

ARTICLE INFO

Keywords:

Ball-on-Three-Balls testing
Finite Element Analysis
Biaxial testing
Strength testing
Brittle failure

ABSTRACT

The Ball-on-Three-Balls-test has proven to be an accurate and easy-to-use option for strength testing. However, the maximum stress must be calculated based on Finite-Element-Analysis results. For this purpose, a fitted function was already provided. This function is based on results which were generated under the assumption of punctiform load introduction. Deviations from these conditions occur through an increase in contact-area between the loading ball and the specimen, large specimen deformations, friction, or plastic deformation of the balls. These non-linear effects are investigated by Finite-Element-Analysis for a wide range of specimens. It is shown that the maximum stress is sensitive to the area of contact between the loading ball and the specimen. Furthermore, thin specimens are subject to large deformations, which significantly decrease the maximum stress. Therefore, a revised fitted function is derived. For specimens with exceptional geometries, non-linear effects are considered with correction factors added to the new fitted function.

1. Introduction

Strength testing is probably the most important tool for ceramic material characterization and material development. It allows the determination of both general mechanical strength and the scatter thereof, which then enables the prediction and reduction of component failure [1]. Today, a number of mechanical testing methods are widely available and well examined. They can be categorized by the type of stress field that the specimen is subjected to, which is usually either uniaxial or biaxial. The main uniaxial testing methods are 3-or 4-point-bending, tensile and compression tests [2,3]. Biaxial testing methods can be classified by the symmetry of their stress distribution, being either axisymmetric or not. Examples for common methods with axisymmetric stress distributions are the Ring-on-Ring-test (RoR), the Ball-on-Ring-test or the Ball-with-flat-on-Ring-test [4–6]. Common methods employing non-axisymmetric stress distributions are the Ball-on-Three-Balls-test (B3B), the Piston-on-Three-Balls-test (P3B), the Ball-on-Ring-of-Balls-test and the Three-Balls-on-Three-Balls-test [7–12]. A significant disadvantage of axisymmetric tests is that a high degree of flatness of the specimen is required in order to guarantee even contact throughout the ring. This results in either additional specimen preparation requirements or deviations from the ideal analytical stress field due to uneven load distribution [13,14]. Therefore, tests utilizing a support of three balls have been

developed since non-planar discs can still be stably supported. The Piston-on-Three-Balls-test shows a similar problem, since the surface beneath the punch has to be planar to ensure uniform load application – the condition that has been assumed to derive the equation for the stress calculation. Furthermore, with increasing deformation of the sample, the assumption of an extended area of uniform pressure is lost and load application shifts towards the outer edge of the piston. This leaves testing methods such as the Ball-on-Three-Balls-test as one of the most tolerant to non-planar specimens and most flexible in terms of specimen geometry. As a result, it is among the most common biaxial testing methods and is employed for a variety of materials [15–24]. An extensive study about the influence of the most important sources of error has been conducted by Börger et al. [25]. Furthermore, the strongly localized area of maximum stress allows testing of specific regions of a component to generate spatially resolved strength results [26]. A prerequisite for an accurate evaluation for all tests that use an analytical stress calculation is to perform them under conditions of small deflections and linear elastic material behavior, i.e. maintaining a linear stress-deflection relationship. This is assured by prescribing that the support radius is smaller than about 6–20 times the specimen thickness [4,13,20]. Taking into account that manufacturing tolerances make support rings smaller than 5 mm in radius impractical [13], the lower limit for the thickness of strong specimens is approximately 0.5 mm in the RoR-test. The B3B-test, however, can easily

^{*} Corresponding author.

E-mail address: maximilian.staudacher@unileoben.ac.at (M. Staudacher).

<https://doi.org/10.1016/j.jeurceramsoc.2022.09.047>

Received 6 July 2022; Received in revised form 23 September 2022; Accepted 24 September 2022

Available online 28 September 2022

0955-2219/© 2022 The Author(s). Published by Elsevier Ltd. This is an open access article under the CC BY license (<http://creativecommons.org/licenses/by/4.0/>).

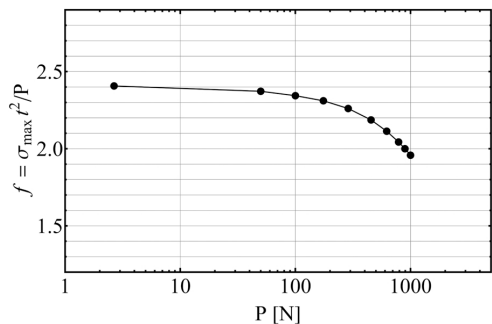


Fig. 1. FEA-results for the factor f in dependence of the applied load P for an exemplary specimen with a radius of 12 mm, a support radius of 10 mm and a thickness t of 1 mm. The specimen’s Young’s modulus and Poisson’s ratio are 70 GPa and 0.22, respectively.

be scaled down to much smaller support radii. With the use of standardized bearing balls, specimens as small as $2 \times 2 \times 0.13 \text{ mm}^3$ have been tested successfully [27–29]. However, the main disadvantage of the B3B-test is that no sufficiently accurate analytical description of the full stress field is available and numerical analysis has to be employed to determine the maximum stress and the effective volume or surface for each specimen [30,31]. This then entails new difficulties in making those results available. One possibility is to provide fitting functions for the factor f , which relates the applied load and the maximum tensile stress, as has been done by Börger et al. [30]. Yet, these functions are cumbersome to use and only provide a solution for the ideal case of punctiform load introduction and small deformations. Deviations from these ideal conditions lead to a load dependency of the factor f , as shown for an exemplary specimen in Fig. 1, which is not represented in [30]. This may lead to a significant overestimation of the specimen’s strength [32].

Within this work, a new expression for the ideal case of both discs and square plate specimens will be derived by utilizing FEA for linear elastic isotropic materials. By modifying the range and variables of the underlying data field, a new and simpler fit with similar accuracy to the one derived by Börger et al. [30] will be presented. Furthermore, the difference between the ideal case and real testing situations, such as an increase in contact-area between the loading ball and the specimen, large specimen deformations, friction, or plastic deformation of the loading ball will be discussed. The effect of large specimen deformations will be investigated by utilizing a combined analytical and numerical approach. The effect of an increasing contact-area at the loading ball will be examined by utilizing FEA. This will yield correction factors which describe the load-dependency of the factor f . The performance of

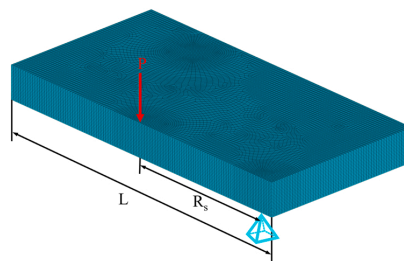


Fig. 3. Meshed Model 2 with a punctiform load P applied.

this new evaluation and its corrections will be assessed by comparison with an elaborate FEA model. The practical aspects given by the new evaluation and its valid domain of application will be discussed.

2. Methods

2.1. Finite-Element-Analysis

FEA was performed to generate grid points for fitting and to investigate specific effects. All simulations were conducted utilizing the commercial FEA-program ANSYS R21.1 (ANSYS Inc., PA 15317, Canonsburg, USA). Each of the following models was implemented as a script written in Ansys-Parametric-Design-Language (APDL). This allowed using them in automated parametric studies for a wide range of geometries and isotropic material properties, covering several thousand unique combinations.

2.1.1. Simplified models for discs

To investigate the dependence of the factor f on the testing geometry as well as the specimen’s elastic properties, the 3D-model shown in Fig. 2a) was utilized. Due to the symmetry of the system and loading conditions, the model could be reduced to one sixth of the full disc. In Model 1A, the loading ball was represented by a punctiform load applied in the center of the disc. The support ball was represented by a punctiform boundary condition at the support radius R_s . Consequently, this model represents the ideal case during testing. The specimen was meshed with 178958 SOLID95 elements (20-node brick elements) and 749574 nodes. The script further facilitates the implementation of various types of load application in the center of the specimen. To examine the influence of a finite area of contact, a Hertzian contact-pressure distribution with varying extent was utilized in Model 1B, as depicted in Fig. 2b).

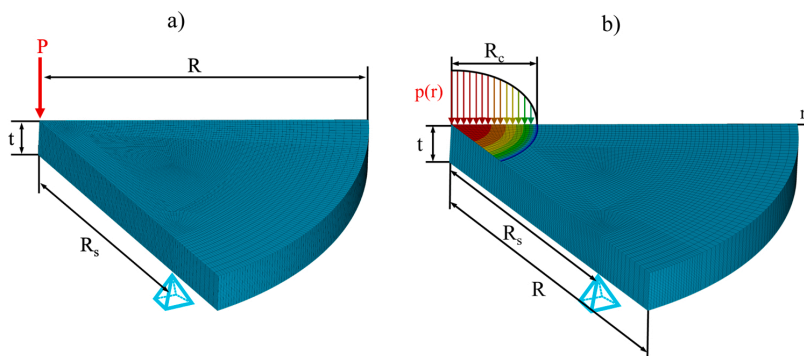


Fig. 2. a) displays the meshed Model 1A with a punctiform load P applied. b) shows Model 1B, but with a Hertzian contact-pressure distribution $p(r)$ applied.

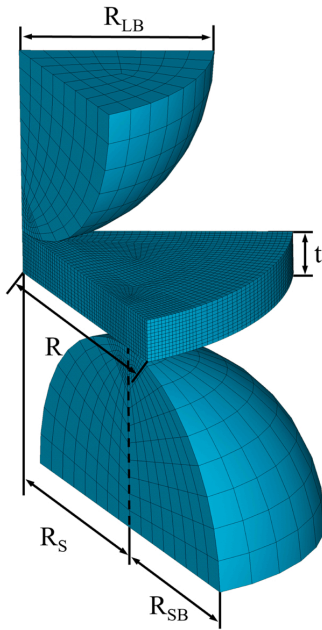


Fig. 4. Meshed model of the specimen and the loading/support balls, Model 3.

2.1.2. Simplified model for square plates

Model 2 serves the same purpose as Model 1A, but for square plates. Due to the reduced symmetry of the system, one half of the plate has to be simulated, as displayed in Fig. 3. Both the loading and the support balls were represented by a punctiform load (or boundary condition) applied in the center of the disc and at the support radius R_s , respectively. The specimen was meshed with a minimum of 162216 SOLID95 elements and 682140 nodes, depending on the specimen’s thickness and overhang.

2.1.3. Complete 3D-Model for discs

Model 3 serves as a validation for the simplified models. It represents a 3D-model of the testing assembly, based on a model first developed by Börger et al. [30]. Symmetry conditions allowed a reduction to one sixth of the full testing assembly, see Fig. 4. The specimen was meshed with a minimum of 40392 SOLID95 elements and 173061 nodes and a maximum of 70668 SOLID95 elements and 301375 nodes, depending on the specimen’s thickness and overhang. The loading ball was meshed with 1750 SOLID95 elements and 8196 nodes, the support ball using 3500 SOLID95 elements and 15582 nodes. The contact between the loading ball and the specimen was meshed with 375 CONTA174 (8-node surface elements) and 375 TARGET170 elements (8-node surface elements), the contact between the support ball and the specimen with 490 CONTA174 and 490 TARGET170 elements. The friction coefficient was set to $\mu = 0.5$ and symmetric contact calculations were employed. Since this model includes interactions between the specimen and the balls as well as load-dependent changes to the testing assembly and is solved under non-linear conditions, a better representation of real testing situations is given. A mesh convergence analysis for this and the other mentioned models can be found in Appendix A of this work.

2.2. Analytic solution for the deflection of plates

Kirstein et al. already developed an analytical solution for the deflection of thin centrally loaded plates on symmetric point supports in 1966 [33]. This solution is valid for a minimum of three supporting

points up to a theoretical maximum of an infinite number of support points, which would represent a ring supported situation. Within the context of this paper, their solution will be utilized for the special case of $m = 3$ support points and a central punctiform load. The deflection w at a position with radial distance r from the center of a disc with radius R and supported on points with distance D_s from the evaluated position is given by:

$$w = w_0 + \frac{3P(1 - \nu^2)}{2\pi Et^3} \left(r^2 \ln r - \frac{1}{m} \sum_{s=1}^m D_s^2 \ln \frac{D_s}{c} \right) \tag{1}$$

with

$$w_0 = \frac{P(1 - \nu^2)}{2\pi \kappa Et^3} \left[\sum_{s=1}^m D_s^2 \ln \frac{D_s'}{r_s'} + (\kappa^2 - 1) c^2 Re\{L_m(\zeta)\} + \frac{m(1 - \rho^2)R_s^2}{\kappa + 1} \right] + \gamma_3 \tag{2}$$

and

$$\gamma_3 = \frac{3P(1 - \nu^2)R_c^2}{2\pi \kappa Et^3} \left[A_m(\beta) + (1 - \kappa^2)B_m(\beta) - \kappa \ln \beta - \frac{1 - \beta^2}{\kappa + 1} \right]. \tag{3}$$

Here, P denotes the applied load, E the specimen’s Young’s modulus, t the specimen’s thickness, R_s the support radius, β the ratio R_c/R , and ν the Poisson’s ratio of the specimen. Other parameters of the equation will not be discussed here, the authors refer to the original work by Kirstein et al. [33].

2.3. Fitting

Every fit in this work has been performed in Mathematica 13.1 (Wolfram Research, IL 61820, Champaign, USA) with the command *NonlinearModelFit*. This command performs a least sum of squared errors fit on any given type of ansatz function by adjusting user-specified constants within the function. The deviation between the value of the fit $x_{i,fit}$ and the fitted data $x_{i,ref}$ for data point i will be referred to as residual error and is determined by

$$Residual\ error\ [\%] = 100 \frac{x_{i,fit} - x_{i,ref}}{x_{i,ref}} \tag{4}$$

For each fit, the maximum positive and negative residual error for the complete data field will be given. Furthermore, the mean residual error for a fit based on n grid points is given by

$$Mean\ residual\ error\ [\%] = 100 \frac{\sum_{i=1}^n Abs\left(\frac{x_{i,fit} - x_{i,ref}}{x_{i,ref}}\right)}{n} \tag{5}$$

3. Simplifying the stress calculation

3.1. Discs

Due to the lack of an accurate analytical solution for the stress field, it must be numerically evaluated instead. Börger et al. [30] performed Finite-Element-analysis for the special case of contacting support balls. If not stated otherwise, this assumption will be maintained throughout this work. For this case, the support radius R_s is given by the radius of the support balls R_{SB} by

$$R_s = R_{SB} \frac{2}{\sqrt{3}} \tag{6}$$

In general, the maximum tensile stress σ_{max} in the center of a bent plate scales with the applied load P and the inverse square of the thickness of the plate t :

$$\sigma_{max} = f \frac{P}{t^2} \tag{7}$$

The factor f is a dimensionless function which takes the material

Table 1
Constants m_1 – m_3 utilized in Eq. (9).

m_1	m_2	m_3
0.697	-0.118	-0.728

Table 2
Accuracy parameters describing the deviation of Eq. (9) to the data field for discs and Eq. (10) used in Eq. (9) to the data field for square plates.

Accuracy parameter	Discs	Square plates
Maximum residual error [%]	+ 1.4	+ 1.6
Minimum residual error [%]	-1.9	-1.6
Mean residual error [%]	+ 0.52	+ 0.63

properties and the involved geometry into account. Within their work, they reduced the factor f for the B3B-test to being dependent on the specimen's thickness t , the specimen's radius R , the support radius R_s and the Poisson's ratio ν . Furthermore, the results of a parametric study were made available by providing a fitted function for f :

$$f_{\text{Börger}}\left(\frac{t}{R}, \frac{R_s}{R}, \nu\right) = c_0 + \frac{c_1 + c_2 \frac{t}{R} + c_3 \left(\frac{t}{R}\right)^2 + c_4 \left(\frac{t}{R}\right)^3}{1 + c_5 \frac{t}{R}} \left(1 + c_6 \frac{R_s}{R}\right) \quad (8)$$

This function covers the range of $0.55 \leq R_s/R \leq 0.9$, $0.05 \leq t/R \leq 0.6$ and $0.2 \leq \nu \leq 0.3$. This range was later extended to $0.1 \leq \nu \leq 0.4$ by Danzer et al. [32]. The value of $f_{\text{Börger}}$ determined with this fit has an error $\leq \pm 1\%$ with respect to the numerical solution. This accuracy is made possible by providing a set of constants c_0 – c_6 for different Poisson's ratios in an increment of 0.05; a total of 49 constants. If the tested material has a Poisson's ratio not tabulated, linear interpolation must be performed. This makes implementation of this equation prone to errors and cumbersome. In order to simplify the calculation of the maximum stress, a new study on f has now been conducted. Up to now, f was always expressed and evaluated with its arguments relative to R . However, the influence of the support radius R_s on the value of f is significantly higher than that of the specimen's radius R . Therefore, a new data field for f based on the now modified parameters t/R_s , R/R_s and ν was generated by FEA utilizing Model 1, with a total of 1400 datapoints. The data field covers $1.05 \leq R/R_s \leq 2$, $0.05 \leq t/R_s \leq 0.6$ and $0.1 \leq \nu \leq 0.4$. Based on this data, a new empirical fit was developed. Now, the factor f can be determined by

$$f_{\text{new}}\left(\frac{t}{R_s}, \frac{R}{R_s}, \nu\right) = \exp\left[m_1(1 + \nu) + m_2 m \frac{t}{R_s} + m_3 \sqrt[4]{\frac{Rt^2}{R_s^3}}\right] \quad (9)$$

with m_1 – m_3 as listed in Table 1 and the limits of valid application as the range of the fitted data field.

An overview of the general deviation from Eq. (9) to the fitted data can be found in Table 2. Fig. 5a)–e) provide a more comprehensive overview of the fit's accuracy. In terms of specimen geometry, the lowest accuracy/largest deviation is generally found in the peripheral regions. Similarly, a low accuracy for exceptionally low and high Poisson's ratios can be observed. However, most technical ceramics exhibit a Poisson's ratio in the range of 0.2 – 0.3 [31], a range well described by the fit. Furthermore, typical specimens for the Ball-on-Three-Balls-test exhibit geometries as marked in Fig. 5c). Here, a maximum and minimum deviation as low as + 0.15% and – 0.7%, respectively, are achieved. In principle, a small loss in (overall) accuracy as compared to the fit by Börger et al. [30] is observed, though only in regions of minimal interest. Fig. 5 further gives the possibility to derive highly accurate strength results for individual geometries by utilizing the given deviation in combination with Eq. (9) to determine the applied stress as originally calculated with FEA.

3.2. Square plates

Another very common specimen geometry are square plates, which can be tested in similar testing fixtures as discs. The factor f for these specimens does not deviate much from similarly sized disc-shaped specimens, but the difference is large enough to necessitate a separate treatment. This is due to the fact that the overhang, i.e. the part of the specimen from the outer edge to the support radius, has a small but still pronounced effect on the maximum tensile stress. Therefore, instead of describing square plates with fit very similar to Eq. (9), the authors opted to provide a conversion from square plates to equivalent discs, as has been done for other methods [4,34]. An equivalent disc is defined by its diameter D_{eff} , which is chosen in a way so that the maximum stress is the same as in the square plate specimen. All other geometry parameters, such as the specimen's thickness and the support radius, remain unchanged. Therefore, only the conversion from the square plate's edge length L to the equivalent diameter is needed. In order to derive this conversion, Model 2 was utilized and 1035 datapoints were generated. The data field covers $2.165 \leq L/R_s \leq 3.899$, $0.0449 \leq t/R_s \leq 0.736$ and $0.05 \leq \nu \leq 0.45$. Based on this data, a conversion from square plates to discs was developed. The effective diameter D_{eff} is determined by

$$D_{\text{eff}} = L \left(1.053 - 0.017 \frac{tL}{R_s^2}\right) \quad (10)$$

An overview of the deviation for the factor f , derived with the conversion to equivalent discs and Eq. (9), to the FEA-data for square plates can be found in Table 2.

It should be noted that this conversion is only valid in the range $2.17 \leq L/R_s \leq 3.9$, $0.1 \leq t/R_s \leq 0.6$ and $0.1 \leq \nu \leq 0.4$.

4. Improving accuracy for high-load testing situations

So far, all simulations have been conducted with Models 1A and 2 described in Sections 2.1.1 and 2.1.2. As previously stated, this model represents the ideal case during testing with both punctiform load introduction and support conditions. It is evident that this will not represent reality in a number of practical cases and that some errors are to be expected. Errors due to geometric deviations of various aspects of the testing setup have already been discussed by Börger et al. and deemed negligible [25]. Therefore, the aforementioned errors mostly arise because no interactions between the loading or support balls and the specimen are represented in the model. First, an increase in load results in deformation of the loading ball and the specimen in the area of contact, whereby the assumption of punctiform load introduction loses its validity. Instead, a finite area of contact and load introduction is established. Second, large deflection of the specimen may occur under certain conditions, causing it to roll off the support balls. This results in a shift of contact position towards the center of the support circle, altering the applied bending moment and with it the maximum tensile stress. Third, friction between the loading ball and the specimen can have a significant influence on the maximum tensile stress of the specimen. It induces shear stresses under the area of contact, which act through the specimen thickness and thus reduce the maximum tensile stress.

Due to these interactions being included, Model 3, as described in Section 2.1.3, is significantly better suited to provide an accurate representation of reality. This then provokes the idea of using this model in a similar way to the previous section and incorporate all the mentioned effects into the evaluation at once. The main drawback of this model is its high processing time due to its use of contact calculations despite a decrease in the overall number of elements. In general, the evaluation takes about 70–80 times longer than for Model 1A. In order to represent the mentioned effects in the calculation of maximum stress, a higher number of parameters would be needed. First, the load-dependence has to be considered, which is influenced by the elastic constants of both the specimen and the support or loading balls. This would result in the

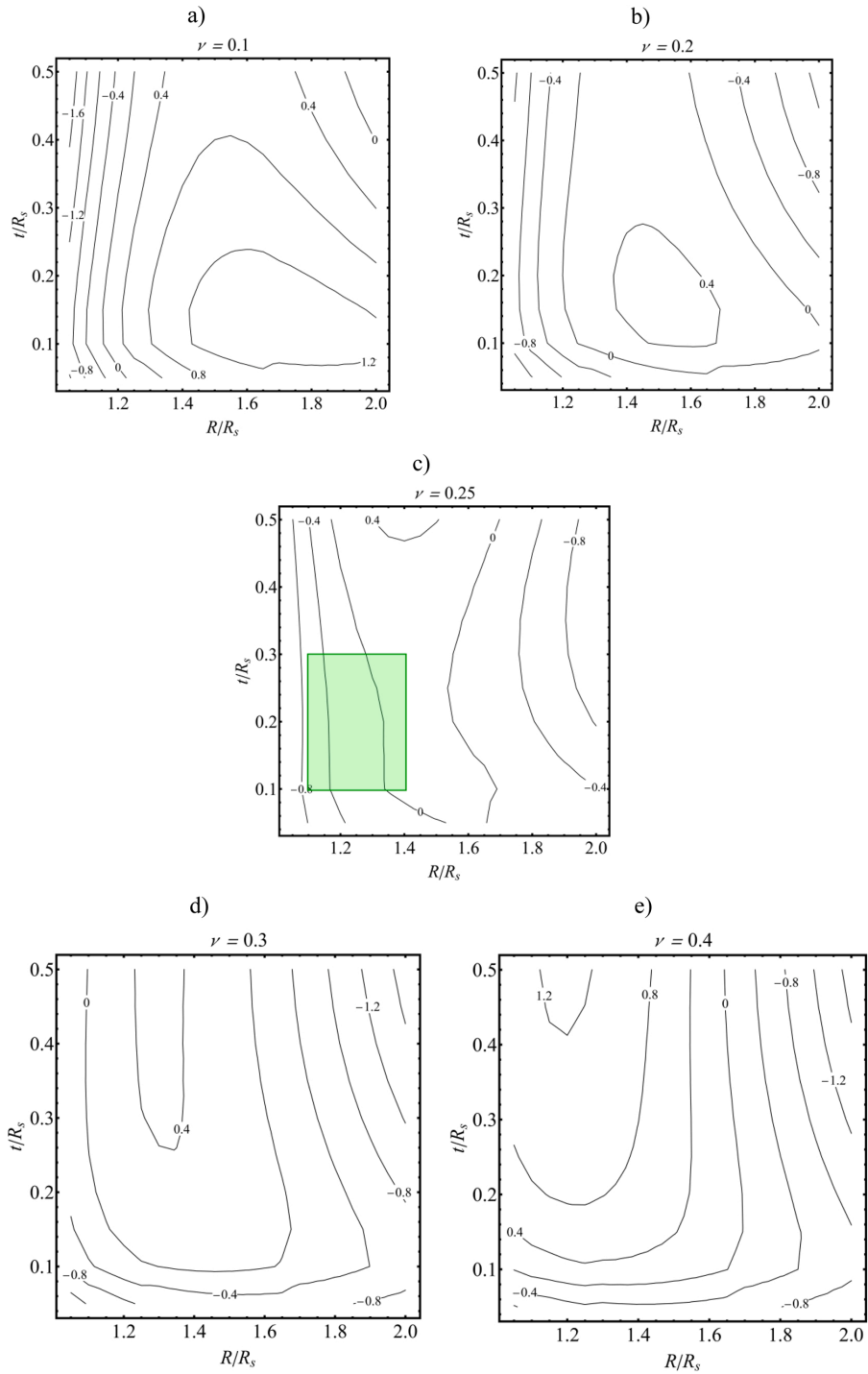


Fig. 5. Overview of the relative error of f_{new} to the fitted data points.

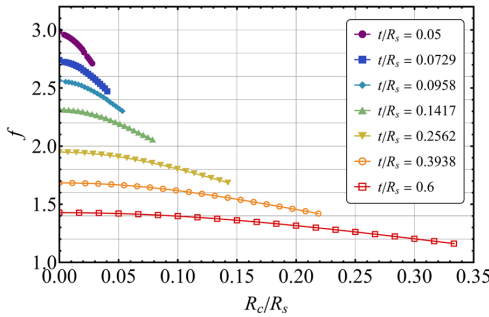


Fig. 6. The factor f in dependence of the relative contact radius and the specimen's relative thickness as predicted by FEA. Values at $R_c/R_s = 0$ are those which correspond to the point-load situation, and which are described by Eq. (7).

addition of up to four new parameters. To properly capture each dependency, each relevant parameter would have to be varied within its relevant range in at least 10 steps. Putting all those considerations together, a new parameter field with a size well within millions of data points would be necessary. In combination with the high processing time, a study like this would require immense computing power. Developing an accurate fit for such a data field would be another challenge by itself.

Therefore, a different method has to be considered. Within this work, a separation approach will be utilized. By taking an individual look at each major effect, a better understanding of its consequences can be achieved. Ideally, the deviations from the ideal solution f_{new} caused by them can be described separately with correction factors k_i . Combining these expressions multiplicatively, as shown in Eq. (11), will yield a corrected factor f_{corr} . If each k_i is a somewhat manageable functional expression with sufficiently similar results to FEA, this method will provide a valuable alternative evaluation, but within a much shorter time.

$$f_{corr} = f_{new} \prod_i k_i \tag{11}$$

In the upcoming sections, a closer look at the change in load application and the specimen's deflection will be taken and functional expressions to describe their influence on the factor f will be provided.

4.1. Contact at the loading ball

As mentioned in the previous section, an increase in load establishes a finite area of contact between the loading ball and the specimen. This causes a change in load introduction from the ideal punctiform load to a distributed load over a circular contact area at the center of the specimen. The size of this area will be quantified by its radius, which will be referred to as the contact radius R_c . In principle, an increase in contact radius reduces the bending moment and with it the stress applied on the specimen. This change in stress has been investigated by FEA with Model 1B described in Section 2.1.1. Instead of a punctiform load, a Hertzian pressure distribution for the contact between a sphere and a flat surface has been applied. With this model, a parametric study of approximately 6000 simulations on the influence of the contact radius R_c on the maximum stress (i.e. the factor f) has been conducted. More specifically, the contact radius R_c was varied for a wide range of specimen geometries, such as the specimen's thickness t , the specimen's radius R and the support radius R_s . Additionally, the influence of the applied load P , the specimen's Young's modulus E and Poisson's ration ν was investigated as well. In conclusion, only the contact radius, specimen's thickness and support radius have a distinct influence on the maximum stress. The other parameters mentioned have an influence on the contact radius, but

Table 3
Constants h_1 - h_5 utilized in Eq. (12).

h_1	h_2	h_3	h_4	h_5
1.0052	0.00063	-0.5928	1.6756	1.3523

Table 4
Accuracy parameters describing the deviation of Eq. (12) and Eq. (15) to their respective fitted data fields.

Accuracy parameter	k_1	$s_{red} (k_2)$
Maximum residual error [%]	+ 1.0	+ 6.4
Minimum residual error [%]	-0.50	-13
Mean residual error [%]	0.16	3.7

not on the maximum stress directly. This allowed to reduce the number of relevant parameters to just three. By using dimensionless relative parameters, e.g. the relative contact radius R_c/R_s and relative thickness t/R_s , the number of parameters could be further reduced to two. Based on these findings, a reduced data field with 525 data points to describe the change in maximum stress, i.e. the factor f , was generated. The influence of these two parameters on f is shown in Fig. 6.

By fitting this data field, a functional expression for the change of f due to the change in contact area can be provided. The correction k_1 can be given as

$$k_1(a/R_s, t/R_s, \nu, E, E_{LB}, \nu_{LB}, P) = h_1 + h_2 \ln(R_c/R_s \cdot t/R_s) + h_3 \frac{(R_c/R_s)^{h_4}}{(t/R_s)^{h_5}} \tag{12}$$

where

$$R_c = \sqrt[3]{\frac{3PR_{LB}}{4} \left(\frac{1-\nu^2}{E} + \frac{1-\nu_{LB}^2}{E_{LB}} \right)} \tag{13}$$

with R_c describing the contact radius based on the Hertzian solution. E_{LB} and ν_{LB} are the Young's modulus and Poisson's ratio of the loading ball, respectively. R_{LB} denotes the radius of the loading ball. The fitting constants h_1 - h_5 are listed in Table 3. An overview of the deviation of Eq. (12) to the fitted data can be found in Table 4.

4.2. Deflection of the specimen

A different problem is raised through the interaction of the specimen and the support balls. With increasing specimen deflection, the point of contact progressively shifts inwards. This reduces the applied bending moment due to decreasing leverage. Since the bending moment is directly proportional to the maximum stress and therefore the factor f , a functional expression for the change in bending moment is equal to the searched correction k_2 . This effect is especially pronounced when materials with high strength (> 1000 MPa) and low Young's modulus (< 100 GPa), such as high-strength glass, are tested. In order to predict the extent of this effect, the change in leverage, i.e. the shift in contact position at the support balls, has to be known. By considering the geometry of the problem, trigonometry can be utilized to express the shift in contact x_{shift} from the slope s_{con} of the specimen with

$$x_{shift} = R_{SB} \sin \arctan s_{con}, \tag{14}$$

where R_{SB} is the radius of the support ball. A schematic of the geometric relations is shown in Fig. 7.

Therefore, the problem can be reduced to the determination of the slope of the specimen's deflection curve at the point of contact. Ideally, this information can be directly deduced from an analytical expression. Favorably, Kirstein et al. [33] derived an analytical description for the deflection of point-loaded plates on an arbitrary number of equally spaced point supports, as explained in Section 2.2. If we differentiate a

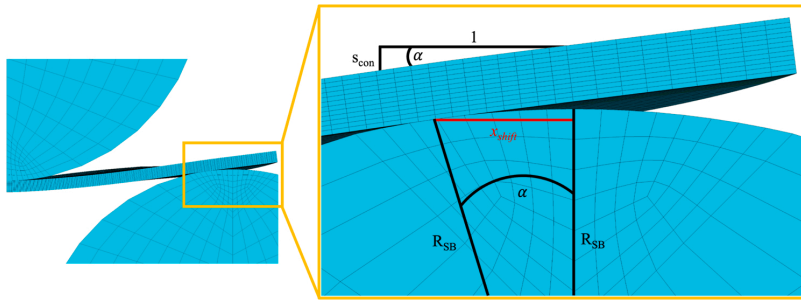


Fig. 7. Geometric relations for the contact point shift between the specimen and the support ball.

function describing the deflection of a specimen, a function describing its slope is obtained. However, due to its complexity, this cannot be done analytically for the solution by Kirstein et al. Therefore, a numerical approach had to be employed. First, the number of variables for the numerical evaluation had to be reduced. This was done by factoring out P/Et^2 , which leaves a reduced function for the deflection that is independent of the applied load and the specimen's Young's modulus. Therefore, the variables had been narrowed down to R , R_s , ν and t . By forming dimensionless relative parameters, i.e. the relative radius R/R_s and relative thickness t/R_s , the number of parameters could be further reduced to three. A parametric study on those three parameters for the reduced slope at the point of support was conducted and a data field comprising 1330 data points was generated. By fitting, an approximation for the analytical derivation of the equation by Kirstein et al. at this position can be given. The fit for the reduced slope s_{red} can therefore be expressed as

$$s_{red} = (1 - \nu^2) \frac{R/R_s}{t/R_s} \left(0.0015 - 1.13 \frac{1}{(R/R_s)^2} \right). \quad (15)$$

A summary of the deviation of Eq. (15) to the fitted data can be found in Table 4. The high relative deviation stems from the deviation for low absolute values of the reduced slope. Here, a small deviation in absolute value causes a large relative deviation due to the reference value being very small. This large error would therefore only come into play when very small deflections are involved, a case where an application of this fit or correction is neither necessary nor recommended. Combining the reduced slope with the load- and material-specific term previously factored out yields the actual slope s_{con} at the contact point between the specimen and the support ball

$$s_{con} = \frac{P}{Et^2} \left[(1 - \nu^2) \frac{R/R_s}{t/R_s} \left(0.0015 - 1.13 \frac{1}{(R/R_s)^2} \right) \right] \quad (16)$$

with the variables as denoted in previous equations. Since the slope at the point of contact is now known, Eq. (14) can be utilized to predict the shift in contact position x_{shift} with

$$x_{shift} = R_{SB} \sin \arctan \frac{P}{Et^2} \left[(1 - \nu^2) \frac{R/R_s}{t/R_s} \left(0.0015 - 1.13 \frac{1}{(R/R_s)^2} \right) \right] \quad (17)$$

Due to the small value of the argument of the trigonometric functions, s_{con} , a small angle approximation ($\sin \arctan x \approx x$) can be performed. This then gives

$$x_{shift} = R_{SB} \frac{P}{Et^2} \left[(1 - \nu^2) \frac{R/R_s}{t/R_s} \left(0.0015 - 1.13 \frac{1}{(R/R_s)^2} \right) \right] \quad (18)$$

for x_{shift} . In order to predict the change in bending moment, the relative change in leverage has to be calculated. This is done by subtracting x_{shift} from the original lever arm, i.e. the support radius R_s , and then dividing

the result by R_s . Since the slope determined with Eq. (16) is negative, x_{shift} is negative as well and has to be added to R_s instead in order to correctly portray the change in leverage. This then yields

$$k_2 = \frac{R_s + x_{shift}}{R_s} \quad (19)$$

for the change in bending moment k_2 . Inserting Eq. (17) into Eq. (19), utilizing the relationship from Eq. (6) and simplifying the resulting expression gives

$$k_2 = 1 + \frac{\sqrt{3}}{2} \frac{P}{Et^2} \left[(1 - \nu^2) \frac{R/R_s}{t/R_s} \left(0.0015 - 1.13 \frac{1}{(R/R_s)^2} \right) \right] \quad (20)$$

4.3. Friction & plastic deformation of the loading ball

The influence of friction and plastic deformation has been investigated through FEA with a model employing contact calculations. It was found that friction between the specimen and the loading ball starts to play an increasingly important role if the specimens are thin. For thin and highly flexible specimens, i.e. $t/R_s = 0.05$ and $E = 70$ GPa, a reduction in the maximum tensile stress of about 4% from the frictionless case to the same setup with $\mu = 0.5$ has been observed. This is due to the shear stresses caused by friction starting to affect the stress at the opposing face, resulting in a reduction of maximum tensile stress. For thicker and less flexible specimens, this effect is in the range of about 1–2%. As will be explained in the upcoming sections, thin and flexible specimens are difficult to describe with the models established in this work and will have to be treated separately. Since this effect is only significant for a small portion of possible specimen geometries, while having only a minor influence on the remaining ones, no functional expression for the influence of friction will be provided. Additionally, friction between the support balls and the specimen is not present if the balls are allowed to rotate freely [25].

Another possible source of error is plastic deformation of the loading ball. The expected effect would be similar to what has been covered in Section 4.1. A FE study using an ideal bilinear elastic-plastic material model for the loading ball [35], solely for the influence of plastic deformation on the contact situation, was conducted. It revealed a nearly linear relation between the increase in load and the increase in contact radius compared to the pure elastic case. If the material properties of the balls are known, this additional increase can be determined and added to the elastic deformation. This would provide a new contact radius R_c' for the usage in k_1 and no further changes to the calculation of the maximum tensile stress would have to be made.

4.4. The load-corrected stress evaluation

Combining the correction factors k_1 and k_2 with f_{new} ultimately yields the corrected factor f_{corr}

Table 5
Material parameters for "typical" specimens.

Specimen material	R/R_s [-]	E [GPa]	ν [-]
Glass	1.2	70	0.22
Zirconia		210	0.25
Alumina		420	0.2

$$f_{corr} \left(\frac{t}{R_s}, \frac{R}{R_s}, \nu, E, \nu_{LB}, E_{LB}, P \right) = f_{new} k_1 k_2 \quad (21)$$

which now takes additional load- and material-dependent effects into account. The following sections will provide an overview of the performance and accuracy of this functional expression for f_{corr} .

5. Validation and Comparison of f_{corr}

Before the comparison of f_{corr} to FEA results obtained with Model 3, some aspects of the behavior of the correction factors k_1 and k_2 have to be discussed. First, thin specimens exhibit the highest relative deflections and with it the strongest curvature. This especially affects the size of the zone of contact between the loading ball and the specimen, where the curvature is most pronounced. As discussed in Section 4.1, the size of the contact area has a strong effect on the maximum stress. However, the correction factor k_1 is based on the assumption of Hertzian contact between a sphere and a flat surface. This suggests a smaller area of contact compared to contact between a sphere and a concave surface. Therefore, k_1 underestimates the effect of contact for large deflections. Second, the geometric assumptions necessary for the equation given by Kirstein et al. [33] lose their validity for large deflections. Due to the correction factor k_2 being deducted from this equation, an error for

exceptionally thin specimens is expected. A comparison of the slope at the point of contact as obtained with FEA and the prediction by Eq. (1) for thin specimens with large deflections shows an overestimation by the analytical solution. Additionally, Kirstein et al. assume punctiform load introduction, while an extended load introduction is closer to real testing situations. This reduces the applied bending moment and with it the deflection, which is another reason for the overestimation of the slope at the point of contact. Therefore, the correction factor k_2 generally overestimates the effect of deflection for exceptionally thin specimens.

Model 3 mentioned in Section 2.1.3 was utilized as a base of comparison and a tool for the validation of Eq. (21). More specifically, the load dependency of the factor f was determined with both methods for a range of parameters. On one hand, this range includes "typical" specimens and testing setups, as one would encounter on a regular basis. On the other hand, the edge-cases of possible parameter combinations were also examined to work out the limits of Eq. (21)'s applicability. All comparisons in this chapter are based on a testing setup that utilizes steel balls with a Young's Modulus of 210 GPa and a Poisson's ratio of 0.33. For typical specimens, a relative radius R/R_s of 1.2 and a range of relative thicknesses t/R_s from 0.05 to 0.4 were chosen. The material-specific parameters are listed in Table 5. Fig. 8a-c) depict the change in f in dependence of the applied load P , predicted by both FEA and Eq. (21). The corresponding maximum stress for each curve is approximately 2 GPa. Except for specimens with a relative thickness of 0.05, exceptional agreement between the two methods is achieved. The maximum relative error for specimens with $t/R_s \geq 0.1$ is less than 1%. It should be noted that FEA was conducted with non-linear geometric behavior considered, which is represented accurately by the functional expressions.

Eight edge-cases were investigated to cover extreme specimen

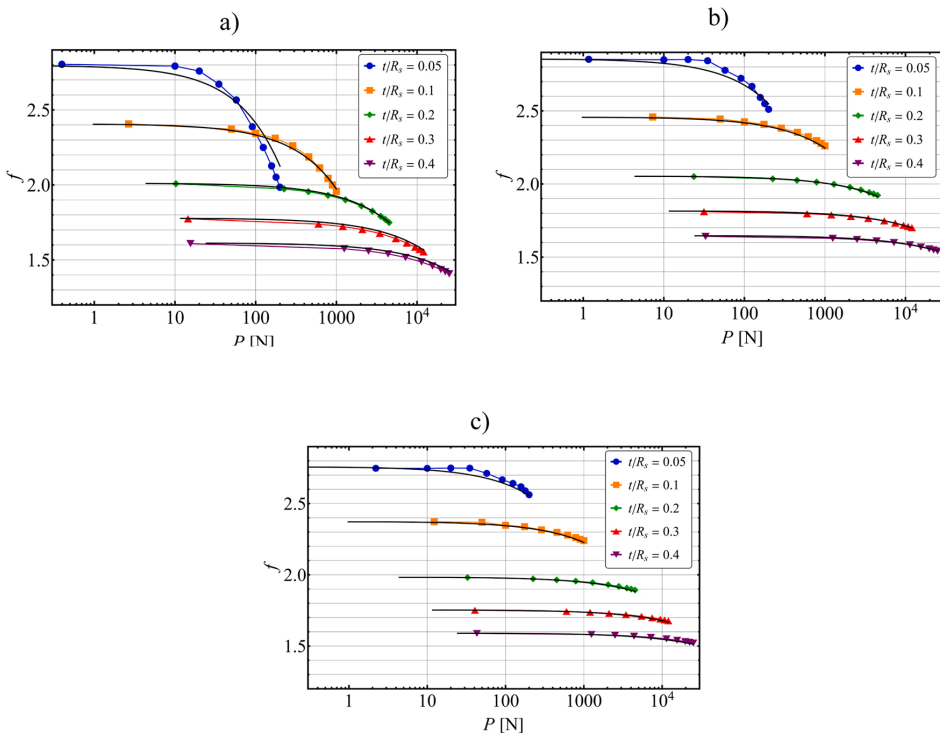


Fig. 8. Dependence of f on the applied load P as predicted by FEA and by Eq. (21). The colored markers represent the results of FEA, the continuous black line represents f_{corr} Eq. (21). The maximum tensile stress for each curve is approximately 2 GPa. The results for glass are shown in a), zirconia in b) and alumina in c).

Table 6
Geometry and material parameters as well as the maximum relative deviation from f_{corr} to FEA for a number of investigated edge cases.

Designation	R/R_s [-]	E [GPa]	ν [-]	Max. dev.
Case 1	1.05	70	0.1	< 2%
Case 2			0.4	< 2%
Case 3			0.1	2%
Case 4			0.4	< 2%
Case 5	1.525	70	0.1	6%
Case 6			0.4	< 2%
Case 7			0.1	< 2%
Case 8			0.4	< 2%

Table 7
Parameter range for the accurate application of Eq. (21).

t/R_s [-]	R/R_s [-]	E [GPa]	ν [-]	σ_{max} [MPa]
0.1 – 0.5	1.05 – 1.525	70–420	0.1 – 0.4	≤ 2000

Note that for the special case of specimens similar to case 5, i.e. highly flexible specimens ($E \leq 100$ GPa) with a high strength ($\sigma_F \geq 1$ GPa) and a Poisson's ratio in the range of 0.1–0.15, deviations of up to 6% are expected.

geometries and extreme material properties. As before, the relative thickness was varied, but now in the range from 0.05 to 0.5. Two main cases were differentiated: An exceptionally small relative radius of 1.05 (i.e. a small overhang) and large relative radius of 1.525 (i.e. large overhang). Within each case, 4 combinations of material parameters were evaluated. The specific parameters are listed in Table 6. Fig. 1 of the supplementary material depicts the results for cases 1–4, while Fig. 2 of the supplementary material depicts the results for cases 5–8. Again, specimens with a relative thickness of 0.05 exhibit the highest deviation, with the exception of case 2 and 8, and will not be included in the following observations. For cases 1–4, i.e. specimens with very low relative radius, an overall good agreement is observed. The highest deviation is displayed in case 3 by the specimen with a relative thickness of 0.1. However, the maximum deviation for this specific combination of parameters is about 2%, which is well within the desired accuracy. For cases 5–8, i.e. specimens with a very high relative radius, a similar situation is found. Cases 6–8 exhibit good agreement, only the specimen with a relative thickness of 0.1 in case 7 displays a deviation of about 1.6%. Case 5 however indicates a problem for highly flexible specimens with a low Poisson's ratio. Here, even the thickest specimen exhibits a constant deviation of about 4%. The specimen with a relative thickness of 0.1 exhibits an error of up to 5.9%, albeit only for a maximum stress of more than 1 GPa.

As discussed in the beginning of this chapter, both corrections either underestimate (k_1) or overestimate (k_2) their respective influences with increasing load. Due to the factors k_1 and k_2 being utilized in multiplicative combination, these errors cancel each other out and an accurate description can evidently be achieved for most specimens. However, they cannot sufficiently describe specimens with a relative thickness < 0.01 . Considering these aspects, the range of parameters for the application for f_{corr} , i.e. Eq. (21), is given in Table 7. Since f_{corr} has been compared to FEA only up to a maximum tensile stress of 2 GPa, the authors do not recommend application for specimens with a higher strength. Within the given range, Eq. (21) replaces individual FEA with an error typically $\leq \pm 2\%$.

6. Practical aspects

The test set-up of the B3B-test was originally designed using three contacting balls to provide the support of the specimen on a perfect circle and a ball of similar size as loading ball, as depicted in [25,30]. Due to the ability of the support balls to rotate at their position during

Table 8
Summary of the valid parameter ranges for the functional expressions of f .

	t/R_s	R/R_s or L/R_s	E [GPa]	ν	σ_{max} [MPa]
f_{new}	0.1 – 0.6	1.05 – 2	–	0.1 – 0.4	material specific, Eq. 23
$f_{new, square}$	0.1–0.6	2.17 - 3.9	–	0.1 – 0.4	material specific, Eq. 23
f_{corr}	0.1 – 0.5	1.05– 1.525	70–420	0.1 – 0.4	≤ 2000

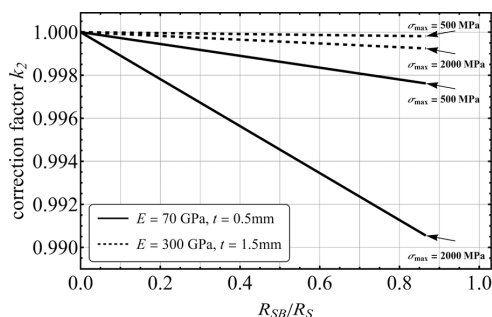


Fig. 9. Correction factor k_2 for exemplary specimens ($R = 6$ mm, $R_s = 5$ mm) in dependence of the radius of the support balls (in fractions of the support radius). Through lines represent thin, flexible (glass) specimens ($t = 0.5$ mm, $E = 70$ GPa), dashed lines represent thicker, more typical ceramic specimens ($t = 1.5$ mm, $E = 300$ GPa). Two cases are shown: $\sigma_{max} = 500$ MPa and $\sigma_{max} = 2000$ MPa.

the test, friction can be minimized, and an important source of error can be eliminated [25]. Furthermore, this set-up facilitates jig-designs with exceptionally easy handling. Preferably, ball bearing grade steel balls are used, since they are easy to obtain and available in a fine grading of radii over a wide range of sizes. The separate description of the influences of two important issues of the B3B test – the contact situation through k_1 and the deflection effects through k_2 - paves the way to an analysis of some practical aspects of the test. In the following sections, these aspects will be discussed within the validity range of Eq. (21), as given in Table 8, for exemplary specimens with radius of $R = 6$ mm on a support radius of $R_s = 5$ mm. The ideal ball radius for this set-up is $R_{SBi} = R_{LBi} = 4.33$ mm.

6.1. Support ball size

In Section 4.2 and in Eqs. (17) and (19), the influence of the specimen's deflection on the maximum stress in the specimen is described and quantified. It is obvious that this effect is more pronounced if the specimen is supported on large balls. The influence of the shift of contact on the maximum stress can be reduced if smaller than ideal support balls are used. For any test geometry, the correction factor k_2 depends linearly on the ratio of the support ball radius over support radius, R_{SB}/R_s . For $R_{SB}/R_s = 0$, $k_2 = 1$, for larger ratios $k_2 < 1$. This trend is illustrated in Fig. 9 for thin specimens with a Young's modulus of $E = 70$ GPa and more typical, thicker specimens with $E = 300$ GPa at two failure stresses. It can be seen that the effect of using smaller support balls is very small unless very flexible materials with extremely high strength are tested. Using smaller balls will also require a new design of the test fixture, which will certainly be more complicated than the one suggested earlier [25,30], especially regarding the exact positioning of the support balls and their ability to rotate.

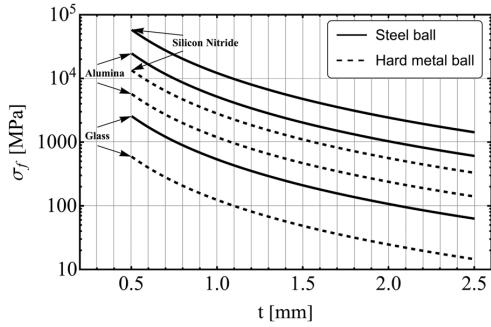


Fig. 10. Strength-thickness map for B3B-tests on exemplary specimens ($R = 6$ mm, $R_s = 5$ mm) of glass, alumina, and silicon nitride. If the measured strength of a specimen with a given thickness t is below its respective line, no contact cracks are expected. The through lines refer to loading with a steel loading ball with the ideal radius $R_{LBi} = 4.33$ mm, the dashed lines refer to loading with hard-metal ball with $R_{LB} = 1$ mm.

6.2. Contact of the specimen with the loading ball

The ideal loading situation in the B3B-test is a punctiform load introduction. Of course, this cannot be achieved using a ball to apply the load. It has been shown in Section 4.1 how an increase in the size of the area of load introduction influences the maximum stress. In practice, the desirable situation of keeping the size of this area as small as possible is favored by two means: by using a loading ball with a higher Young's modulus (see Eq. (13)) or by using a smaller loading ball (i.e. smaller than the ideal size which is equal to the contacting support balls). Eqs. (12) and (13) can be employed to evaluate the influence of using a hard metal loading ball of ideal size with a Young's modulus of $E_{LB} = 600$ GPa instead of steel balls. This only has a negligible influence of less than 1% on the correction factor k_I . The effect of using a smaller loading ball is slightly more pronounced, with deviations up to 3% for very small balls. These numbers were obtained for the condition of a maximum tensile stress of 2000 MPa in the specimens. The effect will be even smaller at lower stresses.

Moreover, any contact of a ball with a surface, as at the site of load introduction in the B3B-test, bears the risk of the formation of contact cracks if a certain critical load P_c is exceeded [36]. Upon increase of the load beyond this critical value such cracks may grow, penetrate the thickness of the specimens and lead to failure [37]. This is an unwanted situation that can be avoided if the load at fracture due to bending, P_f , is less than the critical load P_c for the formation of contact cracks, i.e. $P_f < P_c$.

For common ball sizes used in the B3B test, this situation can be analyzed by using Auerbach's law for the contact between a flat surface and a ball. According to Auerbach's observations [38], the load required to produce contact cracks P_c is proportional to the radius of the loading ball: $P_c = A \cdot R_{LB}$. The constant A (Auerbach constant) has been related to the elastic constants of the involved materials and the surface energy γ of the cracked material [39,40], and has further been determined experimentally for various material (i.e. specimen and ball) combinations [41–45]:

$$P_c = \frac{3\pi^3}{16} \phi_a \left(\frac{1-\nu^2}{E} + \frac{1-\nu_{LB}^2}{E_{LB}} \right) \frac{2\gamma}{(1-\nu^2)} E_{LB} R_{LB} \quad (22)$$

Eq. (22) or experimental values for A can be used to plot curves of $\sigma(P_c)$, using Eq. (7), for a given specimen geometry as a function of the specimen's thickness t . Such curves can be used to find limiting conditions for contact cracking during B3B-tests. An example for such curves for the exemplary specimen is given in Fig. 10 for various specimen materials (glass, alumina, silicon nitride) and a steel loading ball of ideal

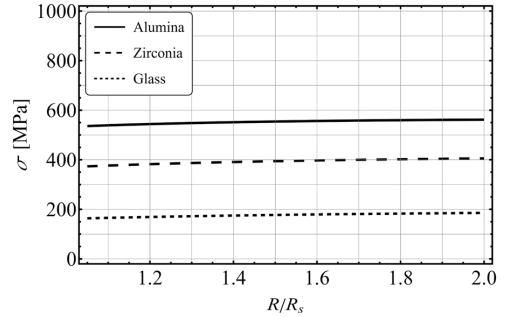


Fig. 11. 2%-Limit for selected specimens with varying Young's modulus in dependence of R/R_s .

size R_{LBi} . If the expected strength of the specimen is below the line at a given thickness, no contact cracks should be generated during the B3B-test. For glass, $A = 62$ N/mm was taken from [41], for alumina, $A = 590$ N/mm from [42] and for silicon nitride, a value of $A = 1360$ N/mm using materials properties given in [46], Eq. (22) $\phi_a = 0.0011$ [39] and the relation $K_{lc}^2 = 2\gamma E / (1 - \nu^2)$ was used. Additionally, Fig. 10 depicts the same limit curves for a loading ball made from hard-metal and with a radius $R_{LB} = 1$ mm.

It is obvious from Eq. (22) how the size and Young's modulus of the loading ball influence the limit curve: the smaller R_{LB} , the smaller is P_c and the higher E_{LB} , the smaller is A . Both trends shift the limit curve towards lower strength values. These findings discourage the use of smaller or stiffer loading balls. However, the use of balls with R_{LBi} and a high Young's modulus may be indicated for cases where high fracture loads prevail, and plastic deformation of the loading ball is an issue.

Several simplifications have been made for the construction of Fig. 10. The data for A are related to the contact between a ball and a thick, flat specimen that does not deform globally. In the case of the B3B-test, the contacted surface is concave and under a general compressive equi-biaxial stress. The curvature will increase the contact area in comparisons to the flat surface case and thus decrease the overall magnitude of the contact stress field. The overall compressive equi-biaxial stress state at the loaded surface of the specimen additionally hinders contact cracking, since tensile stresses are relevant for this phenomenon. The limit curves in the presented map can therefore be regarded as conservative estimates.

6.3. Domains of application

As is evident from the plots in Fig. 6, the factor f does not deviate a lot from f_{new} , i.e. the values of f on the ordinate axis, for certain conditions. These conditions are given by the specimen geometry (relative thickness and relative radius), its elastic properties and the applied load. Even though f_{corr} gives the more accurate result for f , it is not necessary to use this lengthy expression in all cases. In order to determine which expression to use, the impact of the correction factors k_1 and k_2 has been investigated for all valid parameter combinations. A combined correction of k_1 and k_2 of 2% has been set as the limit for the application of f_{new} . This means that if $f_{corr}/f_{new} < 0.98$, f_{new} does not sufficiently describe f anymore and f_{corr} has to be utilized instead. For the following graphs and statements, a testing fixture utilizing steel balls with a Young's modulus of 210 GPa and a Poisson's ratio of $\nu = 0.33$ is assumed. This then reduces the possible parameters to R/R_s , t/R_s , E and ν of the specimen as well as the applied load P . To display the limits in a way that is not dependent on the absolute geometry of the specimen, the applied load will be expressed by the maximum applied stress σ (or the measured strength) instead. Fig. 11 depicts the 2%-limit in dependence of R/R_s for exemplary specimens made from glass, zirconia, and alumina with t/R_s

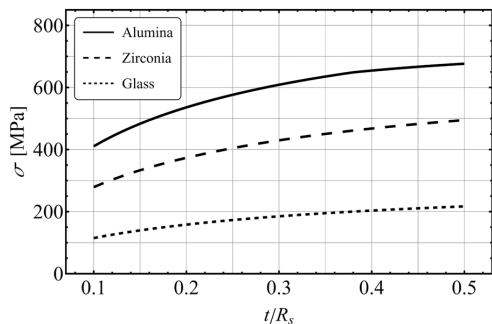


Fig. 12. 2%-Limit for selected specimens with various Young's moduli and Poisson's ratios in dependence of t/R_s .

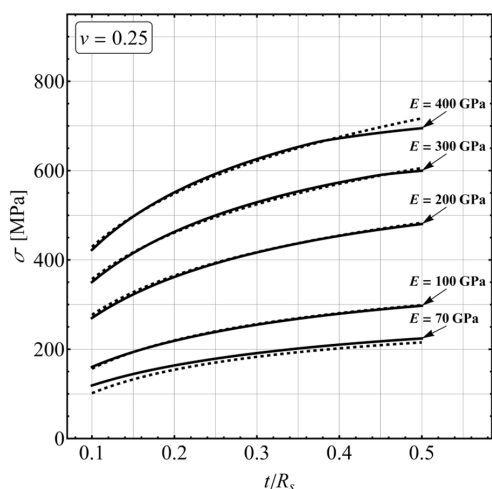


Fig. 13. Comparison of the 2% limit, expressed by the functional expression (dashed), and the curves derived by f_{corr} , for $\nu = 0.25$.

$= 0.2$. The lines in this Figure display the maximum stress that can be applied to the material before the deviation between f_{corr} and f_{new} is $\geq 2\%$. Therefore, if a specimen exhibits a strength below this line, the simplified evaluation, i.e. Eq. (9), can be utilized. If the strength is higher, then Eq. (21) has to be utilized to accurately determine f .

Fig. 11 shows that R/R_s does not strongly influence the limit. This was found to be true for all other possible configurations of t/R_s , E and ν . Therefore, the following graphs will depict the limits only in dependence of t/R_s , E and ν . Fig. 12 displays the application limits for typical materials such as glass, zirconia, and alumina.

In order to ensure that the parameter R/R_s can safely be omitted, each datapoint for a specific configuration (t/R_s , E , ν) actually represents the lowest value of all R/R_s in its valid range of 1.05–2 for that configuration. This means that the limits shown always assume the worst case in terms of R/R_s , so that no matter what value of R/R_s the tested specimen exhibits, the limit shown might actually be lower than 2%, but never higher. Fig. 3(a)–c) of the supplementary material display the limits for more cases, including the special cases discussed in Section 5. An alternative route to convey these limits in a more general form is by providing a functional expression. By setting the Poisson's ratio of the

specimen to a fixed and common value, one function can describe a very broad range of materials and geometries. This has been done for $\nu = 0.25$, which gives

$$\sigma_{lim} \leq -347 - 497\sqrt{t/R_s} - 0.062\sqrt{E} + 68^4\sqrt{E \cdot t/R_s} \tag{23}$$

to describe the limiting strength σ_{Flim} (in MPa) for the application of f_{new} in dependence of t/R_s and E (in MPa). An overview of the accuracy of this expression is shown in Fig. 13. Again, R/R_s was chosen in a way so that it represents the worst-case scenario. Regarding the Poisson's ratio, $\nu = 0.25$ was chosen since it represents a value close to that of many technical ceramics [31]. A change to a higher Poisson's ratio would shift the curves slightly upwards, while lowering the Poisson's ratio would shift them slightly downwards.

Eq. (23) provides a convenient tool to decide which factor, f_{new} (for $\sigma_F < \sigma_{lim}$) or f_{corr} (for $\sigma_F > \sigma_{lim}$), has to be used to obtain the most accurate result for σ_{max} for a given test geometry or which test geometry is suitable to allow for the use of the simple expression of f_{new} , Eq. (7).

Overall, 3 regimes for the evaluation of f can be defined. If the strength of the material is below the limits displayed in Fig. 13, then the simple functional expression f_{new} (Eq. (9)) can be utilized. If the strength of the material is higher, than the more complex functional expression f_{corr} (Eq. (21)) has to be used. Finally, if the geometry- or material parameters of a specimen are not covered by the given range for f_{new} or f_{corr} , as summarized in Table 8, then individual FEA has to be conducted to determine f . Note that this work has been performed for linear elastic isotropic materials. If the tested specimen exhibits anisotropic behavior or material nonlinearities (such as plastic deformation of the specimen), then neither f_{new} nor f_{corr} should be applied. Again, this would then be a typical case where individual FEA has to be performed.

7. Summary

- 1) A simplified model of the B3B-test has been utilized to analyze the factor f for a wide range of geometric and material parameters and a new fitted function f_{new} , for the evaluation of the B3B-test is presented.
- 2) A conversion from square plate specimens to discs with an equivalent diameter D_{eff} for the calculation of f is given. This allows stress evaluation for square plates with the new fitted function f_{new} from 1).
- 3) The influence of the applied load on the factor f was investigated. Two major effects have been considered separately. First, the increase of contact area between the loading ball and the specimen due to high loads and elastic deformation was investigated. Second, the shift in contact position between the specimen and the support balls due to deflection of the specimen was examined. For each effect, a correction factor that describes the deviation in f is presented.
- 4) By utilizing these corrections, a range of geometries and material properties can be defined, for which the ideal punctiform solution f_{new} gives an error $< 2\%$ for the calculated maximum stress. Within this range, the simplified evaluation from 1) is sufficient.
- 5) Cases, which are not included in 4) can be accurately represented by taking the corrections from 3) into account and using $f_{corr} = f_{new}k_1k_2$. Such, the load-dependence of f is given for most practical specimens with strengths up to 2 GPa.
- 6) Cases, which are not included in 5), have been identified. For these cases, the authors recommend referring to individual solutions by Finite-Element-Analysis.
- 7) Using the correction factors, the effect of modifications of the suggested test set-up were discussed. It was shown that the use of small support or loading balls or balls with a high Young's modulus has very limited beneficial effects while making the test less practicable. A simple estimation was proposed that showed that contact cracking

at the loading ball can be avoided by using sufficiently thin specimens.

Declaration of Competing Interest

The authors declare that they have no known competing financial interests or personal relationships that could have appeared to influence the work reported in this paper.

Acknowledgements

M. Staudacher gratefully acknowledges financial support by the Austrian BMVIT and BMWFW in the project "CharAM" (FFG 877684) of the COIN/IraSME program.

Appendix A. – Mesh convergence analysis

In order to obtain the optimum number of elements and mesh configuration for each model, a mesh convergence analysis has been performed. Fig. A1a) shows the absolute factor f for Model 1 in dependence of the total number of elements for three different thicknesses. Fig. A1b) shows the factor f normalized to the value obtained with the highest number of elements. The black markers indicate the mesh utilized in this work.

Since the results of the mesh configuration utilized in this work only display a maximum relative error of 0.5% to the result obtained by approximately tripling the number of elements, it was deemed sufficiently accurate. Model 2 utilizes a similar mesh-density in the central region of maximum stress and is loaded in the same way, hence why no additional mesh convergence analysis was performed for this model.

Due to the different type of loading, the analysis has also been performed for Model 3. As before, Fig. A2a) shows the absolute factor f for three different thicknesses, while Fig. A2b) shows the normalized factor f .

As before, the factor f calculated with the mesh utilized in this work shows a maximum relative error of about 0.6% to the factor f calculated with a model with double the number of elements. For this model, special care was taken to primarily increase the number of elements in the contacting regions of both the balls and the specimen as well as the central tensile loaded regions of the specimen. Due to the iterative nature of the contact analysis, larger deviations between different mesh densities are expected. As soon as the relevant abort criteria are met, the solver is stopped. Since the amount and step size of these iterations changes for each mesh density, final solutions may be just below the abort criteria or well below it. This allows changes of f in both directions, as observed for the thickest specimen in Fig. A2.

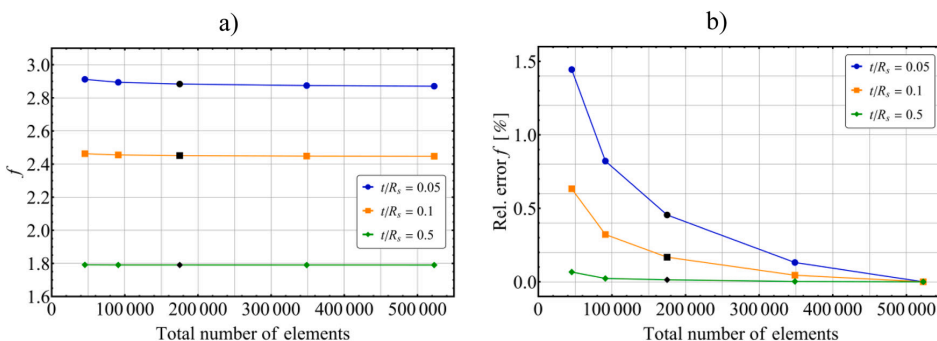


Fig. A1. Results for the factor f (a) absolute values, b) normalized values) in the mesh convergence analysis for the model from Section 2.1.1 for a specimen with $R/R_s = 1.33$, $E = 210$ GPa, $\nu = 0.25$ and varying thickness. The black markers represent the mesh configuration that was either used directly or slightly modified (in dependence of the specimen's geometry) in this work.

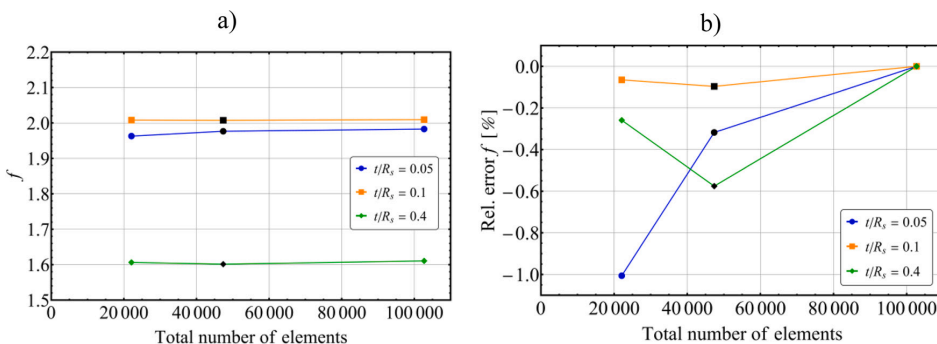


Fig. A2. Results for the factor f (a) absolute values, b) normalized values) in the mesh convergence analysis for the model from Section 2.1.3 for a specimen with $R/R_s = 1.05$, $E = 70$ GPa, $\nu = 0.25$ and varying thickness. The black markers represent the mesh configuration that was either used directly or slightly modified (in dependence of the specimen's geometry) in this work.

Appendix B. Supporting information

Supplementary data associated with this article can be found in the online version at doi:10.1016/j.jeurceramsoc.2022.09.047.

References

- [1] R. Danzer, Mechanical Performance and Lifetime Prediction, in: Encyclopedia of Advanced Ceramics, pp. 385–398.
- [2] DIN EN 843–1:2008–08: Advanced technical ceramics - Mechanical properties of monolithic ceramics at room temperature - Part 1: Determination of flexural strength; German version EN 843–1:2006, German Institute for Standardisation (Deutsches Institut für Normung), 2008.
- [3] D.C. Granmer, D.W. Richerson (Eds.), Mechanical Testing Methodology for Ceramic Design and Reliability, CRC Press, Taylor & Francis Group, Boca Raton, London, New York, 2018.
- [4] ASTM C 1499–05: Test Method for Monotonic Equibiaxial Flexural Strength of Advanced Ceramics at Ambient Temperature, ASTM International, West Conshohocken, PA, 2005.
- [5] D. Shetty, A.R. Rosenfield, P. McGuire, G.K. Bansal, W.H. Duckworth, Biaxial flexure test for ceramics, Am. Ceram. Soc. Bull. (1980) 1193–1197.
- [6] T.R. Wilshaw, Measurement of tensile strength of ceramics, J. Am. Ceram. Soc. 1968 (1968) 111–112.
- [7] D.J. Godfrey, Fabrication, formulation, mechanical properties, and oxidation of sintered Si₃N₄ ceramics using disc specimens, Mater. Sci. Technol. 1 (1985) 510–515.
- [8] R.J. Roark. Roark's Formulas for Stress and Strain, 8th ed., McGraw-Hill, New York, 2012.
- [9] A.F. Kirstein, R.M. Woolley, Symmetrical bending of thin circular elastic plates on equally spaced point supports, Journal of Research of the National Bureau of Standards, Sect. C Eng. Instrum. 71C (1967).
- [10] J.R. Wachtmann Jr, W. Capps, J. Mandel, Biaxial flexure tests of ceramic substrates, J. Mater. (1972) 188–194.
- [11] D.J. Godfrey, S. John, Disc flexure tests for the evaluation of ceramic strength, Proceedings 2nd International Conference of Ceramic materials and Components for Engines 1986, 657–665.
- [12] T. Fett, G. Rizzi, E. Ernst, R. Müller, R. Oberacker, A 3-balls-on-3-balls strength test for ceramic disks, J. Eur. Ceram. Soc. 27 (2007) 1–12.
- [13] R. Morell, Biaxial flexural strength testing of ceramic materials: a National measurement good practice guide no. 12, Natl. Phys. Lab. (2007).
- [14] M. Staudacher, T. Lube, J. Schlacher, P. Supancic, Comparison of biaxial strength measured with the Ball-on-Three-Balls- and the Ring-on-Ring-test, Open Ceram. 6 (2021), 100101.
- [15] E. Chicardi, R. Bermejo, F.J. Gotor, L. Llanes, Y. Torres, Influence of temperature on the biaxial strength of cemented carbides with different microstructures, Int. J. Refract. Met. Hard Mater. 71 (2018) 82–91.
- [16] H.P.R. Corado, P.H.P.M. Da Silveira, V.L. Ortega, G.G. Ramos, C.N. Elias, Flexural strength of vitreous ceramics based on lithium disilicate and lithium silicate reinforced with zirconia for CAD/CAM, Int. J. Biomater. 2022 (2022) 5896511.
- [17] E. Dashjav, M. Gellert, G. Yan, D. Grüner, N. Kaiser, S. Spannenberger, I. Kraveva, R. Bermejo, M.-T. Gerhards, Q. Ma, J. Malzbender, B. Roling, F. Tietz, O. Guillon, Microstructure, ionic conductivity and mechanical properties of tape-cast Li_{1.5}Al_{0.5}Ti_{1.5}P₃O₁₂ electrolyte sheets, J. Eur. Ceram. Soc. 40 (2020) 1975–1982.
- [18] F. Fleischhauer, R. Bermejo, R. Danzer, A. Mai, T. Graule, J. Kuebler, Strength of an electrolyte supported solid oxide fuel cell, J. Power Sources 297 (2015) 158–167.
- [19] L.M. González, E. Chicardi, F.J. Gotor, R. Bermejo, L. Llanes, Y. Torres, Influence of the test configuration and temperature on the mechanical behaviour of WC-Co, Metals 10 (2020) 322.
- [20] J.P. Gross, J. Malzbender, R. Schwaiger, Strength assessment of Al₂O₃ and MgAl₂O₄ using micro- and macro-scale biaxial tests, J. Mater. Sci. 57 (2022) 7481–7490.
- [21] M. Gruber, A. Leitner, I. Kraveva, D. Kiener, P. Supancic, R. Bermejo, Understanding the effect of surface flaws on the strength distribution of brittle single crystals, J. Am. Ceram. Soc. (2018) 5705–5716.
- [22] W. Harrer, R. Danzer, P. Supancic, Influence of surface quality on the biaxial strength of silicon nitride, Prakt. Metallogr. Sonderband 42 (2010) 141–146.
- [23] M.A. Lodes, F.S. Kachold, S.M. Rosiwal, Mechanical properties of micro- and nanocrystalline diamond foils, Philosophical transactions. Series A, Mathematical, physical, and engineering sciences 373, 2015.
- [24] N. Sheth, C. Greenly, R. Bermejo, J.C. Mauro, C.G. Pantano, S.H. Kim, Effects of acid leaching treatment of soda lime silicate glass on crack initiation and fracture, J. Am. Ceram. Soc. 104 (2021) 4550–4558.
- [25] A. Börger, P. Supancic, R. Danzer, The ball on three balls test for strength testing of brittle discs: Part II: analysis of possible errors in the strength determination, J. Eur. Ceram. Soc. 24 (2004) 2917–2928.
- [26] R. Bermejo, P. Supancic, I. Kraveva, R. Morrell, R. Danzer, Strength reliability of 3D low temperature co-fired multilayer ceramics under biaxial loading, J. Eur. Ceram. Soc. 31 (2011) 745–753.
- [27] M. Gruber, I. Kraveva, P. Supancic, J. Bielen, D. Kiener, R. Bermejo, Strength distribution and fracture analyses of LiNbO₃ and LiTaO₃ single crystals under biaxial loading, J. Eur. Ceram. Soc. 37 (2017) 4397–4406.
- [28] W. Harrer, R. Danzer, P. Supancic, T. Lube, Influence of the sample size on the results of B3B-Tests, KEM 409 (2009) 176–184.
- [29] E. Özkol, A.M. Wätjen, R. Bermejo, M. Deluca, J. Ebert, R. Danzer, R. Telle, Mechanical characterisation of miniaturised direct inkjet printed 3Y-TZP specimens for microelectronic applications, J. Eur. Ceram. Soc. 30 (2010) 3145–3152.
- [30] A. Börger, P. Supancic, R. Danzer, The ball on three balls test for strength testing of brittle discs: Stress distribution in the disc, J. Eur. Ceram. Soc. 22 (2002) 1425–1436.
- [31] D. Munz, T. Fett, Ceramics: Mechanical Properties, Failure Behaviour, Materials Selection, Springer, Berlin, Heidelberg, 1999.
- [32] R. Danzer, P. Supancic, W. Harrer, Der 4-Kugerversuch zur Ermittlung der biaxialen Biegefestigkeit spröder Werkstoffe, Kriegsman, J. Hrsng Tech. Keram. Werks. (2009) 1–48.
- [33] A.F. Kirstein, W.H. Pell, R.M. Woolley, L.J. Davis, Deflection of centrally loaded thin circular elastic plates on equally spaced point supports, J. Res. Natl Bur. Std. Sect. C Eng. Instrum. 70C (1966) 227–244.
- [34] J.D.S. Ramos, S. Fraga, G.F. Vogel, L.G. May, Influence of the geometry of ceramic specimens on biaxial flexural strength: Experimental testing and finite element analysis, Cerámica 64 (2018) 120–125.
- [35] B. Scholtes (Ed.), Forschungsberichte aus dem Institut für Werkstofftechnik Metallische Werkstoffe der Universität Kassel, kassel, University Press, 2012.
- [36] H. Hertz, Ueber die Berührung fester elastischer Körper, J. für die reine und Angew. Math. 1882 (1882) 156–171.
- [37] T. Fett, E. Ernst, D. Munz, Contact strength measurements of bars under opposite sphere loading, J. Mater. Sci. Lett. 21 (2002) 1955–1957.
- [38] F. Auerbach, Absolute Härtemessung, Annalen der Physik 279 (1891) 61–100.
- [39] A.C. Fischer-Cripps, Introduction to contact mechanics, 2nd ed., Springer, New York, 2007.
- [40] P.D. Warren, Determining the fracture toughness of brittle materials by Hertzian indentation, J. Eur. Ceram. Soc. 15 (1995) 201–207.
- [41] J.P.A. Tillet, Fracture of Glass by Spherical Indenters, Proc. Phys. Soc. B 69 (1956) 47–54.
- [42] M.T. Laugier, Hertzian indentation of sintered alumina, J. Mater. Sci. 19 (1984) 254–258.
- [43] R. Mougnot, D. Maugis, Fracture indentation beneath flat and spherical punches, J. Mater. Sci. 20 (1985) 4354–4376.
- [44] S.K. Lee, S. Wuttiphon, B.R. Lawn, Role of microstructure in hertzian contact damage in silicon nitride: I. Mechanical characterization, J. Am. Ceram. Soc. 80 (1997) 2367–2381.
- [45] J. Wade, S. Ghosh, P. Claydon, H. Wu, Contact damage of silicon carbide ceramics with different grain structures measured by Hertzian and Vickers indentation, J. Eur. Ceram. Soc. 35 (2015) 1725–1736.
- [46] T. Lube, J. Dusza, A silicon nitride reference material - a testing program of ESIS TC6, J. Eur. Ceram. Soc. 27 (2007) 1203–1209.

Corrigendum to "The Ball-on-Three-Balls strength test for discs and plates: Extending and simplifying stress evaluation" [J. Eur. Ceram. Soc. 43 (2023) 648–660]

In the published article Figure 9 was represented with an incorrectly scaled axis. The corrected figure is:

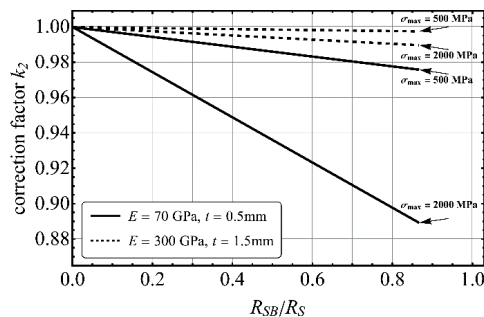


Figure 9: Correction factor k_2 for exemplary specimens ($R = 6 \text{ mm}$, $R_S = 5 \text{ mm}$, $\nu = 0.25$) in dependence of the radius of the support balls (in fractions of the support radius). Through lines represent thin, flexible (glass) specimens ($t = 0.5 \text{ mm}$, $E = 70 \text{ GPa}$), dashed lines represent thicker, more typical ceramic specimens ($t = 1.5 \text{ mm}$, $E = 300 \text{ GPa}$). Two cases are shown: $\sigma_{\max} = 500 \text{ MPa}$ and $\sigma_{\max} = 2000 \text{ MPa}$.

Supplementary material

A) Special (extreme) cases for comparison to FEA

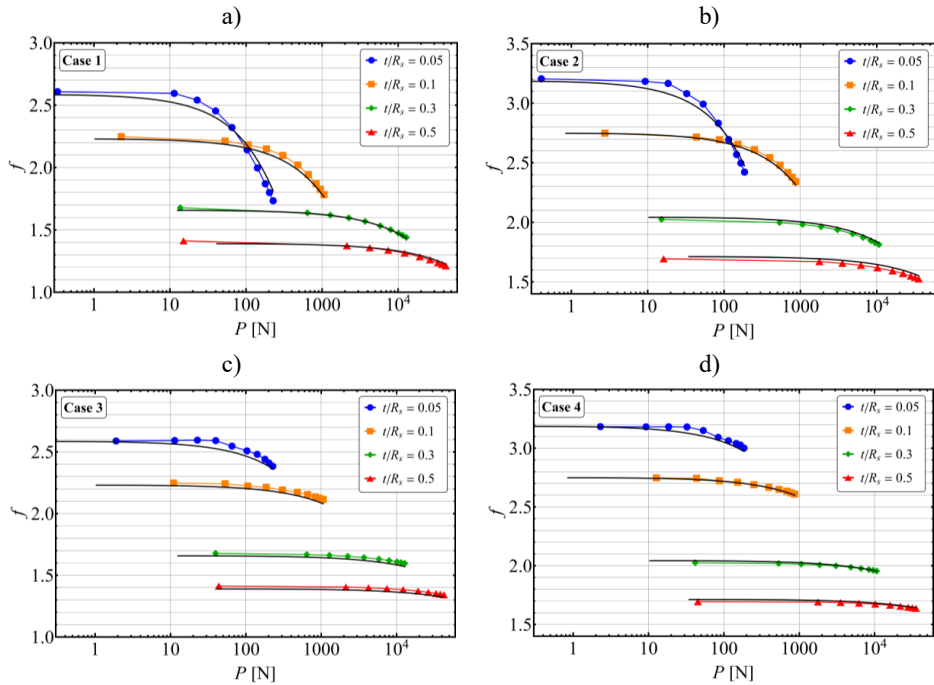
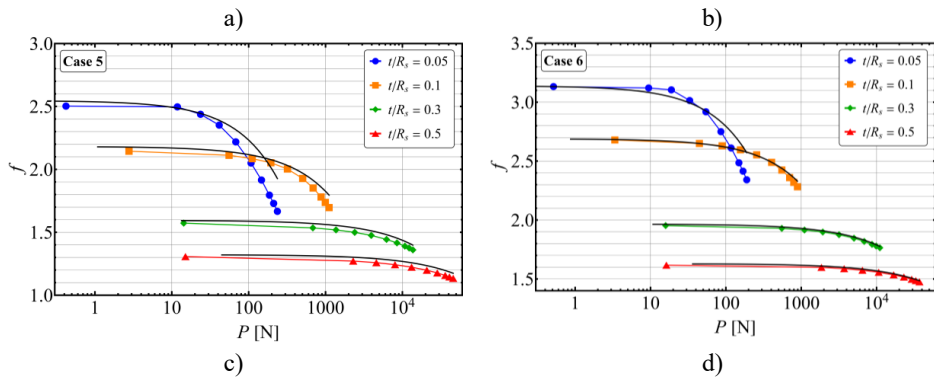


Figure 1: Dependence of f on the applied load as predicted by FEA and eq. **Fehler! Verweisquelle konnte nicht gefunden werden.** Figures a), b), c) and d) show the results of specimen 1, 2, 3 and 4, respectively.



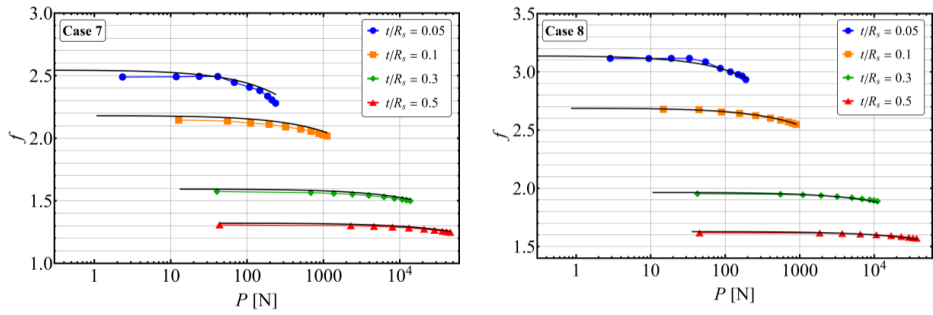
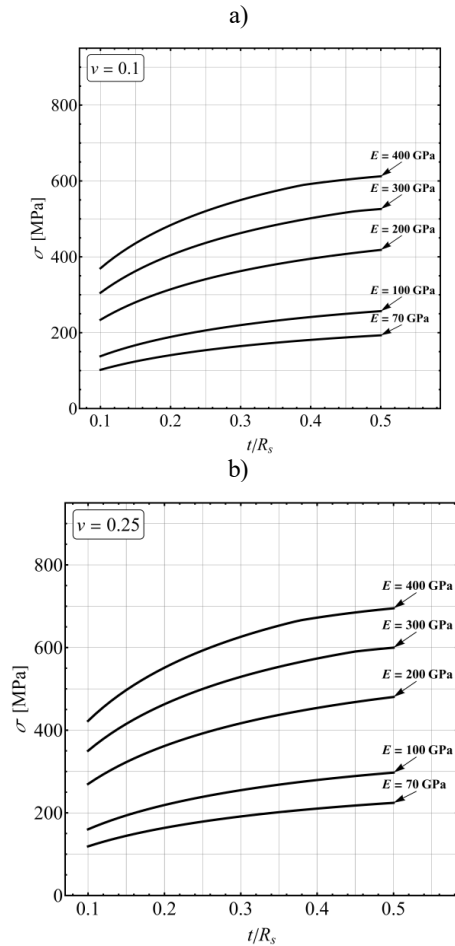


Figure 2: Dependence of f on the applied load predicted by FEA and eq. Fehler! Verweisquelle konnte nicht gefunden werden.. Figures a), b), c) and d) show the results of specimen 5, 6, 7 and 8, respectively.

B) 2% limits for f_{corr} for various materials



c)

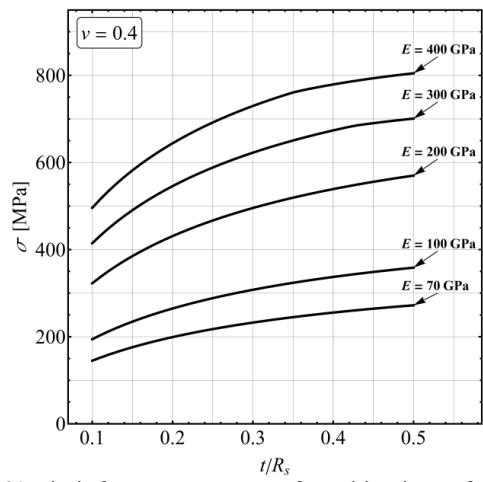


Figure 3: 2%-Limit for extreme cases of combinations of E , ν and t/R_s .

Publication C

The Ball-on-Three-Balls strength test: In-situ testing through X-ray radiography and tomography

Maximilian Staudacher¹, Gustavo Pinzon², Jérôme Adrien², Joël Lachambre², Eric Maire², Jérôme Chevalier², Tanja Lube¹

¹Department of Materials Science, Montanuniversität Leoben, Franz Josef-Strasse 18, A-8700 Leoben, Austria

²University of Lyon, INSA-Lyon, MATEIS UMR CNRS 5510, 20 Avenue Albert Einstein, Villeurbanne 69621, France

(Submitted for publication in Open Ceramics, under review)

The Ball-on-Three-Balls strength test: In-situ testing through X-ray radiography and tomography

Maximilian Staudacher¹, Gustavo Pinzón², Jérôme Adrien², Joël Lachambre², Eric Maire², Jérôme Chevalier², Tanja Lube^{1*}

¹Department of Materials Science, Montanuniversität Leoben, Franz Josef-Strasse 18, Leoben 8700, Austria

²University of Lyon, INSA-Lyon, MATEIS UMR CNRS 5510, 20 Avenue Albert Einstein, Villeurbanne 69621, France

*corresponding author, tanja.lube@unileoben.ac.at

Abstract

Over the past two decades, the Ball-on-Three-Balls-test (B3B) has been increasingly used due to its low systematic error and simple execution. A limiting factor for a more wide-spread use of the B3B-test is the lack of an accurate analytical solution. This demands the use of numerical methods, such as Finite-Element-Analysis (FEA). In a recent work, FEA has been used to assess the influence of non-linear effects on the measured strength. To validate the utilized FEA-model, the experimental measurement of the specimen's deflection can be drawn on. Due to the design of the fixture for the B3B-test, common deflection-measurement methods are not straightforward. Therefore, X-ray tomography is employed in this paper to track the displacement of the load and support balls for thin plates of a high-strength glass and Ce-doped zirconia presenting transformation-induced plasticity. Furthermore, the ball displacement is also determined from two-dimensional radiographs and shows good agreement with FEA results.

Keywords: Strength testing, Biaxial Testing, Ball-on-Three-Balls-Test, In-situ-testing, X-Ray tomography

1 Introduction

Biaxial testing is one of the cornerstones of mechanical strength testing for brittle materials such as ceramics and glasses. Some of the most well-known methods are the Ring-on-Ring-test, the Ball-on-Ring-test, the Piston-on-Three-Balls-test, or the Ball-on-Three-Balls-test [1–11]. Over the past two decades, the use of the Ball-on-Three-Balls-test (B3B) has increased due to its low systematic error and fast and simple execution. However, one of the limiting factors for a more wide-spread use of the B3B-test is the lack of an accurate analytical solution to describe the stress and deflection field (note that it has been shown that the analytical solution of other ball-loaded testing methods, e.g. the Ball-on-Ring-test, can be utilized to determine the maximum stress for the B3B-test to a very reasonable degree of accuracy [12,13]). This demands the use of numerical methods, such as Finite-Element-Analysis (FEA), to evaluate stresses and deflection.

In a recent work on the B3B-test, the influence of load dependent, non-linear effects on the measured strength was investigated [14]. Two major effects were considered and investigated qualitatively and quantitatively. On the one hand, the region of contact between the loading ball and the specimen increases with an increase in load and deflection. This causes a deviation from an ideal, punctiform load introduction (that is usually assumed for stress evaluation through FEA) towards a Hertzian surface load distribution, which changes the leverage and with it the applied bending moment. On the other hand, the specimen deflection causes a shift of the position of contact between the support balls and the specimen. With an increase in deflection, the specimen rolls off the support balls and the contact point shifts towards the specimen center, thus also changing the leverage and applied bending moment. Overall, both effects decrease the applied bending moment and the maximum tensile stress σ_{\max} . If they are not considered adequately, the strength of the investigated material will be overestimated (note that this aspect is relevant for other testing methods as well, especially if the stress evaluation is based on analytical solutions). Figure 1 displays the characteristics of this effect. The results for the normalized maximum stress are based on FEA and are given for high-strength specimens made from a flexible glass with a low Young's modulus. Especially for thin specimens, the combination of the two aforementioned effects can lead to a decrease of the normalized stress of up to 20%, i.e., the strength of the investigated material will be overestimated by 20%.

These findings, which are based on a FEA and theoretical considerations, were implemented through correction factors in the current evaluation of the maximum stress for the B3B-test. For both effects, an analytical expression was presented, which decreases the maximum tensile stress accordingly. These correction factors were validated with non-linear FEA for a wide range of specimen geometries and materials, and excellent agreement for specimens with a relative thickness (i.e. the specimen's thickness divided by the support radius) ≥ 0.1 was achieved. However, the correction factors or the non-linear FEA-model were not validated through experimental results so far.

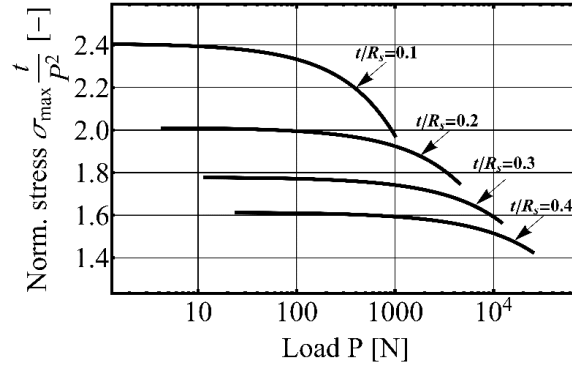


Figure 1: Decrease in the normalized, maximum tensile stress in B3B-tests due to non-linear effects in dependence of the applied load P for multiple relative thicknesses t/R_s of the specimen. The results shown are valid for a specimen with a radius R of 12mm, a support radius R_s of 10mm, a Poisson's ratio ν of 0.22 and a Young's modulus E of 70GPa. The specimen's thickness t was varied from 0.5mm to 4mm. Figure adapted from [14].

Therefore, the aim of this work is to validate the utilized FEA-models for significantly non-linear cases. A suitable base of comparison for validation was found in the experimental determination of the specimen's deflection or its general deformation. Due to the design of the fixture for the B3B-test, common methods, such as digital image correlation (DIC) or the use of a Linear Variable Differential Transformer (LVDT), cannot be implemented in a straightforward way [15–18]. To use these methods, some adjustments to the fixture itself and the overall testing setup would have to be made, at the cost of losing some of the advantages of the test or the comparability to the regular setup. Therefore, an alternative method with minimal influence on the testing setup was sought after, and X-ray tomography and radiography provided the necessary requirements.

In this work, X-ray tomography is employed to track the displacement of the load and support balls in three dimensions. This method relies on a stepwise increase of the load, with each tomography recording being performed at a constant load. In contrast, the balls' positions in three-dimensional space are also determined from two-dimensional radiographs. The latter method significantly decreases the experimental time and allows in-situ image acquisition without holding points at constant loads, which are necessary to obtain a three-dimensional reconstruction of the testing setup through tomography. The experiments were performed on thin plates of high strength glass to emphasize the influence of non-linear effects and to observe comparatively large deflections. Additionally, a Ce-doped zirconia showing some degree of ductility by Transformation Induced Plasticity (TRIP, see [19,20]) was investigated to assess the influence of the material's non-linearity during the B3B-test.

2 Experimental methods

2.1 Specimen preparation

The glass specimens were sourced from Schott AG (Hattenbergstrasse 10, 55122 Mainz, Germany) and are commercially available under the product name AF32[®]eco. The specimens were manufactured through the Down-Draw-Process and were cut into square specimens with an edge length of 10mm. The thickness of each specimen is 130 μ m in the as-delivered condition, and the thickness or surface were not altered in any way. The material's mechanical properties are given in [21].

For the zirconia specimens, a composite consisting of ceria-stabilized zirconia, alumina and aluminates was utilized [20,22]. The material is commercially available under the product name EvoCera[®] from Doceram GmbH (Heßlingsweg 65-69, 44309 Dortmund, Germany). Specimens were received as discs with a diameter of 20mm. They were cut to squares with an edge length of 10mm, ground and then polished to a thickness of about 250 μ m. Special care was taken during polishing to avoid phase transformation from the tetragonal to the monoclinic phase before testing. The monoclinic phase content of each specimen was tested through X-ray Diffraction (XRD) to ensure a low initial monoclinic content and thus a high transformability. An average monoclinic content of about 6% was determined.

2.2 Testing setup

In order to perform the in-situ bending experiments, a tension/compression device as described in [23] was utilized. The testing fixture is placed within a transparent PMMA tube with an outer diameter of 30mm and a wall thickness of 2mm. The tube is fastened and mounted to a compression/tension stage with a 5kN load cell. The testing fixture itself is held in place through a compression fit to a steel rod on both the upper and lower stamp, and it is shown schematically in Figure 2. Each specimen was loaded until failure, with a discontinuous increase in load and holding times at constant load of up to 30min for tomography specimens. For radiography specimens, a constant loading rate of 1 μ m/s was used. In both cases, the load was recorded at 1s⁻¹ and written to a separate file.

The testing fixture itself is a modified version of the B3B-fixture given in [15–18]. It's components and a schematic of the testing setup are given in Figure 2a) and b). Two major adjustments have been performed to allow in-situ testing and observation through X-rays. First, the materials were adapted to minimize the absorption and influence of the fixture and load/support balls. POM was utilized to manufacture the fixture, as shown in Figure 2. For the load/support balls, commercial high-performance bearing balls made from Si₃N₄ with a diameter of 7.144mm were used, which yields a support radius of 4.12mm. Second, the usual multi-step loading process had to be reduced to a single step, as, once inside the PMMA tube, access to the fixture was not possible. Therefore, small misalignments in the testing setup were possible, but could be checked and recorded through the resulting X-ray scans. Due to the high deformation of the glass specimens, Si₃N₄ spacers were utilized to increase the height of the loading ball and allow greater deflection of the specimens before coming into contact with the fixture. A radiograph of the testing setup before loading is given in Figure 3.

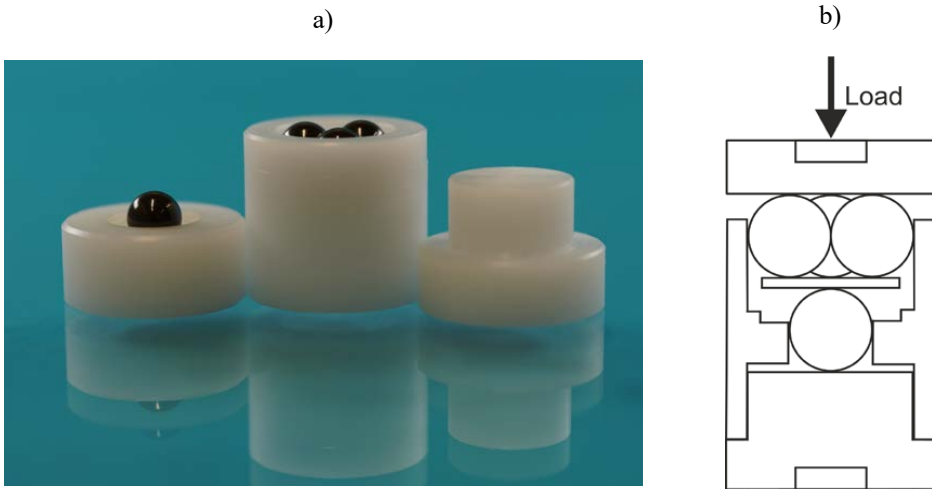


Figure 2: The components of the testing fixture are shown in a), with the top stamp, guide and bottom stamp from left to right, as well as the Si₃N₄-balls for load application. A schematic of the assembly of these components, loaded with a specimen, is given in b).

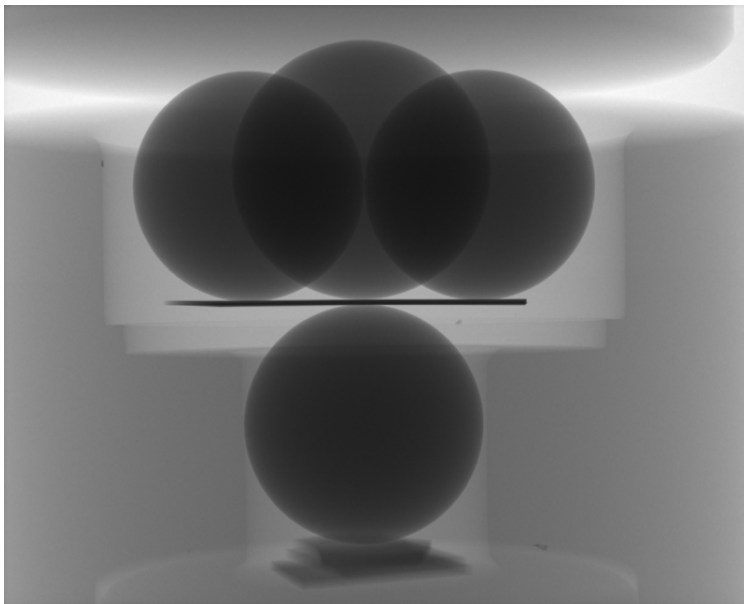


Figure 3: Radiograph of the testing setup with an undeformed glass specimen and the Si₃N₄ spacers beneath the loading ball.

2.3 Tomography analysis

X-ray tomography was used to image the specimen at several stages of the bending test. For each scan, the loading stage was halted, and several projections were taken at equally

spaced angular positions. The projections were used to reconstruct the three-dimensional volume through a classic filtered-back projection algorithm. For the glass specimens, the Vtomex tomograph by phoenix|x-ray systems (Niels-Bohr-Strasse 7, Wunstorf 31515, Germany) located at Laboratoire MATEIS (INSA Lyon, France) was used, where plenty of in-situ experiments have been successfully performed [24–27]. The scanning parameters for each experiment are summarized in Table 1.

Table 1: Equipment parameters for the X-ray analysis. For each of the 900 angular positions, three radiographs were averaged, and a single radiograph was skipped, which ultimately determines the total scanning time.

Parameter	Glass	Zirconia
Number of projections	900	900
Voltage	80kV	140kV
Current	280 μ A	80 μ A
Voxel size	11.91 μ m	11.91 μ m
Exposure time	333ms	500ms
Tomography scanning time	20min	30min

Volume reconstruction was performed on the proprietary software “datos|x”, version 2.0, of the Phoenix system. Before volume reconstruction, the offset from the ideal rotational axis was corrected, and a multi-material filter, a beam hardening correction (bhc+ filter) and a low noise filter were applied.

With the reconstructed volume for each load step, the positions of the balls in three-dimensional space were determined. This procedure was conducted in ImageJ, version 1.53t, with the use of built-in extensions and several plug-ins developed in the MATEIS laboratory. Initially, the stack of images is converted from 16-bit grayscale to 8-bit grayscale, followed by a three-dimensional median filter with a radius of 2 pixels. By setting a threshold value, the balls and sample were separated from the surrounding image and a binary image was created. Once the volume has been binarized, an opening operation (erosion, then dilation) based on a Euclidean distance measurement is used, with a carefully chosen radius so as to retain only the four balls. The dilation radius chosen is also slightly smaller than the erosion radius, so that the four balls are no longer in contact with each other and can be labelled individually. Next, the volume and center of mass is calculated for each labeled ball. These various steps, in particular erosion and

3D dilation based on Euclidean distance, use ImageJ plugins developed in the MATEIS laboratory.

From this point on, any further data analysis was conducted with Mathematica 13.1 from Wolfram Research, Inc. (100 Trade Center Drive, Champaign IL 61820-7237, USA). For each tomograph, the distance between the support balls and the loading ball was determined and their respective positions checked for any deviations from the ideal case. For the results shown in this work, no major misalignments were found. If the testing fixture was tilted in any direction, the measured distances were adjusted accordingly.

2.4 Radiograph analysis

As shown previously, in-situ X-ray tomography is an ideal technique to perform a digital 3D-reconstruction of the experimental setup and measure the position of the balls at a given point of the test. However, this means that the loading system must be halted for each scan, which may affect the mechanical response of the specimen (e.g., through sub-critical-crack-growth) or the measurement itself (e.g., drift of the load cell and stress relaxation) as well as considerably increase the time required for a complete experimental campaign.

Recent techniques propose the use of radiographs, instead of the 3D reconstructed volumes, to measure the kinematics of the process that takes place [28], which requires a substantially lower amount of time and computational resources. Following a similar approach, the open-source technique proposed by [29] is used in this work, where the 3D position of a sphere can be measured using a single radiograph for conic-beam tomographs. Briefly, the technique is based on a series of fast Fourier transform deconvolutions between the measured radiographs and a sequence of structuring elements. In this case, the structuring elements are synthetic radiographs constructed from the projections of a single sphere of the same size as the one used in the B3B setup. By varying the position of the sphere along the X-ray beam, the 3D positions of the spheres can be found. Further details of the technique can be found in [30], while the open-source code is available in [31].

Given that this method can only be used for a system where the measured spheres are all of the same size, the B3B-test represents an ideal test case for tracking the positions of the support and loading balls. As an example, Figure 4a) presents the same radiograph as in Figure 3, after the calibration which allows to transform from attenuation values to the path length of the x-rays through the balls. After measuring the 3D positions of the balls, the balls are projected-back into a radiograph, as shown in Figure 4b). To quantify the quality of the measurement, the residual between the two images (i.e., the squared difference between them) is shown in Figure 4c) as well. The technique does not take the presence of the specimen into account, and thus it is not back-projected into the radiograph of Figure 4b), which results in the middle region of the image with higher values. This proposed measurement technique was used only on the glass specimens, since the zirconia specimens had an attenuation coefficient higher than that of the bearing balls, which causes a substantial error when performing the convolutions between the radiographs and the structuring elements.

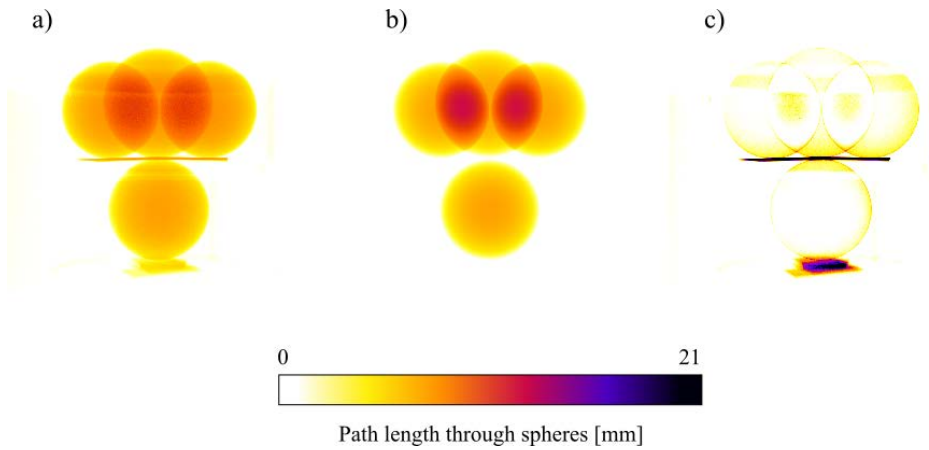


Figure 4: Measurement of the three-dimensional positions of the balls using radiographs. a) shows the original radiograph after applying the calibration, b) gives a synthetic radiograph generated with the measured positions of the balls, and c) displays the residual of the correlations between the two previous images.

To test the quality of 3D measurements from this technique, the positions of the balls are computed for the initial tomography scan at a constant load, prior to any further loading. This initial scan serves the purpose of comparison of the tomography- and radiography results. As the tomography scan is performed, the setup is rotated along the vertical axis, and at each angular position, a different radiograph is taken. Figure 5 shows the temporal evolution of the position for the different balls of the testing assembly along the horizontal plane. As expected, the three support balls (particle 1-3) show a circular path, while the loading ball shows almost no displacement.

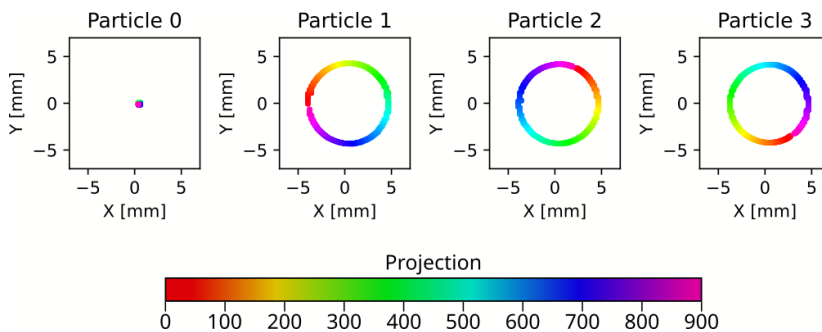


Figure 5: Temporal evolution of ball positions in the horizontal (XY) plane during a tomography scan. The graph to the far left gives the position of the loading ball, and the three other graphs the position of each support ball.

For all radiographs, the same equipment and machine parameters as given in Table 1 were utilized. Three images were acquired per second, resulting in a total of more than 2000 radiographs for each specimen tested.

3 Numerical Methods

The main FEA-model utilized in this work is shown in Figure 6a). Due to the symmetry of the problem, it is sufficient to model only one half of the setup. The model is implemented in ANSYS Mechanical Release 2022R1 by ANSYS Inc. (Southpointe 2600 Ansys Drive, PA 15317, Canonsburg, USA). It is implemented through an APDL (Ansys Parametric Design Language) script to allow detailed control of the model and full documentation of all input parameters and changes to the model. The model consists of approximately 50000 SOLID186 20-node brick elements (the exact number depends on the thickness of the specimen) and 200000 nodes. The regions of contact between the balls and the specimen are modeled through a symmetrical contact using CONTA174 and TARGE170 elements, with a friction coefficient of $\mu=0.5$. A mesh convergence analysis was performed for the deflection of the specimen to ensure consistent results. After a small initial displacement, a load is incrementally applied to the loading ball until a specified target load is reached. Since the interaction between the balls and the specimen are considered, this model is able to include the influence of non-linear effects. More specifically, the term “non-linear effects” refers to the non-linear change in contact area between the balls and the specimen, the influence of friction in these regions and the geometrically non-linear deformation of the specimen and consequent shift of the contact point of the support balls and the specimen. Additionally, a model for square plates, utilized in previous work (Model 2 in [14] for further details on the mesh and convergence analysis), was employed to analyze the linear behavior of the specimen as another point of reference, as shown in Figure 6b). This model will serve as a point of reference for an idealized testing situation through punctiform load application and boundary conditions. Furthermore, the non-linear geometrical behavior is not considered in this model, therefore any results provided by this model are independent of the magnitude of the applied load. For both models, linear-elastic material behavior is assumed.

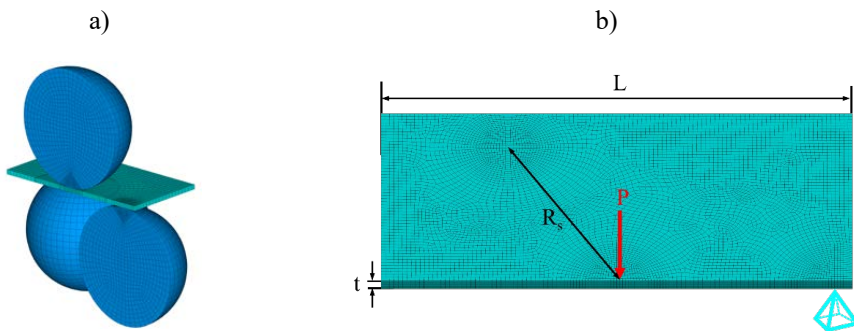


Figure 6: a) gives the meshed FEA model of the loading balls, support balls and glass specimen that was utilized for non-linear analysis as a base of comparison to the experimental results. The linear model is shown in b), with L as the edge length of the specimen, t as its thickness and R_s as the support radius determined by the support ball radii [14].

4 Results

4.1 Tomography

Figure 7 shows a comparison of the tomography results to the numerical results for glass specimens. More specifically, the distance between the center of the loading balls and the center of the support balls is given as a function of the measured/applied load. For the experimental results, the deflection at 0N is defined through the diameter of the balls and the specimen thickness, as a load-free setup could not be scanned. This is due to the movement of the whole fixture during a tomography scan, which would unsettle the testing setup if no load is applied. While the slope of all curves is initially well aligned with the results from the linear model, it is obvious that this is not the case for loads greater than 3N. With an increase in load, a decrease of the specimen's deflection (relative to the expected deflection from the linear model) is observed. This is in good agreement with the results from previous work [14]. Furthermore, the experimental results from two different tests give nearly identical results to FEA, with a maximum deviation of about $20\mu\text{m}$.

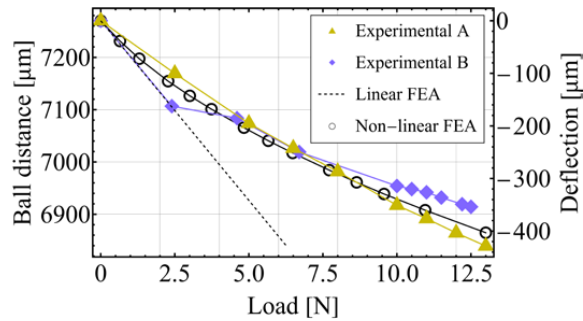


Figure 7: Comparison of the vertical distance between the center of the loading ball and the center of the support balls obtained through experimental results, linear FEA and non-linear FEA. The experimental results were obtained for two glass specimens through tomography, with the results of glass specimen A shown in yellow and glass specimen B shown in purple.

Figure 8a) displays the comparison between the experimental and numerical results for the Ce-doped zirconia specimen. The initial measured deflection showed a constant offset to FEA of about $10\mu\text{m}$, which lead to the measured distance at 5N to be slightly larger than the theoretical maximum given through the specimen's average thickness (this aspect will be discussed further in chapter 5). Therefore, the measured data was corrected by this constant offset of $10\mu\text{m}$, as shown in Figure 8a). Compared to the glass specimens, the opposite behavior is observed. With an increase in load, an increase in deflection compared to the linear FEA-results is measured, indicating the onset of the TRIP-effect at approximately 28N. Note that the non-linear FEA-model does not consider the non-linear mechanical behavior of the material itself, thus the phase transformation process and resulting plastic deformation is not considered. Hence, no alignment between those two curves was expected. However, it still gives a better estimate for the specimen deflection than the linear model, as the aforementioned non-linear effects (see chapter 3) are considered. Figure 8b) displays the corresponding tensile loaded surface after failure,

examined with an optical light microscope (BX53M by Olympus K.K. (2-3-1 Nishi-Shinjuku, 163-0914 Tokyo, Japan)). By utilizing differential interference contrast, the regions of phase transformation are clearly visible due to their increase in volume and subsequent formation of surface structures. Phase transformation is visible within a circular region in the center of the specimen, with a diameter of approximately 5mm. Furthermore, phase transformation occurred in the vicinity of the crack path up to the edge of the specimen.

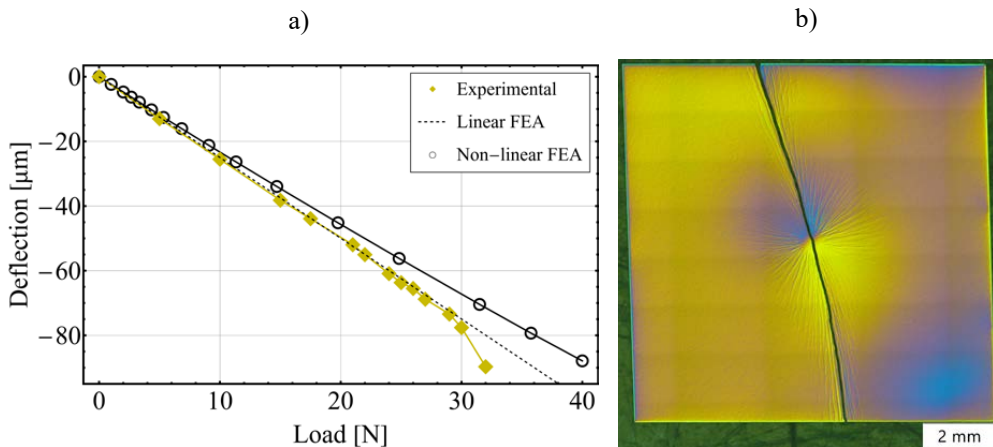


Figure 8: a) shows a comparison of the vertical distance between the center of the loading ball and the center of the support balls for a Ce-doped zirconia specimen, with the experimental results obtained through tomography and corrected by an offset of $10\mu\text{m}$. The fractured specimen is given in b), with the transformed regions clearly visible as surface undulations (differential interference contrast).

4.2 Radiography

Figure 9a) shows the results from the radiograph analysis compared to the results from linear and non-linear simulations. Note that for better visualization, only every twentieth measurement from the experimental data is shown. In comparison to the results from the tomography experiments, the maximum load has doubled. While the tendencies are very similar to the non-linear FEA results, the absolute value has an offset. More specifically, a difference of about $180\mu\text{m}$ is found for the distance between the balls at a load of about 1N. The presence of such an offset is discussed in the following section. If every measured distance is corrected by this difference, Figure 9b) is obtained. Through this correction, the tendencies between the experimental measurements and non-linear FEA results are easier to compare. With an increase in load, a higher deflection compared to the simulations is measured. Just before failure, a total deflection of about $620\mu\text{m}$ was measured, which equates to more than 4.5 times the specimen's thickness. The resulting deformation is shown in Figure 10c), along with earlier stages of deformation at the initial state and at half of the failure load in Figure 10a) and Figure 10b), respectively. Similar to the results obtained for glass specimen C, significantly higher loads and deflections compared to tomography were achieved for specimen D. The total deflection of this specimen was $580\mu\text{m}$ at a maximum load of 20.8N. Again, the tendencies between

experimental results and the simulations are very similar, but an offset in the range of about 200 μm of the absolute deflection values was observed, as shown in Figure 9c) and d).

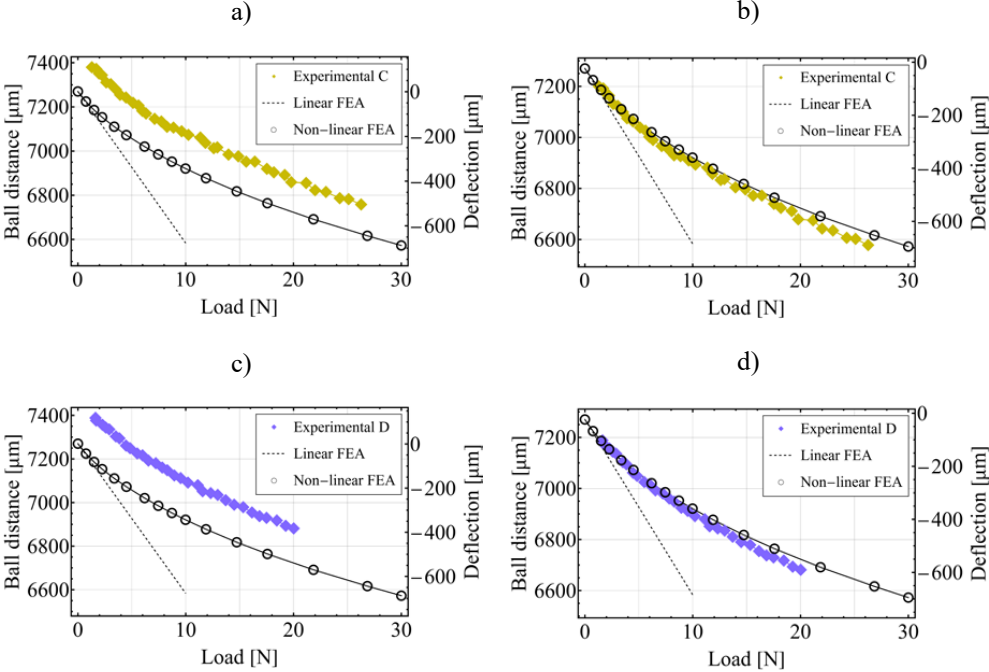


Figure 9: Comparison of the vertical distance between the center of the loading ball and the center of the support balls obtained through experimental results, linear FEA and non-linear FEA. The experimental results were obtained for glass specimens C and D through radiography, with the uncorrected values for specimen C given in a) and the values corrected by an offset of 180 μm given in b). For specimen D, the uncorrected values are given in c) and the values corrected by an offset of 200 μm are given in d).

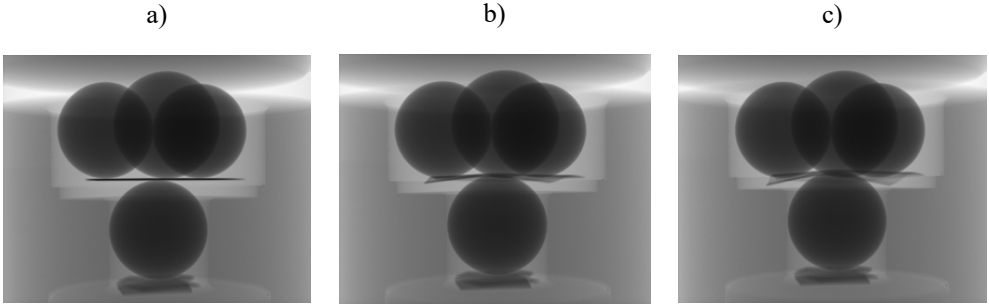


Figure 10: Radiographs of glass specimen C at 1N (a), 13N (b) and 26.6N (c), where the large deflection of the specimen is visible, especially in c).

5 Discussion

In general, the experimental results from the tomographs are well aligned with theoretical considerations and the behavior expected from FEA. While both glass specimens show a difference of about $20\mu\text{m}$ to the simulations, the general behavior of the deflection versus applied load is the same. It is important to note that the experimentally determined parameter was not the deflection of the specimens, but the full distance between the loading and support balls, which is in the range of about $7200\mu\text{m}$. In this case, a difference of $20\mu\text{m}$ to the simulations is less than 0.3% of the total distance measured. However, if just the deflection is considered (which is in the range of $300\mu\text{m}$ to $400\mu\text{m}$), the difference of $20\mu\text{m}$ corresponds to an error of about $\pm 6\%$.

For the zirconia specimen, a similar comparison to FEA is not possible, as the phase transformation is not implemented in the utilized model. Note that an implementation of phase transformation might be possible through a simple material model, that is linear-elastic in compression and elastic-plastic (without hardening) in tension (a material model like this is often referred to as a “cast-iron-model”). Compared to the non-linear model, an opposing trend to the glass specimens (i.e. a non-linear *increase*) of the deflection in dependence of the applied load was observed. This aligns well with theoretical considerations, as a plastic deformation through phase transformation would lead to increased deformation without the expected increase in load. As shown in Figure 8b), it is evident that phase transformation occurred in the highly stressed regions. As with the glass specimens, an error of about $10\mu\text{m}$ of the uncorrected measurements to the FEA results is detected. Due to the higher stiffness of the zirconia specimens, the total deflection (about $100\mu\text{m}$) is much smaller as compared to the glass specimens, and the relative error is larger. Furthermore, the uncorrected measurement at 5N is higher than the theoretical maximum. This might be attributed to the imperfect shape of the specimen. More specifically, due to the high amount of polishing that was necessary to remove the transformed surface layer, the parallelism of the two main surfaces was lost and the specimen thickness varied by about $30\mu\text{m}$. For the simulations and the initial state, an average specimen thickness from three measurements was utilized for the uncorrected measurements, which is $15\mu\text{m}$ less than the highest value. While this difference in thickness would not noticeably affect the general behavior of the simulations, the absolute value of the distance between the balls would be increased and better aligned with the measurements. This could also explain the observed difference for the other datapoints, which are all offset by about $10\mu\text{m}$, thus giving the reasoning behind the correction performed to obtain Figure 7a).

The results from the radiographs align with the observations from the tomography results. While the same tendencies as in the simulations are obtained, an offset error in the absolute distance between the balls was observed, which simply corresponds to the discretization performed when measuring the position of the balls – as explained before, several structuring elements are used for the convolution from which the 3D position is measured. It is important to note that the main advantage of the distance evaluation through radiographs is the significantly faster measurement. While the measurement of a specimen through tomography takes about half a day to obtain a reasonable amount of data, this alternative provides considerably more data within a few minutes. Through the fast experimental procedure, it is

also possible to achieve higher maximum loads and increased deformation, as effects such as sub-critical crack growth play a less important role [32,33]. Note that for the evaluation of radiographs and tomographs (reconstruction excluded), a different amount of time for the post-processing of the acquired data is necessary. While the total time for post-processing for tomography is lower, this is mainly due to the small number of scans that can be obtained for a given specimen (usually in the range of 5-20 scans per specimen). For radiography, one scan containing 1500-2500 projections was regularly obtained, thus vastly increasing the amount of datapoints, which naturally causes longer post-processing times if all projections are evaluated. If this is not the case, and only a few select projections are evaluated, post-processing times are in the same range as for a typical tomography measurement. Additionally, there is no need for volume reconstruction and each image is evaluated through an automated script, which minimizes the potential for human error and requires less overall attention.

Improvements to this first iteration of this method can easily be made if a better-suited load cell is utilized. For the investigated specimens, which fractured at less than 50N, the range of the load cell was not ideal, but it was the only one available for this testing setup. Consequently, the load signal oscillated and an average value was used. Another improvement related to the load measurement is an increase of the sampling rate, which was limited to 1s^{-1} . While this is not relevant for the tomography experiments, the continuous in-situ experiments would greatly be improved by a higher sampling rate. Furthermore, through the use of a synchrotron beamline, smaller deflections which usually occur for thicker or stiffer specimens could be tested due to a higher achievable resolution.

A potential source of error with the testing setup in general is friction. Due to the inaccessibility of the testing fixture within the tomograph, the usual testing procedure for the B3B-test, which involves pre-loading the specimen and subsequently removing a spacer, could not be conducted. Therefore, the testing fixture had to be slightly adapted so that the support balls stay in place throughout the whole loading sequence. This leads to contact of the support balls with the sides of the guide of the testing fixture, which is not the case for the usual B3B testing setup. Consequently, additional resistance against ball movement due to friction is built up, and a higher load as compared to the regular setup is necessary to achieve the same amount of specimen deformation. Preliminary testing has shown that this effect is increasingly relevant at higher loads, and the results obtained in this work do not show an overestimation of the applied load. Still, this influence should be investigated in more detail by a comparison of both testing setups with well-established methods of deflection measurement.

As of now, the accuracy of this method (or rather these two approaches) is not sufficient to provide an alternative to other well-established methods for deflection measurement such as digital image correlation, video extensometer or contacting deflection measurements, such as LVDT. This is especially true if specimens with a high stiffness and/or thickness must be investigated, where deformations are in the range of only a few micrometers. But, for use cases like the B3B-test, where established methods are not feasible, it provides a promising alternative, which also provides additional information about the deflection at specified positions.

Overall, while some improvements could be made to this method to provide a higher degree of accuracy, it is shown that the predictions by FEA align well with the experimental data, especially for the glass specimens. Even for specimens with such a large deformation and significant non-linear effects, an accurate prediction could be made. Therefore, the results from this work serve as one point of experimental validation of the FEA for the comparisons and conclusions drawn in earlier work, notably in [14].

6 Summary

A follow-up to a previous publication on the Ball-on-Three-Balls-test is provided in this work [14]. In that publication, the influence of non-linear effects on the measured strength was discussed, quantified, and validated through Finite-Element-Analysis (FEA). Consequently, additional validation through experimental results is desired in the form of deflection measurements. In order to measure the specimen's deflection during testing, X-ray tomography was employed to open the opportunity for a "direct" view at the testing assembly.

The specimen's deflection is determined from a three-dimensional reconstruction (tomograph) of the specimen and load/support balls. Additionally, two-dimensional radiographs were also used as a continuous alternative to the discontinuous tomography measurements. Through this approach, a vast increase in the amount of time steps is achieved and better load-wise resolution is obtained.

In general, excellent agreement between the deflection measured through tomography and the deflection obtained through FEA was observed. The radiography measurements show good agreement with the general tendencies, but they do not yield comparable absolute values to FEA. A systematic deviation in the form of an offset of about 200 μm was observed and discussed for the radiography measurements presented in this work.

Overall, measuring the deflection of thin, flexible ceramic specimens through X-ray tomography or radiography is promising, but several aspects need to be improved until these methods are a suitable alternative to other, well-established methods. Still, the validity of FEA was demonstrated, thus also validating the findings which were obtained in previous work.

Acknowledgements.

M. Staudacher gratefully acknowledges financial support by the Austrian BMVIT and BMWFW in the project "CharAM" (FFG 877684) of the COIN/IraSME program. The authors are grateful to the JECS Trust for funding the visit of M. Staudacher to INSA Lyon (Contract No. 2022305). The authors further thank SKF Austria AG for providing the Si₃N₄ bearing balls.

Data availability

Data will be made available on request.

References

- [1] ASTM C 1499-05: Test Method for Monotonic Equibiaxial Flexural Strength of Advanced Ceramics at Ambient Temperature, ASTM International, West Conshohocken, PA, 2005.
- [2] R. Morrell, Biaxial flexural strength testing of ceramic materials: A National Measurement Good Practice Guide No. 12, National Physical Laboratory, 2007.
- [3] G. With, H.H.M. Wagemans, Ball-on-Ring Test Revisited, *J American Ceramic Society* 72 (1989) 1538–1541.
- [4] H.L. Frandsen, The small displacement elastic solution to the ball-on-ring testing method, *Mechanics of Materials* 55 (2012) 33–40.
- [5] C.W. Huang, C.H. Hsueh, Piston-on-three-ball versus piston-on-ring in evaluating the biaxial strength of dental ceramics, *Dental materials official publication of the Academy of Dental Materials* 27 (2011) e117-23.
- [6] Y. Torres, R. Bermejo, F.J. Gotor, E. Chicardi, L. Llanes, Analysis on the mechanical strength of WC-Co cemented carbides under uniaxial and biaxial bending, *Materials & Design* 55 (2014) 851–856.
- [7] M. Staudacher, T. Lube, J. Schlacher, P. Supancic, Comparison of biaxial strength measured with the Ball-on-Three-Balls- and the Ring-on-Ring-test, *Open Ceramics* 6 (2021) 100101.
- [8] J. Malzbender, R.W. Steinbrech, Fracture test of thin sheet electrolytes for solid oxide fuel cells, *Journal of the European Ceramic Society* 27 (2007) 2597–2603.
- [9] W. Adler, D. Mihora, Biaxial Flexure Testing: Analysis and Experimental Results, in: *Fracture Mechanics of Ceramics*, pp. 227–245.
- [10] R. Morrell, N.J. McCormick, J. Bevan, M. Lodeiro, J. Margetson, Biaxial disc flexure – modulus and strength testing, *British Ceramic Transactions* 98 (2013) 234–240.
- [11] J.d.S. Ramos, S. Fraga, G.F. Vogel, L.G. May, Influence of the geometry of ceramic specimens on biaxial flexural strength: Experimental testing and finite element analysis, *Cerâmica* 64 (2018) 120–125.
- [12] A. F. Kirstein, R. M. Woolley, Symmetrical bending of thin circular elastic plates on equally spaced point supports, *Journal of Research of the National Bureau of Standards, Section C: Engineering and Instrumentation* 71C (1967).
- [13] M. Staudacher, P. Supancic, T. Lube, The Ball-on-Ring-test: Enhancing an analytical solution by numerical analysis for elastic deformation and small displacements, *Journal of the European Ceramic Society* 43 (2023) 7167–7177.
- [14] M. Staudacher, T. Lube, P. Supancic, The Ball-on-Three-Balls strength test for discs and plates: Extending and simplifying stress evaluation, *Journal of the European Ceramic Society* 43 (2023) 648–660.
- [15] W. Harrer, R. Danzer, P. Supancic, T. Lube, The Ball on Three Balls Test: Strength Testing of Specimens of Different Sizes and Geometries, *Proceedings 10th ECerS Conf. 2008* (2008) 1271–1275.
- [16] R. Danzer, P. Supancic, W. Harrer, Der 4-Kugelversuch zur Ermittlung der biaxialen Biegefestigkeit spröder Werkstoffe, *Kriegsmann, J. (Hrsg): Technische keramische Werkstoffe* (2009) 1–48.

- [17] R. Danzer, W. Harrer, P. Supancic, T. Lube, Z. Wang, A. Börger, The ball on three balls test—Strength and failure analysis of different materials, *Journal of the European Ceramic Society* 27 (2007) 1481–1485.
- [18] A. Börger, P. Supancic, R. Danzer, The ball on three balls test for strength testing of brittle discs: Stress distribution in the disc, *Journal of the European Ceramic Society* 22 (2002) 1425–1436.
- [19] J. Chevalier, A. Liens, H. Reveron, F. Zhang, P. Reynaud, T. Douillard, L. Preiss, V. Sergo, V. Lughi, M. Swain, N. Courtois, Forty years after the promise of «ceramic steel?»: Zirconia-based composites with a metal-like mechanical behavior, *J American Ceramic Society* 103 (2020) 1482–1513.
- [20] H. Reveron, M. Fornabaio, P. Palmero, T. Fürderer, E. Adolfsson, V. Lughi, A. Bonifacio, V. Sergo, L. Montanaro, J. Chevalier, Towards long lasting zirconia-based composites for dental implants: Transformation induced plasticity and its consequence on ceramic reliability, *Acta biomaterialia* 48 (2017) 423–432.
- [21] Schott AG, Datasheet AF32@eco, <https://www.schott.com/de-at/products/af-32-eco-p1000308/downloads>, accessed 4 October 2023.
- [22] P. Palmero, M. Fornabaio, L. Montanaro, H. Reveron, C. Esnouf, J. Chevalier, Towards long lasting zirconia-based composites for dental implants. Part I: innovative synthesis, microstructural characterization and in vitro stability, *Biomaterials* 50 (2015) 38–46.
- [23] A. Sibellas, J. Adrien, D. Durville, E. Maire, Experimental study of the fiber orientations in single and multi-ply continuous filament yarns, *The Journal of The Textile Institute* 111 (2020) 646–659.
- [24] J. Seuba, E. Maire, J. Adrien, S. Meille, S. Deville, Mechanical properties of unidirectional, porous polymer/ceramic composites for biomedical applications, *Open Ceramics* 8 (2021) 100195.
- [25] E. Maire, P.J. Withers, Quantitative X-ray tomography, *International Materials Reviews* 59 (2014) 1–43.
- [26] T. Lacondemine, J. Réthoré, É. Maire, F. Célarié, P. Houzot, C. Roux-Langlois, C.M. Schlepütz, T. Rouxel, Direct observation of the displacement field and microcracking in a glass by means of X-ray tomography during in situ Vickers indentation experiment, *Acta Materialia* 179 (2019) 424–433.
- [27] A. Bouterf, E. Maire, S. Roux, F. Hild, X. Brajer, E. Guillard, E. Boller, Analysis of compaction in brittle foam with multiscale indentation tests, *Mechanics of Materials* 118 (2018) 22–30.
- [28] H. Leclerc, S. Roux, F. Hild, Projection Savings in CT-based Digital Volume Correlation, *Experimental Mechanics* (2015).
- [29] E. Andò, B. Marks, S. Roux, Single-projection reconstruction technique for positioning monodisperse spheres in 3D with a divergent x-ray beam, *Meas. Sci. Technol.* 32 (2021) 95405.
- [30] O. Stamati, B. Mark, E. Ando, S. Roux, N. Machicoane, X-ray radiography 4D particle tracking of heavy spheres suspended in a turbulent jet, *Zenodo*, 2022.
- [31] Y. Haouchat et al., Code repository, <https://gricad-gitlab.univ-grenoble-alpes.fr/ttk/radioSphere>, accessed 4 October 2023.
- [32] J.B. Wachtman, M.J. Matthewson, W.R. Cannon, *Mechanical properties of ceramics*, Wiley, Hoboken, New Jersey, 2009.

[33] D. Munz, T. Fett, *Ceramics: Mechanical Properties, Failure Behaviour, Materials Selection*, Springer, Berlin, Heidelberg, 1999.

Publication D

The Ball-on-Three-Balls strength test: Effective volumes and surfaces for Weibull strength scaling

Maximilian Staudacher, Anna Eggel, Peter Supancic, Tanja Lube

Department of Materials Science, Montanuniversität Leoben, Franz Josef-Strasse 18, A-8700 Leoben, Austria

Journal of the European Ceramic Society 44, Issue 1 (2024) 173-183
doi: <https://doi.org/10.1016/j.jeurceramsoc.2023.09.018>

Reuse under the terms of license CC-BY 4.0



Contents lists available at ScienceDirect

Journal of the European Ceramic Society

journal homepage: www.elsevier.com/locate/jeurceramsoc

The Ball-on-Three-Balls strength test: Effective volumes and surfaces for Weibull strength scaling

Maximilian Staudacher, Anna Eggel, Peter Supancic, Tanja Lube*

Department of Materials Science, Montanuniversität Leoben, Franz Josef-Strasse 18, A-8700 Leoben, Austria

ARTICLE INFO

Keywords:

Effective volume
Weibull theory
Strength testing
Biaxial testing
B3B-test

ABSTRACT

In order to compare the strength results of brittle materials from various testing methods or use the data for design purposes, it is essential to know the effective volume (V_{eff}) or surface (S_{eff}) for every loading scenario. For the Ball-on-Three-Balls-test (B3B), V_{eff} and S_{eff} have to be determined and investigated through Finite-Element-Analysis due to the lack of an accurate analytical description of the stress field. Through this work, the effective volume and surface of the B3B-test are made available as tabulated data for a wide range of specimen geometries and materials, along with the tools to utilize the data. A fitting model for the dependency of V_{eff} and S_{eff} on the Weibull-modulus for any given specimen geometry is provided. The influence of load-dependent non-linear effects on V_{eff} and S_{eff} is discussed. Finally, the necessity of V_{eff} and S_{eff} for statistical strength analysis is demonstrated through a practical example.

1. Introduction

Due to the brittle nature of ceramics and glasses, special care has to be taken during component design. Most notably, the scatter of strength has to be considered adequately. For this purpose, a multitude of uniaxial and biaxial strength testing methods have been developed over the past decades. Some of the most commonly used uniaxial testing methods are 3- and 4-point bending, while the Ring-on-Ring-test (RoR), Ball-on-Ring-test (BoR) or Ball-on-Three-Balls-test (B3B) make up some of the most common biaxial testing methods [1]. Each method differs in the general shape of the specimen, e.g. bars for uniaxial tests or plates for biaxial tests, and the general concept of the fixture to apply the respective bending moment on the specimen, e.g. with rollers, rings or balls. Therefore, each testing method applies a unique stress field on the respective specimen. In combination with the statistical nature of failure of ceramics, strength results for the same material may vary immensely between each of the mentioned methods. Through Weibull-theory and its underlying assumptions [2–4], it is possible to take the differing stress fields of each method into account and to compare the respective strength results [5]. This comparison is based on the concept of the effective volume, V_{eff} , or the effective surface, S_{eff} . For some testing methods, these quantities can be derived analytically if a closed form solution for the stress field is available [6–9]. However, this is not the case for the B3B-test, where Finite-Element-Analysis (FEA) has to be

employed for stress evaluation. In this work, FEA will be utilized to assess the influence of various testing geometries on V_{eff} and S_{eff} for the B3B-test. The influence of nonlinear effects on these values will be discussed and quantified in the context of strength comparison. Ultimately, an example for a pooled Weibull evaluation will be given, showcasing the application of the results and expressions provided in this work. The numerical values of V_{eff} and S_{eff} are made available for a wide range of testing geometries and materials. Additionally, the FEA-postprocessing routine to evaluate the effective volume and surface is outlined in the appendix of this work.

2. Theoretical Background

It is well accepted that the strength of brittle specimens tested in tension can be statistically described by the two-parameter Weibull distribution [3,4,10], which is typically represented by its cumulative form (CDF=Cumulative Distribution Function)

$$P(\sigma) = 1 - \exp \left[- \left(\frac{\sigma}{\sigma_0} \right)^m \right] \quad (1)$$

The scale and shape parameters of the Weibull distribution are σ_0 and m , which correspond to the characteristic strength and the Weibull modulus of the considered sample. The expression Eq. (1) represents the probability of failure at a given applied tensile stress level σ , i.e. the

* Corresponding author.

E-mail address: tanja.lube@unileoben.ac.at (T. Lube).

<https://doi.org/10.1016/j.jeurceramsoc.2023.09.018>

Received 3 August 2023; Received in revised form 7 September 2023; Accepted 7 September 2023

Available online 9 September 2023

0955-2219/© 2023 The Authors. Published by Elsevier Ltd. This is an open access article under the CC BY license (<http://creativecommons.org/licenses/by/4.0/>).

expectation value of the fraction of specimens which fail at stresses less or equal to σ . The choice of the stress σ in a general test configuration is not definite. Usually, it is defined as the maximum value in a given stress field, e.g. the applied stress in a homogeneous tensile test or the edge fiber tension in a uniaxial bending test, or a meaningful equivalent stress in a complicated, multiaxial stress field. Therefore, the resulting Weibull parameters depend on the details of strength test interpretation. Due to its flexibility, the Weibull distribution can be used as an empirical strength distribution to describe the measured strength of brittle samples for many cases.

If specimens of a single material with varying geometry or varying loading configurations are tested, systematic shifts of the expectation value of the Weibull parameters, predominately the characteristic strength, are observed. This effect is attributed to the size effect of strength and can be described by the Weibull-theory of the strength of brittle materials. This concept is linked to the material's behavior under several assumptions (e.g. defect-controlled failure; randomly distributed and independent defects from a unimodal size distribution, weakest link hypothesis, etc. [2,4,11,12]) and leads to material specific strength parameters, namely the Weibull modulus m and the Weibull material scale parameter Σ_0 . While the Weibull modulus is a pure number, the unit of the scale parameter is given by stress·(volume)^{1/m}, i.e. Pa· $\sqrt[m]{\text{m}^3}$. The knowledge of these parameters allows the calculation of the characteristic strength σ_0 of a homogeneously tensile loaded specimen with volume V , namely by:

$$\sigma_0 = \Sigma_0 \cdot (V)^{-1/m} \quad (2)$$

Consequently, the size effect of the characteristic strength is inherently implemented by the scaling law, Eq. (2), so that the empirical ansatz Eq. (1) can be rewritten as:

$$P(\sigma, V) = 1 - \exp \left[-V \left(\frac{\sigma}{\Sigma_0} \right)^m \right] = 1 - \exp \left[-\frac{V}{V_0} \left(\frac{\sigma}{\sigma_0} \right)^m \right] \quad (3)$$

For practical (dimensional) reasons, the Weibull material scale parameter Σ_0 is often replaced by an arbitrary reference volume V_0 (in m^3 or mm^3) and its related characteristic strength σ_0 (in Pa or MPa, respectively). The failure probability for specimens loaded in inhomogeneous tensile stress fields can be determined by taking the scaling law Eq. (2) into account. For a given stress distribution $\sigma(x, y, z)$, the corresponding probability of failure can be expressed by:

$$P(\sigma, V) = 1 - \exp \left[-\int_V \left(\frac{\sigma(x, y, z)}{\Sigma_0} \right)^m dV \right] \\ = 1 - \exp \left[-\frac{V}{V_0} \int_V \left(\frac{\sigma(x, y, z)}{\sigma_0} \right)^m dV \right] \quad (4)$$

The integration has to be performed over the entire specimen's tensile loaded regions. For stress fields with a spatial distribution that is independent of the applied load, $\sigma(x, y, z)$ can be expressed as

$$\sigma(x, y, z) = \sigma_{\text{ref}} \cdot g(x, y, z) \quad (5)$$

with a load-dependent amplitude factor σ_{ref} and a dimensionless, load-independent and spatially varying shape function $g(x, y, z)$. Note that if the spatial distribution of the stress field, i.e. $g(x, y, z)$, changes during the loading history, this has to be considered appropriately [13]. A recommended choice for σ_{ref} is the maximum first principal stress, so that g is normalized and restricted to a numerical range between 0 and +1 in the case of uniaxial stress fields. Many important loading configurations (e.g. uniaxial 3- or 4-point bending test, the RoR-test, etc.) sufficiently fulfill the assumption for Eq. (5). It should be noted that the accuracy of Eq. (5) depends on the extent of any non-linearities in the test setup, which will be discussed in Section 4.3 of this work. To simplify Eq. (4), Eq. (5) is utilized to define the effective volume V_{eff} by

$$V_{\text{eff}} = \int_V \left(\frac{\sigma(x, y, z)}{\sigma_{\text{ref}}} \right)^m dV = \int_V g(x, y, z)^m dV \quad (6)$$

which can be considered as the equivalent, homogeneously loaded volume of the tested specimen. The advantage of introducing the effective volume is that it can be calculated only once for a given type of test-setup or loading case. The expression for the probability of failure for inhomogeneous stress distributions can therefore be generalized to

$$P(\sigma, V) = 1 - \exp \left[-V_{\text{eff}} \left(\frac{\sigma}{\Sigma_0} \right)^m \right] = 1 - \exp \left[-\frac{V_{\text{eff}}}{V_0} \left(\frac{\sigma}{\sigma_0} \right)^m \right] \quad (7)$$

where $\sigma = \sigma_{\text{ref}}$. To relate the effective volume to the specimen's volume in a given setup or load-configuration, a ratio k

$$k = \frac{V_{\text{eff}}}{V} \quad (8)$$

can be defined [4,14]. In the case of uniaxial stress fields and with the recommended choice of σ_{ref} to normalize $g(x, y, z)$, the resulting effective volume is always less or equal to the specimen's volume and therefore $k \leq 1$. In the limiting case of a homogeneous tensile stress field, k equals 1. For multiaxial stress states, an equivalent uniaxial stress σ_{eq} must be defined through a failure criterion in order to replace $\sigma(x, y, z)$ with $\sigma_{\text{eq}}(x, y, z)$ in Eq. (6). For some failure criterions (e.g. the PIA-criterion), k can exceed 1, which would represent a more critical test compared to uniaxial loading. Within the field of technical ceramics, two of the most prominent and widely employed failure criteria are the First-Principal-Stress criterion (FPS) [15] and the Principle-of-Independent-Action (PIA) [16–18]. As implied by the name, the FPS-criterion assumes that only the first principal stress contributes to failure, and therefore $\sigma_{\text{eq,FPS}}$ is given through

$$\sigma_{\text{eq,FPS}} = \sigma_I \quad (9)$$

with σ_I as the first principal stress. On the other hand, the PIA-criterion includes the contribution of all principal stresses, which is especially relevant when they are of similar magnitude. The equivalent stress $\sigma_{\text{eq,PIA}}$ is determined by

$$\sigma_{\text{eq,PIA}} = \sqrt[m]{\langle \sigma_I \rangle^m + \langle \sigma_{II} \rangle^m + \langle \sigma_{III} \rangle^m} \quad (10)$$

With σ_{II} and σ_{III} as the second and third principal stress, respectively, and m as the Weibull-modulus of the investigated material. If any of the principal stresses is compressive, they will be discarded from this evaluation, which is indicated by the “Macaulay-Brackets” (\cdot).

If defects on tensile loaded surfaces or edges dominate the strength behavior, an effective surface or effective edge length can be defined analogously to Eq. (6). Through calculating a surface or path integral with respect to the normalized stress field, a corresponding expression to Eq. (7) for the probability of failure is given by

$$P(\sigma, V) = 1 - \exp \left[-S_{\text{eff}} \left(\frac{\sigma}{\Sigma_0} \right)^m \right] = 1 - \exp \left[-\frac{S_{\text{eff}}}{S_0} \left(\frac{\sigma}{\sigma_0} \right)^m \right] \quad (11)$$

(Note, that in this case the Weibull material scale parameter Σ_0 is different from Eq. (2) and has the units Pa· $\sqrt[m]{\text{m}^2}$). For many uniaxial stress states, closed form solutions for V_{eff} or S_{eff} can be derived analytically according to Eq. (6), and are widely used due to their simplicity and accuracy. As an example, the effective volume of a rectangular beam with width b , height h tested in flexure on a support span l subjected to 4-point bending (4PB) in a 1/4-point-setup is given as [7].

$$V_{\text{eff,4PB}} = \frac{lbh(m+2)}{4(m+1)^2} = V \cdot \frac{(m+2)}{4(m+1)^2} \quad (12)$$

Note that the effective volume depends on the Weibull modulus, which is always the case for inhomogeneous stress fields. For more complicated stress fields, approximate expressions can be found in literature. One example is the effective volume for the Ring-on-Ring-test under the PIA-criterion developed by Salem et al. [9,19] which was incorporated into the corresponding standard. Another example is the

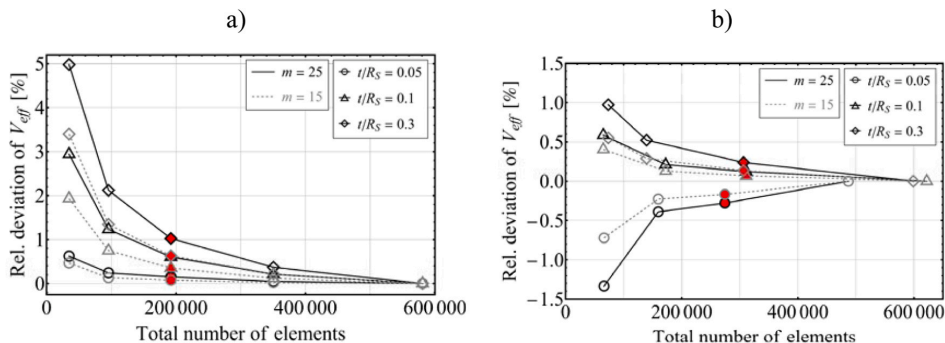


Fig. 1. Mesh convergence analysis for each model. a) shows the relative error to the result with the highest number of elements for *Model 1*, b) for *Model 2*. The red markers represent the approximate number of elements used in this work.

Table 1
Minimum and maximum number of elements and nodes used in each model.

Model	<i>Model 1</i>	<i>Model 2</i>	<i>Model 3</i>
Min/Max num. of elements	155936 / 202734	225472 / 422730	47373 / 78009
Min/Max num. of nodes	652265 / 847223	933429 / 1775043	197379 / 325153

analytically derived expression for the Ball-on-Ring-test under the PIA-criterion, which is restricted to values of m from the range of natural numbers [20]. Note that for both cases, the stress field is well described through analytical expressions. Unfortunately, a simple analytical expression for the stress field of the Ball-on-Three-Balls-test is not available and consequently no analytical expression for the effective volume can be found. Instead, numerical analysis through FEA must be performed in order to determine the effective volume or effective surface for any given specimen.

3. Methods

3.1. FEA-Models

All simulations conducted in this work utilized ANSYS Mechanical Release 2022R1 by ANSYS Inc. (Southpointe 2600 Ansys Drive, PA 15317, Canonsburg, USA). Each model is implemented in APDL (Ansys Parametric Design Language) to allow detailed, script-based access to the model and documentation with varying input parameters. The Finite-Element-Analysis models utilized in this work are based on the ones already discussed in previous work [21], and the same designation will be utilized. Furthermore, a more detailed description of the models and their boundary conditions is given in that work. *Model 1* is a 3D-model of a disc-specimen with punctiform displacement constraints, i.e. a punctiform load applied at the central node of the specimen and punctiform boundary conditions representing the support balls. Due to symmetry, it is sufficient to evaluate just one sixth of the total disc. This results in constraining the out-of-plane displacements of the nodes on the mirror-symmetry faces. *Model 2* is a 3D-model of a square-plate-specimen. Again, the load is applied at a single node in the center of the specimen, and the support balls are represented by punctiform boundary conditions. Due to the symmetry of this problem, it is sufficient to model one half of the full specimen and the constraints of nodes in the symmetry plane are set as described for *Model 1*. The difference to previous iterations of both *Model 1* and *Model 2* is a complete overhaul of the mesh, to achieve a significantly finer mesh in the center and a coarser mesh at the edge of the disc or square plate. This overhaul was necessary since the effective volume is much more sensitive to the

mesh size, especially in the high-stress regions. Finally, *Model 3* represents a 3D-model of the full testing assembly, including the load- and support balls. The main difference to the other models is the way that the load is applied on the specimen. By displacing the load ball and utilizing contact simulations under the assumption of a friction coefficient $\mu = 0.5$ for the contact pairs, a closer representation of a real-world load application is given. The same applies for the support balls. With this model, load-dependent effects, such as specimen deformation and increasing contact areas between the balls and the specimen, can be considered. Since disc-specimens are analyzed, the problem can be reduced to one sixth of the full testing assembly. It should be mentioned that the results generated with *Model 3* are only valid for a testing setup as described in [22,23] where supporting balls are large and in contact with each other.

The effective volume and surface were determined as outlined in Appendix A and 5th order Gauss-Legendre-Quadrature was utilized for numerical integration. Preliminary studies were conducted to determine the error of 5th order Gauss-Legendre-Quadrature compared to the exact analytical result for a linear stress distribution within a single element. If an error $\leq 2\%$ has to be achieved for all $m \leq 50$, the difference between the maximum and minimum stress within a single element must be smaller than 40% of the maximum stress. Therefore, for each model, special care was taken to avoid large stress gradients by adjusting the number of elements in both radial and vertical direction, depending on the respective specimen geometry. A mesh convergence analysis for the effective volume was performed for *Model 1* and *Model 2*, and the results are shown in Fig. 1a) and b). A mesh convergence analysis for the maximum stress for *Model 3* was already performed in [21]. Due to the large computational demand of *Model 3*, it was not feasible to significantly increase the number of elements. Therefore, this model is not fully converged for the accurate determination of the effective volume and surface and will only be utilized for qualitative analyses instead. The minimum and maximum number of elements utilized for each model are given in Table 1. For the specimen and loading or support balls, 20-node brick elements (SOLID186) were utilized. The contacting regions were modelled with CONTA174 and TARGE170 elements. To determine the effective surface, only the tensile loaded face of the model was evaluated. To avoid any influence of the tensile stress field around the contact regions between the balls and the specimen on both the effective volume and surface, a small part of the specimen was removed at the respective regions for each model. The removed region is determined by a circle around the contact region and a depth of about one third of the specimen's thickness. In the case of *Model 1* and *Model 2*, this removal was especially important due to the punctiform load introduction and boundary conditions, which caused numerical artifacts.

Model 1 and *Model 2* were each used to calculate the effective volume and surface for a wide range of specimen geometries. The relevant

Table 2
Range of parameters.

Parameter	t/R_S	R/R_S (L/D_S)	ν	m
Range	0.05–0.5	1.05–2	0.1–0.4	0–50
Step size	0.05	0.05	0.05	1

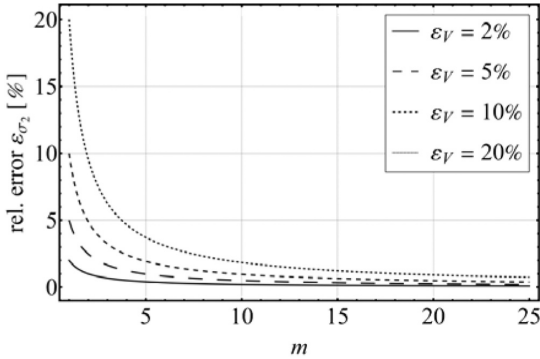


Fig. 2. Relative error in σ_2 through strength extrapolation, i.e. ϵ_{σ_2} , in dependence of the Weibull modulus m . Each line represents ϵ_{σ_2} for a different value of the error in $V_{eff,1}$.

specimen geometries for discs are the specimen’s thickness t , the specimen’s radius R and the support radius R_S , which is determined from the support ball radius R_{SB} through

$$R_S = R_{SB} \frac{2}{\sqrt{3}} \tag{13}$$

if the support balls are in contact with each other. For square plates, the same parameters are used, with the plate’s edge length L instead of R , and the support diameter D_S instead of R_S . For each specimen geometry, the effective volume and surface were determined for different Poisson’s ratios ν and a range of m from $m=0$ to $m=50$. The full range of investigated parameters is given in Table 2. To reduce the total number of variables, the geometric parameters were combined to the relative thickness t/R_S and the relative specimen radius R/R_S for discs or L/D_S for square plates.

For each of the 71400 combinations of these parameters (10 steps for $t/R_S \times 20$ steps for $R/R_S \times 7$ steps for $\nu \times 51$ steps for m), Model 1 and Model 2 were utilized to determine the values of the effective volume and the effective surface with both the FPS-criterion and the PIA-

criterion. If not stated otherwise, all data evaluation for this work has been conducted with Mathematica 13.1 from Wolfram Research, Inc. (100 Trade Center Drive, Champaign IL 61820–7237, USA).

3.2. The necessary accuracy of V_{eff} and S_{eff}

One aspect to consider is the accuracy of V_{eff} that is needed to convert the characteristic strength from one testing method or specimen geometry to a different one. Through equating Eq. (7) for the same probability of failure, but two characteristic strengths $\sigma_{0,1}$ and $\sigma_{0,2}$ with their respective effective volume $V_{eff,1}$ and $V_{eff,2}$, Eq. (14) can be derived:

$$\sigma_{0,2} = \sigma_{0,1} \left(\frac{V_{eff,1}}{V_{eff,2}} \right)^{1/m} \tag{14}$$

Note that this relationship can also be derived through Eq. (2). The Weibull modulus m plays a very important role when relating the strength levels, and for typical technical ceramics, m is often found to be in the range of 10–25. Therefore, assuming that m is high enough, even a large error in one of the effective volumes does not influence the error in characteristic strength $\sigma_{0,2}$ significantly. To better understand this influence, we assume that a Weibull-analysis was performed on specimens tested with the B3B-test, and the characteristic strength $\sigma_{0,1}$ was determined. If this characteristic strength shall be extrapolated to that of a different specimen size or testing method, i.e. $\sigma_{0,2}$, the effective volume of the B3B-test, $V_{eff,1}$, and the effective volume of the other specimen’s or method, $V_{eff,2}$, is necessary. If the effective volume of the B3B-test, $V_{eff,1}$ is not well known and affected by an error ϵ_V , an erroneous converted characteristic strength $\sigma_{0,2,err}$ is obtained. The relative error ϵ_{σ_2} between $\sigma_{0,2,err}$ and $\sigma_{0,2}$ can be defined through

$$\epsilon_{\sigma_2} = \frac{\sigma_{0,2,err} - \sigma_{0,2}}{\sigma_{0,2}} = \frac{\sigma_{0,1} \left(\frac{V_{eff,1}(1+\epsilon_V)}{V_{eff,2}} \right)^{1/m} - \sigma_{0,1} \left(\frac{V_{eff,1}}{V_{eff,2}} \right)^{1/m}}{\sigma_{0,1} \left(\frac{V_{eff,1}}{V_{eff,2}} \right)^{1/m}} = (1 + \epsilon_V)^{1/m} - 1 \tag{15}$$

with the variables as defined before. Fig. 2 depicts ϵ_{σ_2} in dependence of the Weibull modulus m for several fixed errors ϵ_V of $V_{eff,1}$.

For $m \geq 10$, even with ϵ_V as large as 20%, a relative error of less than 2% for $\sigma_{0,2}$ is obtained. While the effective volume still has to be determined accurately for materials with a low Weibull modulus ($m \leq 5$), this is not the case for materials with a medium to high Weibull modulus ($m \geq 10$). Note that this consideration is only relevant for strength extrapolation and is not generally true for all applications of V_{eff} .

4. Results

The following results will only be shown and discussed for disc-

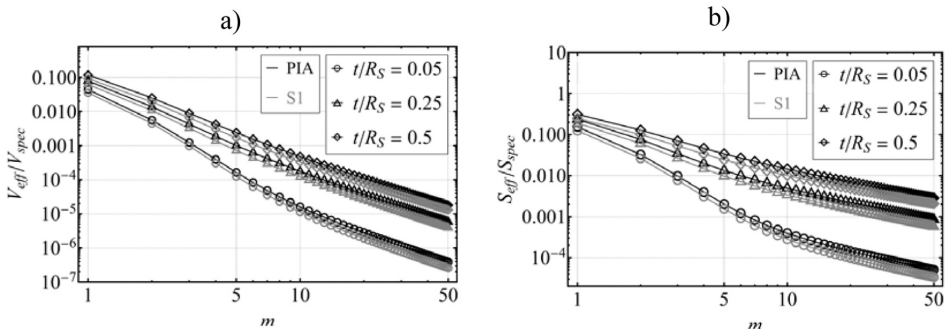


Fig. 3. Dependence of the relative effective volume (a) and relative effective surface (b) for the PIA criterion on the Weibull modulus m for different relative specimen thicknesses t/R_S and $\nu=0.25$. The effective volume and surface were divided by the specimen’s volume V_{spec} or tensile loaded face S_{spec} , respectively, and are plotted on a double-logarithmic scale.

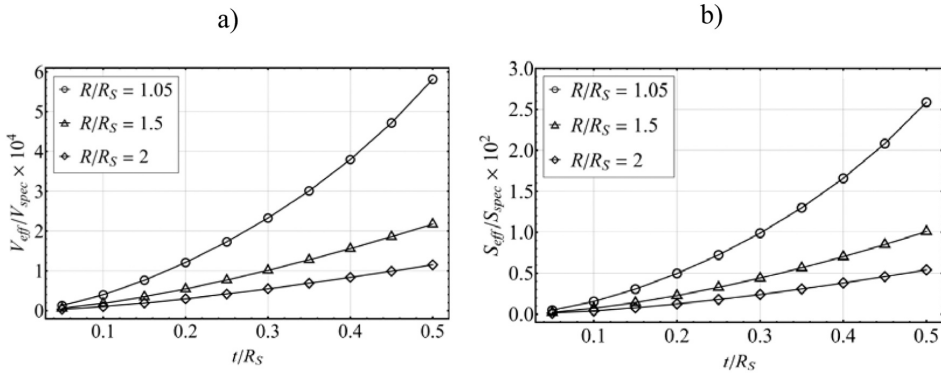


Fig. 4. Dependence of the relative effective volume (a) and effective surface (b) for the PIA criterion on the specimen's thickness t for different relative specimen radii R/R_S for $\nu=0.25$ and $m=15$. The effective volume and surface were divided by the specimen's volume V_{spec} or tensile loaded face S_{spec} , respectively.

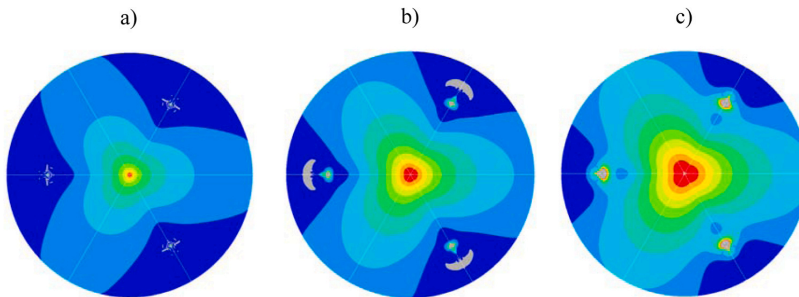


Fig. 5. Variation of the tensile stress field (first principal stress) for different relative thicknesses of a specimen with $R/R_S=1.5$ and $\nu=0.25$. a) displays the result for a specimen with $t/R_S=0.05$, b) for $t/R_S=0.25$ and c) for $t/R_S=0.5$. Each contour gives a 10%-percentile of the maximum stress from 0 (blue) to the maximum stress (red). Gray represents compressive stresses.

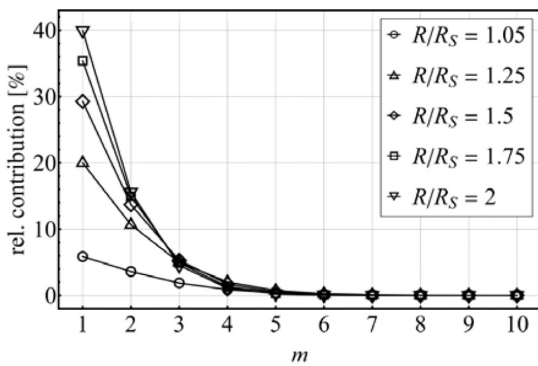


Fig. 6. Contribution of the overhang to the effective volume (PIA criterion). The results were obtained with Model 1 for discs with $t=0.2$ mm, $R_s=10$ mm and $\nu=0.25$.

shaped specimens, but almost identical tendencies are found for square plates. The maximum first principal stress in the center of the specimen was utilized for σ_{ref} .

4.1. Geometrical dependencies of V_{eff} and S_{eff}

The effective volume in dependence of the Weibull modulus m is

given in Fig. 3. Note the strong decrease of V_{eff} (more than six orders of a magnitude) with an increase in m and the change of slope at approximately $m=2$ and $m=10$.

The influence of the specimen's thickness on the effective volume and effective surface is shown in Fig. 4a) and b) for an exemplary geometry. Contrary to initial assumptions based on the behavior of S_{eff} for the Ring-on-Ring-test, the effective surface for the B3B-test is strongly dependent on the specimen's thickness, similar to the effective volume, where this effect was expected. This is due to a change in the general shape of the stress field, i.e. a widening of the region of maximum stress with an increase in thickness, as shown in Fig. 5a)-c).

To assess the influence of the relative specimen radius R/R_S , V_{eff} was evaluated for either the full specimen, $V_{eff,full}$, or just the regions included within R_S , $V_{eff,support}$. Fig. 6 displays the relative contribution of the overhang

$$rel.contr. = \frac{V_{eff,full} - V_{eff,support}}{V_{eff,full}} \quad (16)$$

in dependence of the Weibull modulus m for several geometries. It is evident that the overhang significantly influences V_{eff} for very low Weibull moduli ($m < 5$) but has a vanishing influence as soon as m increases.

4.2. The relation of V_{eff} to S_{eff}

For many bending-based testing methods, it is possible to analytically derive a relationship between the effective surface and the effective

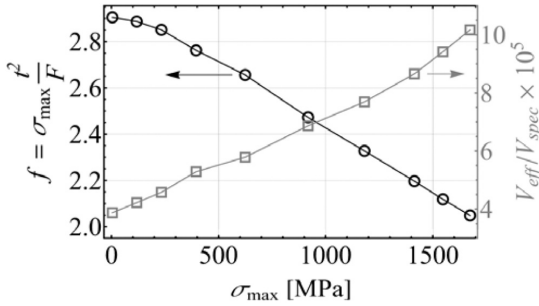


Fig. 7. Normalized maximum tensile stress and normalized effective volume (PIA criterion) in dependence of the maximum tensile stress σ_{max} for $m=10$. The results were obtained with *Model 3* for a disc with $t=0.5$ mm, $R=10.5$ mm, $R_s=10$ mm, a Young's modulus of 70 GPa and $\nu=0.25$.

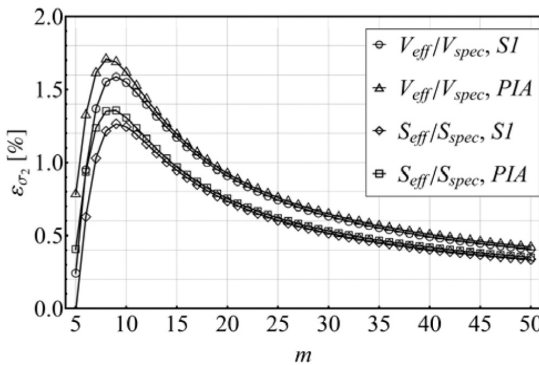


Fig. 8. Relative error in strength extrapolation, ϵ_{σ_2} , in dependence of the Weibull modulus m for the same parameters as in Fig. 7. The maximum tensile stress is 233 MPa.

Table 3

Geometry and testing parameters. N gives the number of tested specimens, t_{mean} the average specimen thickness and the related standard deviation (STD), t_{min} and t_{max} the minimum and maximum specimen thickness, respectively, and s gives the crosshead-speed.

Designation	N	$t_{mean} \pm STD$ [mm]	t_{min} [mm]	t_{max} [mm]	s [mm/min]
Sample A	37	0.246 ± 0.013	0.222	0.281	0.6
Sample B	53	1.548 ± 0.024	1.460	1.608	1.5

volume for the same multiaxial stress criteria. In the ideal bending case, a linear decrease of the magnitude of stress within a specimen from the tensile surface to the neutral plane (a path perpendicular to the bending axis/plane, parallel to the loading direction) is observed, independent of the position on the specimen. Considering this behavior and disregarding the lateral surfaces, Eq. (6) can be utilized to derive the relationship

Table 4

Results of strength testing, with \hat{m}_b as the biased and \hat{m}_{ub} as the unbiased Weibull modulus, and all other variables as defined before. The subscripts *lower* and *upper* indicate the extent of the 90% confidence intervals for the respective variable.

Designation	\hat{m}_b	\hat{m}_{ub}	\hat{m}_{lower}	\hat{m}_{upper}	$\hat{\sigma}_0$	$\hat{\sigma}_{0,lower}$	$\hat{\sigma}_{0,upper}$	S_{eff}	$S_{eff,lower}$	$S_{eff,upper}$
	[-]	[-]	[-]	[-]	[MPa]	[MPa]	[MPa]	[mm ²]	[mm ²]	[mm ²]
Sample A	12.1	11.7	9.4	14.5	1134	1106	1162	0.048	0.037	0.075
Sample B	17.5	17.1	14.3	20.4	906	894	919	0.639	0.540	0.802

$$V_{eff} = S_{eff} \frac{t}{2(m+1)} \tag{17}$$

to relate V_{eff} and S_{eff} , with the other variables as defined before [9,24]. Through analyzing the B3B-test with FEA, it was found that an ideal linear decrease of stress is not given for the centermost region of the specimen. Since the central region determines the majority of V_{eff} , this deviation from the ideal case is too severe ($\pm 50\%$) to utilize the conversion given in Eq. (17). Therefore, separate results for V_{eff} and S_{eff} have to be utilized to accurately determine both quantities.

4.3. The impact of non-linear effects

Previous work of the authors has shown that the maximum tensile stress may strongly depend on the applied load, especially for thin and flexible specimens. This is due to non-linear effects, e.g. specimen deformation and deviations from the ideal punctiform load introduction [21]. However, not just the maximum tensile stress, but the general shape of the tensile stress field changes due to these effects. Consequently, this impacts the results for V_{eff} and S_{eff} , in particular for high values of the Weibull-modulus m . To assess the influence of non-linear effects on the effective volume and surface, *Model 3* was utilized. Due to the increase in computational complexity by the use of contact simulations, the number of total elements had to be lower than that of the other models. Therefore, the absolute values for V_{eff} and S_{eff} differ slightly from the values generated through *Model 1* and *Model 2*, but the general tendencies can still be analyzed. Through previous investigations [21], it has been determined that thin glass specimens, e.g. with a relative thickness $t/R_s=0.05$ and a Young's modulus = 70 GPa, exhibit the strongest load-dependency within the valid range of parameters (see Table 2). For the following analysis, these parameters along with $R/R_s=1.05$ and $\nu=0.25$ were utilized. Fig. 7 displays the results for the normalized stress f

$$f = \sigma_{max} \frac{t^2}{F} \tag{18}$$

with F as the applied load and t as the specimen's thickness. On the secondary vertical axis, the normalized effective volume V_{eff}/V_{spec} in dependence of the maximum tensile stress for $m=10$ is shown. The effective volume has been calculated with the respective maximum tensile stress σ_{max} as the reference stress σ_{ref} and by utilizing the PIA-criterion. While f decreases by about 30% through a decrease in bending moment, the normalized effective volume increases nearly threefold at a maximum stress of about 1600 MPa. The increase is caused by a widening of the central region of maximum tensile stress.

However, this strong dependency of V_{eff} on the applied load is not as

Table 5

Results of the pooled evaluation based on the maximum-likelihood method.

Parameter	Result
Reference surface S_0 [mm ²]	0.041
$\hat{\sigma}_0$ [MPa]	1132
\hat{m} [-]	13.5
$\hat{\Sigma}_0$ [MPa ¹³ √mm ²]	894

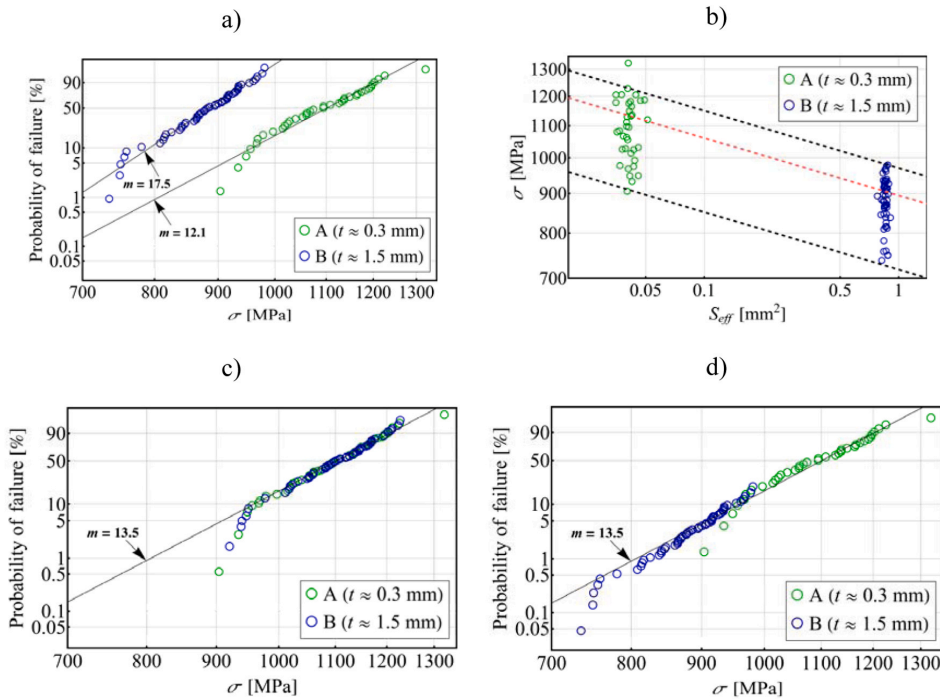


Fig. 9. a) depicts a Weibull plot of each sample individually. b) displays individual specimen strength plotted with their respective effective surface. The red line displays the 63% quantile. The negative inverse slope of the line corresponds to $\hat{m}_{pooled} = 13.5$. The upper and lower black lines represent the 95% and 5% quantiles, respectively. c) shows both samples in a traditional format, with each specimen’s strength extrapolated to $S_0 = 0.041$ mm². d) shows both samples in a traditional format as well, but with the probability of failure of each specimen extrapolated to $S_0 = 0.041$ mm². The slope of the black line in c) and d) is the Weibull modulus obtained through the pooled evaluation.

Table 6

Natural coordinates of the corner nodes of an element in three-dimensional space.

i	1	2	3	4	5	6	7	8
ξ_i	-1	1	1	-1	-1	1	1	-1
η_i	1	1	-1	-1	1	1	-1	-1
ζ_i	-1	-1	-1	-1	1	1	1	1

Table 7

Integration points r_i and associated weights w_i for 5th order Gauss-Legendre-Quadrature.

Index i	Integration points r_i	Weights w_i
1	0	0.568889...
2 & 3	$\pm 0.538469...$	0.478629...
4 & 5	$\pm 0.90618...$	0.236927...

relevant as it might first appear. This is due to two reasons: First, the results shown represent the worst-case scenario within the investigated parameter range. Second, V_{eff} and S_{eff} are most commonly used to convert or extrapolate strength results, as given through Eq. (14). As shown in Section 3.2, the influence of an error in V_{eff} or S_{eff} on the error in strength extrapolation using Eq. (14) is strongly dependent on the material’s Weibull-modulus m . For the results shown in Fig. 7, the observed relative error in V_{eff} , ϵ_V , has been translated to an error in strength extrapolation, i.e. $\epsilon_{\sigma 2}$, according to Eq. (15). Fig. 8 gives the result for $\epsilon_{\sigma 2}$ in dependence of m for V_{eff} and S_{eff} , each calculated with

both the PIA and S1 multiaxial stress criterion. In various previous work on the B3B-test, a general error of 2% on the obtained results was often utilized as an accuracy limit [21–23,25]. Therefore, these findings are discussed in the context of this accuracy limit and the displayed results correspond to a reduction of f by about 2%, which occurs at 233 MPa.

A maximum for $\epsilon_{\sigma 2}$ is reached between $m = 8$ and $m = 9$, depending on the effective size and stress criterion. This behavior is caused by two contrasting effects. On one hand, the error of the effective volume ϵ_V increases with an increase in m , see Fig. 7. On the other hand, the effect of this error on the stress extrapolation $\epsilon_{\sigma 2}$ decreases rapidly with an increase in m , as shown in Fig. 2. Most notably, $\epsilon_{\sigma 2}$ is always smaller than the error in f , i.e. 2%. If the maximum stress is increased further, the maximum of $\epsilon_{\sigma 2}$ increases and shifts to slightly higher Weibull-moduli. For the highest loaded case in Fig. 7, with a maximum tensile stress of about 1600 MPa, the maximum of $\epsilon_{\sigma 2}$ reaches nearly 10% and is found between $m = 9$ and $m = 10$. Note that this analysis has been performed on the “worst-case scenario”. For thicker and stiffer specimens, the influence of non-linear effects will decrease drastically, as will the value of $\epsilon_{\sigma 2}$. Therefore, for the range of parameters given in Table 2, $\epsilon_{\sigma 2}$ will always be smaller than the error of f . To determine an accurate result for the effective size, $\epsilon_{\sigma 2}$ should be smaller than 2%. This is guaranteed if the error of f is less than or equal to 2%. Through an equation and figures given in [21], a limit for the maximum applied load (in the form of a maximum specimen strength) to achieve an error of less than 2% in f can easily be predicted. These tools are valid for any combination of testing and material parameters as given in Table 2. If the tested specimens are within or close to these limits, non-linear effects don’t need to be considered and the results given in this work are sufficiently accurate. If the tested specimens surpass these limits significantly, the authors

recommend individual FEA to determine the most accurate results for the effective volume and surface.

4.4. Data availability

Any attempt to provide a functional expression describing the effective volume and surface were deemed either insufficiently accurate or too unwieldy to provide any meaningful benefit. The most accurate way to evaluate V_{eff} or S_{eff} for a specific geometry is to rely on interpolation of the generated data field. Therefore, all datapoints for discs and square plates, i.e. each effective size for both multi-axial stress criteria, are provided in the [supplementary material](#) of this work. These files are available in the comma-separated value format (.csv), the tab-separated format (.tsv) and as Excel-files (.xlsx). Each line contains the respective geometry- or material parameters (t/R_S , R/R_S , v and m) as well as the associated value for the effective size. To aid data evaluation, scripts for the interpolation of these data-files are provided in several coding languages (Mathematica & Python) as well as integrated in an Excel-file. Note that data evaluation through the Excel-file is limited to linear interpolation, while the other scripts allow higher order interpolation and are defaulted to third-order interpolation. For $m \geq 2$, the difference between linear and third-order interpolation is in the range of -8.2% to $+8.0\%$, with the highest differences obtained for specimens with a small relative thickness ($t/R_S < 0.2$). Due to the aforementioned effect of the Weibull-modulus on the size-scaling of strength data, this difference will only be relevant for small Weibull-moduli such as $m < 5$.

For some applications, such as a pooled evaluation of several sets of data, it is necessary to describe the dependence of the effective volume on the Weibull-modulus m . For common strength tests such as 3- or 4-point-bending, this dependency is given through their closed form solutions for the effective volume and effective surface. Since no closed form solution is available for the B3B-Test, a different method must be employed. For each fixed combination of geometric and material parameters, the effective volume V_{eff} or surface S_{eff} can be described through the expression

$$V_{eff}(m)_{t/R_S, R/R_S, v} = V_{spec} \times \exp \left[v_0 + v_1 \frac{m-1}{m+1} + v_2 \ln m + v_3 m^4 + v_4 \frac{1}{m} \right] \quad (19)$$

$$S_{eff}(m)_{t/R_S, R/R_S, v} = S_{spec} \times \exp \left[s_0 + s_1 \frac{m-1}{m+1} + s_2 \ln m + s_3 m^4 \right] \quad (20)$$

with v_0 - v_4 (or s_0 - s_3) as constants determined through fitting of the respective datapoints and the other variables as defined before. V_{spec} and S_{spec} are the total volume of the specimen or the area of the tensile loaded face, respectively. This expression can be utilized to fit both discs and square plates and both multi-axial stress criteria. The determination of v_0 - v_4 (or s_0 - s_3) is included in the Python and Mathematica scripts in the [supplementary material](#). The authors recommend to fit Eqs. (19) & (20) to the results from $m=2$ to $m=50$ to achieve an error of less than 5% (which is the default range within the provided scripts). If this range in m is narrowed, the error of the fits will decrease.

5. Employing V_{eff} and S_{eff} for pooled Weibull evaluation

To give an example for the need and application of the data and expressions provided above, strength results from B3B-testing of Si_3N_4 will be utilized. Due to the high variability in geometry in some of the tested specimens, the standard procedure according to EN-843-5 provides erroneous results. Instead, a pooled data evaluation through taking the effective volume or surface of each specimen into account is performed and the results are discussed.

The specimen material SL200 B ($\nu=0.27$, Young's modulus=305 GPa) was produced by CeramTec (CeramTec-Platz 1-9, 73207 Plochingen, Germany) and provided as rectangular billets [26]. From these, square plates with an edge length $L=11$ mm and an approximate

thickness $t=0.25$ mm or $t=1.5$ mm were cut. The tension-loaded side of each specimen was ground with a D46-diamond grit grinding wheel to purposely introduce surface defects. The testing fixture is built according to the design outlined in [23,27,28] and support balls with a diameter of $2R_{SB}=7.5$ mm were utilized, resulting in a support radius $R_S=4.33$ mm. All specimens were tested with the universal testing machine Z010 (ZwickRoell GmbH & Co. KG, August-Nagel-Strasse 11, 89079 Ulm, Germany) at a constant crosshead-speed s and failure occurred within 5–15 s. The dimensions of the tested specimens and their testing parameters are given in Table 3.

The strength was calculated according to [21]. The results of the statistical strength evaluation according to EN-843-5 are given in Table 4 [29]. Note that this procedure assumes the same geometry for each specimen in each sample. To differentiate from the true, unknown parameters σ_0 and m , the results obtained from an “estimator”, e.g. maximum likelihood, will be denoted as $\hat{\sigma}_0$ and \hat{m} . Fractography has shown that failure is caused by surface flaws, hence why the effective surface S_{eff} will be utilized for any further analyses. For these results, the average geometry of each sample was utilized to determine S_{eff} through interpolation of the data provided in the [supplementary material](#) of this work. Note the difference in S_{eff} of more than one order of magnitude between the samples.

To determine the material's Weibull-modulus from the information gained from both samples, the characteristic strength of each set of strength data is plotted in dependence of the effective surface or volume on a logarithmic scale. This is a graphical representation of Eq. (14). Then, the slope of a linear regression k_{reg} through all pairs of data is determined. From k_{reg} , the “regression modulus” \hat{m}_{reg} is determined through $\hat{m}_{reg} = -1/k_{reg}$. From the results given in Table 4, a “regression modulus” \hat{m}_{reg} of 11.5 is determined.

However, the specimens of Sample A show a significant variation in thickness, with a relative difference of approximately 26% from the thinnest to the thickest specimen. As shown in previous chapters, the specimen's thickness has a pronounced effect on the effective surface and effective volume of B3B-specimens. Therefore, statistical strength evaluation according to EN-843-5 for this set of data is flawed, since a nearly constant specimen geometry, i.e. similar effective surface for each individual specimen, is assumed. Instead, strength evaluation for multiple specimen geometries should be performed through a pooled Weibull evaluation, as first outlined by Johnson & Tucker in 1992 [4,11,30]. The method will be presented utilizing the effective volume, but it can equally be applied using the effective surface. Similar to data evaluation in EN-843-5, this procedure is based on the maximum-likelihood method to obtain point estimates of the parameters of the distribution that describes the scatter of strength data. In the context of measuring the strength σ_i of n specimens, the likelihood function L is defined through

$$L = \prod_{i=1}^n p_i \quad (21)$$

with p_i as the probability density to obtain σ_i . Consequently, the likelihood L is a measure for the probability to obtain the measured sample. The estimates for the searched parameters are defined to be those for which L becomes maximal. To simplify the numerical evaluation, the likelihood can be expressed as the log-likelihood function

$$\ln L = \sum_{i=1}^n \ln p_i \quad (22)$$

instead, since it has been shown that the maximum of L corresponds to the maximum of $\ln L$. In the case of the Weibull distribution, the distribution parameters are m and σ_0 for a chosen reference volume V_0 , with p_i as the probability density function (PDF) of the Weibull distribution. The PDF is obtained by differentiating the cumulative distribution function, i.e. Eq. (7), with respect to σ_i , which gives

$$p_i = \left(\frac{dP}{d\sigma} \right)_{\sigma=\sigma_i} = m \frac{V_{eff,i}}{V_0} \frac{\sigma_i^{m-1}}{\sigma_0^m} \exp \left[- \frac{V_{eff,i}}{V_0} \left(\frac{\sigma_i}{\sigma_0} \right)^m \right] \quad (23)$$

with the variables as defined before. Inserting Eq. (23) into Eq. (22) yields an expression for the log likelihood function L

$$\ln L = n \ln(m) - n m \ln(\sigma_0) + \sum_{i=1}^n \ln \left(\frac{V_{eff,i}}{V_0} \right) + (m-1) \sum_{i=1}^n \ln(\sigma_i) - \sum_{i=1}^n \frac{V_{eff,i}}{V_0} \left(\frac{\sigma_i}{\sigma_0} \right)^m \quad (24)$$

for a set of n strength measurements. To maximize $\ln L$, partial derivatives with respect to either m or σ_0 are taken and set equal to zero, respectively. By combining the two resulting equations, a function solely depending on m is obtained. Solving this equation gives a maximum-likelihood estimate \hat{m} for m :

$$0 = \frac{n}{\hat{m}} + \sum_{i=1}^n \frac{1}{V_{eff,i}} \frac{dV_{eff,i}}{dm} + \sum_{i=1}^n \ln \sigma_i - n \frac{\sum_{i=1}^n \left(V_{eff,i} \sigma_i^{\hat{m}} \ln \sigma_i + \sigma_i^{\hat{m}} \frac{dV_{eff,i}}{dm} \right)}{\sum_{i=1}^n V_{eff,i} \sigma_i^{\hat{m}}} \quad (25)$$

Since the term $dV_{eff,i}/dm$ occurs, it is necessary to know the functional dependence of the effective volume for each specimen on the Weibull-modulus m (see Eq. (20)). With \hat{m} determined, the maximum-likelihood estimate $\hat{\sigma}_0$ for σ_0 is obtained through

$$\hat{\sigma}_0 = \sqrt[n]{\frac{1}{n} \sum_{i=1}^n \frac{V_{eff,i} \sigma_i^{\hat{m}}}{V_{0,i}}} \quad (26)$$

Following this procedure for the experimental data and utilizing S_{eff} instead of V_{eff} , new and consistent results for $\hat{\sigma}_0$ and \hat{m} were determined, as given in Table 5. Similarly, the method can be applied using average specimen geometries for each sample instead of individual specimen geometries. This vastly reduces the necessary number of functional expressions for S_{eff} to just one per sample. It should be mentioned that \hat{m} can also be determined from Eq. (24) by utilizing a maximizing algorithm and avoiding the usage of derivatives (as has been done in this work) instead of finding the root of Eq. (25). The benefit of utilizing Eq. (25) over Eq. (24) is a more reliable convergence towards \hat{m} due to the reduction of two variables to one.

Fig. 9a) shows a traditional Weibull plot for each sample, with the data as measured from strength testing. As expected, smaller specimens exhibit a higher strength due to the size effect [3,4]. Fig. 9b) shows the strength of each sample, but now in dependence of the effective surface for each individual specimen. Through this presentation, the large scatter of the effective surface of specimens of sample A is clearly visible. In Fig. 9c), a traditional Weibull plot is depicted again, but with the strength of both samples extrapolated to the same reference surface, i.e. $S_0 = 0.041 \text{ mm}^2$, through strength scaling according to Eq. (14). This results in a horizontal shift of the individual datapoints, especially those of Sample B, as the reference surface is the average effective surface of Sample A. If the material behaves according to Weibull theory, a mixing of both distributions should be observed, as shown in this case. Finally, Fig. 9d) shows a Weibull plot with the probability of failure of each specimen extrapolated to the reference surface $S_0 = 0.041 \text{ mm}^2$. The extrapolated probability of failure $P_{0,i}$ for each specimen i is obtained through

$$\ln \ln \left(\frac{1}{1-P_{0,i}} \right) = \ln \ln \left(\frac{1}{1-P_i} \right) + \ln \left(\frac{S_0}{S_{eff,i}} \right) \quad (27)$$

with P_i as the probability of failure for each specimen, and $S_{eff,i}$ as the

respective effective surface of that specimen [4]. This approach gives insight into the material's behavior at low strengths and if an extrapolation based on Weibull-Theory is reasonable. If the material behaves according to Weibull theory, a single linear trend with a clear distinction between the individual samples should be observed, as shown in Fig. 9d).

In conclusion, through testing several different specimen geometries and a subsequent pooled data evaluation, more information about the tested material can be acquired. First, testing at several different V_{eff} or S_{eff} (through varying the specimen geometry or the testing method) gives a better understanding whether the investigated material can be considered a "Weibull-material" or not [31]. Furthermore, due to the increased number of individual specimens for statistical analysis, the confidence intervals will be reduced [32]. Finally, testing larger specimens results in testing larger defects, through which lower probabilities of failure are measured, instead of extrapolated, as depicted in Fig. 9d) [33,34].

6. Summary

In this work, the effective volume V_{eff} and the effective surface S_{eff} have been investigated for the Ball-on-Three-Balls-test (B3B). While the B3B-test is a commonly used biaxial strength testing method, these quantities have only been available for a small range of specimen geometries and materials so far. This is due to the lack of an accurate analytical description for the stress field of the B3B-test. Consequently, V_{eff} and S_{eff} must be numerically determined through Finite-Element-Analysis (FEA).

Therefore, a thorough analysis of the effective volume and surface for the B3B-test for a wide range of specimen geometries and materials has been conducted. Two models were implemented in ANSYS to determine the effective volume and surface for both discs and square plates. In the supplementary material of this work, the effective volume and surface is provided as tabulated data in various formats together with the tools to utilize them for specific specimens. Furthermore, the influence of non-linear effects on the accuracy of the provided data is discussed and quantified through a separate FEA-model. Additionally, the necessary accuracy of the provided results for Weibull strength scaling is investigated.

For any given choice of geometry parameters within the range of this work, a fitting model that describes V_{eff} and S_{eff} as a function of the Weibull modulus is given. Finally, the application of the results and functions provided in this work for the statistical analysis of experimental strength data is demonstrated through an example of pooled Weibull evaluation. In the appendix of this work, the determination of the effective volume and surface through a FEA-post-processing routine is outlined in detail.

Declaration of Competing Interest

The authors declare that they have no known competing financial interests or personal relationships that could have appeared to influence the work reported in this paper.

Acknowledgements

M. Staudacher gratefully acknowledges financial support by the Austrian BMVIT and BMWFW in the project "CharAM" (FFG 877684) of the COIN/IraSME program. The authors would like to thank Johannes Neumüller for his work on the scripts provided in the supplementary material of this work.

Appendix A. Numerical evaluation of V_{eff} and S_{eff}

This section will demonstrate the determination of V_{eff} and S_{eff} from the results of FEA, based on the procedure given in [35]. It will be outlined for the determination of V_{eff} and the use of linear elements, but it can equally be applied to the determination of S_{eff} or the use of higher order elements.

Generally speaking, the procedure aims to determine $V_{eff}^{(e)}$ in each element individually through

$$V_{eff}^{(e)} = \iiint_{V^{(e)}} \left[\frac{\sigma^{(e)}(x, y, z)}{\sigma_{ref}} \right]^m dV \quad (28)$$

with the superscript (e) referring to quantities of the individual elements and the other variables as defined before. The maximum first principal stress in the center of the specimen was utilized for σ_{ref} . Through numerical integration of Eq. (28) and subsequent summation of the results of all individual elements, V_{eff} for the full model is obtained. To simplify the integration limits for an element in an arbitrary position in three-dimensional space, its position in cartesian coordinates (x, y, z) is transformed to a natural coordinate system (ξ, η, ζ), in which each element is represented as a cube within the space $(-1, 1)$.

Within natural coordinates, each element is described through $i = 8$ shape functions $h_i(\xi, \eta, \zeta)$, which give the value 1 at each respective node with position (ξ_i, η_i, ζ_i) and 0 at all other nodes:

$$h_i(\xi, \eta, \zeta) = \frac{1}{8} (1 + \xi_i \xi) (1 + \eta_i \eta) (1 + \zeta_i \zeta) \quad (29)$$

The coordinates (ξ_i, η_i, ζ_i) of each node within an element are given in Table 6. Superimposing these functions gives a linear interpolation within the element for any value at each node. If this is performed for the cartesian coordinates x_i, y_i and z_i of each node, the following transformation functions are derived:

$$x^{(e)}(\xi, \eta, \zeta) = \sum_{i=1}^8 x_i^{(e)} h_i(\xi, \eta, \zeta) \quad (30)$$

$$y^{(e)}(\xi, \eta, \zeta) = \sum_{i=1}^8 y_i^{(e)} h_i(\xi, \eta, \zeta) \quad (31)$$

$$z^{(e)}(\xi, \eta, \zeta) = \sum_{i=1}^8 z_i^{(e)} h_i(\xi, \eta, \zeta) \quad (32)$$

In order to use this transformation in the following calculations, the determinant of the Jacobian-Matrix $J^{(e)}(\xi, \eta, \zeta)$ for the three-dimensional case will be necessary, which is given through

$$J^{(e)}(\xi, \eta, \zeta) = Det \begin{bmatrix} \frac{\partial x}{\partial \xi} & \frac{\partial y}{\partial \xi} & \frac{\partial z}{\partial \xi} \\ \frac{\partial x}{\partial \eta} & \frac{\partial y}{\partial \eta} & \frac{\partial z}{\partial \eta} \\ \frac{\partial x}{\partial \zeta} & \frac{\partial y}{\partial \zeta} & \frac{\partial z}{\partial \zeta} \end{bmatrix} \quad (33)$$

Similarly, superimposing the shape functions for the results of stress evaluation, i.e. the equivalent stress $\sigma_{eq,i}^{(e)}$ at each node, gives a function $f^{(e)}(\xi, \eta, \zeta)$ that allows stress interpolation within each element:

$$f^{(e)}(\xi, \eta, \zeta) = \sum_{i=1}^8 \sigma_{eq,i}^{(e)} h_i(\xi, \eta, \zeta) \quad (34)$$

This finally allows stress integration with natural coordinates within a single element to determine its effective volume $V_{eff}^{(e)}$ according to

$$V_{eff}^{(e)} = \iiint_{V^{(e)}} \left[\frac{f^{(e)}(\xi, \eta, \zeta)}{\sigma_{ref}} \right]^m dV = \int_{-1}^1 \int_{-1}^1 \int_{-1}^1 \left[\frac{f^{(e)}(\xi, \eta, \zeta)}{\sigma_{ref}} \right]^m J^{(e)}(\xi, \eta, \zeta) d\xi d\eta d\zeta \quad (35)$$

with the variables as defined before. The next step is a numerical integration of Eq. (35). In this work, Gauss-Legendre-Quadrature is utilized, which gives accurate estimates for the definite integral of a function in the space $(-1, 1)$ through

$$\int_{-1}^1 f(x) dx \approx \sum_{i=1}^n w_i f(r_i) \quad (36)$$

for the one-dimensional case. The points of integration r_i are given by the order n of the Gauss-Legendre-Quadrature as the roots of the n^{th} Legendre polynomial, and w_i are the respective quadrature weights. The integration points and associated weights for 5th-order quadrature are given in Table 7. For multiple dimensions, the integration points are iterated in every dimension and the associated weights are the product of their respective one-dimensional weights.

Applying this procedure to Eq. (35) with a n^{th} order quadrature converts the integral to

$$V_{eff}^{(e)} = \sum_{i=1}^n \sum_{j=1}^n \sum_{k=1}^n \left[\frac{f^{(e)}(r_i, r_j, r_k)}{\sigma_{ref}} \right]^m w_i w_j w_k J^{(e)}(r_i, r_j, r_k) \quad (37)$$

for the effective surface of a single element. By conducting this evaluation for every tensile loaded element and adding them up, the effective volume V_{eff} for the full model is determined. In the same way, the effective surface can be determined for two-dimensional elements. For higher-order elements, the procedure doesn't have to be changed as long as the results of stress evaluation are saved on the nodes at the corners of elements.

However, a problem arises for two-dimensional elements or element-faces in a three-dimensional model (e.g. when S_{eff} shall be determined for a three-dimensional model). While these faces are defined by two dimensions in natural coordinates, their position is determined by three dimensions in the cartesian space. Therefore, the transformation functions yield a non-square Jacobi-Matrix, for which the determinant can't be formed. In that case, the determinant of the Gram-Matrix $J^{(e)T}(\xi, \eta) \times J^{(e)}(\xi, \eta)$ is formed instead and its square root $G^{(e)}(\xi, \eta)$ replaces $J^{(e)}(\xi, \eta)$ in Eq. (35).

$$G^{(e)}(\xi, \eta) = \sqrt{Det[J^{(e)T}(\xi, \eta)J^{(e)}(\xi, \eta)]} \quad (38)$$

Appendix B. Supporting information

Supplementary data associated with this article can be found in the online version at [doi:10.1016/j.jeurceramsoc.2023.09.018](https://doi.org/10.1016/j.jeurceramsoc.2023.09.018).

References

- [1] R. Morrell, Biaxial flexural strength testing of ceramic materials: A National Measurement Good Practice Guide No. 12, National Physical Laboratory, 2007.
- [2] Weibull W., A Statistical Theory of the Strength of Materials, Generalstabens Litografiska Anstalts Förlag, Stockholm, 1939.
- [3] D. Munz, T. Fett, Ceramics: mechanical properties, failure behaviour. Materials Selection, Springer, Berlin, Heidelberg, 1999.
- [4] J.B. Wachtman, M.J. Matthewson, W.R. Cannon, Mechanical Properties of Ceramics, Wiley, Hoboken, New Jersey, 2009.
- [5] G.K. Bansal, W.H. Duckworth, D.E. Niesz, Strength-size relations in ceramic materials: investigation of an alumina ceramic, J. Am. Ceram. Soc. 59 (1976) 472–478.
- [6] R. Jain J. Lock S.F. Duffy Effective area and effective volume calculations for ceramic test SPECimens, in: ASME Turbo Expo Orlando (Ed.) ASME Turbo Expo. 2009 231 239.
- [7] G.D. Quinn, Weibull strength scaling for standardized rectangular flexure specimens, J. Am. Ceram. Soc. 86 (2003) 508–510.
- [8] G.D. Quinn, Weibull effective volumes and surfaces for cylindrical rods loaded in flexure, J. Am. Ceram. Soc. 86 (2003) 475–479.
- [9] ASTM C 1499-05: Test Method for Monotonic Equibiaxial Flexural Strength of Advanced Ceramics at Ambient Temperature, ASTM International, West Conshohocken, PA, 2005.
- [10] H. Rinne, The Weibull Distribution: A Handbook, CRC Press, Boca Raton, 2009.
- [11] C.A. Johnson, W.T. Tucker, Advanced Statistical Concepts of Fracture in Brittle Materials, Ceramics and Glasses, Eng. Mater. Handb. 4 (1991) 709–715.
- [12] R. Danzer, A general strength distribution function for brittle materials, J. Eur. Ceram. Soc. 10 (1992) 461–472.
- [13] I.E. Reimanis, R.A. Schaut, Hertzian testing to obtain flaw distributions in high strength glasses and glass-ceramics, J. Am. Ceram. Soc. 99 (2016) 3712–3718.
- [14] ASTM C 1683 - 10: Practice for Size Scaling of Tensile Strengths Using Weibull Statistics for Advanced Ceramics, ASTM International, West Conshohocken, PA, 2019.
- [15] D. Gross, T. Seelig, Bruchmechanik: Mit einer Einführung in die Mikromechanik, 6th ed., Heidelberg Springer Vieweg, Berlin, 2016.
- [16] P. Stanley, H. Fessler, A.D. Sivill, An engineer's approach to the prediction of failure probability of brittle components, Proc. Brit. Ceram. Soc. 22 (1973) 453–487.
- [17] A.M. Freudenthal, Statistical approach to brittle fracture, Fracture 2 (1968) 591–619.
- [18] R.L. Barnett, P.C. Hermann, J.R. Wingfield, C.L. Connors, Fracture of Brittle Materials Under Transient Mechanical and Thermal Loading, 1967.
- [19] J.A. Salem, L. Powers, Guidelines for the testing of plates, in: H.-T. Lin, W. M. Kriven (Eds.), 27th International Cocoa Beach Conference on Advanced Ceramics and Composites: January 26-31, 2003, Cocoa Beach, Florida, American Ceramic Society, Westerville, Ohio, 2003, pp. 357–364.
- [20] D.J. Godfrey, S. John, Disc flexure tests for the evaluation of ceramic strength, Proc. 2nd Int. Conf. Ceram. Mater. Compon. Engines 14–17 (1986) 657–665.
- [21] M. Staudacher, T. Lube, P. Supancic, The Ball-on-Three-Balls strength test for discs and plates: Extending and simplifying stress evaluation, J. Eur. Ceram. Soc. 43 (2023) 648–660.
- [22] A. Börger, P. Supancic, R. Danzer, The ball on three balls test for strength testing of brittle discs: Stress distribution in the disc, J. Eur. Ceram. Soc. 22 (2002) 1425–1436.
- [23] R. Danzer, P. Supancic, W. Harrer, Der 4-Kugelversuch zur Ermittlung der biaxialen Biegefestigkeit spröder Werkstoffe, Kriegsman, J. (Hrsg): Tech. Keram. Werkst. (2009) 1–48.
- [24] H.L. Frandsen, Weibull statistics effective area and volume in the ball-on-ring testing method, Mech. Mater. 73 (2014) 28–37.
- [25] A. Börger, P. Supancic, R. Danzer, The ball on three balls test for strength testing of brittle discs: Part II: analysis of possible errors in the strength determination, J. Eur. Ceram. Soc. 24 (2004) 2917–2928.
- [26] T. Lube, J. Dusza, A silicon nitride reference material—A testing program of ESIS TC6, J. Eur. Ceram. Soc. 27 (2007) 1203–1209.
- [27] W. Harrer, R. Danzer, P. Supancic, T. Lube, The Ball on Three Balls Test: Strength Testing of Specimens of Different Sizes and Geometries, Proc. 10th ECerS Conf. 2008 (2008) 1271–1275.
- [28] R. Danzer, A. Börger, P. Supancic, M.A. Ruiz, Villanueva, Ein einfacher Festigkeitsversuch für Scheiben aus spröden Werkstoffen, Mat.-Wiss. U. Werkst. 34 (2003) 490–498.
- [29] DIN EN 843-5: 2007: Advanced technical ceramics - Mechanical properties of monolithic ceramics at room temperature - Part 5: Statistical analysis, German Institute for Standardisation (Deutsches Institut für Normung), 2007.
- [30] C.A. Johnson, W.T. Tucker, Weibull estimators for pooled fracture data life prediction methodologies and data for ceramic materials, ASTM STP 1201 (1994).
- [31] R. Danzer, T. Lube, P. Supancic, R. Damani, Fracture of ceramics, Adv. Eng. Mater. 10 (2008) 275–298.
- [32] R. Danzer, T. Lube, P. Supancic, Monte Carlo simulations of strength distributions of brittle materials – type of distribution, specimen and sample size, Int. J. Mater. Res. 92 (2001) 773–783.
- [33] R. Danzer, P. Supancic, J. Pascual, T. Lube, Fracture statistics of ceramics – Weibull statistics and deviations from Weibull statistics, Eng. Fract. Mech. 74 (2007) 2919–2932.
- [34] R. Danzer, T. Lube, New fracture statistics for brittle materials, Fract. Mech. Ceram. 11 (1996) 425–439.
- [35] D. Mevec, Auslegung einer Festigkeitsprüfung von Dentalkeramik mittels des B3B-Tests, Chair of Structural and Functional Ceramics, Montanuniversität Leoben, 2016, (<https://pureadmin.unileoben.ac.at/ws/portalfiles/portal/1861498/AC13285197n01vt.pdf>).

Publication E

Comparison of biaxial strength measured with the Ball-on-Three-Balls- and the Ring-on-Ring-test

Maximilian Staudacher, Tanja Lube, Josef Schlacher, Peter Supancic

Department of Materials Science, Montanuniversität Leoben, Franz Josef-Strasse 18, A-8700
Leoben, Austria

Open Ceramics 6, (2021) 100101

doi: <https://doi.org/10.1016/j.oceram.2021.100101>

Reuse under the terms of license CC-BY-NC-ND 4.0



Comparison of biaxial strength measured with the Ball-on-Three-Balls- and the Ring-on-Ring-test



Maximilian Staudacher^{*}, Tanja Lube, Josef Schlacher, Peter Supancic

Department of Materials Science, Montanuniversität Leoben, Franz Josef-Strasse 18, A-8700, Leoben, Austria

ARTICLE INFO

Keywords:

Ball-on-Three-Balls testing
Ring-on-Ring testing
Finite element analysis
Alumina
Weibull size effect
Biaxial testing

ABSTRACT

The Ball-on-Three-Balls-test (B3B) and the Ring-on-Ring-test (RoR) were conducted on alumina discs and compared based on Weibull-Theory. The influence of various intermediate layers was evaluated. To support these findings, Finite-Element-Analysis was conducted to analyze the effects of deviations from ideal loading conditions. The influence of friction between sample and fixture and the effects of an inhomogeneous load distribution on the maximum stress were investigated. The experiments demonstrated that measuring corresponding strength values with both testing methods is possible. To properly assess the strength using the RoR-test, intermediate layers must be used. Teflon-foils or adhesive tapes are considered suitable. If no intermediate layer is used, the materials strength will be underestimated. Finite-Element-calculations show that this effect cannot be explained by the influence of friction and is rather caused by a non-homogeneous load distribution along the load-ring. Fractography supports these findings.

1. Introduction

Ceramic components have found their way into a multitude of highly technological and specific fields of application due to their unique thermal, electrical, chemical and mechanical properties [1]. However, some of their most notable downsides are the lack of ductility and a large scattering of mechanical strength [2]. On the upside, if the mechanisms behind these problems are understood well, component failure can be predicted and minimized [3]. Mechanical strength testing is well known as one of the key methods in order to understand failure behavior and a wide number of tests have been developed. The most common testing methods are some types of uniaxial tensile or compressive tests, uniaxial bending tests and biaxial bending tests [4]. The latter two are established as the main methods for strength testing of ceramic materials [4].

One of the main benefits of biaxial testing compared to uniaxial testing is the reduced influence of specimen preparation on its edges and the consequential possibility to omit edge preparation at all. Machining of ceramic materials is usually very time- and cost-intensive due to their inherent hardness and wear resistance. Additionally, any preparation method may introduce defects or flaws at already failure sensitive locations such as edges and surfaces. During uniaxial bending, edges and surfaces are subjected to the maximum stress as well and therefore influence failure significantly. On the other hand, biaxial tests like the

Ring-on-Ring-test are less dependent on specimen preparation at the edges since the maximum stresses occur at or in the area close to the specimen's center. Thus, the quality of the edge preparation is in most cases negligible with respect to the strength measurement in the specimen's center. If the specimens are manufactured in compatible size and shape, even testing in as-fabricated condition is possible [5]. Furthermore, biaxial loading provides a better representation of real-world loading scenarios of typical ceramic parts than uniaxial loading.

To ensure an independence of specimen orientation and uniform load distribution, equi-biaxial stress states are preferred. Several different tests with widely varying stress fields have been developed. The most common ones are the Ring-on-Ring-test [6,7], the Ball-on-Ring-test [8], the Piston-on-Balls-test [9], the Ball-on-Three-Balls-test [10,11] and the Three-Balls-on-Three-Balls-test [12]. In this work, the focus will be on the Ring-on-Ring-test (RoR) and the Ball-on-Three-Balls-test (B3B).

The Ring-on-Ring test is standardized in ASTM C1499 [6]. This establishes a good understanding of its capabilities and limitations. Alongside that, the loading condition exhibits a cylindrical symmetry which leads, in the case of isotropic materials, to a cylindrical symmetrical stress field that can be expressed in an analytical closed form. This allows an easy calculation of results and "effective" specimen sizes. Due to the comparatively large portion of maximum stress in the specimen's center, a good representation of the materials general strength can be

^{*} Corresponding author.

E-mail address: maximilian.staudacher@unileoben.ac.at (M. Staudacher).

measured. The major drawback of the Ring-on-Ring method is the need for some sort of lubricant or intermediate layer to reduce friction between the specimen and the loading fixture [6,13]. Especially intermediate layers might change load application depending on their material and thickness. Miniaturization of testing rigs is impeded by manufacturing tolerances of loading and support rings, resulting in a minimum support ring diameter of about 10 mm [13]. Moreover, concentric alignment of loading and support ring has to be ensured since small deviations of about 1% cause a difference in measured strength of about 2% [14]. No definitive numbers concerning the accuracy are available. However, an indication of precision (i.e. the coefficient of variation) of about 5–14% is mentioned in ASTM C1499 [6]. If intermediate layers are used, testing proves to be rather time consuming and cumbersome compared to other biaxial testing methods.

In contrast to the RoR-test, the Ball-on-Three-Balls-test does not require any intermediate layers. This major upside is achieved through elimination of all sources of friction by using freely movable balls as a support structure instead of a fixed ring [10]. The use of large balls (diameter typically approx. 70% of the specimens diameter) inhibits contact failure associated with the loading ball [15]. Furthermore, the combination of an easy testing procedure and the general benefits of biaxial testing (little to no specimen preparation) allow a comparatively high testing output. Typically, standardized bearing balls are used as support and load members, which allows test miniaturization with specimens as small as 2.0 mm × 2.0 mm due to the balls tight manufacturing tolerances [16–19]. This can prove to be very useful if only small batches of material, like in the dental ceramic field, are available [20,21]. The stress field exhibits a characteristic three-fold symmetry with the maximum tensile stress in the center between the three supporting balls. Since the region of maximum stress is comparatively small, localized strength testing of specific features or regions of interest within a specimen is possible [22]. However, if the general strength of a specimen has to be determined, the small region of maximum stress proves to be a significant drawback in terms of effective volume or area [23]. Another drawback is the absence of any analytical description of the stress field. Therefore, Finite-Element-Analysis results obtained for a large variety of possible test geometries have to be interpolated in order to determine the maximum stress in the center of the disc [24], or approximated using a fitted expression [10,25]. So far, the B3B-test has not been standardized. All in all, the B3B-test is robust against inaccurate specimen shapes and alignment errors and can be performed with a typical error of less than 2% [11].

According to ASTM C1499, and in order for the analytical stress expression to be valid, the possible specimen geometries for the RoR-test are limited by plate theory (and contact pressure) and the maximum amount of deflection [6,14,26]. As a result, typical values (for materials tested in this work) for the ratio of thickness to support ring diameter range between 0.1 and 0.023 in order to limit the error to ±2% [27]. As for the B3B-test, the authors refer to work published by Danzer et al. [25]. It describes suitable combinations of the parameters of relative strength (fracture strength divided by Young's modulus) and relative thickness (thickness divided by specimen radius), to guarantee a sufficiently small area of contact between the balls and the specimen. Ceramics generally show a low relative strength, which allows testing with $0.1 < t/R < 0.5$, with t being the specimen's thickness and R the specimen's radius.

So far, not many comparisons of strength results obtained with the B3B-test and with other test methods, especially standardized biaxial ones are available [28,29]. The main emphasis of the present work was to investigate whether the strength results measured with the Ball-on-Three-Balls-test and the Ring-on-Ring-test are comparable to each other in the framework of the statistical theory of fracture, i.e. in a similar way to 4- and 3-point bend tests [30]. Another topic of investigations was the role of intermediate layers on the strength. Furthermore, the influence of friction on the stress field was analyzed. To complement a series of performed fracture tests, Finite-Element-Analysis was conducted for the Ring-on-Ring-test.

2. Methods and material

2.1. Weibull fracture statistics and size effect

In order to compare the strength values and Weibull distributions determined with different test configurations, we presume that we investigate a "Weibull material" [31], i.e. a material which shows a size effect on strength as described by the Weibull theory [32–34]. In the following this idea is outlined for cases where specimens fail due to a defect located within the bulk of the material, but the concept can analogously be applied to failure due to surface located defects [16]. According to Weibull-Theory, the probability of failure P at a certain (equivalent) stress σ_r is given by:

$$F(\sigma, V) = 1 - \exp \left[- \frac{V_{eff}}{V_0} \left(\frac{\sigma_r}{\sigma_0} \right)^m \right] \quad (1)$$

with m being the "Weibull-modulus", which describes the scatter of measured strengths, and the characteristic strength σ_0 , which is related to the reference volume V_0 . Characteristic strength is defined as the stress necessary to achieve a 63.2% probability of failure at $V_{eff}/V_0 = 1$. The effective Volume V_{eff} is defined by the integral over the positive values of the stress field $\sigma(\vec{r})$:

$$V_{eff} = \int_{\sigma > 0} \left(\frac{\sigma(\vec{r})}{\sigma_r} \right)^m dV \quad (2)$$

with σ_r as an arbitrary reference stress, usually representing the maximum stress in the specimen [30]. V_{eff} describes the theoretical volume of a tensile specimen with the same probability of failure at σ_r as the non-homogeneously loaded specimen. In the case of biaxial loading, some form of equivalent stress has to be defined to properly quantify the complex stress state. Several methods such as the S1 criteria or PIA are proposed [30,35]. For this work, the "Principle of Independent Action", or PIA, was used [36]. If σ_I , σ_{II} and σ_{III} are the (positive, tensile) principle stresses and m is the Weibull modulus, the equivalent stress σ_e is calculated as:

$$\sigma_e = (\sigma_I^m + \sigma_{II}^m + \sigma_{III}^m)^{1/m} \quad (3)$$

and can be used in the same way as in an uniaxial scenario in all equations previously mentioned (note: in case of compressive stress components, these contributions are clipped to zero). Utilizing eq. (1) to compare different volumes at the same probability of failure, the following relationship can be derived:

$$\frac{\sigma_1}{\sigma_2} = \left(\frac{V_{eff,2}}{V_{eff,1}} \right)^{1/m} \quad (4)$$

with σ_i and $V_{eff,i}$ describing strength and effective volume of specimen type 1 or 2. Elaborating on eq. (4), larger effective volumes result in a lower strength and vice versa. This behavior can be utilized to compare different specimen sizes or testing methods for the same material. If characteristic strength of different specimen types is plotted as a function of effective volume on logarithmic scales, all data pairs should yield a straight line with slope $-1/m_{reg}$ [30]. If that condition is satisfied and the Weibull modulus m_{reg} derived from the slope is similar to that of each dataset, the tested material is a "Weibull material" [31]. This principle will be the basis for the comparison of samples tested with different testing methods in this work.

2.2. Investigated material

The investigated material Frialit F99.7 contains 99.5% alumina [37]. Its grain size is about 10 μm , and its microstructure contains about 2% pores as well as 1%–2% Mg-spinel. The microstructure of Frialit is shown

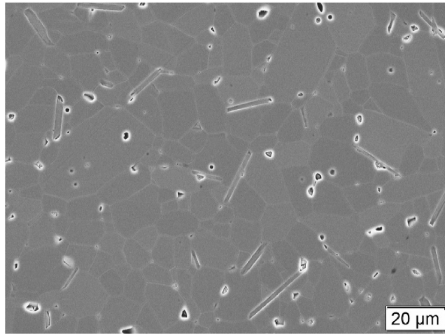


Fig. 1. Microstructure of KYOCERA Frialit, SEM, with clearly visible pores and elongated spinel grains.

in Fig. 1. The basic material properties can be found in Table 1. It was sourced from KYOCERA Fineceramics Solutions GmbH (68229, Mannheim, Germany) [37]. The material was provided as a rod of 28 mm diameter, which was cut and diamond ground into 1 mm and 1.7 mm thick discs. The prospective tension-loaded side of each specimen received a final grinding step using a D15 diamond grit wheel.

2.3. Experimental

The first developments on the Ball-on-Three-Balls method started in the 80s and were later further developed by Börger et al. [10,11,38,39]. It allows testing of discs and plates with minimal specimen preparation or even in as-sintered condition. It utilizes a single steel or carbide ball to apply the load and three moveable balls (which are in contact with each other) as a support structure [25]. The basic design is shown in Fig. 2(a) and a typical specimen after testing is shown in Fig. 3(a). The result is a localized maximum of stress in the center of the disc on the opposite side of the loading ball [40]. The maximum stress at failure σ_f of the specimen is calculated by the following formula [10,25]:

$$\sigma_f = f \left(\frac{2t}{D}, \frac{D_s}{D}, \nu \right) \cdot \frac{F}{t^2} \quad \text{with } D_s = \frac{2D_B}{\sqrt{3}} \quad (5)$$

with F as the applied force, ν as the Poisson's ratio, D as the specimen's diameter, t as the specimen's thickness, D_s as the diameter of the circle on which the three support points lie (i.e. support diameter) and D_B as the support ball diameter. The factor f is determined by interpolation of Finite-Element-Analysis results which assume load introduction by a point load [24] or by using a fitted polynomial on these FEA-results depending on the specimen's geometry and Poisson's ratio [10,25]. For this work, the maximum stress at failure was evaluated by using a third order interpolation function calculated with Mathematica 12.0 (Wolfram Research, IL 61820, Champaign, USA). The effective volumes and areas were determined by interpolation of FEA results as well.

The principle of the RoR-test can be seen in Fig. 2(b) and a specimen after testing in is shown in Fig. 3(b). Coaxial steel-rings are used to apply the load evenly along a certain radius and to provide support for the specimen. The result is a stress field with nearly equal and constant radial and tangential stresses within the diameter of the loading-ring and a drop-off towards the edge of the specimen. The stress field is ideally symmetric with respect to the central axis. An analytical solution of the stress field can be derived. The maximum stress at failure σ_f for discs is determined by Ref. [6]:

$$\sigma_f = \frac{3F}{2\pi t^2} \left[(1-\nu) \frac{D_s^2 - D_L^2}{2D^2} + (1+\nu) \ln \frac{D_s}{D_L} \right] \quad (6)$$

where F is the applied force, ν the Poisson's ratio, t the specimen's

Table 1
Mechanical properties of KYOCERA Frialit [37].

Property	Unit	KYOCERA Frialit
Density	[g/cm ³]	≥3.90
Purity	[weight-%]	>99.5
Open porosity	[Vol.-%]	0
Average grainsize	[μm]	10
Flexural strength DIN-EN 843-1	[MPa]	350
Weibull modulus	[–]	>10
Fracture toughness K_{Ic} (SEVNB)	[MPa m ^{1/2}]	3.5
Compressive strength	[MPa]	3500
Young's modulus	[GPa]	380
Poisson's ratio	[–]	0.22
Vickers Hardness HV1	[–]	1760

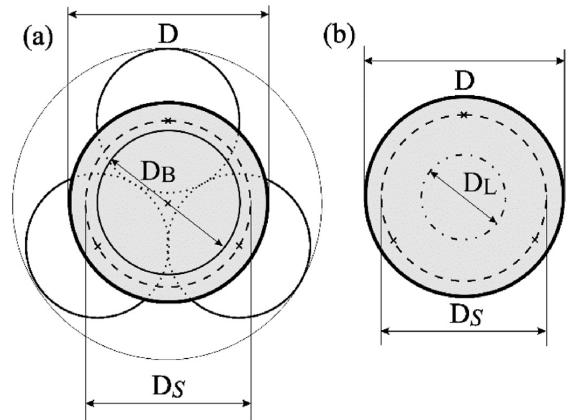


Fig. 2. Schematic of the B3B (a) and the RoR (b) loading layout [ref 36,43].

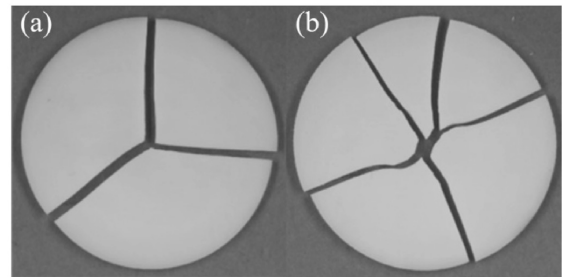


Fig. 3. Typical crack-patterns of fractured specimens for the B3B- (a) and RoR- (b) test.

thickness, D the specimen's diameter, D_L the load ring diameter and D_s the support ring diameter. The RoR-method has been proven to allow testing of discs and plates as well [6,41]. However, some limitations related to the specimen's thickness apply. If the specimen is too thin, large deformations restrict the use of linear geometric relations. If specimens are too thick, plate theory does not apply anymore and contact stress increase to a level where localized contact failure occurs [14,26, 42].

An important task during testing is to reduce friction between specimen and support and loading rings in order to avoid additional stresses which are not taken into account in eq. (6). The common approach is to either use intermediate layers or lubricants. Lubricants allow testing without any influence on the stress field, but greatly impede

fractographic analysis, whereas intermediate layers might change load application and distribution. In this work, several different loose and adhesive materials were employed as intermediate layers. Their names, manufacturers, materials and properties are found in Table 2. Adhesive tape was used because of two reasons: i) to eliminate friction and - a beneficial side effect - ii) to keep the fracture pieces together to facilitate fractographic analysis. If adhesive tape was used, it was always applied to the compression-loaded side to ensure the smallest possible impact on strength results. Care was taken to use intermediate layers only for tests with expected fracture loads below loads that lead to failure of the layer itself. Loose layers were solely utilized between the support ring and the specimen (tension-loaded side). Sample strength was evaluated using eq. (6). The effective volumes and areas were calculated in the same manner as done for the Ball-on-Ring test by Frandsen [43]. The occurring integrals were solved numerically in Mathematica 12.0.

All experiments were conducted using a Zwick Z010 test frame (ZwickRoell GmbH & Co. KG, 89079, Ulm, Germany) equipped with a Doli control system (Doli, 72525, Münsingen, Germany). B3B tests were conducted using 15.08 mm diameter balls (resulting in a support diameter of 17.42 mm). RoR testing rigs were manufactured from 42CrMo4 (1.7225) and hardened to HRC > 40 and has a surface -finish of about 1.2 μm . The discs were tested using a support-ring diameter of 17.24 mm and a loading-ring diameter of 8.31 mm, both with a cross-section diameter of 1.2 mm. In order to compare both testing methods, different thicknesses and intermediate layers were used. Table 3 shows all tested samples and gives details on the testing conditions. F_p describes the pre-load, v the constant cross-head speed, RH relative humidity, T the ambient temperature and N the number of tested specimens. Each sample, with the exception of R-28-1 and B-28-1.7-BT, was in alignment with standards [6] or with previously published guidelines [47,48]. R-28-1 was tested without any layers or lubricants and was therefore not tested according to standards. In contrast, the B3B-method does not call for any compliant layers, hence why B-28-1.7-BT was not tested correctly.

The Weibull parameters m (unbiased) and σ_0 were estimated from the strength of the individual specimens for each dataset using the Maximum-Likelihood-Method [2,4]. Confidence-intervals for m and σ_0 provide additional information about the statistical uncertainty which is essential when comparing multiple datasets [49]. In this work, 90% confidence intervals will be used.

2.4. Finite-Element-Analysis

Finite-Element-Analysis was conducted to complement the experiments. More specifically, the influence of friction during Ring-on-Ring testing for 28 mm diameter discs with a thickness of 1 mm, was evaluated. In order to ensure consistent model properties throughout different scenarios, the commercial FEA-program ANSYS R19.1 (ANSYS Inc., PA 15317, Canonsburg, USA) was chosen for its ability to implement Ansys-Parametric-Design-Language (APDL) scripts. To investigate the influence of friction within a geometrically perfect test situation, a simple 2D-

Table 2

Names, manufacturers, materials and properties of utilized intermediate layers [44–46].

Trade name	Manufacturer	Material	Layer thickness	Adhesive thickness
PTFE virginal foil 0.05-600	High-tech-flon (78467, Konstanz, Germany)	Teflon	50 μm	–
PTFE tape 0.08 V SW	High-tech-flon (78467, Konstanz, Germany)	Teflon	51 μm	38 μm
Flashbreaker® 1	Airtech International, Inc. (CA 91708, Chino, USA)	Polyester	25 μm	30 μm

Table 3

Summary of tested sets. The prefix indicates the testing method: B3B-method (B-) or the RoR-method (R-). The first number is the specimen diameter; the second number the specimen thickness, both in mm. The suffix indicates the intermediate layers: BT (Flashbreaker® 1 compression side, loose Teflon tension side) or T (Teflon-tape compression side, loose Teflon foil tension side). F_p describes the pre-load, v the constant cross-head speed, RH relative humidity, T the ambient temperature and N the number of tested specimens.

Designation	F_p [N]	v [mm/min]	RH [%]	T [°C]	N [–]
B-28-1	10	0.5	24	23.2	30
B-28-1.7	20	2	52	22.6	30
B-28-1.7-BT	20	2	51	22.4	32
R-28-1	20	1.5	50	24.5	28
R-28-1-T	20	1.5	21	22.6	30
R-28-1-BT	20	8.5	49	21.5	29

contact-model was sufficient to assess the full problem due to rotational symmetry. This model allows quantitative statements and comparison with existing analytical solutions [40]. More specifically, the specimen (Young's Modulus = 380 GPa, $\nu = 0.22$) was meshed with 3145 PLANE183 (8-node quad elements) elements and 9948 nodes. The loading and supporting rings (Young's Modulus = 210 GPa, $\nu = 0.3$) were meshed with 490 PLANE183 elements and 1516 nodes. Surfaces, which will come into contact during testing, were meshed with 338 CONTA172 and 338 TARGET169 elements. Symmetric contact calculation was utilized and the friction coefficient μ between specimen and both rings was varied between 0 and 0.5 in steps of 0.1. The model was loaded by a force of 600 N. The model is shown in Fig. 4(a).

Additionally, the influence of uneven surfaces of the loading ring and thus uneven load application was examined using FEA. For this investigation, a simplified 3D-model had to be used (no contact calculations). Therefore, only qualitative statements can be deduced. This model was meshed with 35266 SOLID 95 elements (20-node brick elements) and 140759 nodes. Due to symmetry, the model could be reduced to one half. The uneven load application was realized by applying an oscillating force with equally spaced maxima and minima along the load-ring contour. The script allowed for changes in both frequency and number of load maxima (Z) and amplitude (A) in percentage of the applied total force. An example of the model with an uneven force applied is shown in Fig. 4(b).

To verify the simplified model as described above, a single contact scenario of the full testing assembly was modeled with a 3D-contact-model (material properties as mentioned above). The surface of the loading ring was modified so that it follows a sine with an amplitude of 5 μm and 3 full periods along its circumference, similar to the load in Fig. 4(b). The model is shown in Fig. 4(c).

3. Results & discussion

As previously explained, the size effect will be used to compare different testing methods. Since fractography did not show volume flaws to be responsible for failure, the effective area will be used instead of effective volume as the basis for future comparison [16,35]. A comparison is valid, when two requirements are met. First, RoR samples have to exhibit a lower strength than B3B samples due to the larger effective area. Second, if a fit of eq. (4) through all data pairs (which appears as straight line in the plot of characteristic strength versus effective area), results in a fitted Weibull modulus m_{reg} (the inverse slope of the straight line) which is close to the Weibull moduli of the individual sets.

The number of specimens N , Weibull parameters m and σ_0 as well as their 90% confidence intervals and effective area S_{eff} for each dataset are found in Table 4. Fig. 5(a) allows for a better overview of these results. R-28-1 specimens stand out due to their low Weibull modulus ($m = 15$) and poor characteristic strength. All other samples have a comparable Weibull modulus of $25 \leq m \leq 35$. Other findings are the slightly increased Weibull moduli for samples tested with intermediate layers, as all of them exhibit $m > 34$. Furthermore, the datasets R-28-1-T and R-28-1-BT are

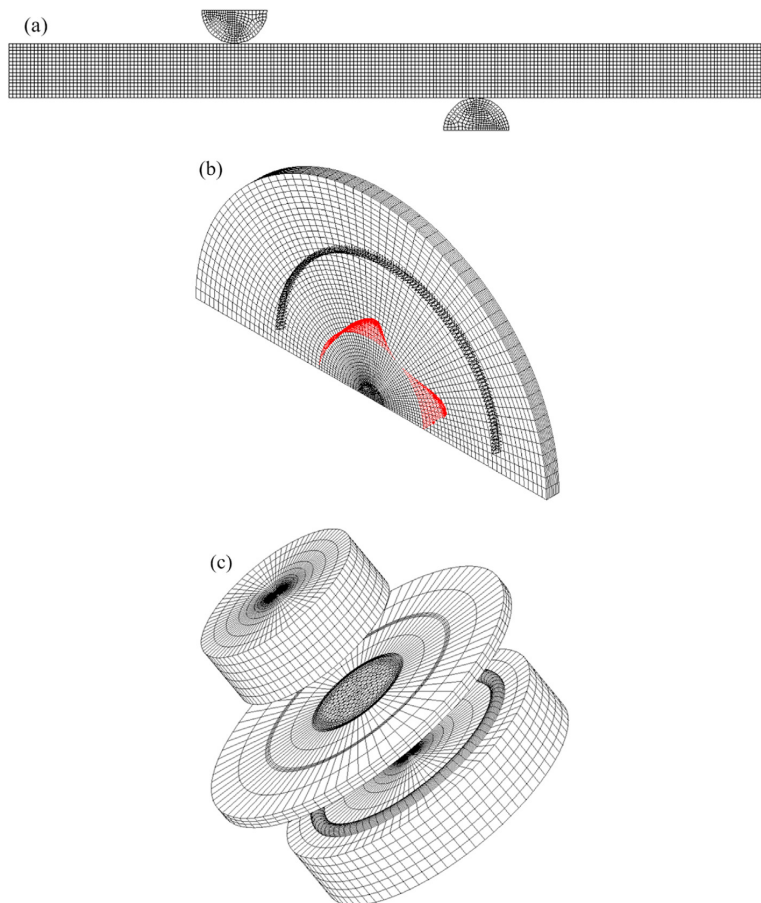


Fig. 4. Models and mesh for the FEA analysis. (a) Shows the model to investigate the influence of friction, (b) shows the model to test the influence of uneven loading with parameters $A = 100\%$ and $Z = 3$. The bottom plane in (b) marks the symmetry plane employed to reduce processing time. (c) Shows the model of the full testing assembly for more precise calculations of uneven surfaces.

nearly identical. A significant difference in strength and effective area between B3B and RoR samples is evident. When the effective area is considered, RoR specimens show a lower strength and higher effective area than B3B samples, as seen in Fig. 5(b). The regression fits all but two datasets (R-28-1 and B-28-1.7-BT), which were not considered since their testing details deviated from the standard procedure. The fit according to eq. (4) implies $m_{\text{reg}} = 30$, which is in excellent agreement with all datasets except R-28-1. Note the high difference in strength between all RoR sample sets and R-28-1. Furthermore, B-28-1.7-BT samples deviate by exhibiting significantly higher strength than other B3B sample sets.

Two samples were not tested in accordance with standards or

established guidelines: B-28-1.7-BT and R-28-1. B-28-1.7-BT was tested with Flashbreaker® 1 on its compressive side to observe the influence of intermediate layers on force application and strength measurement for the B3B test. The R-28-1 RoR-specimens were tested without any intermediate layers. It is evident that a significant deviation from other samples ensued.

In the B3B test, as compared to B-28-1.7, specimens tested with an interlayer on the compressive side (B-28-1.7-BT) show a significantly increased strength (i.e. +5%). This can be explained by a change in load application.

The factor f was determined assuming a point load, i.e. with a contact

Table 4

Results of strength testing of various specimens. m and σ_0 as described beforehand, with indices “lower” and “upper” referring to the borders of their 90% confidence interval. S_{eff} refers to the average effective area of specimens tested.

Designation	N [-]	m [-]	m_{lower} [-]	m_{upper} [-]	σ_0 [MPa]	$\sigma_{0, \text{lower}}$ [MPa]	$\sigma_{0, \text{upper}}$ [MPa]	S_{eff} [mm ²]
B-28-1	30	26	19	31	375	370	380	0.245
B-28-1.7	30	29	22	36	360	356	364	0.965
B-28-1.7-BT	32	34	26	41	381	378	385	0.770
R-28-1	28	15	11	19	242	237	248	126.8
R-28-1-T	30	34	26	42	305	302	308	116.8
R-28-1-BT	29	36	27	44	307	304	310	116.4

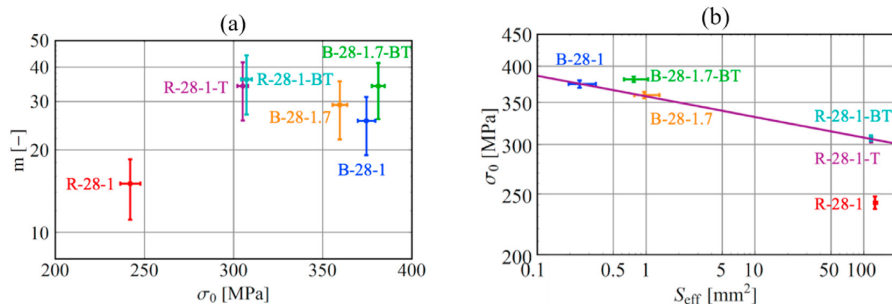


Fig. 5. Results of strength testing. (a) Depicts the Weibull modulus m and the characteristic strength σ_0 as well as their confidence intervals, (b) depicts the characteristic strength for each sample depending on their effective area S_{eff} .

radius $R_c = 0 \text{ mm}$. For load introduction over an actual contact area under the ball with a Hertzian contact pressure [50] $f(R_c > 0 \text{ mm})$ depends on the contact radius (which increases with applied load), as can be seen in Fig. 6. Note that the circles in Fig. 6 indicate the values of $f(R_c = 0 \text{ mm})$. For most testing situations covered with available FEA results [10,11] the specimens will fracture at loads which are low enough to give small contact areas. For such small contact areas, the actual f is not much different from $f(R_c = 0 \text{ mm})$. For example, the dashed areas in Fig. 6 refer to a decrease of maximal 2% in f , which is an experimental error that is acceptable.

Using the information from Fig. 6 the effect of a compliant interlayer on B3B strength results can be explained qualitatively. A soft interlayer will lead to an increased contact area between the loading ball and the specimens as compared to the situation without any layer, resulting in a lower value of $f(R_c)$ and a lower maximum stress. An increased load will be necessary to break the specimen. If $f(R_c = 0 \text{ mm})$ which is greater than $f(R_c > 0 \text{ mm})$ is used for the evaluation of strength from the fracture load, the strength of each specimen will be overestimated. This statement relies on the assumption that the effective area is not changed substantially. Using compliant layers for the Ball-on-Three-Balls-test creates a load

introduction situation which deviates from the assumptions that were made for theoretical stress evaluation. Consequently, incorrect stress results will be obtained.

For the RoR set-up, tests without interlayers (R-28-1) which are influenced by friction, lead to an approximately 20% lower strength as compared to tests with applied interlayers (R-28-1-T and R-28-1-BT).

To investigate the influence of friction on the stress in the disc, the stress on the tensile surface along a radial path from the disc center to its edge was evaluated for varying friction coefficients and compared with the analytical solution found by Fessler & Fricker [40]. The numbers presented were evaluated for a typical fracture load for our specimens, i.e. 600 N. Only radial stresses are shown since tangential stress exhibit the same behavior with a lower stress concentration near the loading ring position. Fig. 7(a) shows the FEA results of radial (σ_r) stress in absolute values, Fig. 7(b) displays the radial stress results σ_r normalized by the central stress $\sigma_i = \sigma_r(r = 0)$. Fig. 7(c) shows the results as predicted by equation 14–16 in Fessler & Fricker in absolute values, and the normalized curves are found in Fig. 7(d). The dashed line represents the position of the loading ring. The exact results of σ_i and $\sigma_{r,max}$ and their comparison to Fessler & Fricker can be found in Table 5.

As indicated by the FEA results, an increase in friction results in a decrease in radial stress at the loading ring radius (up to $\sim 8\%$ with $\mu = 0.5$) and a decrease in radial and tangential stress in the central region (up to $\sim 10\%$ with $\mu = 0.5$). The position of maximum stress moves towards the loading ring radius but not outside the central region. These findings for the central region are in good accordance with Fessler & Fricker [40]. As indicated by the FEA results, an increase in friction results in a decrease of stress throughout the specimen. The relative stress concentration near the load ring position ($\sigma_{r,max}/\sigma_i$) increases as friction increases. According to FEA this effect is not very strong (1.6% for $\mu = 0-3.4\%$ for $\mu = 0.5$, cp. Table 5). This is much lower than predicted by the Fessler & Fricker solution which results in up to 13% for $\mu = 0.5$. However, it is stated in Ref. [40] that the analytical model overestimates the stress at the loading ring radius due to a discontinuity in the equations, which explains the difference with respect to the FEA results. Thus, only a very small influence on the effective area can be expected from this effect, but an increased probability of failure from locations near the load ring radius. If friction is not eliminated, higher loads are necessary for specimens to fail and thus the strength would be overestimated. For the given geometry, and from the data in Table 5 this effect is estimated to be in the order of 5%–10%. With our RoR-tests without any intermediate layers a significant decrease in apparent strength was observed. We conclude that the action of friction alone cannot explain the observed result.

Another approach to explain the low strength is a change in load application due to the omission of any intermediate layers. More precisely, instead of a perfect line contact along both the load and support ring, an uneven load application through several contact points is suspected. If layers were used, the slight differences of height along the rings

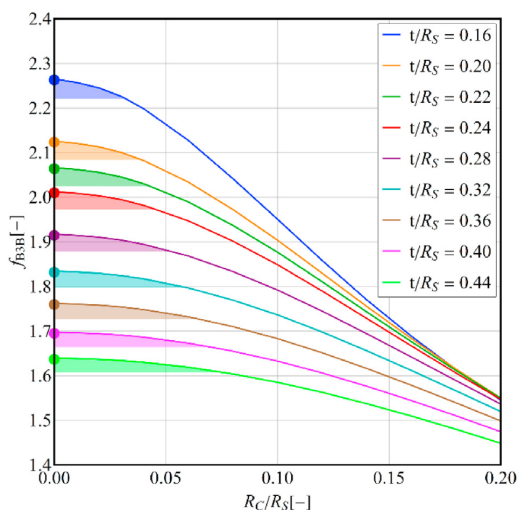


Fig. 6. Factor f depending on the Hertzian contact zone under the central loading ball for different values of thickness t to support radius R_s and the geometry $D = 12 \text{ mm}$, $D_s = 10 \text{ mm}$ and $\nu = 0.3$. The circles represent the values of f_{B3B} which are used for the evaluation of strength from fracture load. The shaded areas indicate an error $< 2\%$ [50].

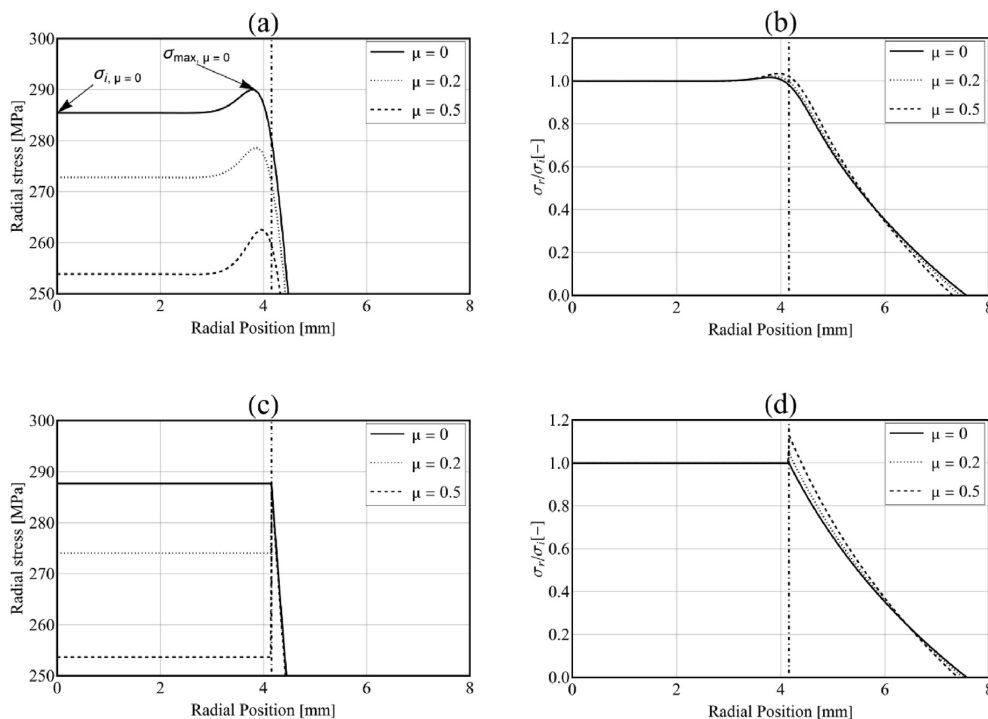


Fig. 7. Radial stress for different friction coefficients: (a) shows the absolute FEA results, (b) the normalized FEA results, (c) the absolute results of Fessler & Fricker and (d) the normalized results of Fessler & Fricker [40]. The dash-dotted line marks the position of the loading ring.

Table 5 Detailed results of FEA and Fessler & Fricker’s analytical solution for radial stress.

Friction Coefficient	$\sigma_i/\sigma_{i,\mu=0}$ FEA	$\sigma_i/\sigma_{i,\mu=0}$ Fessler	$\sigma_{r,max}/\sigma_i$ FEA	$\sigma_{r,max}/\sigma_i$ Fessler	$\sigma_{max,FEA}/\sigma_{max,Fessler}$
$\mu = 0$	1	1	1.016	1	1.008
$\mu = 0.1$	0.978	0.976	1.018	1.024	0.988
$\mu = 0.2$	0.956	0.953	1.021	1.048	0.969
$\mu = 0.3$	0.934	0.929	1.025	1.075	0.951
$\mu = 0.4$	0.911	0.905	1.029	1.102	0.933
$\mu = 0.5$	0.890	0.882	1.034	1.131	0.915

and specimens would be mitigated out, but without any layers they might influence load introduction in a way that would underestimate the samples strength. The FEA results in the case of ideal conditions (i.e. a constant line load) and 5 load maxima are shown in Fig. 8. The parameter A was set to 100%, meaning that the force along the loading ring diameter oscillates between 0% and 200% of the constant line load. Alongside that, the maximum stress at the tensile face is displayed in Table 6 and selected stress trends are shown in Fig. 9. Localized stress concentration along the loading ring circumference occur, while the stress level in the center of the disc remains unchanged. With an increasing amount of load maxima, the maximum stress decreases. Note that these results were obtained without considering friction. As previous results have shown, friction would result in a small general decrease of stress, similar to the trend shown in Fig. 7(a). However, the large stress concentrations at the loading ring radius would still be present.

It can be expected that this leads to an increased number of fractures from these locations of stress concentration. Additionally, these specimens will also fracture at a lower load compared to specimens that fail from the central region and consequently their strength will be

underestimated. It can also be expected, that this results in an increased scatter in strength, i.e. a lower Weibull modulus.

Note the difference in maximum stress for the case of three load maxima compared to ideal conditions, which is equal to an increase of nearly 20%. The difference in strength between the datasets R-28-1-T and R-28-1 is approximately 20% as well.

For a more accurate representation of the real loading scenario, the full model with a modified surface on the loading ring was evaluated. The results for the contact model shown in Fig. 4(c) with a maximum difference of 10 μm between the highest and lowest points of the loading ring surface are shown in Fig. 10(a). Even at a load similar to the fracture load during our experiments, full contact along the load ring cannot be achieved. Alternating regions of contact and no contact ensue. As can be seen in Fig. 10(b), a 3D-scan of the loading ring used in this work shows that even by machining with care a variation of about 20 μm between the highest and lowest points of such a ring can be present. Even smaller differences than what we found on a turned ring can result in a partial loss of contact along the circumference and an increase in stress at the remaining contact areas.

To verify the predicted results, the fractures of specimens from sets R-28-1, R-28-1-T and R-28-1-BT were investigated on a macroscopic scale. According to the positions of fracture origins, specimens were allocated to one of three groups:

- Fracture origin at or very close to the loading ring
- Fracture origin in the central region
- Location of fracture origin not identifiable, unknown

Since the number of unknown fracture origins were about 30% independent of the investigated sample, only the differences in clearly assignable fractures are discussed. In Fig. 11, it is evident that dataset R-

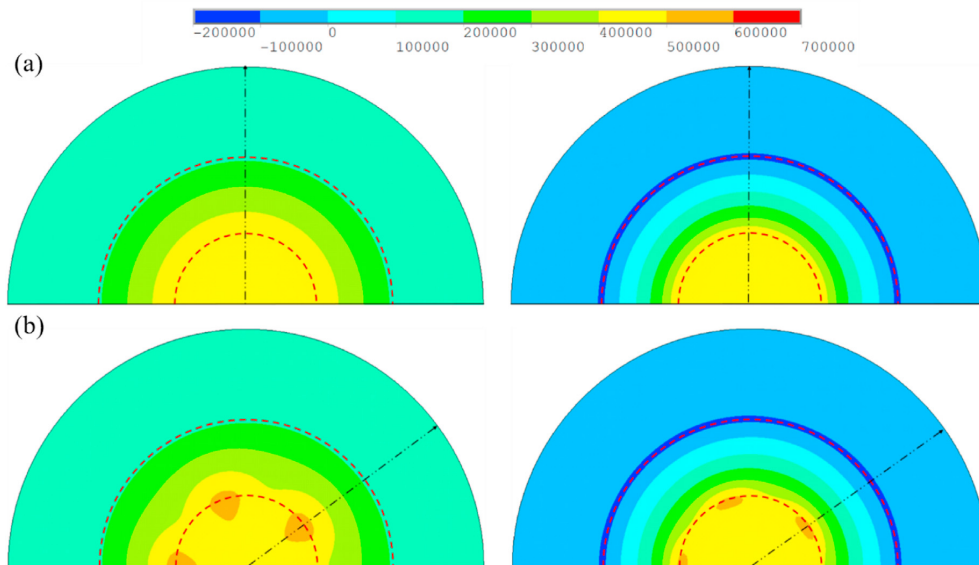


Fig. 8. Tangential (left) and radial (right) stress field (in Pa/N) for two cases of load introduction: ideal load introduction (a) and 5 load maxima (b). The dashed lines mark the load- and support-ring positions. The paths along which the stress trends in Fig. 9 are evaluated are marked by the dashed-dotted arrow.

Table 6

Maximum radial ($\sigma_{r,max}$) and tangential ($\sigma_{t,max}$) tensile stress for different load introduction cases as well as their ratios to the central stress (σ_i).

No. of Osz. [-]	$\sigma_{r,max}$ [MPa]	$\sigma_{r,max}/\sigma_i$ [-]	$\sigma_{t,max}$ [MPa]	$\sigma_{t,max}/\sigma_i$ [-]
Z = 0	290	1.016	287	1.005
Z = 3	337	1.181	338	1.184
Z = 5	312	1.093	320	1.121
Z = 10	296	1.037	301	1.054

28-1 (without interlayers) exhibits a significantly higher fraction of fractures from the loading ring, while the specimens with interlayers (R-28-1-T and R-28-1-BT) have a higher number of fractures from the center. No major distinction between dataset R-28-1-T and R-28-1-BT were found. Contrary to the Ball-on-Three-Balls-test, using no compliant layers for the Ring-on-Ring-test creates a load introduction situation which deviates from the assumptions that were made for analytical stress evaluation. Consequently, incorrect stress results will be obtained.

4. Summary

Biaxial strength tests were conducted on a commercial alumina ceramic (Frialit 99.7, Kyocera) using the Ball-on-Three-Balls-test and the Ring-on-Ring-test. Two different specimen thicknesses were investigated and details of the test procedure, namely the use of compliant layers, were varied. The results were compared based on the size effect predicted by Weibull fracture statistics. Additionally, the influence of friction and uneven loading was investigated using Finite-Element-Analysis.

Generally, it could be shown experimentally that both tests deliver comparable results within a Weibull approach. The B3B test can thus be used to evaluate the strength of specimen that may be too small or too thin to be tested with the RoR-test. This holds true as long as the tests are performed in a way where the real loading situation is as close as possible to the one assumed for the theoretical description of the test.

For the numerical evaluation of the B3B-test, load application by a point load is assumed, which is realized in most testing situations. If compliant interlayers are used between the loading ball and the specimen, the assumption is corrupted and a significant strength

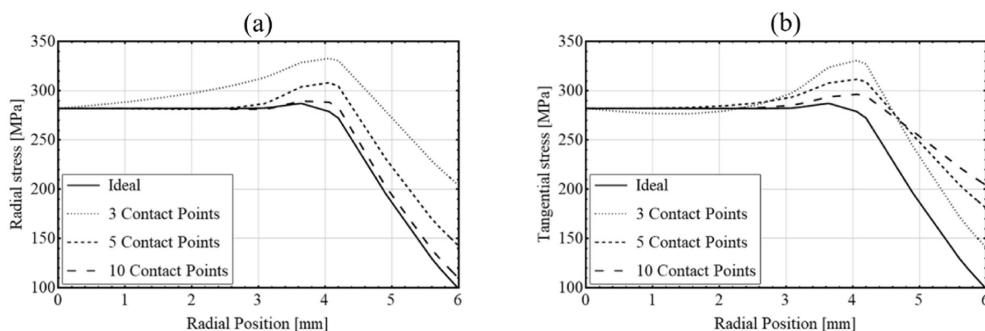


Fig. 9. Comparison of radial (a) and tangential (b) stress trends for various pointwise and ideal load introduction cases.

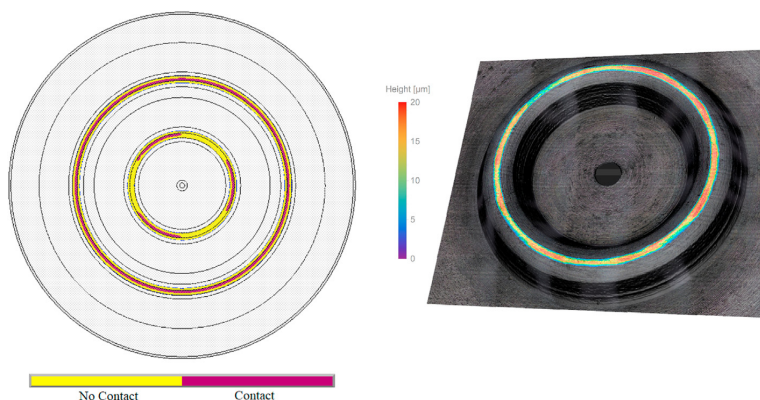


Fig. 10. (a) shows the contact status of the FEA model with a wavy loading ring surface, (b) shows a scan of the used loading ring.

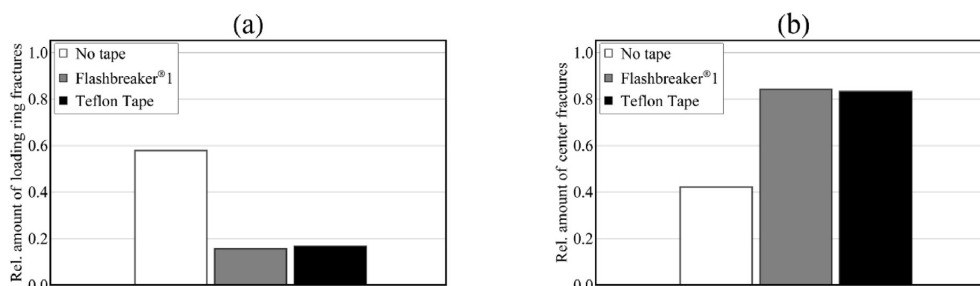


Fig. 11. Positions of fracture origins for the datasets R-28-1 (white), R-28-1-BT (gray) and R-28-1-T (black). (a) Shows the amount of fracture origins at or very close to the loading ring, (b) the amount of fracture origins at the center.

overestimation may result.

For the analytical description of the RoR-test, frictionless testing and uniform load introduction is assumed. If friction is not avoided, the specimen strength will be overestimated. If deviations from uniform ring-load introduction are present, the specimen strength will be underestimated due to the formation of regions of increased stress at the loading ring circumference. Even for deviations as small as a waviness of the loading ring surface of $\pm 5 \mu\text{m}$, regions without any contact of the loading ring and the specimen form and an increase in stress in the remaining regions ensues. Compliant interlayers help to achieve uniform load introduction with the additional benefit of a reduction of friction in the RoR-test.

Finite Element Analysis findings are supported by experimental results and fractography.

Declaration of competing interest

The authors declare that they have no known competing financial interests or personal relationships that could have appeared to influence the work reported in this paper.

Acknowledgements

M. Staudacher gratefully acknowledges financial support by the Austrian BMVIT and BMWFV in the project “CharAM” (FFG 877684) of the COIN/IraSME program. J. Schlacher gratefully acknowledges financial support by the ERC Consolidator Grant 817615 – “CeraText”. Furthermore, the authors want to thank the reviewers for their valuable input during revision.

References

- [1] R.N. Katz, Overview of ceramic materials, design, and application, in: M. Kutz (Ed.), *Mechanical Engineers' Handbook 1: Materials and Mechanical Design*, third ed., Wiley, Hoboken, N.J., 2006, pp. 433–449.
- [2] D. Munz, T. Fett, *Ceramics: Mechanical Properties, Failure Behaviour, Materials Selection*, Springer, Berlin, Heidelberg, 1999.
- [3] C.R. Brinkman, S.F. Duffy, *Life Prediction Methodologies and Data for Ceramic Materials*, ASTM International, 100 Barr Harbor Drive, PO Box C700, West Conshohocken, PA, 1994, 19428-2959.
- [4] J.B. Wachtman, M.J. Matthewson, W.R. Cannon, *Mechanical Properties of Ceramics*, Wiley, Hoboken, New Jersey, 2009.
- [5] D. Shetty, A.R. Rosenfield, P. McGuire, G.K. Bansal, W.H. Duckworth, *Biaxial Flexure Test for Ceramics*, American Ceramic Society Bulletin, 1980, pp. 1193–1197.
- [6] C. ASTM, *Test Method for Monotonic Equibiaxial Flexural Strength of Advanced Ceramics at Ambient Temperature*, ASTM International, West Conshohocken, PA, 2005, 1499-05.
- [7] ISO 17167:2018, *Fine Ceramics (Advanced Ceramics, Advanced Technical Ceramics) — Mechanical Properties of Monolithic Ceramics at Room Temperature — Determination of Flexural Strength by the Ring-On-Ring Test*, International Organization for Standardization, Geneva, Switzerland, 2018.
- [8] G. Isgro, P. Pallav, J.M. van der Zel, A.J. Feilzer, The influence of the veneering porcelain and different surface treatments on the biaxial flexural strength of a heat-pressed ceramic, *J. Prosthet. Dent* 90 (2003) 465–473.
- [9] EN ISO 6872:2015, *Zahnheilkunde - Keramische Werkstoffe*, Europäisches Komitee für Normung, 2015.
- [10] A. Börger, P. Supancic, R. Danzer, The ball on three balls test for strength testing of brittle discs: stress distribution in the disc, *J. Eur. Ceram. Soc.* 22 (2002) 1425–1436.
- [11] A. Börger, P. Supancic, R. Danzer, The ball on three balls test for strength testing of brittle discs: Part II: analysis of possible errors in the strength determination, *J. Eur. Ceram. Soc.* 24 (2004) 2917–2928.
- [12] T. Fett, G. Rizzi, E. Ernst, R. Müller, R. Oberacker, A 3-balls-on-3-balls strength test for ceramic disks, *J. Eur. Ceram. Soc.* 27 (2007) 1–12.
- [13] R. Morell, *Biaxial Flexural Strength Testing of Ceramic Materials: A National Measurement Good Practice Guide No. 12*, National Physical Laboratory, 2007.

- [14] L.M. Powers, J.A. Salem, A.S. Weaver, Stresses in ceramic plates subjected to loading between concentric rings, in: J.A. Salem (Ed.), *Fracture Resistance Testing of Monolithic and Composite Brittle Materials*, ASTM International, West Conshohocken, Pa., 2002, pp. 30–45.
- [15] W. Harrer, R. Danzer, P. Supancic, T. Lube, Einfluss von Kontaktspannungen auf die Festigkeit im 4-Kugerversuch, *Pharm. Manag. PM* 45 (2008) 18–32.
- [16] R. Danzer, P. Supancic, W. Harrer, T. Lube, A. Börger, Biaxial strength testing on mini specimens, in: Gdoutos E.E. (eds) *Fracture of Nano and Engineering Materials and Structures*. Springer, Dordrecht, pp. 589–590.
- [17] M. Deluca, R. Bermejo, M. Pletz, P. Supancic, R. Danzer, Strength and fracture analysis of silicon-based components for embedding, *J. Eur. Ceram. Soc.* 31 (2011) 549–558.
- [18] M. Gruber, I. Kraveva, P. Supancic, J. Bielen, D. Kiener, R. Bermejo, Strength distribution and fracture analyses of LiNbO₃ and LiTaO₃ single crystals under biaxial loading, *J. Eur. Ceram. Soc.* 37 (2017) 4397–4406.
- [19] E. Özkol, A.M. Wätjen, R. Bermejo, M. Deluca, J. Ebert, R. Danzer, R. Telle, Mechanical characterisation of miniaturised direct inkjet printed 3Y-TZP specimens for microelectronic applications, *J. Eur. Ceram. Soc.* 30 (2010) 3145–3152.
- [20] M. Wendler, R. Belli, A. Petschelt, D. Mevec, W. Harrer, T. Lube, R. Danzer, U. Lohbauer, Chairside CAD/CAM materials. Part 2: flexural strength testing, *Dent. Mater.* 33 (2017) 99–109.
- [21] J.R. Wachtmann, Jr, W. Capps, J. Mandel, Biaxial flexure tests of ceramic substrates, *J. Mater.* (1972) 188–194.
- [22] R. Bermejo, P. Supancic, I. Kraveva, R. Morrell, R. Danzer, Strength reliability of 3D low temperature co-fired multilayer ceramics under biaxial loading, *J. Eur. Ceram. Soc.* 31 (2011) 745–753.
- [23] W. Harrer, R. Danzer, P. Supancic, T. Lube, Influence of the sample size on the results of B3B-tests, *KEM* 409 (2009) 176–184.
- [24] Chair of structural and functional ceramics, ball-on-3-balls test (B3B) – strength testing, <https://www.isfk.at/interaktive-berechnungstools/b3b-strength-test>, accessed 14 December 2020.
- [25] R. Danzer, P. Supancic, W. Harrer, (Hrsg), in: J. Kriegsmann (Ed.), *Der 4-Kugerversuch zur Ermittlung der biaxialen Biegefestigkeit spröder Werkstoffe*, Technische keramische Werkstoffe, 2009, pp. 1–48.
- [26] J.A. Salem, L. Powers, Guidelines for the testing of plates, in: H.-T. Lin, W.M. Kriven (Eds.), 27th International Cocoa Beach Conference on Advanced Ceramics and Composites: January 26–31, 2003, Cocoa Beach, Florida, American Ceramic Society, Westerville, Ohio, 2003, pp. 357–364.
- [27] ASTM F394-78: Test Method for Biaxial Flexure Strength (Modulus of Rupture) of Ceramic Substrates (Discontinued 2001), ASTM International, West Conshohocken, PA, 1996.
- [28] C. Quintana, C. Rodríguez, F.J. Belzunce, A.C. Caballero, C. Baudin, Ceramic materials characterization using miniature mechanical tests: comparison between B3B and SPT tests, *J. Eur. Ceram. Soc.* 39 (2019) 4113–4121.
- [29] Y. Torres, R. Bermejo, F.J. Gotor, E. Chicardi, L. Llanes, Analysis on the mechanical strength of WC-Co cemented carbides under uniaxial and biaxial bending, *Mater. Des.* 55 (2014) 851–856.
- [30] C. ASTM, Practice for Size Scaling of Tensile Strengths Using Weibull Statistics for Advanced Ceramics, ASTM International, West Conshohocken, PA, 2019, 1683 - 10.
- [31] R. Danzer, T. Lube, P. Supancic, R. Damani, Fracture of ceramics, *Adv. Eng. Mater.* 10 (2008) 275–298.
- [32] W. Weibull, A Statistical Theory of the Strength of Materials, Generalstabens Litografiska Anstalts Förlag, Stockholm, 1939.
- [33] R. Danzer, A general strength distribution function for brittle materials, *J. Eur. Ceram. Soc.* 10 (1992) 461–472.
- [34] W. Weibull, A statistical distribution function of wide applicability, *J. Appl. Mech.* 18 (1951) 293–297.
- [35] S. Nohut, A general formulation for strength prediction of advanced ceramics by ball-on-three-balls (B3B)-test with different multiaxial failure criteria, *Ceram. Int.* 38 (2012) 2411–2420.
- [36] R.L. Barnett, P.C. Hermann, J.R. Wingfield, C.L. Connors, Fracture of Brittle Materials under Transient Mechanical and Thermal Loading, IIT Research Inst, Chicago IL, 1967.
- [37] FRIATEC GmbH, Division Keramik (Mannheim, DE), Werkstoffdatenblatt FRIALIT F99,7.
- [38] D.J. Godfrey, S. John, Disc flexure tests for the evaluation of ceramic strength, Proceedings 2nd International Conference of Ceramic materials and Components for Engines (1986) 657–665.
- [39] R. Danzer, A. Börger, P. Supancic, M.A. Ruiz Villanueva, Ein einfacher Festigkeitsversuch für Scheiben aus spröden Werkstoffen, *Mat.-wiss. u. Werkstofftech.* 34 (2003) 490–498.
- [40] H. Fessler, D.C. Fricker, A theoretical analysis of the ring-on-ring loading disk test, *J. Am. Ceram. Soc.* 67 (1984) 582–588.
- [41] W. Adler, D. Mihora, Biaxial flexure testing: analysis and experimental results, in: *Fracture Mechanics of Ceramics*, pp. 227–245.
- [42] A. Wereszczak, T.P. Kirkland, K. Breder, H. Lin, M. Andrews, Biaxial strength, strength-size-scaling, and fatigue resistance of alumina and aluminum nitride substrates, *Int. J. Microcircuits Electron. Packag.* 22 (1999) 446–458.
- [43] H.L. Frandsen, Weibull statistics effective area and volume in the ball-on-ring testing method, *Mech. Mater.* 73 (2014) 28–37.
- [44] High-tech-flon® films and fabrics (konstanz, DE), produktinformation PTFE virginale folie 0.05 - 600. <https://shop.hightechflon.com/ptfe-folie-teflon-folie-virginale-0.05mm-wei%9c3%9f/Page-16-1-126-176.aspx>, 2020. (Accessed 18 February 2020).
- [45] High-tech-flon® films and fabrics (konstanz, DE), produktinformation PTFE klebeband 0.08 V SW. <https://shop.hightechflon.com/P/TFE-Teflon-virginale-Klebeband-0,08-V-SW-0,08mm/Page-16-1-97-71.aspx>, 2020. (Accessed 18 February 2020).
- [46] AIRTECH europe sarl (differdange, LU), datenblatt Flashbreaker®, https://catalog.airtechintl.com/product_estore.php?product_id=1145&lang=EN, 2019. (Accessed 18 February 2020), 1.
- [47] T. Lube, W. Harrer, P. Supancic, Practical Guide to Ball-on-three-Balls (B3B-) Testing. Ber-2010-066-Tlu,wha,phs, ISFK, 2019.
- [48] R. Danzer, W. Harrer, P. Supancic, T. Lube, Z. Wang, A. Börger, The ball on three balls test—strength and failure analysis of different materials, *J. Eur. Ceram. Soc.* 27 (2007) 1481–1485.
- [49] R. Danzer, T. Lube, P. Supancic, Monte-carlo simulations of strength distributions of brittle materials - type of distribution, specimen- and sample size, *Z. Metallkd.* 92 (2001) 773–783.
- [50] T. Lube, P. Supancic, t. Aalbrecht, H. Bürke, Strength Tests with Biaxial Loading - a Comparison of Methods, Messe München, 2018.

Publication F

A novel test specimen for strength testing of ceramics for additive manufacturing

Maximilian Staudacher, Tanja Lube, Jürgen Glettler, Uwe Scheithauer, Martin Schwentenwein

Department of Materials Science, Montanuniversität Leoben, Franz Josef-Strasse 18, A-8700 Leoben, Austria

Open Ceramics 15, (2023) 100410

doi: <https://doi.org/10.1016/j.oceram.2023.100410>

Reuse under the terms of license CC-BY 4.0



A novel test specimen for strength testing of ceramics for additive manufacturing

Maximilian Staudacher, Tanja Lube^{*}, Jürgen Glettler, Uwe Scheithauer, Martin Schwentenwein

Department of Materials Science, Montanuniversität Leoben, Franz Josef-Strasse 18, A-8700, Leoben, Austria

ARTICLE INFO

Handling Editor: Dr P Colombo

Keywords:
Strength testing
Vat photopolymerization
Orientation dependency

ABSTRACT

This paper introduces a new method for strength testing of additively manufactured ceramics, which was designed to take the characteristics of the manufacturing process into account. It was developed for time- and material efficient specimen fabrication and its design allows adjustment so that different surface orientations can be investigated. This gives insight into the influence of surface structures on the measured strength, which vary significantly depending on the surface orientation.

Functional expressions for strength evaluation and the determination of effective volume are given and validated through Finite Element Analysis (FEA). The influence of surface structures on the measured strength is analyzed based on Weibull theory and FEA. Other influences on the accuracy of this testing method are discussed and quantified based on practical observations. The manufacturing process, testing setup and statistical evaluation for specimens of three different configurations is outlined and the results and applicability of this method are discussed.

1. Introduction

In the past decades, ceramic materials have taken an increasingly prominent position in many technical fields, which can frequently be traced back to their unique combination of mechanical and functional properties. Some of their most relevant characteristics are a high hardness, strength, and wear resistance. Whilst these properties are sought after in many applications, they severely limit the geometric complexity of ceramic components due to time- and cost intensive machining. Therefore, new shaping and manufacturing methods have been developed, aiming to increase component complexity while simultaneously reducing machining effort. Amongst the most promising methods to achieve this goal are the different additive manufacturing (AM) technologies. Through layered material deposition, AM has opened the path to near-net-shaped ceramic components with similar properties to conventionally manufactured ones. It should be noted that many different AM technologies exist, and all have their merits and limitations [1,2].

In order to optimize the manufacturing process, it is of utmost importance to accurately determine the component's functional and mechanical properties. However, AM introduces a number of additional challenges that have to be considered for the determination of the

component's mechanical properties. Notable differences to regular bulk ceramics are the layered structure, the layers' orientation in relation to the applied load or the influence of periodically structured surfaces. As an example, digital-light-processing (DLP) based vat photopolymerization enables the fabrication of a ceramic green body with high spatial resolutions. The starting point for the green body is a slurry consisting of ceramic-powder dispersed in a photo curable polymer. The light source is directed at the slurry with a plethora of small mirrors, whose size determine the maximum resolution of the process, as each of them represent a curable pixel [3–7]. As a consequence, aliasing effects occur if a structure of any incline is manufactured, as depicted in Fig. 1a). This effect causes the surface to exhibit unique wave patterns for each inclination, i.e. surface orientation, as shown in Fig. 1b). It is well known that surface defects can have a severe effect on the measured strength due to the higher geometry-factor compared to defects found within the bulk material [8]. Due to the orientation dependent surface structures, stress concentrations may form and amplify this effect. This results in changes of the measured strength in dependence of the surface orientation [9]. Moreover, recent work has shown that the strength of specimens manufactured with AM is significantly dependent on whether the specimen is loaded perpendicular or parallel to the building direction. It has to be noted that this difference can be eliminated if the

^{*} Corresponding author.

E-mail address: tanja.lube@unileoben.ac.at (T. Lube).

<https://doi.org/10.1016/j.oceram.2023.100410>

Received 9 May 2023; Received in revised form 13 June 2023; Accepted 13 July 2023

Available online 13 July 2023

2666-5395/© 2023 The Authors. Published by Elsevier Ltd on behalf of European Ceramic Society. This is an open access article under the CC BY license (<http://creativecommons.org/licenses/by/4.0/>).

surface of both specimen types is machined [10,11]. However, machining of the final component is not always possible and would reduce the benefit gained through additive manufacturing and should therefore be avoided altogether. Apart from these two extreme orientations, the mechanical properties of the intermittent orientations are of high interest as well.

Ideally, all of this information can be gathered through a single testing method for a wide range of surface orientations. Then, it could be directly implemented into the design process of an additively manufactured component to increase material efficiency and component reliability.

Testing methods such as four-point bending or biaxial testing methods have the upside of already being established and standardized [12,13]. One of their major downsides is the time- and material intensive process of manufacturing each specimen. Especially with high resolution methods, such as DLP-based vat photopolymerization, the number of specimens that can be manufactured simultaneously is severely limited. Additionally, the high number of layers causes long manufacturing times. Furthermore, if specimens are not oriented parallel or perpendicular to the building direction, support structures are necessary, which further increases material consumption and decreases surface quality. Therefore, new testing methods have to be developed to accurately assess the mechanical properties with respect to the specifics of AM.

Within this work, a new strength testing method for DLP-based vat photopolymerization based on a novel specimen geometry, as displayed in Fig. 2, is presented. An introduction to the test specimen itself, its stand-out characteristics, and the reasoning behind them is given. Based on practical observations, a thorough analysis of possible sources of error and their influence on the measured results is carried out. The possible sources of error are quantified by theoretical considerations, Monte-Carlo analysis, and Finite-Element-Analysis (FEA). Limits for the influence of surface structures on the measured strength are given through a numerical analysis based on Weibull-theory. The implementation of the new testing method with the use of widely available testing equipment is shown. Empirical results obtained with the new testing method are given and discussed in relation to AM-specific features. Although this testing method was developed for DLP-based vat photopolymerization, its applicability to other manufacturing methods is conceivable.

2. Theoretical considerations

2.1. Specimen characteristics

The development of this test specimen was performed at IKTS

Dresden and is given in Refs. [14,15]. The basic elements of the test specimen are a baseplate and 48 cantilevers attached to the baseplate's upper surface. Through increasing the thickness of the cantilevers towards the baseplate, a strong support for loading is formed. The other end of the cantilevers will be loaded perpendicular to their longitudinal axis (see Fig. 3), resulting in a bending load. The specimen's baseplate is formed by two solid plates with an arched structure in between, as shown in Fig. 3.

In combination with the anchoring points at each end of the longitudinal edge, a rigid base for clamping or mounting of the test specimen is formed. The angle of the upper solid plate can be adjusted to subsequently yield any desired surface orientation for the cantilevers attached to it. Within this work, three configurations of the test specimen have been investigated, as shown in Fig. 4. Fig. 4a) displays the reference specimen, which will be referred to as "Type A". The inclination of the longitudinal axis of the cantilevers to the z-axis (see Fig. 3) is 0°. The cantilevers in specimen "Type B1", as shown in Fig. 4b), are angled at 15° to the z-axis. The same angle is chosen for specimen "Type B2", as shown in Fig. 4c), but with the cantilevers rotated along their longitudinal axis by 180°. Therefore, the tension loaded side is downskin for cantilevers of configuration B1 and upskin for configuration B2.

The design of the cantilever is the same for each configuration of the test specimen. A detailed overview of its geometry is given in Fig. 5. A small bulge at the front of the cantilever ensures load introduction at the correct position. Due to the linear increase of the cross section in the marked region, a constant bending moment acts within this part of the cantilever. This section serves as the intended region of failure and the maximum tensile stress σ_{max} at the specimen's surface is given through

$$\sigma_{max} = \frac{6P}{kh^2} \quad (1)$$

with P as the applied load and h as the thickness of the specimen within this region. The variable k describes the slope of the inclined flanks and is determined by

$$k = \frac{b_2 - b_1}{L} = 2 \tan\left(\frac{\alpha}{2}\right) \quad (2)$$

with L as the length and b_1 & b_2 as the width at the beginning and end of the region of constant bending moment. Another way to determine k is by the opening angle α of the cantilever's flanks.

In order to trace the broken cantilevers to their respective counterparts on the baseplate after testing, each cantilever is marked by two binary codes which indicate the row and the column of the cantilever on the baseplate [15]. This allows testing of all cantilevers on the specimen in one session without the need to demount the specimen or collect each broken cantilever directly after failure.

To get a better understanding of the accuracy of the new testing

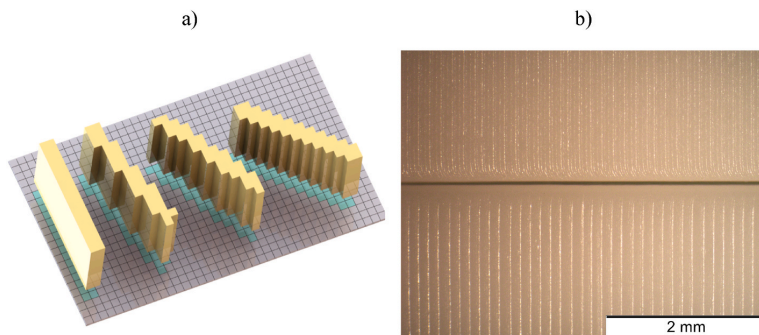


Fig. 1. a) shows a schematic of the aliasing effect due to the pixel-based nature of the DLP-based vat photopolymerization process (incline from left to right: 0°; 15°; 30° and 45°). The same effect occurs in building direction as well due to the layered manufacturing process. A side-by-side comparison of the surface structures due to differing surface orientations is given in b). The upper surface was manufactured at an incline of 45°, the lower one at 15°.

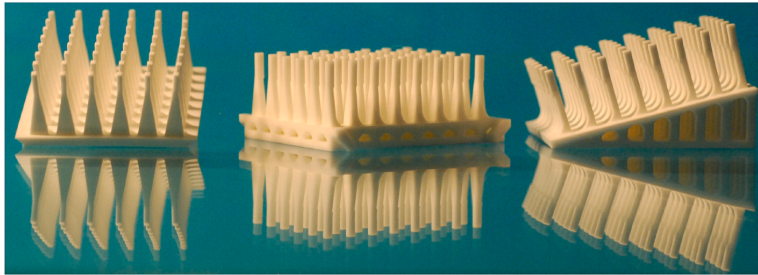


Fig. 2. Sintered test specimen in three different configurations. For size indication refer to Fig. 3.

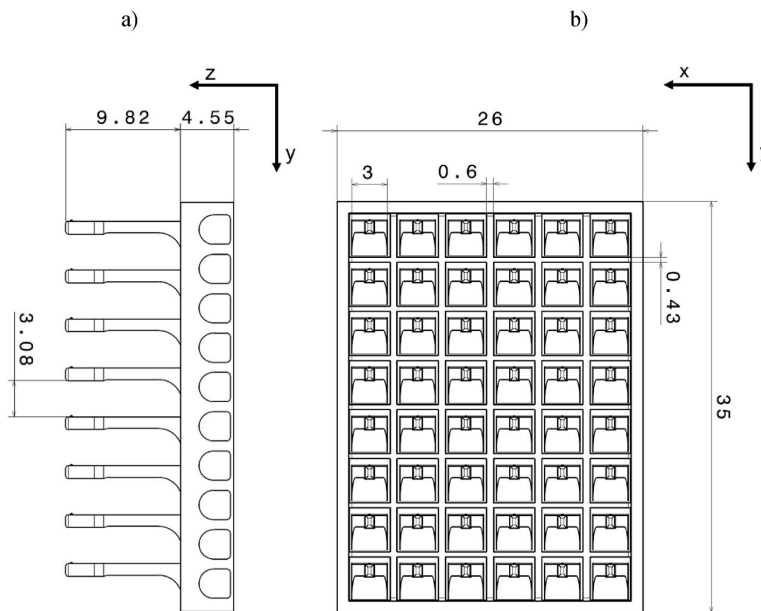


Fig. 3. Overview of the test specimen in side-view in a) and top-view in b), with its most significant dimensions given and the load direction along the y-axis.

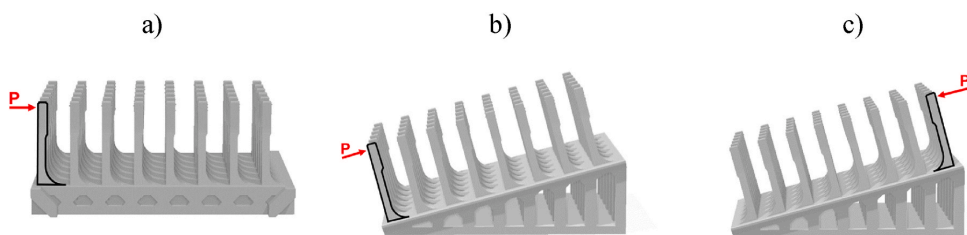


Fig. 4. Schematic for each variation of the test specimen, with the orientation of the cantilever highlighted by the black lines and the direction of the applied load P given in red. The 0° configuration is shown in a), the 15° configuration in b) and the rotated 15° configuration, i.e. 15° - 180° , is shown in c). (For interpretation of the references to colour in this figure legend, the reader is referred to the Web version of this article.)

method, some aspects have been investigated with FEA. A model of the cantilever attached to a part of the baseplate was implemented in ANSYS Mechanical R.22.1 by ANSYS Inc. (Southpointe 2600 Ansys Drive, PA 15317, Canonsburg, USA) through APDL (Ansys Parametric Design Language) by importing a CAD-file of the model. The model was meshed with 224868 SOLID186 elements (20-node elements), and 316950

nodes and is shown in Fig. 6. A mesh convergence analysis was performed to ensure the use of sufficiently small elements.

2.2. Stress field validation

Since eq. (1) was derived by utilizing Euler-Bernoulli beam theory,

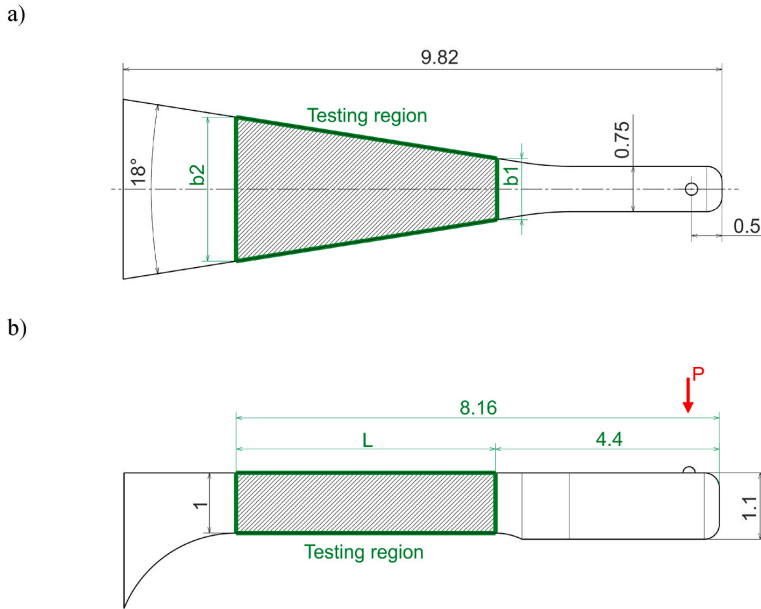


Fig. 5. Geometry of the cantilever, shown in top view in a) and side view in b). All measurements are given in mm. The region of constant bending moment is marked in green and the applied load P is marked in red. (For interpretation of the references to colour in this figure legend, the reader is referred to the Web version of this article.)

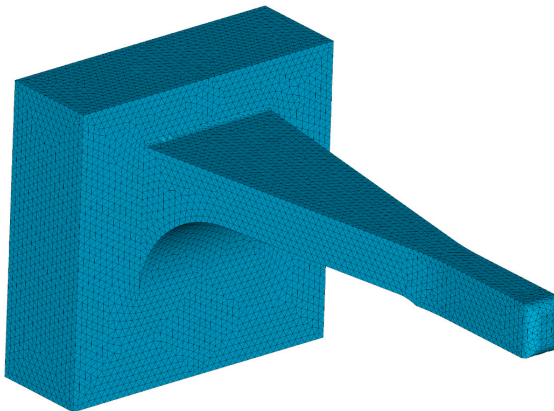


Fig. 6. Meshed model of the cantilever with a small portion of the baseplate.

some effects such as transverse shear strains are not considered [16]. Even though these effects are minor for thin beams and small displacements, a comparison between the FEA-derived stress field and the ideal stress field given by eq. (1) for the tensile surface was conducted. The results are shown in Fig. 7. Eq. (1) underestimates the stress in the central region by about 1.6% and overestimates the stress in the edge-regions by about 0.5%. Overall, excellent agreement between eq. (1) and FEA-results is achieved, validating the use of Euler-Bernoulli beam theory to calculate the maximum stress.

2.3. Effective volume and surface

An important consideration during design was material efficiency. More specifically, as much as possible of the manufactured volume

should be stressed at or close to the maximum tensile stress. This efficiency can be quantified by calculating the effective volume V_{eff} or effective surface S_{eff} in relation to the overall stressed volume V or surface S of the specimen. For the region of constant bending moment, an analytical solution for V_{eff} can be derived by solving the integral

$$V_{eff} = \iiint_{\sigma>0} \left[\frac{\sigma(x,y,z)}{\sigma^*} \right]^m dx dy dz \quad (3)$$

for the tensile regions of the stress field $\sigma(x,y,z)$ normalized by an arbitrary tensile stress σ^* with m as the Weibull-modulus [8,17]. If the maximum tensile stress in the specimen is used for σ^* , this then yields

$$V_{eff} = \frac{hL(b_1 + b_2)}{4(m + 1)} \quad (4)$$

for the effective volume, with h as the thickness of the region of maximum stress of the cantilever. The other symbols are as defined previously. If the small contribution of the side faces of the beam are neglected, the effective surface S_{eff} is derived by the general relationship between S_{eff} and V_{eff} for a stress distribution induced through bending:

$$S_{eff} = V_{eff} \frac{2(m + 1)}{h} = \frac{L(b_1 + b_2)}{2} \quad (5)$$

Fig. 8 shows the relative effective volume of the testing region, i.e. the ratio of V_{eff} to the total stressed volume V , of one cantilever of the novel test specimen in comparison to traditional flexural strength tests [18]. Note that the volume of the supporting structures, i.e. the base plate, is not taken into account, as this material would also be needed to a similar extent for the overhang or support structures for the other tests. Due to the large region of constant maximum stress at the surface of the cantilever, a high material-efficiency compared to traditional bend-testing methods is achieved. If the total volume V_{tot} of the specimen, i.e. including all supporting structures, is considered, the new specimen exhibits slightly higher efficiency than 3-point-bending bars.

Similar to before, the functional expressions for the effective volume

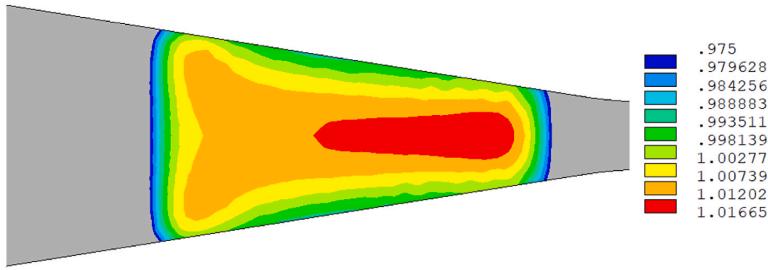


Fig. 7. Result of the stress field determined by FEA, σ_{FEA} , in relation to the constant stress at the surface σ_{max} as given by eq. (1). The contours give the ratio $\sigma_{FEA}/\sigma_{max}$.

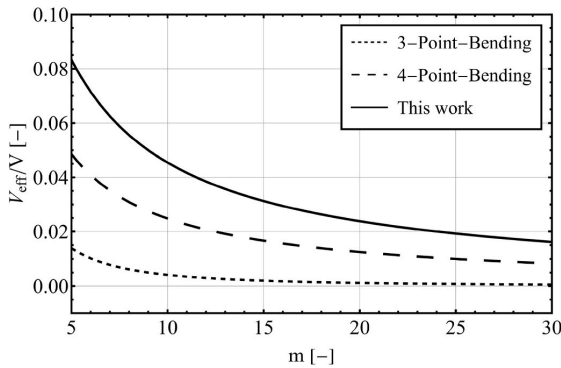


Fig. 8. Comparison of the relative effective volume for the novel test specimen, 3-point-bending bars and 4-point bending bars.

and surface (eq. (4) and (5)) were derived under the assumption of ideal conditions, i.e. a constant bending moment. In order to validate these expressions, the FEA-model from the previous section was utilized. The analytical and the numerical results in dependence of the Weibull modulus m are shown in Fig. 9. For $m \geq 10$, good agreement between eq. (4) and FEA is achieved. Note that the numerical results were generated for the full cantilever (excluding the region in immediate proximity of load introduction) while the analytical solution describes only the region of constant bending moment. This explains the increasing error for low Weibull moduli ($m < 5$) due to the increasing contribution of low-stress regions to the effective volume.

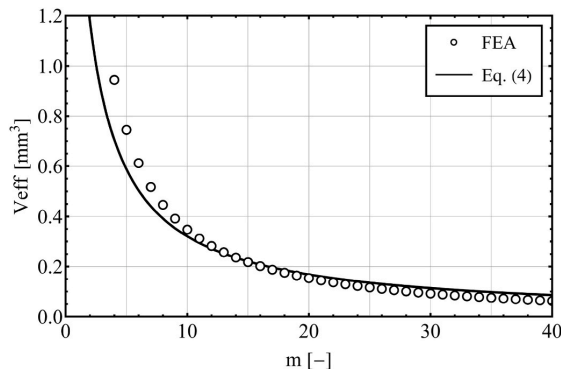


Fig. 9. Effective volume for the cantilever in dependence of the Weibull modulus calculated with either eq. (4) or FEA.

2.4. Influence of surface orientation

To assess the influence of surface structures, an approach based on Weibull theory was considered [19]. Since these surface structures modify the tensile stress field, the effective sizes (V_{eff} and S_{eff}) will change as well. Based on the size-effect, a change in measured strength is to be expected [8]. To accurately represent these surface structures, which are on a sub-millimeter scale, the mesh of the FEA-model has to be several times smaller than in the previous model. By utilizing sub-modelling, the region of constant bending moment can be modelled and meshed individually. Due to the simpler geometry of the sub-model, a mapped mesh with element sizes on a sub-micrometer scale can be implemented [20,21]. The sub-model is meshed with 52404 SOLID186 elements and 244031 nodes. With this sub-model, the observed periodic surface structures of the manufactured specimens are directly implemented in FEA. A sinusoidal wave was deemed as the best representation of the measured data, with the amplitude and wavelength for each specimen type determined through surface characterization (see chapter 4.3). These structures were subsequently implemented in the sub-model and compared to the case of an ideal flat surface structure, i.e. specimens of type A. The investigated results were the change in maximum tensile stress and the influence of the surface structures on the effective volume and surface. The maximum tensile stress of the flat specimen was chosen as the reference stress σ^* for the calculation of V_{eff} and S_{eff} for the other specimen types. Utilizing the size effect described by Weibull theory [8], the expected measured strength of a specimen σ_B of an effective volume $V_{eff,B}$ is given by

$$\frac{\sigma_B}{\sigma_A} = \left(\frac{V_{eff,A}}{V_{eff,B}} \right)^{1/m} \tag{6}$$

with $V_{eff,A}$ and σ_A as the known effective volume and strength, respectively. In the case presented here, the subscript B corresponds to the specimen with a structured surface and A corresponds to the flat specimen. The very same principle can be applied utilizing the effective surface instead of the effective volume. The ratio σ_B/σ_A for each specimen type, based on either V_{eff} or S_{eff} , will be used to quantify this effect.

3. Practical aspects

All equations and investigations presented in the last section were derived or conducted under the assumption of ideal specimen geometries, i.e. as given in Fig. 5. A comprehensive analysis of the first prototypes revealed a number of deviations from the ideal geometry. On one hand, the general dimensions of the sintered cantilever did not correspond to those given in Fig. 5, even though a state-of-the-art printer (see chapter 4) was utilized. On the other hand, these dimensions fluctuated for each cantilever, even within one test specimen. Therefore, the initial concept of measuring a single cantilever, which is representative for the whole specimen, had to be investigated and reworked. In the upcoming section, the observed deviations from the ideal specimen

geometry and ideal loading situation will be discussed.

3.1. Non-ideal geometry of the cantilevers

The most relevant dimensions for stress evaluation are the thickness h and the opening angle α of the cantilevers, as given in eq. (1). Contrary to initial assumptions, these dimensions are different for each cantilever within each test specimen. Therefore, measuring the dimensions of just a single cantilever is not adequate to accurately determine the fracture stress for each cantilever. Other options are to either determine mean values from the measurements of several cantilevers or to use individual measurements from every cantilever. In order to determine a suitable number of measurements for the average values, a Monte-Carlo (MC) analysis was conducted with Mathematica 12.0 by Wolfram Research, Inc. (100 Trade Center Drive, Champaign IL 61820-7237, USA) [22,23]. More specifically, the characteristic strength σ_0 and Weibull modulus m were determined with dimensions from either individual or average measurements. An overview of the principle of this analysis is given in Fig. 10. The dimensions for each specimen were randomly generated based on normal distributions, which are determined from measurements of manufactured specimens. The final result of the MC analysis is the relative difference between the Weibull parameters determined with either individual or average dimensional measurements.

3.2. Position of load introduction

Another problem caused by the deviation from intended cantilever dimensions is a shift of the point of load introduction away from the ideal loading position. The cantilever is designed so that the extensions of the inclined flanks intersect at the point of load introduction. At this location, a small bulge is added to facilitate a well-defined load application. This condition is needed so that the maximum stress in the intended region of failure can be determined by eq. (1). If the slope k of the edges, i.e. the opening angle α , changes, the intersection point does no longer coincide with the position of the bulge, as shown by the blue lines in Fig. 11. Instead, the intersection of the edges is shifted by a distance a , depending on α , while the load will still be applied at the bulge. A schematic of this effect is given in Fig. 11.

The influence of a on the maximum stress $\sigma_{\max,shifted}$ can be considered analytically and is given through

$$\sigma_{\max,shifted}(x, a) = \frac{3F(x-a)}{h^2 x \tan\left(\frac{\alpha}{2}\right)} \quad (7)$$

with x as the distance from the ideal loading point for $\alpha = 18^\circ$ and the other symbols as defined before. The relative error in maximum stress in dependence of x and a is defined by

$$Rel. error[\%] = \frac{\sigma_{\max,shifted} - \sigma_{\max}}{\sigma_{\max}} \quad (8)$$

with σ_{\max} as defined in eq. (1).

3.3. Shape of the cantilever cross-section

Further deviations from the ideal specimen geometry are related to the cross-section of the cantilevers. Even directly after specimen fabrication, the desired rectangular cross-section is not achieved by DLP-based vat photopolymerization, resulting in a barrel shaped cross-section instead. This effect is still evident after sintering, as shown in Fig. 12. Another reason for geometric deviations might be the subsequent thermal crosslinking of suspension that is still adhering because it has not been cleaned off.

For the derivation of eq. (1), a rectangular cross-section with height h was assumed to derive a simple functional expression for the section modulus. If the maximum thickness of the cantilever in the center, h_{\max} , is utilized as h , the section modulus will be overestimated. This will result in an underestimation of the measured strength of the cantilever.

4. Experimental

4.1. Specimen fabrication

The test specimens were manufactured in-house from the alumina-based slurry LithaLox350 with the DLP-based vat photopolymerization printer CeraFab 7500, both produced by Lithoz GmbH (Mollardgasse 85A, 1060 Vienna, Austria). The most relevant printing parameters are given in Table 1.

All specimens were manufactured from the same slurry batch and excess slurry was removed with the solvent LithaSol20 produced by Lithoz GmbH. A total of 18 test specimens were manufactured, with 6 specimens per specimen type. The size of the building platform allows manufacturing of two specimens side by side as a single batch. All specimens of the same type, i.e. A, B1 or B2, were treated simultaneously during thermal postprocessing and according to the procedure recommended by Lithoz GmbH. Debinding was performed in a KU15/06/A furnace and sintering in a HTL10/17 furnace, both manufactured by ThermConcept (Friedrich-List-Strasse 17, 28309 Bremen, Germany). The maximum temperature during debinding was 430°C , then the specimens were transferred into the sintering furnace. Sintering of the specimens was conducted at 1650°C for 2 h. For the sintering process, special care was taken to guarantee an upright position of the cantilevers by tilting the angled specimens by 15° . Thus, the deformation of cantilevers due to their own weight was kept to a minimum.

4.2. Strength testing

The specimens were tested with the universal testing machine Z010 by ZwickRoell GmbH & Co. KG (August-Nagel-Strasse 11, 89079 Ulm,

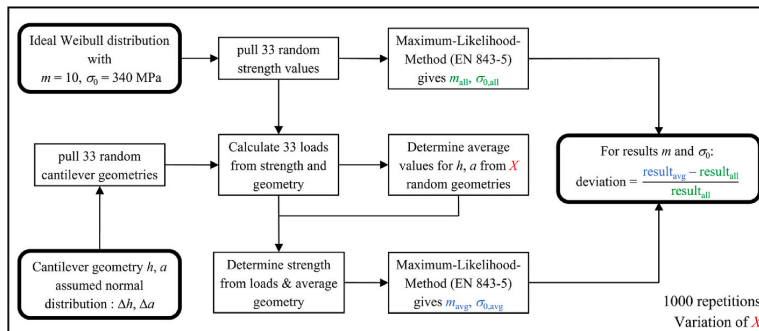


Fig. 10. General Principle of the Monte-Carlo analysis.

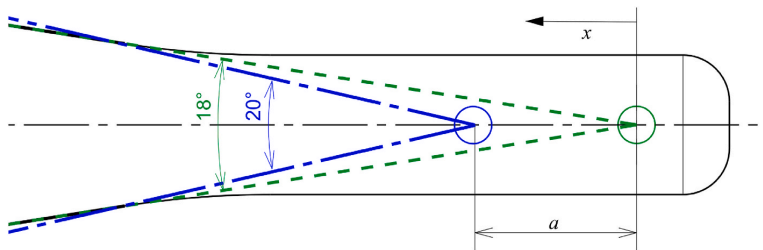


Fig. 11. Positional change of the ideal point of load introduction due to the change in opening angle α . Green: ideal situation, blue: situation for a cantilever with a larger than ideal flank opening angle. The load will always be applied at the green circle due to the bulge at this position. (For interpretation of the references to colour in this figure legend, the reader is referred to the Web version of this article.)

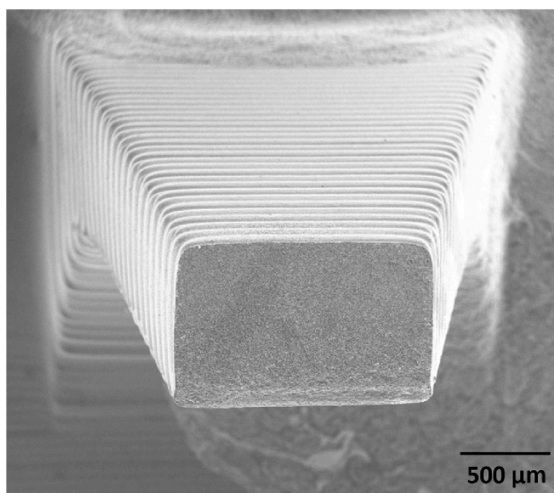


Fig. 12. Fracture surface of a sintered cantilever of specimen type B1. Note that the observed cross-section deviates significantly from the assumed rectangular cross-section.

Table 1
Printing parameters utilized for specimen manufacturing.

Layer thickness [μm]	Lateral resolution [μm]	DLP-Intensity [mW/cm^2]	DLP-Energy [mJ/cm^2]
25	40	100	150

Germany) equipped with a KAP-S load cell (maximum load = 200 N) by AST GmbH (Marschnerstrasse 26, 01307 Dresden, Germany) and operated through a control system by Doli Elektronik GmbH (Rudolf-Diesel-Strasse 3, 72525 Münsingen, Germany). Each specimen was mounted on an X–Y table by clamping two sides of the baseplate, as shown in Fig. 13. The cantilevers of each specimen were tested successively through a slim metal probe. The X–Y table enabled an adjustment of the specimen’s position in the X–Y plane (see Fig. 13), so that each cantilever was loaded perpendicular to its longitudinal axis at the intended point of load introduction (bulge). The cantilevers were loaded at a constant crosshead speed of 1 mm/min.

Prior to strength analysis, the validity of each individual bending test was verified. This involves checking for unsteady loading curves, large geometric imperfections, and failures outside the region of constant bending moment. The relevant dimensions of each cantilever, i.e. the thickness h_{max} and the opening angle α , were determined on the

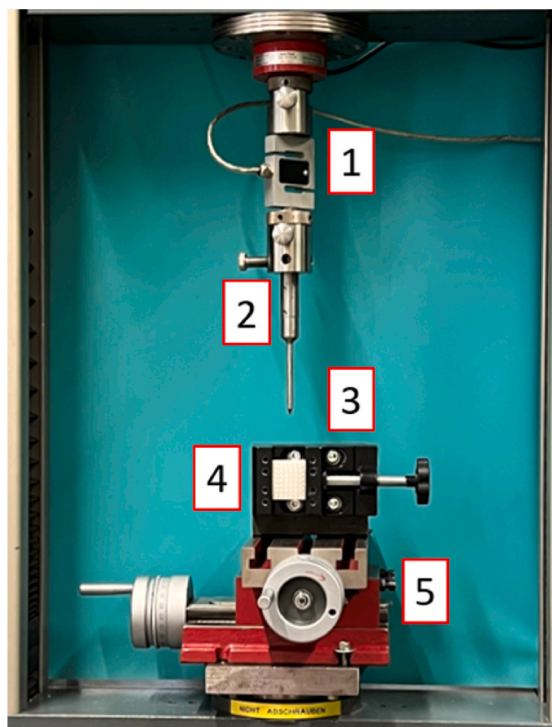


Fig. 13. Testing setup for a specimen of Type A (4), which is held in place by a clamping fixture (3) that is mounted on a X–Y table (5). The metal probe (2) is fixed to the load cell (1). This setup can be used for each specimen type without modification.

remainders of the cantilevers on the baseplate (h_{max}) and on the fractured cantilevers (a), respectively, with a SZH10 stereomicroscope by Olympus K.K. (2-3-1 Nishi-Shinjuku, 163-0914 Tokyo, Japan) within the Olympus Stream Motion Software 2.2. Strength results were obtained utilizing eq. (1). Statistical Weibull analysis was performed with the Maximum-Likelihood method in accordance with the standard EN-843-5 [24].

4.3. Surface characterization and fractography

The surface structures of the cantilevers were characterized with a VK-X1000 Laser-Confocal-Microscope by Keyence Corporation (1-3-14 Higashi-Nakajima, 533-8555 Osaka, Japan). 6 cantilevers of each type

were examined, and an average surface structure was determined from 60 line-measurements on each cantilever. Fracture surfaces were investigated using a JEOL K.K. (3-1-2 Musashino Akishima-Shi, 196-8558 Tokyo, Japan) NeoScope JCM-6000Plus. Prior to imaging, the cantilevers were coated with gold sputtering.

5. Results

5.1. Errors affecting single strength values

To quantify the influence of the shift in loading position a on the measured strength, typical values of a were determined for five cantilevers of each type of specimen. For specimens of type A, the average shift was $a = -158\mu\text{m}$, with $a = -161\mu\text{m}$ and $a = -133\mu\text{m}$ for type B1 and B2, respectively. With these values, an average relative error in maximum stress between +1.6% and +3.7% is expected, depending on the position of failure, as displayed in Fig. 14. Combining the largest single value for the shift in load introduction $a = -281\mu\text{m}$ (measured on a specimen of type B1) with the shortest possible failure length $x = 4.4$ mm would yield a maximum error of about +6.4%.

Similarly, the influence of non-rectangular cross-sections is quantified by evaluating the shapes of ten cross-sections of each specimen type in detail. The section moment of the barrel shaped cross section W_{barrel} was determined numerically with CATIA Version 5.19 (Dassault Systèmes, 78140 Vélizy-Villacoublay, France) and compared to the ideal section moment W_{ideal} given through

$$W_{ideal} = \frac{b_{max}h_{max}^2}{6} \tag{9}$$

with b_{max} as the cross-section's maximum width and h_{max} as defined before. The relative error between W_{barrel} and W_{ideal} is calculated with

$$Rel. error[\%] = \frac{W_{ideal} - W_{barrel}}{W_{barrel}} \tag{10}$$

and the results are shown in Fig. 15. On average, the section moment will be overestimated by about 3.5%–5.7% if h_{max} and b_{max} are used for the calculation. This leads to the same underestimation for the maximum strength.

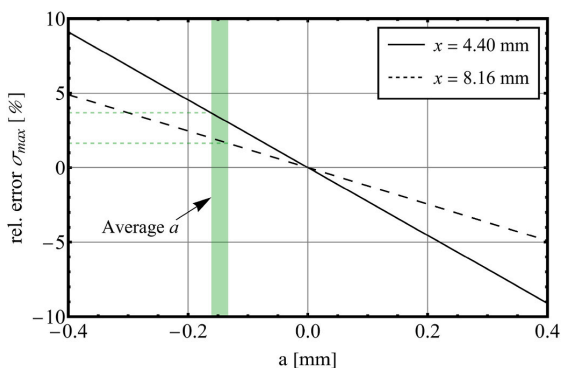


Fig. 14. Influence of the shift a in loading position on the maximum stress. The black through line represents the solution of eq. (8) for the upper limit (failures at the very beginning of the region of constant bending moment) of this effect, whereas the dashed black line indicates the solution for the lower limit (failures at the end of the region of constant bending moment). The green bar represents the range of typical average values of a for all three specimen types. (For interpretation of the references to colour in this figure legend, the reader is referred to the Web version of this article.)

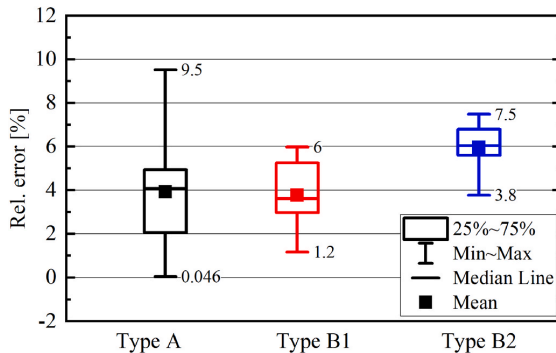


Fig. 15. Relative error between the barrel shaped cross-section and the ideal rectangular cross-section for each specimen type.

5.2. Errors affecting the Weibull distribution

The influence of utilizing average dimensions instead of individual dimensions on the Weibull evaluation is assessed through MC-analysis. The parameters of the underlying distributions for the dimensions h_{max} and α are given Table 2. They were determined with measurements taken from four specimens of the 0° configuration, with a minimum of 47 cantilevers per specimen. The final result of the MC analysis is the relative difference between the Weibull parameters determined with individual or average dimensional measurements. 1000 randomized runs were conducted, and the results are displayed as distribution densities in Fig. 16(a)-c).

Note that the extent of the deviation in σ_0 does decrease with an increased number of measurements for the average dimensions, while the extent of the deviation in m does not change substantially. In general, the center of the density distribution is at about +1% deviation in σ_0 and -12% deviation in m . Further investigations based on MC analysis have shown that the influence of Δh on the deviation of σ_0 and m is significantly higher than that of $\Delta \alpha$.

5.3. Strength and orientation dependency

The number of valid bending tests N , the characteristic strength σ_0 , and the Weibull modulus m as well as their respective 90% confidence intervals are given in Table 3 for each specimen. Table 4 gives the same parameters for a combined evaluation of multiple test specimens. This has only been performed if the confidence intervals of all test specimens included overlap. Fig. 17 displays the individual results of strength testing and for the combined evaluations sorted by each specimen type.

It is evident that the characteristic strength of both 15° configurations (Type B1 & B2) is lower than that of the 0° -configuration (Type A). The difference in characteristic strength between specimens of Type B1 and B2 is not statistically relevant as most of their confidence intervals overlap. The same is true for the Weibull modulus of each specimen type. Furthermore, significant differences between batches can be observed, e. g. specimens of batch two and three of Type A. An exemplary fracture surface for a specimen of Type B2 is given in Fig. 18. It is evident that the origin of failure is within the groove of the surface. This was found in the majority of observed cases. In the displayed case, the

Table 2
Parameters used for the normal distributed values of the height h_{max} and the opening angle α for the Monte-Carlo analysis.

Parameter	Mean μ	Standard deviation Δ
Height h_{max} [mm]	1.13	0.017
Opening angle α [°]	17.76	0.72

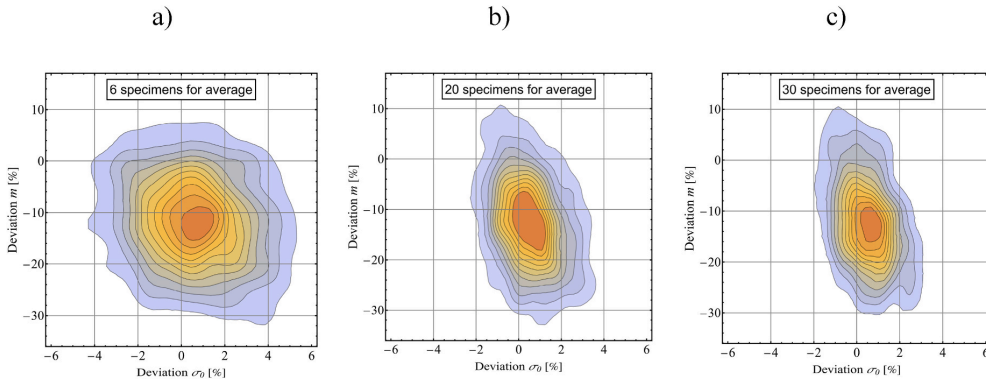


Fig. 16. Results of the MC analysis. Each figure shows the density distribution of the relative difference in m and σ_0 between individual and average dimension measurements for 1000 simulations. In a), 6 random dimensions are used to determine the average dimensions, 20 in b) and 30 in c).

Table 3

Results of strength testing for each specimen. N gives the number of valid bending tests, m and m_{ub} the biased and unbiased Weibull modulus, and σ_0 the characteristic strength with *lower* and *upper* indicating the respective 90% confidence intervals. The designation starts with the specimen type, followed by the batch number and finally the specimen number within that batch.

Type	Designation	N [-]	m [-]	m_{ub} [-]	m_{lower} [-]	m_{upper} [-]	σ_0 [-]	$\sigma_{0,lower}$ [-]	$\sigma_{0,upper}$ [-]
A	A.1.1	25	12.3	11.7	8.9	15.2	342	332	352
	A.1.2	19	12.4	11.5	8.5	15.8	352	340	365
	A.2.1	33	9.1	8.8	7.0	11.1	335	323	346
	A.2.2	29	10.7	10.2	8	13.1	336	326	348
	A.3.1	18	8.8	8.1	5.9	11.2	376	357	396
B1	A.3.2	32	11.5	11.0	8.7	13.9	364	354	375
	B1.1.1	44	16.3	15.8	13.0	19.2	301	296	306
	B1.1.2	41	13.7	13.3	10.8	16.3	287	281	293
	B1.2.1	27	9.9	9.4	7.3	12.2	320	309	332
	B1.3.2	32	8	7.7	6.1	9.8	281	270	292
B2	B2.1.1	47	13.6	13.2	10.9	15.9	323	317	330
	B2.1.2	47	12.3	11.9	9.9	14.5	296	290	302
	B2.2.2	29	15.9	15.2	11.8	19.5	317	311	324
	B2.3.1	44	11.5	11.2	9.2	13.6	333	325	341

Table 4

Results of the combined evaluation of strength testing results for specimens of type A.

Designation	N [-]	m [-]	m_{ub} [-]	m_{lower} [-]	m_{upper} [-]	σ_0 [-]	$\sigma_{0,lower}$ [-]	$\sigma_{0,upper}$ [-]
A.1.1+ A.1.2	44	12.2	11.8	9.7	14.4	347	339	354
A.2.1+ A.2.2	62	9.8	9.5	8.1	11.3	336	328	343
A.3 (A.3.1+ A.3.2)	50	10.0	9.8	8.1	11.7	369	360	378
A.1 & A.2 (A.1.1+ A.1.2 + A.2.1+ A.2.2)	106	10.6	10.4	9.2	11.9	340	335	346

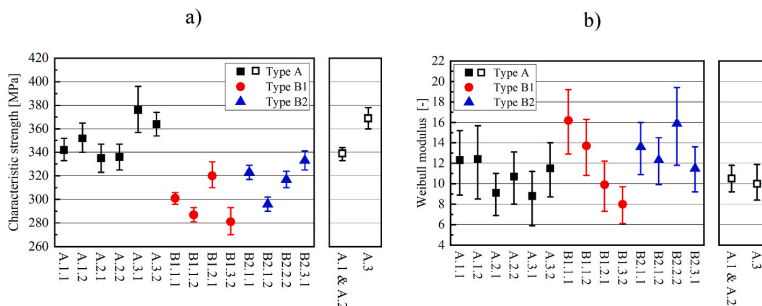


Fig. 17. a) shows the characteristic strength and b) shows the (unbiased) Weibull modulus of each tested specimen. The combined evaluation of multiple test specimens is displayed separately through the black open markers. The 90%-confidence intervals are given by the error bars.

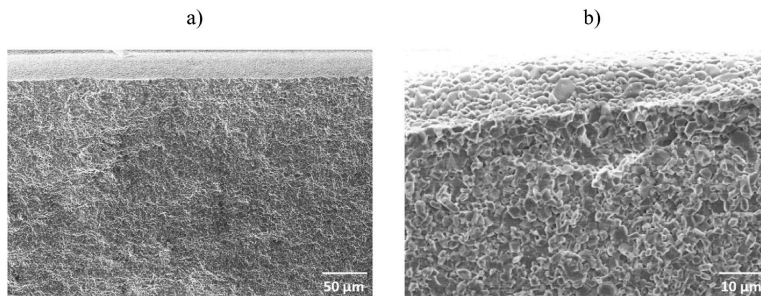


Fig. 18. SEM-image of a typical fracture surface of a 15°–180° specimen in a) with the failure-causing defect depicted in b).

failure is caused by a pore as shown in Fig. 18b).

To assess the influence of surface orientation on the measured strength, the surface structures are investigated in detail. Surface characterization has shown that specimens of Type A did not exhibit any surface structures except the regular surface roughness after sintering, which appeared on all specimen types. Therefore, this configuration will be considered as ideally flat for further comparison and discussions. Characterization of the surface structures of the other configurations revealed a periodical wave-like structure. This structure can be quantified with two parameters, the wavelength and the wave's amplitude. The average values for both 15° configurations are given in Table 5.

These structures were subsequently implemented in the sub-model and compared to the case of an ideal flat surface structure, i.e. specimens of Type A. As shown in Fig. 19, the maximum stress at the surface increases significantly. The stress increase for each type of specimen is given in Table 6. The maximum stress increases by about 54% for Type B1 and 45% for Type B2, with the maximum stress located in the valleys of the grooves. These are thus preferred locations for fracture.

Further results from FEA are the effective volume V_{eff} and effective surface S_{eff} . Each value was determined by utilizing the same normalization stress σ^* , that is the maximum tensile stress of specimen Type A. Note that for specimens of Type B1, the structured surface increases the effective volume by more than a factor of ten, while the effective surface increases by approximately 60%. The ratio σ_B/σ_A gives the influence of the increase in effective sizes on the measured strength based on either V_{eff} or S_{eff} . These results are also shown in Table 6.

6. Discussion

Regarding each individual strength result, the shift in ideal loading position a causes an average overestimation of the applied stress from 1.6% to 3.7%, which results in an underestimation of the materials' strength by the same amount. The further the cantilevers fail from the point of load introduction, the smaller this effect becomes. In this work, the majority of cantilevers failed at a distance of 6mm–7mm from the point of load introduction, meaning that the deviation in stress is likely to be smaller than 2.7%. Therefore, this effect is rather small and a does not have to be evaluated for each specimen, but the authors recommend to check this issue on several random cantilevers. In a similar way, the deviating shape of the cross section causes a general underestimation of the materials strength by 8%–10% through an overestimation of the section modulus. In combination with the problem of the shift in loading

Table 5
Average quantification parameters of the surface structures for each specimen type.

Parameter	Type A (0°)	Type B1 (15°)	Type B2 (15°–180°)
Amplitude [μm]	–	12.8	10.7
Wavelength [μm]	–	122.6	123.3

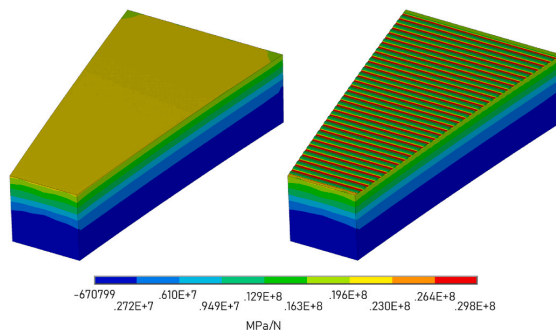


Fig. 19. Distribution of the first principal stress for an ideal specimen without surface structures (Type A, left) and with surface structures (Type B2, right). Both simulations were conducted for specimens with the same length and width. The height of the wavy specimen was chosen so that the zero line of the sinusoidal wave is the same as the height of the ideal specimen, which gives the same specimen volume.

Table 6
Relative increase of the maximum tensile stress σ_{max} , effective volume V_{eff} and effective surface S_{eff} for each specimen type as well as the expected change in the measured strength σ_B/σ_A due to the change in either V_{eff} or S_{eff} for $m = 10$.

Parameter	Flat surface Type A (0°)	Type B1 (15°)	Type B2 (15°–180°)
σ_{max}	1	1.54	1.45
V_{eff}	1	1.62	1.39
S_{eff}	1	12.82	8.45
$\sigma_B/\sigma_A (V_{eff})$	1	0.95	0.97
$\sigma_B/\sigma_A (S_{eff})$	1	0.78	0.8

position, an average underestimation of the material's strength of about 12% with an uncertainty of about ±4% remains, which is similar for all specimen types. This means that a direct comparison between different specimen types, i.e. different surface orientations, of the same material is feasible. If the absolute strength of the tested material is of high importance, both effects have to be checked and considered for strength evaluation.

Due to the dimensional inconsistency, the influence of utilizing average values for the cantilever's dimensions on the results of Weibull evaluation was investigated. Monte-Carlo analysis has shown that utilizing average values will slightly shift both the average characteristic strength (+1%) and the average Weibull modulus (–12%). While these values would still be acceptable, the possible deviation in m ranges from +10% to –30%, which is too much to allow Weibull evaluation with average dimensions. Increasing the number of measurements to

determine the average dimensions does not decrease the possible variation in Weibull modulus. Therefore, individual measurements of both the specimen's thickness and the opening angle for each cantilever are recommended to neglect this effect. However, the aforementioned uncertainty of $\pm 4\%$ for each individual strength result limits the maximum detectable scatter of the material's strength. With this uncertainty, a precise determination of the material's Weibull modulus m is possible for $m \leq 20$ [23].

The analysis of the influence of surface structures on the measured strength shows that the increase in effective surface from a flat to a structured specimen is notably larger than in effective volume. This is due to the surface structures mainly affecting the stress distribution at the surface and the first $10 \mu\text{m}$ of the bulk material. A long-range influence on the stress distribution in the bulk material was not detected. This forms a strong initial stress gradient from the increased surface stress towards the neutral plane. S_{eff} is only dependent on the stress in the edge fiber, where the stress increases the most. Additionally, the regions of increased stress make up a significant portion of the total surface, hence why a stress increase of 54% (to the power of $m = 10$) results in an extreme increase in S_{eff} . For V_{eff} , the regions of increased stress only make up a very small part of the total volume, which is why its increase is much smaller compared to that of S_{eff} . Usually, the defects found at the origin of failure are either surface defects (for which S_{eff} is relevant) or volume defects (for which V_{eff} is relevant). Therefore, these results give the upper and lower limits for the influence of the observed surface structures, with σ_B/σ_A as an estimation of the change in measured strength. The actual decrease in measured strength depends on whether the defects are more akin to surface- or volume defects.

The strength results obtained in this work show a significant drop-off in strength from the 0° configuration to the other configurations. This decrease is in good agreement with the expected results based on the concept of effective volume or surface and previous work [11,19]. It is evident that the influence of surface structures on the measured strength should not be neglected. This observation is further supported by the results of fractographic analysis, which shows that a high number of fractures originated in the grooves of the surface structures.

Despite these uncertainties, this novel testing method provides a number of promising advantages over common testing methods such as uniaxial and biaxial bending. First and foremost, it allows the fabrication of 96 test specimens, i.e. cantilevers, with a single manufacturing batch. This is well enough to perform a well-founded Weibull analysis on each specimen. Therefore, two different configurations could be manufactured within one batch, which further increases the time- and material efficiency of this method. Additionally, since all cantilevers are manufactured within one batch, it is possible to make out differences between individual batches and thermal treatments. Other methods often require a number of batches to fabricate the necessary number of specimens for statistical evaluation, which adds an additional layer of variation to those methods. This variation may stem from differences in specimen handling and cleaning or, if not handled properly, from modification of the slurry. The observed deviations from the ideal specimen geometry are the most important sources of error. If the non-rectangular cross-section of the cantilevers is not taken into account, a direct comparison of specimens manufactured from the same material is still possible. However, this error is too large to accurately determine the absolute characteristic strength and Weibull modulus of the utilized material. The other errors, which also affect the individual strength results, can be minimized by increasing the reproducibility during manufacturing. As an example, the specimens tested in this work were individually cleaned by hand, with low variations in the amount of solvent used. The solvent interacts with the specimen's surface and could therefore easily influence the measured results. Similarly, specimens were successively manufactured throughout three to five days without a complete exchange of slurry. During this time, interaction with the environment or contamination of the slurry might have occurred, changing the properties of the source material.

Taking these manufacturing-related effects into account, the next step in the development of this testing method would be a higher degree of automation. This includes procedures such as 3D-scanning the whole specimen, from which the cantilevers dimensions are evaluated automatically. Furthermore, a round robin with individual manufacturing and controlled testing could aid in determining the most important areas of improvement.

7. Summary

In this work, a new method for strength testing of additively manufactured materials is presented. The testing method is based on a novel specimen, which was designed to take the characteristics of additive manufacturing into account. On one hand, it was developed for time- and material efficient fabrication. Each specimen consists of a base plate and 48 cantilevers attached to it, thus generating enough data to perform statistical analysis. A large effective volume in comparison to well-known strength testing methods further contributes to the specimen's efficiency. On the other hand, the specimen can easily be adjusted so that different surface orientations can be investigated. This gives insight into the influence of surface structures on the measured strength, which vary significantly depending on the surface orientation.

Functional expressions for strength evaluation and the determination of effective volume and surface are given and validated with Finite Element Analysis (FEA). The influence of surface structures on the measured strength is analyzed based on Weibull theory and FEA. Other possible influences on the accuracy of this testing method are discussed through analytical considerations, Monte-Carlo analysis, and FEA. These effects are quantified based on practical observations and their impact is discussed. An example for a possible testing fixture is shown and demonstrated for multiple specimen configurations. More specifically, a minimum of four specimens for three different configurations were fabricated and tested. The results are evaluated statistically through Weibull theory. The observed influence of surface structures on the measured strength is in good agreement with the predictions based on FEA.

Overall, the deviation of the dimensions of the manufactured specimens from the ideal geometry limits the achievable accuracy of this testing method for strength determination. This effect can be minimized if the dimensions for each tested cantilever are individually recorded and if the fabrication process is streamlined and reproducibility is increased. However, the testing method can depict differences between different surface orientations and between specimens from each manufacturing batch. The latter is especially important for additive manufacturing, as regular testing methods such as uniaxial four-point bending and biaxial bending often require multiple batches to produce the necessary number of specimens for statistical analysis.

Data availability

Data will be made available on request.

Declaration of competing interest

The authors declare that they have no known competing financial interests or personal relationships that could have appeared to influence the work reported in this paper.

Acknowledgements

M. Staudacher gratefully acknowledges financial support by the Austrian BMVIT and BMWFW in the project "CharAM" (FGF 877684) of the COIN/IraSME program.

References

- [1] Z. Chen, Z. Li, J. Li, C. Liu, C. Lao, Y. Fu, C. Liu, Y. Li, P. Wang, Y. He, 3D printing of ceramics: a review, *J. Eur. Ceram. Soc.* 39 (2019) 661–687.
- [2] A. Zocca, P. Colombo, C.M. Gomes, J. Günster, Additive manufacturing of ceramics: issues, potentialities, and opportunities, *J. Am. Ceram. Soc.* 98 (2015) 1983–2001.
- [3] A. de Blas Romero, M. Pfaffinger, G. Mitteramkogler, M. Schwentenwein, C. Jellinek, J. Homa, A. Díaz Lantada, J. Stampfl, Lithography-based additive manufacture of ceramic biodevices with design-controlled surface topographies, *Int. J. Adv. Manuf. Technol.* 88 (2017) 1547–1555.
- [4] A.D. Lantada, A. de Blas Romero, M. Schwentenwein, C. Jellinek, J. Homa, Lithography-based ceramic manufacture (LCM) of auxetic structures: present capabilities and challenges, *Smart Mater. Struct.* 25 (2016), 54015.
- [5] S. Nachum, J. Vogt, F. Raether, Additive manufacturing of ceramics: stereolithography versus binder jetting, *Ceram. Forum Int.* 93 (2016).
- [6] N. Travitzky, A. Bonet, B. Dermeik, T. Fey, I. Filbert-Demut, L. Schlier, T. Schlördt, P. Greil, Additive manufacturing of ceramic-based materials, *Adv. Eng. Mater.* 16 (2014) 729–754.
- [7] M. Schwentenwein, J. Homa, Additive manufacturing of dense alumina ceramics, *Int. J. Appl. Ceram. Technol.* 12 (2015) 1–7.
- [8] D. Munz, T. Fett, *Ceramics: Mechanical Properties, Failure Behaviour, Materials Selection*, Springer, Berlin, Heidelberg, 1999.
- [9] T. Lube, M. Staudacher, A.-K. Hofer, J. Schlacher, R. Bermejo, Stereolithographic 3D printing of ceramics: challenges and opportunities for structural integrity, *Adv. Eng. Mater.* 25 (2023), 2200520.
- [10] T. Lube, J. Schlacher, W. Harrer, R. Danzer, G. Mitteramkogler, M. Schwentenwein, *Mechanische Eigenschaften von gedruckten Keramiken, Praktische Metallographie Sonderband*, 2018, pp. 229–234.
- [11] J. Schlacher, T. Lube, W. Harrer, G. Mitteramkogler, M. Schwentenwein, R. Danzer, R. Bermejo, Strength of additive manufactured alumina, *J. Eur. Ceram. Soc.* 40 (2020) 4737–4745.
- [12] ASTM C1161 - 18, Test Method for Flexural Strength of Advanced Ceramics at Ambient Temperature, ASTM International, West Conshohocken, PA, 2018.
- [13] DIN EN 843-1:2008-08, Advanced Technical Ceramics - Mechanical Properties of Monolithic Ceramics at Room Temperature - Part 1: Determination of Flexural Strength, German Institute for Standardisation (Deutsches Institut für Normung), 2008. German version EN 843-1:2006.
- [14] Werkstoffe und Bauteile auf dem Prüfstand. Prüftechnik - Kennwertermittlung - Schadensvermeidung, Tagung Werkstoffprüfung 2022, DGM, 2022.
- [15] A.L. Gebhardt, Prüfkörperauslegung und Ergebnisinterpretation für die Festigkeitsbewertung gedruckter flügraner Keramikstrukturen, Master's Thesis, Dresden, 2020.
- [16] S. Timoshenko, *History of Strength of Materials: with a Brief Account of the History of Theory of Elasticity and Theory of Structures*, Dover Publications, New York, 1983.
- [17] J.B. Wachtman, M.J. Matthewson, W.R. Cannon, *Mechanical Properties of Ceramics*, Wiley, Hoboken, N.J., 2009.
- [18] G.D. Quinn, Weibull strength scaling for standardized rectangular flexure specimens, *J. Am. Ceram. Soc.* 86 (2003) 508–510.
- [19] C. Liu, S. Aengenheister, S. Herzog, Y. Deng, A. Kaletsch, K. Schmitz, C. Broeckmann, Application of Weibull theory to laser surface textured Al2O3, *J. Eur. Ceram. Soc.* 41 (2021) 1415–1426.
- [20] E. Narvydas, N. Puodziuniene, A.K. Thorappa, Application of finite element sub-modeling techniques in structural mechanics, *Mechanika* 27 (2021) 459–465.
- [21] N.G. Cormier, B.S. Smallwood, G.B. Sinclair, G. Meda, Aggressive submodelling of stress concentrations, *Int. J. Numer. Methods Eng.* 46 (1999) 889–909.
- [22] R. Danzer, T. Lube, P. Supancic, Monte Carlo simulations of strength distributions of brittle materials – type of distribution, specimen and sample size, *Int. J. Mater. Res.* 92 (2001) 773–783.
- [23] R. Bermejo, P. Supancic, R. Danzer, Influence of measurement uncertainties on the determination of the Weibull distribution, *J. Eur. Ceram. Soc.* 32 (2012) 251–255.
- [24] DIN EN 843-5 2007, Advanced Technical Ceramics - Mechanical Properties of Monolithic Ceramics at Room Temperature - Part 5: Statistical Analysis, German Institute for Standardisation (Deutsches Institut für Normung), 2007.